TECHNISCHE
UNIVERSITÄT
DRESDEN

Fakultät Mathematik und Naturwissenschaften Fachrichtung Physik

Ab Initio Simulation of Warm Dense Matter: Combining Density Functional Theory and Linear Response Methods

Kushal Ramakrishna M.Sc.

Dissertation

to achieve the academic degree

Doctor rerum naturalium (Dr. rer. nat.)

First referee
Prof. Dr. Thomas Cowan
Second referee
Prof. Dr. Aurora Pribram-Jones
Supervisor
Dr. Jan Vorberger

Submitted on: July 11, 2022
Defended on: May 8, 2023

Abstract

Warm dense matter (WDM) is an extreme state of matter induced by extreme conditions and characterized as an intermediary state between (high-pressure) condensed matter and plasma. It has sparked a lot of attention in recent years as a result of current innovations in experiments and theoretical methods for modeling such complex systems. Such conditions naturally occur in astrophysical objects such as the interiors of the planets, and in white and brown dwarfs. WDM can be created in the laboratory via various methods such as laser compression, Z-pinches and heated diamond anvil cells.

This thesis describes the results obtained for many such systems across a range of conditions modeled using *ab-initio* simulation methods. The first testbed concerns the electronic structure and linear response of the carbon phases under high-pressure and warm dense matter conditions. The focus is on modeling inelastic x-ray scattering spectra across a range of conditions useful for the analysis and interpretation of x-ray Thomson scattering (XRTS) experiments. Another major goal is to improve the existing models to compute static properties such as the equation of state, density of states with the inclusion of highly accurate data from quantum Monte Carlo (QMC) simulations relevant at finite-temperatures. This approach improves the accuracy and is also computationally inexpensive compared to path integral Monte Carlo (PIMC) methods. Lastly, improvements in linear response theory relevant for XRTS are incorporated with the inclusion of local field corrections (LFC) and finite-temperature local field corrections (T-LFC) using data from QMC simulations.

Publications by the Author

- *K. Ramakrishna* and J. Vorberger. "Ab initio dielectric response function of diamond and other relevant high pressure phases of carbon". *J. Phys.: Condensed Matter* ***32****, 095401 (2020)* DOI: `10.1088/1361-648x/ab558e`.
- M. Bonitz, T. Dornheim, Zh. A. Moldabekov, S. Zhang, P. Hamann, H. Kählert, A. Filinov, *K. Ramakrishna*, and J. Vorberger. "Ab initio simulation of warm dense matter". *Physics of Plasmas* ***27****, 042710 (2020)* DOI: `10.1063/1.5143225`.
- *K. Ramakrishna*, T. Dornheim and J. Vorberger. "Influence of finite temperature exchange-correlation effects in hydrogen". *Phys. Rev. B* ***101****, 195129 (2020)* DOI: `10.1103/PhysRevB.101.195129`.
- S. Frydrych, J. Vorberger, N. J. Hartley, A. K. Schuster, *K. Ramakrishna*, A. M. Saunders, T. van Driel, R. W. Falcone, L. B. Fletcher, E. Galtier, E. J. Gamboa, S. H. Glenzer, E. Granados, M. J. MacDonald, A. J. MacKinnon, E. E. McBride, I. Nam, P. Neumayer, A. Pak, K. Voigt, M. Roth, P. Sun, D. O. Gericke, T. Döppner and D. Kraus. "Demonstration of X-ray Thomson scattering as diagnostics for miscibility in warm dense matter", *Nature Communications* ***11****, 2620 (2020)* DOI: `10.1038/s41467-020-16426-y`.
- T. Dornheim, A. Cangi, *K. Ramakrishna*, M. Böhme, S. Tanaka and J. Vorberger. "Effective Static Approximation: A Fast and Reliable Tool for Warm-Dense Matter Theory", *Phys. Rev. Lett.* ***125****, 235001 (2020)* DOI: `10.1103/PhysRevLett.125.235001`.
- *K. Ramakrishna*, A. Cangi, T. Dornheim, A. Baczewski and J. Vorberger. "First-principles modeling of plasmons in aluminum under ambient and extreme conditions", *Phys. Rev. B* ***103****, 125118 (2021*) DOI: `10.1103/PhysRevB.103.125118`.
- K. Voigt, M. Zhang, *K. Ramakrishna*, A. Amouretti, K. Appel, E. Brambrink, V. Cerantola, D. Chekrygina, T. Döppner, R. W. Falcone, K. Falk, L. B. Fletcher, D. O. Gericke, S. Göde, M. Harmand, N. J. Hartley, S. P. Hau-Riege, L. G. Huang, S. Humphries, M. Lokamani, M. Makita, A. Pelka, C. Prescher, A. K. Schuster, M. Šmíd, T. Toncian, J. Vorberger, U. Zastrau, T. R. Preston and D. Kraus. "Demonstration of an X-ray Raman Spectroscopy setup to study warm dense carbon at the High Energy Density Instrument of European XFEL", *Physics of Plasmas* ***28****, 082701 (2021)* DOI: `10.1063/5.0048150`.
- S. Nikolov, J. Tranchida, *K. Ramakrishna*, M. Lokamani, A. Cangi and M. Wood. "Dissociating the phononic, magnetic and electronic contributions to thermal conductivity: a computational study in alpha-iron", *Journal of Materials Science* ***1573-4803****, (2022)* DOI: `10.1007/s10853-021-06865-3`.
- *K. Ramakrishna*, M. Lokamani, A. Baczewski, J. Vorberger and A. Cangi. "Electrical conductivity of iron in earth's core from microscopic Ohm's Law", *Phys. Rev. B* ***107****, 115131 (2023*) DOI: `10.1103/PhysRevB.107.115131`.

- T. Dornheim, Zh. A. Moldabekov, *K. Ramakrishna*, P. Tolias, A. Baczewski, D. Kraus, T. R. Preston, D. Chapman, M. Böhme, T. Döppner, F. Graziani, M. Bonitz, A. Cangi and J. Vorberger. "Electronic density response of warm dense matter", *Physics of Plasmas* ***30****, 032705 (2023)* DOI: `10.1063/5.0138955`.
- D. Ranjan, *K. Ramakrishna*, K. Voigt, O. S. Humphries, B. Heuser, M. G. Stevenson, J. Lütgert, Z. He, C. Qu, S. Schumacher, P. T. May, A. Amouretti, K. Appel, E. Brambrink, V. Cerantola, D. Chekrygina, L. B. Fletcher, K. Falk, S. Göde, M. Harmand, N. J. Hartley, S. P. Hau-Riege, M. Makita, A. Pelka, A. K. Schuster, M. Šmíd, T. Toncian, M. Zhang, T. R. Preston, U. Zastrau, J. Vorberger, and D. Kraus. "Toward using collective x-ray Thomson scattering to study C–H demixing and hydrogen metallization in warm dense matter conditions ", *Physics of Plasmas* ***30****, 052702 (2023)* DOI: `10.1063/5.0146416`.

Contents

1 Introduction 2
1.1 Thesis Outline 7

2 Theoretical Description 9
2.1 Plasma Theory 11
2.1.1 Random Phase Approximation 11
2.1.2 Local Field Corrections 15
2.1.3 Mermin Function 18
2.2 Theoretical Description of the X-ray Scattering Signal 19
2.3 Density Functional Theory 22
2.3.1 Exchange-Correlation Functionals 25
2.3.2 Finite-Temperature Exchange-Correlation Functionals 27
2.3.3 Density Functional Theory-Molecular Dynamics 29
2.3.4 Kubo-Greenwood Formula 31
2.4 Time-Dependent Density Functional Theory 31
2.5 GW Approximation 35
2.6 Bethe-Salpeter Equation 38
2.7 Conclusions 42

3 Ab Initio Dielectric Response Function of Diamond and Other Relevant High-Pressure Phases of Carbon 45
3.1 Electronic Properties under High-Pressure 48
3.1.1 Diamond 49
3.1.2 Lonsdaleite 52
3.1.3 BC8 54
3.2 Linear Response under Ambient and High-Pressure Conditions 57
3.2.1 Diamond 58
3.2.2 Lonsdaleite 62
3.2.3 BC8 65
3.3 Linear Response under Warm Dense Matter Conditions 66
3.4 X-ray Thomson Scattering 71
3.5 X-ray Raman Scattering 74
3.6 Conclusions 79

4 Influence of Finite-Temperature Exchange-Correlation Effects in Hydrogen 81
4.1 Computational Details 86
4.2 High-Pressure Fluid 89
4.3 Warm Dense Matter 93
4.4 Moderately Coupled Plasma and Electron Liquid Regime 96
4.5 Density of States 99
4.6 Electronic Density 99
4.7 Conclusions 102

5 Ab Initio Modeling of Plasmons in Aluminum under Ambient and Extreme Conditions 104
5.1 Computational Details 106
5.2 Ambient Conditions 108
5.2.1 Dynamic Structure Factor 108
5.2.2 Plasmon Dispersion 111
5.2.3 Plasmon Lifetimes 111
5.3 Extreme Conditions 113
5.3.1 Plasmon dispersion 114
5.3.2 Plasmon Lifetimes 116
5.3.3 Temperature Dependence of the Dynamic Structure Factor 117
5.3.4 Static Structure Factor 120
5.4 Conclusions 121

6 Conclusions and Perspectives 122

Bibliography 127

List of Tables 161

List of Figures 163

Appendix 174
.1 List of Acronyms 175
.2 Codes Utilized in this Work 177

Statement of authorship 183

1 Introduction

The study of warm dense matter (WDM) is an exciting topic as it encompasses a wide variety of distinct physical regimes. At the crossroads of condensed matter and non-ideal plasmas, the theoretical description of WDM faces several obstacles as the interplay of several physical effects, none of which can be treated perturbatively, makes the theoretical description of WDM challenging [Davidson, 2003]. There is no straightforward way to develop models based on the restriction imposed by the density-temperature parameter space along with other approximations. The parameters are characterized as follows [Graziani et al., 2014, Bonitz, 2016, Bonitz et al., 2020, Dornheim et al., 2023]:

- Electron degeneracy parameter

$$\theta = \frac{T}{T_F}. \tag{1.0.1}$$

- Degeneracy parameter

$$\chi = n_e \Lambda^3. \tag{1.0.2}$$

- Thermal de Broglie wavelength

$$\Lambda = \frac{\sqrt{2\pi}\hbar}{\sqrt{mK_BT}}. \tag{1.0.3}$$

- Electron Fermi energy

$$E_F = \frac{\hbar^2(3\pi^2 n_e)^{2/3}}{2m}. \tag{1.0.4}$$

- Brueckner parameter

$$r_s = \frac{a}{a_B}. \tag{1.0.5}$$

- Coupling parameter

$$\Gamma = \frac{E_{pot}}{E_{kin}} = \frac{1}{aK_BT}, \tag{1.0.6}$$

where K_B is the Boltzmann constant, $\hbar$ is the reduced Planck constant, m is the electron mass, a_B is the Bohr radius, a is the average separation between two electrons in the medium, n_e is the electron density, E_{pot} and E_{kin} are the potential and kinetic energy terms respectively, T is the the electronic temperature, and T_F is the Fermi temperature where thermal effects are comparable to quantum effects.

Here, r_s is related to the density of the system by $r_s = (3/4\pi n_e)^{1/3}$. In the limit of high density ($r_s \to 0$) at low temperatures, the electrons exhibit ideal Fermi gas behavior and in the low density, low temperature limit, Wigner crystallization can occur due to the dominance of the Coulomb repulsion [Wigner, 1934]. The degeneracy parameter $\theta \leq 1$ characterizes a degenerate quantum system and in the classic limit, it holds $\theta \gg 1$. The coupling parameter indicates

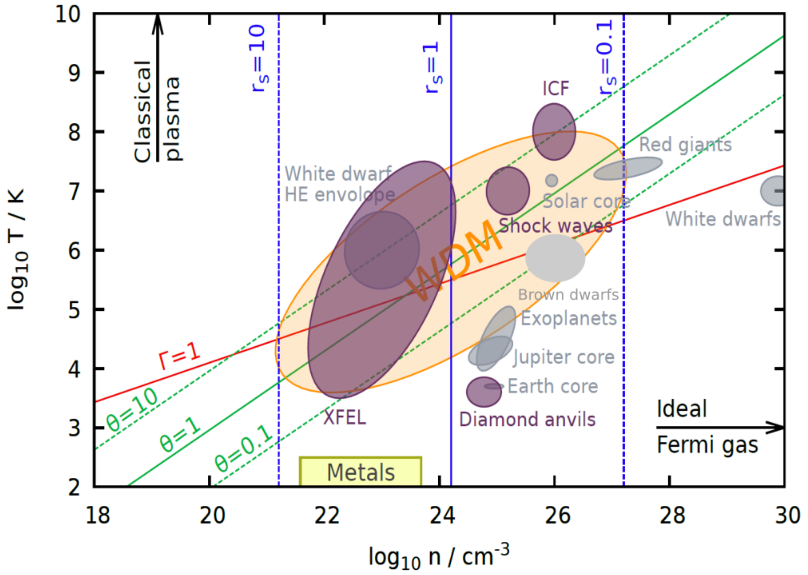

Figure 1.0.1: The temperature and the density plane describing warm dense parameters. The x-axis corresponds to the electronic density in logarithmic scale. The y-axis corresponds to the temperature in logarithmic scale. The electronic parameters are fully defined by (r_s, θ). The coupling parameter Γ as it is given in the figure follows from (r_s, θ). Republished with permission of Elsevier from The uniform electron gas at warm dense matter conditions, Physics Reports **744**:1-86 (2018) [Dornheim et al., 2018a]. Permission conveyed through Copyright Clearance Center, Inc.

the interplay of the kinetic and the potential energy. In the WDM regime, $\Gamma \approx 1$ hence both the terms have to be treated effectively and many-body interactions are still determining the physics. When $\Gamma << 1$, the system is weakly coupled with the kinetic energy dominating and when $\Gamma >> 1$ the system is strongly coupled. Figure. 1.0.1 gives an overview of the parameters describing WDM and the conditions encountered in experiments and astrophysical systems.

Significant progess has been made in studying warm dense matter with the aid of *ab-initio* methods. The most common simulation technique includes the combination of density functional theory (DFT) and molecular dynamics (MD) commonly denoted as DFT-MD. DFT is effectively an equilibrium theory applicable to systems of any temperature (Mermin formulation) [Hohenberg and Kohn, 1964, Kohn and Sham, 1965, Mermin, 1965], but is heavily reliant on the XC functional to incorporate (temperature dependent) many-body interactions within the electronic subsystem [Car and Parrinello, 1985, Rahman, 1964, Allen and Tildesley, 2017, Mermin, 1965]. In the Mermin formulation, the Hohenberg-Kohn theorem applicable to the ground state is extended to $T\neq0$ for an inhomogeneous electron gas at local thermodynamic equilibrium. This is based on minimizing the grand potential at a constant temperature and chemical potential in the grand canonical ensemble [Hohenberg and Kohn, 1964, Kohn and Sham, 1965, Mermin, 1965]. Hence exchange correlation (XC) functionals developed for studying solid state systems in their ground state only take the implicit temperature dependence into account, but neglect the explicit temperature dependence of correlated electrons. The *ab-initio* approach which, so far, has been moderately successful in modeling WDM, uses this approach of treating the electrons at $T=0$ via DFT and the ions at $T\neq0$ using classical

MD. For the solution of the Schrödinger equation in DFT, to minimize the computational cost and the complexity, the Born-Oppenheimer approximation is employed. Under this assumption, the electronic and the nuclear motion in a molecule can be treated separately based on the physical basis that the nuclear mass are heavier than the electrons. This difference leads to the nuclear motion much more slower than the electrons. Hence a good approximation to describe the electronic states of a molecule are by treating the nuclei as stationary. The treatment follows the adiabatic connection and reduces the computational cost. By treating the ions and electrons on a similar time scale more dynamic information of the electronic component can be evaluated which is now possible with novel non-adiabatic methods such as Ehrenfest dynamics [Li et al., 2005, Walter et al., 2008, Tully, 2012, Ojanperä et al., 2012, Curchod et al., 2013, Ding et al., 2015, Magyar et al., 2016, Correa, 2018] and Bohmian mechanics [Larder et al., 2019]. Further developments include stochastic DFT [Baer et al., 2013, Cytter et al., 2018, Fabian et al., 2019, Cytter et al., 2019] providing a bridge between Kohn-Sham (KS) DFT [Kohn and Sham, 1965] and orbital-free methods which is generally fast, but inaccurate, potentially helpful at high temperature. This is achieved by computing the electron density directly from the KS-Hamiltonian using a trace formula henceforth avoiding the computation of density matrix or KS orbitals. White *et al.* [White and Collins, 2020] have further extended this scheme to work at a wide range of temperatures using a stochastic-deterministic scheme avoiding the computational cost and the stochastic errors encountered in intermediate temperatures with the stochastic DFT scheme.

The equation of state (EOS) describes the state of matter under equilibrium conditions using thermodynamic variables. It is essential for describing the properties of elemental solids, fluids, and gases, as well as real materials as mixtures of elements. In WDM, it is particularly important for modeling the interiors of planets under high pressures and temperatures [Nettelmann et al., 2008], in white dwarfs [Kritcher et al., 2020] and also for modelling the conditions of inertial confinement fusion (ICF) [Ross, 1981, Kraus et al., 2017, Kraus et al., 2018, Knudson et al., 2008, Biener et al., 2009, Atzeni and Meyer-ter Vehn, 2004, Hurricane et al., 2014, Moses et al., 2009]. Standard EOS using *ab-initio* methods are based on the data obtained from DFT-MD or path integral Monte Carlo (PIMC) simulations with considerable agreement between the two methods. Currently, the "zero-temperature approximation" do not take into account the temperature of the system which is very relevant for building accurate EOS models [Karasiev et al., 2016, Bonitz et al., 2020, Ramakrishna et al., 2020]. Improvements in the WDM regime are now possible thanks to the advancements in XC functionals with the availability of data from accurate PIMC simulations for the uniform electron gas (UEG) in the WDM regime [Brown et al., 2013a, Malone et al., 2016, Dornheim et al., 2016b, Groth et al., 2017c, Dornheim et al., 2018a, Dornheim, 2018, Bonitz et al., 2020]. The derived temperature dependent XC functionals can now be used in the simulations involving DFT to treat the electrons at $T \neq 0$, with the inclusion of the XC free energy as a function of density and temperature. Further improvements in finite-temperature XC functionals are possible with the effort led by Karasiev *et al.* and co-workers. They have further extended the LDA finite-temperature XC to the generalized gradient approximation (GGA) and meta-GGA forms which are effectively better in treating hydrogen bonds and molecular systems. They have reported better Hugonoit results for deuterium through their parametrized finite-temperature GGA XC functional. Their effort seems to be promising as they are on the way to developing hybrid functionals, a research that might eventually lead to the development of the whole suite of the "Jacob's ladder" [Perdew and Schmidt, 2001] of finite-temperature XC functionals [Karasiev et al., 2013, Karasiev et al., 2014c, Karasiev et al., 2014b, Karasiev et al., 2014a, Karasiev et al., 2016, Luo et al., 2018, Karasiev et al., 2019a, Mihaylov et al., 2020, Luo et al., 2020, Karasiev et al., 2022] and with a systematic construction of XC functionals with explicit temperature dependence [Baldsiefen et al., 2015, Baldsiefen et al., 2017]. Shen *et al.* [Zhang et al., 2016, Blanchet et al., 2020] have developed an extended first principles molecular dynamics (FPMD) based on the KS scheme to treat systems at elevated temperatures by using the plane wave approximation of the electrons at high temperatures and densities. The computational cost for large systems can be reduced with the use of orbital-free DFT-MD with the exclusion of KS orbitals. This is achieved by constructing an approximation for the kinetic energy functional which is otherwise fully dependent on the orbitals based on the KS functionals. Under the KS approach, the kinetic energy term is accurately obtained and hence the success of orbital-free approach heavily relies on the formulation of the kinetic energy density functionals [Pearson et al., 1993, Wang and Carter, 2002, Karasiev and Trickey, 2012, Cangi and Pribram-Jones, 2015]. Traditional plane-wave codes become difficult at low density and high temperatures because the number of partially occupied states increases dramatically. The unique Spectral Quadrature DFT (SQDFT) approach for large-scale parallel KS DFT calculations, addresses this issue [Suryanarayana et al., 2018, Bethkenhagen et al., 2020]. These developments in *ab-initio* methods can result in accurate EOS with less computational cost.

Linear response theory is an important part of the theoretical description of the x-ray scattering signal or electrical conductivity as obtained in experiments on WDM. Through it, important physics parameters like temperature, density, charge state, and the structure of the system might be infered. Diagnostics such as electron temperature can be extracted through the detailed balance relation of the dynamic structure factor using x-ray Thomson scattering (XRTS). Traditionally, plasma theory or Kubo-Greenwood approach with DFT-MD are used to model XRTS spectra [Fortmann et al., 2010, Plagemann et al., 2012]. With the advancements in time-dependent density functional theory (TDDFT) and better local field corrections (LFC), the available tools provide a more realistic description of XRTS. The linear-response TDDFT (LR-TDDFT) [Gross and Kohn, 1985] is based on the KS orbitals obtained using DFT which are further required for the computation of the density response function using an appropriate form of the exchange-correlation (XC) kernel. The XC kernel for LR-TDDFT includes the many-body effects and is an active topic of interest [Onida et al., 2002, Böhme et al., 2022, LeBlanc et al., 2022]. Real-time TDDFT (RT-TDDFT) [Yabana and Bertsch, 1996, Yabana et al., 2006] involves propagating the integrals over time instead of the frequency space approach of LR-TDDFT. By moving to the domain of real-time and real-space, information on a shorter time scale can be obtained providing insight into the dynamics of the system [Provorse and Isborn, 2016]. The challenges included in this approach is in obtaining the spectra with the application of windowing techniques and efficient algorithms for the propagator with the advantages of a computational linear scaling compared to cubic scaling of LR-TDDFT. Baczewksi *et al.* [Baczewski et al., 2016, Baczewski et al., 2021] have produced groundbreaking simulations with the help of RT-TDDFT for compressed beryllium which can treat large finite momentum transfers effectively, contrary to LR-TDDFT [Mo et al., 2020]. This also allows one to access other experimental quantities like stopping power [Yost et al., 2017, Yao et al., 2019] and electrical conductivity [Andrade et al., 2018, Ramakrishna et al., 2023] via the dielectric response function. Further improvements in linear response are possible with the availability of the finite-temperature local field corrections obtained using PIMC simulations much relevant for experiments involving XRTS [Dornheim et al., 2020a, Ramakrishna et al., 2021]. These can be included in linear response calculations as a free parameter based on the density-temperature parameter space of the system and is a cost-effective way of improving the models without resorting to computationally expensive methods [Groth et al., 2019, Dornheim et al., 2019, Bonitz et al., 2020, Dornheim et al., 2020a, Dornheim et al., 2022, Dornheim et al., 2023].

1.1 Thesis Outline

Chapter 1 outlines the motivation of studying WDM and the challenges. Chapter 2 contains a theoretical review of the *ab-inito* methods used in this work. The main results of the study are presented in the following Chapters 3-5. The systems considered and the results of several publications describing them in detail are used to categorize them. In the end, Chapter 6 summarizes this work discussing the current results and further developments.

- Chapter 3: Ab Initio Dielectric Response function of Diamond and Other Relevant High-Pressure Phases of Carbon

  The electronic structure of the high-pressure carbon phases are computed using DFT and the linear response using many-body perturbation theory. The linear response under high-pressure and warm dense matter conditions are computed using the random phase approximation (RPA), time-dependent density functional theory (TDDFT), and the Bethe-Salpeter equation (BSE). These approximations are compared based on the accuracy and the computational complexity. Furthermore, various approximations are used in the linear response theory to model x-ray Thomson scattering (XRTS) and x-ray Raman scattering (XRS) as obtained in recent experimental campaigns. TDDFT is used to fit the inelastic XRTS signal of diamond essential for understanding the miscibility in WDM experiments involving carbon-hydrogen mixtures. X-ray absorption spectroscopy (XAS) measurements under the warm dense matter regime pose a significant challenge, particularly for low-Z materials which have K-edge energies in the soft x-ray regime. A potential alternative that overcomes the difficulties of XAS measurements of transmission on low-Z materials is the study of XRS, which can provide similar details. The XRS spectra is computed for diamond under ambient, compressed and iscohorically heated conditions. This presents an opportunity to examine phase transitions and the effect of pressure and temperature on the electronic structure of carbon in the WDM regime.

- Chapter 4: Influence of Finite-Temperature Exchange-Correlation Effects in Hydrogen

  Finite-temperature exchange correlation (XC) effects are included in density functional theory using the KS approach by replacing the XC energy $E_{\mathrm{XC}}(r_s)$ with the XC free energy $f_{\mathrm{XC}}(r_s, \theta)$. This is obtained via parametrized path integral Monte Carlo (PIMC) data for the uniform electron gas (UEG) at WDM conditions within the local density approximation (LDA). Using DFT-MD, static properties such as equation of state (EOS) and density of states (DOS) can be computed. The standard EOS is computed using the ground state XC (T=0), which is not accurate at the extreme conditions encountered in WDM and electron liquid regimes. Significant changes in the EOS are observed in the WDM regime. In the electron liquid regime, the EOS shows larger impact (up to 20% at r_s=14). Improvements to the EOS and other static properties are of relevance to many applications such as quantum hydrodynamics and in astrophysical models.

- Chapter 5: Ab Initio Modeling of Plasmons in Aluminum under Ambient and Extreme Conditions

  The theoretical framework for numerical modeling of plasmon behavior are crucial for accurate diagnostics and interpretation of the x-ray scattering experiments. The use of linear-response time-dependent density functional theory (LR-TDDFT) is highlighted as an appropriate first-principle framework for consistent modeling of plasmon properties from ambient to warm dense conditions. For various scattering angles and sample conditions, we exemplify our assessment of properties such as the dynamic structure factor, static structure factor, the plasmon dispersion, and the plasmon lifetimes on experimental measurements of aluminum accessible through x-ray Thomson scattering (XRTS). The accuracy of LR-TDDFT is evaluated by comparing with other dielectric models such as the basic Lindhard function, the Mermin approximation based on parametrized collision frequencies, and the recently developed static local field corrections from path integral Monte Carlo (PIMC) data for the uniform electron gas (UEG) at finite-temperature. The results of this study indicate that the theoretical methods so far involved in obtaining the XRTS spectra are not sufficient and further improvents are essential via local field corrections and better XC functionals.

2 Theoretical Description

In this chapter, the description of the theoretical models is presented in order to understand the methodology behind the *ab-initio* methods starting from the established basics to the incorporation of new techniques. The properties are given in a quantum mechanical description which is later required to understand the theoretical description of the x-ray scattering spectrum. Moving on to the main focus of this work, density functional theory (DFT) is presented with its various approximations. The essence of the DFT scheme is that the many-body problem is formulated within a single-particle theory, where the many-body complexity of the problem enters through an exchange-correlation (XC) functional. DFT is generally labelled as a ground-state theory quite incorrectly and with few exceptions [Oliveira et al., 1990, Levy, 1995, Petersilka et al., 1996] is used primarily for the treatment of electronic ground states and their properties [Görling, 1996]. Hence, the language of Green's function is utilized to understand the excited state properties through many-body theory and in obtaining the linear response. Various cases are presented in dealing with the many-body effects and computational complexity.

2.1 Plasma Theory

A plasma consists of a system of many species i.e., charged particles like electrons and ions of varying masses and densities. In equilibrium, the distribution of momenta of particles of a species is given by the Boltzmann distribution for the classical/non-degenerate case

$$f(p) = e^{-\beta(\frac{p^2}{2m}-\mu)}, \tag{2.1.1}$$

where μ is the chemical potential, m the mass of the particle species, and $\beta = 1/K_BT$. Using the definition of the thermal wavelength $\Lambda = (h/\sqrt{2\pi m K_B T})$, plasmas can be categorized based on the spin statistic theorem as

a) non-degenerate and Boltzmann-like for $n\Lambda^3 \ll 1$,
b) as strongly degenerate for $n\Lambda^3 \gg 1$,

where n is the density of the species [Kremp et al., 2006]. Considering the quantum nature of the particles, the Fermi-Dirac distribution applies for particles of half-integer spin

$$f(p) = \frac{1}{e^{\beta(\frac{p^2}{2m}-\mu)} + 1}, \tag{2.1.2}$$

and for an integer spin, the Bose-Einstein distribution is valid

$$f(p) = \frac{1}{e^{\beta(\frac{p^2}{2m}-\mu)} - 1}. \tag{2.1.3}$$

2.1.1 Random Phase Approximation

The Lindhard dielectric function [Lindhard, 1954] also commonly known as RPA is an approximation widely applicable to condensed matter, plasma, and nuclear physics describing the collective properties of interacting electrons (jellium model) surrounded by an uniform positive background charge. It accounts for the weakly screened Coulomb interaction and is used to explain the linear response of a free electron gas at a mean-field level. This is based on the collective work of Bohm and Pines in a series of papers [Bohm and Pines, 1951, Pines and Bohm, 1952, Bohm and Pines, 1953] which explains the collective behavior of the electron gas, including plasmons. The formulation was later proved to be the equivalent of summing ring diagrams based on diagrammatic perturbation theory originating from quantum electrodynamics (QED) [Gell-Mann and Brueckner, 1957] shown in Fig. 2.1.1. The graphical notation and the *bubble diagram* are further explored in section 2.5.

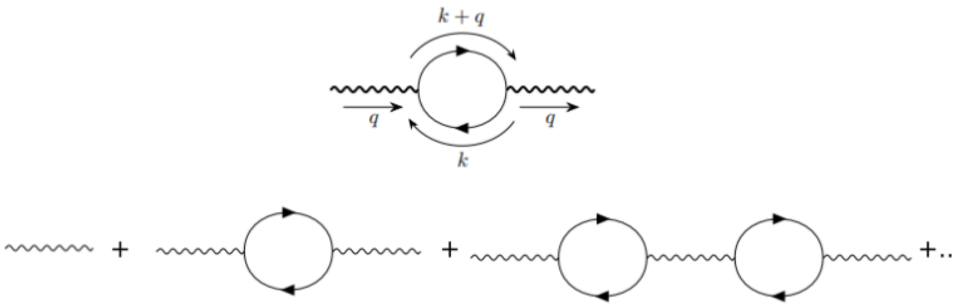

Figure 2.1.1: The bubble diagram and the diagramatic sum of the Feynman diagrams to obtain the RPA sum.

The correlation functions of the density response function $\Pi^{\gtrless}_{ab}$ for species a and b can be represented in RPA using the correlation functions of the single-particle Green's function $g^{\gtrless}_{a}$. The retarded polarization function in the frequency space (ω) at a certain momentum (q) can be represented in the integral form as [Kremp et al., 2006]

$$\Pi^R_{ab}(q,\omega) = i\int \frac{d\omega'}{2\pi}\frac{\Pi^>_{ab}(q,\omega') - \Pi^<_{ab}(q,\omega')}{\omega-\omega'+i\mathcal{E}}, \tag{2.1.4}$$

where $\mathcal{E}$ is energy in the complex plane.

Substituting the form $\Pi^{\gtrless}_{ab}(12) = -\delta_{ab}g^{\gtrless}_{a}(12)g^{\lessgtr}_{a}(12)$ and the use of spectral representation for the single particle correlation functions

$$\pm ig^<(p,\omega) = 2\pi\delta[\hbar\omega - E(p)[f(p), \tag{2.1.5}$$

$$\pm ig^>(p,\omega) = 2\pi\delta[\hbar\omega - E(p)]\,(1\pm f(p))\,, \tag{2.1.6}$$

where $f(p)$ is the Fermi-Dirac distribution. The polarization function can be further simplied to the form

$$i\Pi^{\gtrless}_{aa}(q,\omega) = \int\frac{d^3p}{(2\pi\hbar)^3}2\pi\delta[\omega - E(p+q) + E(p)]f^{\gtrless}(p+q)f^{\lessgtr}(p), \tag{2.1.7}$$

$$\Pi^R_{aa}(q,\omega) = \int \frac{d^3p}{(2\pi\hbar)^3} \frac{f_a(p) - f_a(p+q)}{\hbar\omega + E(p) - E(p+q) + i\mathcal{E}}. \tag{2.1.8}$$

Using the expression for the dielectric function

$$\varepsilon(q,\omega) = 1 - \sum_{a,b} V_{ab}(q)\Pi_{ab}(q,\omega), \tag{2.1.9}$$

where $V_{ab}(q)$ is the Coulomb potential between species a and b. The dielectric function is written in an integral form as

$$\varepsilon(q,\omega) = 1 + \sum_{a,s^z_a} \frac{4\pi\hbar^2 e_a^2}{q^2} \int \frac{d^3p}{(2\pi\hbar)^3} \frac{f_a(p+q) - f_a(p)}{\hbar\omega + E(p) - E(p+q) + i\mathcal{E}}, \tag{2.1.10}$$

where s^z_a accounts for the spin of the system for species a.

Using the Sokhotski-Plemelj theorem [Sokhotskii, 1873],

$$\lim_{\mathcal{E}\to 0^+} \int_a^b \frac{f(x)dx}{x - x_0 \pm i\mathcal{E}} dx = \int_a^b \frac{f(x)}{x - x_0} \mp i\pi \int_a^b \delta(x - x_0) f(x) dx, \tag{2.1.11}$$

the imaginary part of the dielectric function reduces to

$$\Im[\varepsilon(q,\omega)] = \sum_{a,s^z_a} \frac{4\pi\hbar^2 e_a^2}{q^2} \int \frac{d^3p}{(2\pi\hbar)^3} \delta\left[\hbar\omega + E(p) - E(p+q)\right]\left(f_a(p) - f_a(p+q)\right). \tag{2.1.12}$$

The limits of the momentum integral are given by evaluating $\hbar\omega = \frac{p^2}{2m} + \frac{q^2}{2m} + \frac{2pq\cos\theta}{2m}$. Since $\cos\theta \to [-1,1]$, the limits of the integral are obtained as $p = \frac{q}{2} \pm \frac{\hbar m\omega}{q}$. The consideration of the electron-hole pairs in the electron gas are explained by the limits. Considering an electron of initial momentum p and energy E_p is excited by a perturbation (q,ω). The new state of the electron is given by momentum p+q and energy $E_{p+q} = E_q + \omega$. The electron can only scatter to states which are unoccupied, hence E_{p+q} is above the occupied Fermi sea of electrons, and the process excites an electron from below to above the Fermi level leaving a vacancy in the Fermi sea, a hole [Mahan, 2013].

Replacing the limits, the expression for the imaginary part is given by

$$\begin{aligned}\Im[\varepsilon(q,\omega)] = \frac{2me^2\hbar^3}{q^3}\Bigg[& mT\log\left(1 + e^{\left(-\mu + \frac{1}{2m}(-\frac{\hbar m\omega}{q} + \frac{q}{2})^2\right)/k_BT}\right) \\ & - mT\log\left(1 + e^{\left(-\mu + \frac{1}{2m}(\frac{\hbar m\omega}{q} + \frac{q}{2})^2\right)/k_BT}\right) \\ & - \frac{1}{2}\left(-\frac{\hbar m\omega}{q} + \frac{q}{2}\right)^2 + \frac{1}{2}\left(\frac{\hbar m\omega}{q} + \frac{q}{2}\right)^2\Bigg],\end{aligned} \tag{2.1.13}$$

where μ is the chemical potential. The expression for the real part of the dielectric function is given by

$$\Re[\varepsilon(q,\omega)] = 1 + \sum_{a,s_a^z} \frac{4\pi\hbar^2 e_a^2}{q^2} \mathcal{P}\int \frac{d^3p}{(2\pi\hbar)^3} \frac{f_a(p+q) - f_a(p)}{\hbar\omega + E(p) - E(p+q)}. \tag{2.1.14}$$

With the evaluation of the angular integral in the expression for the real part, the expression can be represented as

$$\begin{aligned} \Re[\varepsilon(q,\omega)] = 1 - \frac{16\pi^2 m e^2 \hbar^2}{q^2} \mathcal{P}\int_{-\infty}^{+\infty} \frac{d^3p}{(2\pi\hbar)^3} p f(p) \\ \times \frac{1}{2q}\left[\log\left(\frac{pa_b}{\hbar} - \frac{qa_b}{2\hbar} - \frac{m\omega a_b}{q}\right) + \log\left(\frac{pa_b}{\hbar} - \frac{qa_b}{2\hbar} + \frac{m\omega a_b}{q}\right)\right]. \end{aligned} \tag{2.1.15}$$

The real and imaginary part are also related by the Kramers-Kronig relations

$$\Re[\varepsilon(q,\omega)] = 1 + \mathcal{P}\int_{-\infty}^{+\infty} \frac{d\omega'}{2\pi} \frac{\Im[\varepsilon(q,\omega')]}{\omega' - \omega}, \tag{2.1.16}$$

$$\Im[\varepsilon(q,\omega)] = -\mathcal{P}\int_{-\infty}^{+\infty} \frac{d\omega'}{2\pi} \frac{\Re[\varepsilon(q,\omega')] - 1}{\omega' - \omega}, \tag{2.1.17}$$

and follow the frequency sum (f-sum) and conductivity sum rules respectively

$$\int_{-\infty}^{+\infty} \frac{d\omega}{\pi} \omega \Im[\varepsilon^{-1}(q,\omega)] = -\omega_{pl}^2, \tag{2.1.18}$$

$$\int_{-\infty}^{+\infty} \frac{d\omega}{\pi} \omega \Im[\varepsilon(q,\omega)] = +\omega_{pl}^2, \tag{2.1.19}$$

where ω_{pl} is the plasma frequency. The retarded polarization function has the analytical property $\Pi(q,-\omega) = \Pi(q,\omega)^*$ therefore the real part is an even function of frequency and the imaginary part an odd function.

As the theory is based on the grand canonical ensemble, the chemical potential, rather than the density is a state variable. The chemical potential is defined as the energy required to add or remove an electron from the system. At zero temperature, it corresponds to the Fermi energy. It is based on the definition of the energy difference between a system with N particles and $N+1$ particles given by

$$\mu = E_{tot}(N+1) - E_{tot}(N), \tag{2.1.20}$$

with the assumption that the total energy $E_{tot} = NE_g$, volume and the positive charge of the system are fixed and E_g is the ground state energy per particle [Mahan, 2013]. In order to obtain the chemical potential for a specified density, the density equation needs to be inverted, which for the general case is only possible numerically through a self-consistency cycle

$$n_e(\mu, T) = \int \frac{d^3p}{(2\pi)^3} d\omega a(p, \omega) f(p) = \frac{1}{\pi^2} \int_0^\infty dp \frac{p^2}{1 + e^{\beta(p^2-\mu)}}, \tag{2.1.21}$$

where $a(p, \omega)$ is the spectral function given by

$$a(p, \omega) = i \left(g^>(p, \omega) - g^<(p, \omega) \right), \tag{2.1.22}$$

and obeys the normalization condition

$$\int_{-\infty}^{+\infty} \frac{d\omega}{2\pi} a(p, \omega) = 1. \tag{2.1.23}$$

The plasmon dispersion relation using RPA is given by [Thiele et al., 2008]

$$\omega^2(q) = \omega_{pl}^2 \left[1 + \frac{\langle p^2 \rangle}{m^2} \frac{q^2}{\omega^2(0)} + \frac{\langle p^4 \rangle}{m^4} \frac{q^4}{\omega^4(0)} + \ldots \right], \tag{2.1.24}$$

where the moments $\langle p^i \rangle$ are evaluated using the Fermi integral [Galassi et al., 2002]. Experimentally via electron energy loss spectroscopy (EELS) or inelastic x-ray scatering (IXS), the plasmon dispersion is obtained by fitting a parameter α to [Pines, 2018a]

$$\omega(q) = \omega_{pl} + \alpha \frac{\hbar q^2}{m} + \mathcal{O}(q^4). \tag{2.1.25}$$

Neglecting higher order terms beyond the order of q^2 and restricting the considerations to the classical limit with the assumptions $\theta \gg 1$, $\langle p^2 \rangle = 3 m_e K_B T_e$ leads to the Gross-Bohm dispersion relation [Bohm and Gross, 1949]

$$\omega_{GB}^2 = \omega_{pl}^2 + \frac{3 K_B T_e}{m_e} q^2. \tag{2.1.26}$$

Considering a weakly degenerate plasma $\theta \approx 1$, Eq. (2.1.24) can be reduced to the form known as improved dispersion relation (IDR) [Thiele et al., 2008, Höll et al., 2007]

$$\omega_{IDR}^2 = \omega_{pl}^2 + \frac{3 K_B T_e}{m_e} q^2 (1 + 0.088 n_e \Lambda_e^3) + \left(\frac{\hbar q^2}{2 m_e} \right)^2. \tag{2.1.27}$$

Equation (2.1.27) extends the application range of the plasmon dispersion in Eq. (2.1.26) to larger q-vectors and higher densities.

2.1.2 Local Field Corrections

The RPA expression given in the preceding section for the polarization function leads to the expression for the density response function χ, which describes the correlation of density fluctuations on a mean field level and takes already into account the screening due to the long range nature of the Coulomb potential. In order to take into account, e.g., local fields, strong correlations, electron-electron collisions or anything beyond mean field, the concept of a local field correction (LFC) is essential. The density response function is given by

$$\chi(q,\omega) = \frac{\chi_0(q,\omega)}{1 - V(q)[1 - G(q,\omega)]\chi_0(q,\omega)}, \tag{2.1.28}$$

with $\chi_0(q,\omega)$ being the density response function of the noninteracting system at the same conditions. By replacing $G(q,\omega) = 0$ in Eq. (2.1.28), the form for RPA is recovered. Hence $G(q,\omega)$ contains the full wave-vector resolved information regarding the XC effects in $\chi(q,\omega)$ or the dynamic structure factor, see Eq. (2.2.1).

A simple correction to the RPA to account for the exchange and correlation hole around the electron was introduced by Hubbard [Hubbard, 1957] of the static form [Mahan, 2013]

$$G(q) = \frac{1}{2}\frac{q^2}{q^2 + q_F^2}, \tag{2.1.29}$$

where q_F is the Fermi wavevector. The correction factor arises from the vertex corrections to the polarization diagram of the electron gas and the simple formula was regarded as an improvement to the RPA in the evaluation of many properties.

A simple fitted expression $G(q) = A[1 - e^{-B(q/q_{TF})^2}]$ was suggested by Singwi and Vashishta *et al.* [Singwi et al., 1970, Vashishta and Singwi, 1972, Mahan, 2013] with dimensionless constants A and B for various values of r_s. Here, q_{TF} is the Thomas-Fermi wavevector. The fitted expression works reasonably well at small and intermediate wavenumbers, but not at larger values. Singwi and collaborators proposed a scheme known as *STLS* where the LFC is expressed as a function of the static structure factor with significant improvement in treatment of the short-range exchange and correlation effects [Singwi et al., 1970, Tanaka and Ichimaru, 1986, Ichimuru, 2004, Dornheim et al., 2018a]

$$G^{STLS}(q) = -\frac{1}{n_e}\int \frac{dq}{(2\pi)^3}\frac{\mathbf{k.q}}{\mathbf{q}^2}[S(|\mathbf{k}-\mathbf{q}|) - 1]. \tag{2.1.30}$$

With the STLS scheme, the pair correlation function have vast improvements over the RPA. The plasmon dispersion is also improved with good agreement between experiments. However, the compressibility sum rules is violated leading to unrelaible behavior for the LFC at small q [Giuliani and Vignale, 2005].

Over the last few decades various efforts have been made in obtaining expressions for the LFC. Ichimaru *et al.* [Ichimaru and Utsumi, 1981] obtained an analytic LFC expression for a strongly coupled electron liquid which reproduced the QMC results of Ceperley *et al.* [Ceperley and Alder, 1980]. Farid *et al.* [Farid et al., 1993] used Green's function Quantum Monte Carlo (QMC) results on the interacting electron gas to obtain the correlation energy density based on the parametrization of Vosko *et al.* [Vosko et al., 1980]. Based on ground state QMC simulations in the static limit ($\omega \to 0$), Moroni *et al.* [Moroni et al., 1992, Moroni et al., 1995] have obtained accurate LFC for the uniform electron gas (UEG). This has been further parametrized by Corradini *et al.* [Corradini et al., 1998] hereafter referred to as CDOP. The static CDOP LFC as a function of density and wavenumber is given by [Corradini et al., 1998]

$$G(q, r_s) = Cq^2 + \frac{Bq^2}{g + q^2} + \alpha q^4 e^{-\beta q^2}, \tag{2.1.31}$$

where $g = B/(A - C)$. The expressions for the coeffcients are given by

$$A = 0.25 - \frac{q_F^2}{4\pi e^2} \frac{d\mu_C}{dn_e}, \tag{2.1.32}$$

$$B(r_s) = \frac{1 + 2.15 r_s^{1/2} + 0.435 r_s^{3/2}}{3 + 1.57 r_s^{1/2} + 0.409 r_s^{3/2}}, \tag{2.1.33}$$

$$C = -\frac{\pi}{2q_F e^2} \frac{d(r_s e_C)}{dr_s}, \tag{2.1.34}$$

with e_C, the correlation energy per particle and μ_C, the correlation contribution to the chemical potential. α and β are the fitted parameters with the best results obtained by taking

$$\alpha = \frac{A}{Bg} \frac{1.5}{r_s^{1/4}}, \tag{2.1.35}$$

$$\beta = \frac{1.2}{Bg}. \tag{2.1.36}$$

All these data for the LFC of the electron gas have been obtained from ground state calculations and are strictly speaking only applicable to such. With the efforts of Dornheim *et al.* [Dornheim et al., 2019, Dornheim et al., 2020a], the problem has been overcome with a machine learning representation of finite-temperature QMC data of the static LFC with respect to the density, reduced temperature and the momentum vector (r_s, θ, and q). The parametrization covers the entire range of WDM and is hereafter referred to as T-LFC. This is illustrated in Fig. 2.1.2, where the static LFC of the UEG is shown at the density of aluminum ($r_s = 2.07$, $\rho = 2.7\ g/cm^3$) for four different temperatures.

At T=0 eV, the curve reproduces the CDOP ground state parametrization. With a raise in temperature, at T=3 eV, the reduced temperature is still small ($\theta \approx 0.26$) and therefore the effect on the $G(q, \omega)$ is small and starts to manifest at large wave numbers. With further increase in temperature at T=8 eV ($\theta \approx 0.69$), there are significant deviations to the ground-state result and at large q, the tail becomes negative. This is due to the lowering of kinetic energy taking place due to XC effects for the conditions [Dornheim et al., 2019]. Finally, the largest deviations appear at T=12 eV (dashed blue, $\theta \approx 1.03$), where G is systematically lower than for T=0 starting around the Fermi wave number. The temperature effects of the LFC are clearly observable for temperatures $T \gtrsim 8$ eV and wave numbers $q > q_F$. It has been shown that the frequency dependence of $G(q, \omega)$ in general has a smaller impact for $r_s \lesssim 4$, especially for the systems considered in chapter 5 [Dornheim et al., 2018b, Groth et al., 2019].

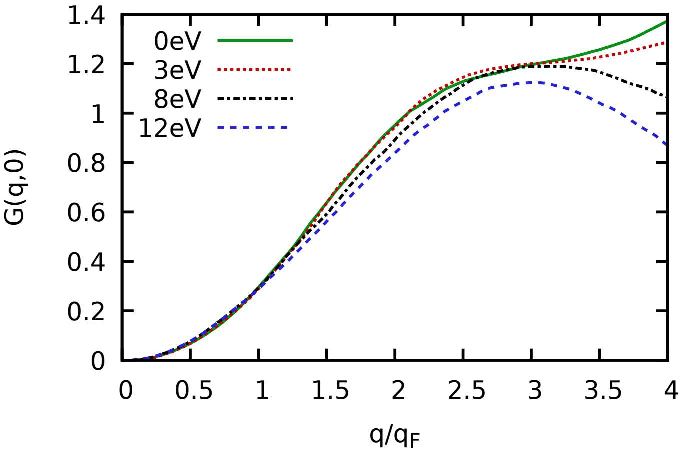

Figure 2.1.2: Static LFC of aluminum at four different temperatures. The static LFC data have been obtained from the machine-learning representation from Ref. [Dornheim et al., 2019]. Reprinted figure with permission from **K. Ramakrishna** *et al.*, Phys. Rev. B **103**, 125118 (2021). Copyright 2021 by the American Physical Society.

2.1.3 Mermin Function

To account for electron-ion interactions and bound states, one needs to go beyond the RPA with LFC which can account for the electron-electron collisions. A possible way to do so is by the method of Mermin [Mermin, 1970], who used density conservation and a relaxation time approximation to introduce a damping or relaxation term (ν) which can account for the electron-ion collisions using

$$\varepsilon^{MA}(q,\omega) = 1 + \frac{(1+i\frac{\nu}{\omega})\left(\varepsilon(q,\omega+i\nu)-1\right)}{1+(i\frac{\nu}{\omega})\frac{(\varepsilon(q,\omega+i\nu)-1)}{(\varepsilon(q,\omega\to 0)-1)}}, \tag{2.1.37}$$

where the dielectric function accounts for electron correlations with the inclusion of a local field correction term $G(q,\omega)$ using Born-Mermin approximation as

$$\varepsilon(q,\omega) = 1 - \frac{1-\varepsilon^{RPA}(q,\omega)}{1+G(q,\omega)\left(1-\varepsilon^{RPA}(q,\omega)\right)}, \tag{2.1.38}$$

which then results in the extended Mermin Ansatz (MA) [Fortmann et al., 2010]

$$\varepsilon^{MA}(q,\omega) = (1-\frac{i\omega}{\nu(\omega)})\frac{\varepsilon\left(q,\omega+i\nu(\omega)\right)\varepsilon(q,0)}{\varepsilon\left(q,\omega+i\nu(\omega)\right)-\left(i\omega/\nu(\omega)\right)\varepsilon(q,0)}. \tag{2.1.39}$$

The extended Mermin Ansatz allows the inclusion of electron-ion collisions through the dynamical collision frequency term $\nu(\omega)$. Using the Born approximation, the collision frequency is given by

$$\nu(\omega) = -i\frac{\varepsilon_0 n_i \Omega_0^2}{6\pi^2 e^2 n_e m_e}\int_0^\infty dq q^6 V_s^2(q) S_{ii}(q)\frac{1}{\omega}\left(\varepsilon^{RPA}(q,\omega)-\varepsilon^{RPA}(q,0)\right), \tag{2.1.40}$$

where $V_s(q)$ is the statically screened potential, n_i is the ion density, $S_{ii}(q)$ the ion-ion static structure factor which can be taken, e.g., from MD simulations, and Ω_0 is the normalization volume. Substituting $\nu(\omega)$ into Eq. (2.1.39) and using it in the formula for the dynamic structure factor, yields dielectric functions, stopping power, structure factors and thus XRTS spectra with LFC's and collision terms included. The application of the dielectric function in evaluating the XRTS spectra is discussed in the next section.

2.2 Theoretical Description of the X-ray Scattering Signal

X-ray Thomson scattering (XRTS) is a powerful technique for the diagnostics of solid density and shock-compressed matter due to the penetrative nature of the x-rays on the sample which otherwise is opaque towards optical lasers/probes [Glenzer and Redmer, 2009]. This allows to study properties such as ion-ion correlations, electron temperature and ionization. The wavelength required to probe the target ideally should be the screening length ($\lambda < 2\pi c\sqrt{\varepsilon_0 m_e / n_e e^2}$). The scattered x-rays are collected at specific scattering angles and the frequency resolved spectra is used for the analysis. Due to the scattering of photons from electrons, XRTS is an ideal probe to understand the behavior of electrons in the system [Graziani et al., 2014, Saunders, 2018].

Figure. 2.2.1 shows the capability of the commonly used x-ray sources in probing the electron density. Hard x-rays with λ of the order of 1 nm are required for probing matter at typical solid densities 10^{23} cm^{-3}. Latest XFEL sources like the LCLS [Bostedt et al., 2016] and European XFEL [Tschentscher et al., 2017] feature tunable hard x-ray source of up to 25 KeV. The scattering of the x-rays consist of the elastic scattering from the tightly bound electrons, inelastic scattering from partially bound and from free electrons, also refered to as bound-bound, free-free and bound-free scattering. In the inelastic scattering involving partially bound electrons, the momentum transfer of the photon to an electron is given by $\hbar\vec{k}$ where $\vec{k}$ is the scattering vector. Figure. 2.2.2 shows the schematics of photons scattering off of electrons and the resulting scattering vector $k = |\vec{k}| = (4\pi/\lambda)\sin(\theta/2)$ for small momentum transfers [Glenzer et al., 2007]. The length scale ($\lambda^* \approx 2\pi/k$) of the electron density fluctuations compared to the screening length ($\lambda_s = 1/\alpha k$) of the plasma determines the scattering regime. The collective scattering regime is defined for $\alpha > 1$ where the length scale for the density fluctuations are larger than the screening length. In the non-collective scattering regime defined for $\alpha < 1$, resolution of the density fluctuations of individual electrons are possible.

The response of the system to external pertubations (charge density fluctuations) is given by the density response function. The description of XRTS always assumes linear response theory [Dornheim et al., 2020c]. The dynamic structure factor (DSF) is related to the density response function using the fluctuation-dissipation theorem

$$S(k,\omega) = \frac{1}{\pi n_e} \frac{\Im[\chi(k,\omega)]}{1 - e^{-\hbar\omega/k_B T_e}}. \tag{2.2.1}$$

The DSF is also related to the density-density correlation function via Fourier transform

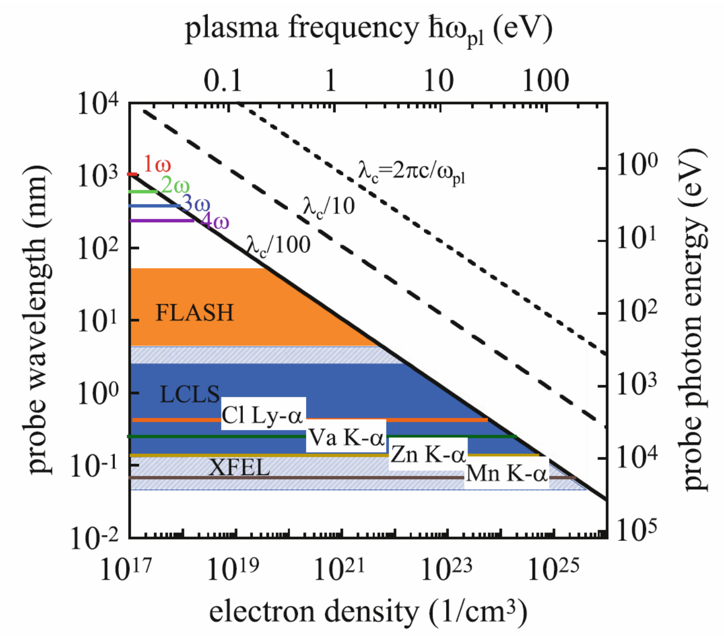

Figure 2.2.1: Comparison of the x-ray sources and the capability of probing the electron density. Republished with permission of Springer from Frontiers and Challenges in Warm Dense Matter (2014) [Fortmann, 2014]. Permission conveyed through Copyright Clearance Center, Inc.

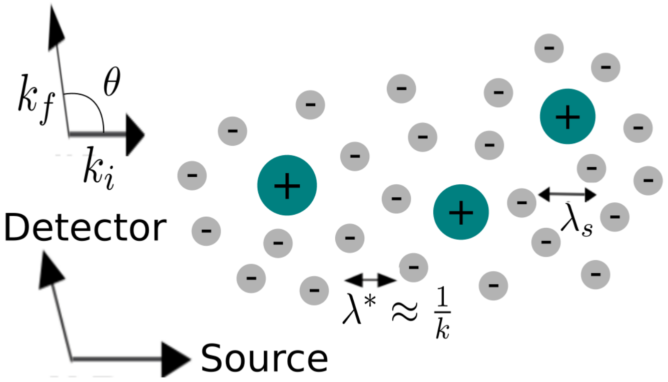

Figure 2.2.2: A schematic cartoon of x-ray Thomson scattering illustrating the length of the scattering vector. The screening length (λ_s) and the length scale of the density fluctuations (λ^*) are also shown for comparison.

$$S(k,\omega) = \int_{-\infty}^{+\infty} dte^{i\omega t} \left\langle \delta\rho(k,t)\delta\rho(k,0) \right\rangle. \tag{2.2.2}$$

The system response can now be evaluated based on the knowledge of the experimental parameters like the solid angle of the detector $d\Omega$, area of irradiation A, the incoming power P_i, the scattered power P_s, $\vec{E}_0$ the electromagnetic field, and the information of the x-ray source: wavevector $\vec{k}$ and frequency interval $d\omega$ using the expression for the scattered power [Graziani et al., 2014]

$$P_s(r,\omega)d\Omega d\omega = \frac{P_i r^2 d\Omega}{2\pi A} |\vec{k}_f \times (\vec{k}_f \times \vec{E}_0)|^2 NS(k,\omega)d\omega. \tag{2.2.3}$$

Using the appropriate Chihara decomposition, the total dynamic structure factor of the electrons can be evaluated as [Chihara, 1987].

$$S(k,\omega) = \underbrace{Z_f S^0_{ee}(k,\omega)}_{\text{inelastic scattering from free electrons}} + \underbrace{|f(k)+q(k)|^2 S_{ii}(k,\omega)}_{\text{elastic scattering}} + \underbrace{Z_c S_c(k,\omega)}_{\text{inelastic scattering from bound electrons}}. \tag{2.2.4}$$

In Eq. (2.2.4), the three terms correspond to the Compton term for the free electrons, the Rayleigh term for the electrons following the ion and the Raman term corresponding to the inelastic scattering of the bound electrons to the continuum respectively. Z_f is the free electrons per nucleus and Z_c is the core charge. S^0_{ee} is the DSF for the free electrons (see chapters 3 and 5 for the results of this work). $f(k)$ and $q(k)$ corresponds to the form factor of bound and free electrons respectively. $S_c(k,\omega)$ is the term for the bound-free scattering [Graziani et al., 2014, Plagemann et al., 2012]. $S_{ii}(k,\omega)$ is the dynamic ion-ion structure factor. In principle, the entirety of the DSF can be extracted from real-time TDDFT based on all-electron calculations for Beryllium demonstrated by Baczewski *et al.* [Baczewski et al., 2016].

It is possible to infer the electron density from the position of the plasmon peaks in collective scattering for small momentum transfers. The ionization state of the system can also be infered using XRTS. This is due to the scaling of the ionization state with the ratio of the elastic and inelastic scattering signal. The elastic scattering component is related to the ion-ion structure factor along with the form factors in Eq. (2.2.4). At large momentum transfers, the ion-ion structure factor and the form factor of the bound electrons reach the conditions of ideal plasma i.e. unity and zero respectively. This results in the sensitivity of elastic scattering to the ionic form factor related to the Fourier transform of the electron density bound to the ions.

The quantities of interest are computed as follows [Kraus, 2012]:

$$f(\vec{k}) = \left\langle \sum_{j=1}^{Z_c} e^{i\vec{k}\vec{r}_{jl}(t)} \right\rangle, \tag{2.2.5}$$

$$q(\vec{k}) = \frac{1}{2\pi N} \frac{\sqrt{Z_f}}{S_{ii}(k,\omega)} \int dt' \left\langle \sum_{l}^{N} \sum_{m}^{Z_f} e^{i\vec{k}[\vec{R}_l(t)-\vec{r}_m(t+t')]} \right\rangle \exp^{i\omega t'}, \tag{2.2.6}$$

$$S_{ii}(k,\omega) = \frac{1}{2\pi N}\int dt' \left\langle \sum_{l,m}^{N}\sum_{m}^{Z_f} e^{i\vec{k}\left[\vec{R}_l(t)-\vec{R}_m(t+t')\right]} \right\rangle \exp^{i\omega t'}, \tag{2.2.7}$$

$$S^0_{ee}(k,\omega) = \frac{1}{2\pi N}\int dt' \left\langle \sum_{l,m}^{Z_f,N}\sum_{m}^{Z_f} e^{i\vec{k}[\vec{r}_l(t)-\vec{r}_m(t+t')]} \right\rangle \exp^{i\omega t'}, \tag{2.2.8}$$

where $\vec{R}_l(t)$ is the position of the l^{th} ion and $\vec{r}_m(t)$ is the position of the m^{th} free electron.
The asymmetry in the DSF with respect to the frequency shift ($\pm\omega$) is a key feature to unlock the plasma properties in a Thomson scattering experiment. Let a photon with initial momentum $\vec{k}_i$ and frequency ω_i scatter inelastically into final momentum $\vec{k}_f$ and frequency ω_f. The probability of the final state is proportional to the final momentum $\vec{k}_f$ and frequency ω_f. Under the conditions of equilibrium, the DSF is proportional to the Boltzmann factor [Höll et al., 2007]

$$S\left(\omega_i \rightarrow \omega_f, k_i \rightarrow k_f \propto e^{-\frac{\hbar\omega_f}{K_BT}}\right). \tag{2.2.9}$$

This conditions also holds true for the case of reverse scattering

$$S\left(\omega_f \rightarrow \omega_i, k_f \rightarrow k_i \propto e^{-\frac{\hbar\omega_i}{K_BT}}\right). \tag{2.2.10}$$

Using the expression for DSF in Eq. (2.2.1) and the analytical property of the retarded polarization function $\Pi(k,\omega) = \Pi^*(-k,-\omega)$ (see section 2.1.1) via fluctuation dissipation theorem [Kubo, 1966] leads to the detailed balance equation

$$\frac{S(-k,-\omega)}{S(k,\omega)} = e^{-\frac{\hbar\omega}{K_BT}}, \tag{2.2.11}$$

where $\omega = \omega_f - \omega_i$ and $k = |\vec{k}| = |\vec{k}_f - \vec{k}_i|$. The detailed balance relation is hence a useful way to infer the temperature of the plasma based on the scattering spectra obtained in the experiments. In practice, this method does not always work, and that determining plasma properties is an active area of research [Dornheim et al., 2022].

2.3 Density Functional Theory

For the computational modelling of materials, density functional theory (DFT) is of paramount importance. The many-body problem of interacting electrons can be effectively reformulated into a single particle problem. It greatly reduces the computational cost of calculating both ground state and equilibrium (finite-temperature) properties. This follows from the Hohenberg-Kohn theorem [Hohenberg and Kohn, 1964] which states that in a system consisting of interacting electrons, the ground state density can be mapped uniquely to a system subjected to an external potential. The electron density of the ground state leads to the lowest value for the ground state energy. Hence, the ground state density contains sufficient information about the interacting many particle system.
Consider a system of N electrons subjected to an external potential $V(r)$. The Hamiltonian is

given by

$$H(r_1, \ldots r_N) = \sum_{j=1}^{N} \left(-\frac{1}{2}\nabla^2_{r_j} + V(r_j) \right) + \frac{1}{2}\sum_{j \neq k}^{N} V(r_j, r_k). \tag{2.3.1}$$

The Hamiltonian can be written as the sum of the kinetic and potential energy operators as $\hat{H} = \hat{T} + \hat{V}_{el} + \hat{V}_{ext}$ where $\hat{T}$ is the kinetic energy operator, $\hat{V}_{el}$ is the interaction between electrons and $\hat{V}_{ext}$ is the external potential. Let a functional F be defined such that it is minimized to obtain the interacting density n for all the antisymmetric wavefunction of N electron system as [Martin, 2020, Varsano, 2006]

$$F[n] = \min_{\psi \to n} \langle \psi | \hat{T} + \hat{V}_{el} | \psi \rangle, \tag{2.3.2}$$

where $\psi_{\text{min}}[n]$ is the wavefunction that minimizes the functional for an interacting system at a given density. Defining the energy functional for an external potential as

$$E[n] = F[n] + \int drn(r)V(r), \tag{2.3.3}$$

with $E[n]$ the expectation value of the Hamiltonian evaluated for $\psi_{\text{min}}[n]$ as $E[n] = \langle \psi_{\text{min}}[n] | \hat{H} | \psi_{\text{min}}[n] \rangle$. This ensures that the energy functional is always an upper bound for the energy of the ground state E_{gs} as

$$E[n] \geq E_{gs}, \tag{2.3.4}$$

and has a global minimum at the exact ground state energy. The ground state energy is obtained by minimizing $E[n]$ with respect to the density using the conditions

$$\int drn(r) = N, \tag{2.3.5}$$

$$\frac{\partial F}{\partial n(r)} + V(r) = \mu, \tag{2.3.6}$$

where μ is the chemical potential. Henceforth with the full knowledge of the external potential, the ground state energy of the system can be evaluated. A practical way of obtaining the ground state energy is using the scheme introduced by Kohn-Sham (KS) [Kohn and Sham, 1965] denoted hereafter by S in the subscript. The KS scheme involves using the density of non-interacting electrons akin to the density of the interacting electrons with the system subjected to an external potential V_S. The KS functional is written as

$$F_S[n] = \hat{T}_S[n] = \min_{\psi \to n} \langle \psi | \hat{T} | \psi \rangle. \tag{2.3.7}$$

The normalization conditions imposes

$$\frac{\partial T_S}{\partial n(r)} + V_S(r) = \mu, \tag{2.3.8}$$

and in comparsion with Eq. (2.3.6), the external potential can be obtained as

$$V_S(r) = V(r) - \frac{\partial T_S}{\partial n(r)} + \frac{\partial F}{\partial n(r)}. \tag{2.3.9}$$

Therefore the ground state energy of the system can be evaluated through the solution of the non-interacting system. The full knowledge of the evaluation further requires an energy term defined as exchange-correlation energy (E_{XC}) and its functional derivative–exchange correlation potential (V_{XC}) in the following form

$$E_{XC}[n] = F[n] - T_S[n] - U[n], \tag{2.3.10}$$

$$V_{XC}[n(r)] = \frac{\partial E_{XC}}{\partial n(r)}, \tag{2.3.11}$$

where $U[n]$ is the Hartree energy functional which describes the classical electrostatic interacting energy defined as

$$U[n] = -\frac{1}{2}\int d^3r \int d^3r' \frac{n(r)n(r')}{|r - r'|}. \tag{2.3.12}$$

The Hartree potential is obtained through the functional derivative via

$$V_H[n(r)] = \frac{\partial U}{\partial n(r)} = \int dr' \frac{n(r')}{|r - r'|}. \tag{2.3.13}$$

The potential for the non-interacting system or the KS potential can now be expressed as

$$V_S[n(r)] = V(r) + V_H[n(r)] + V_{XC}[n(r)]. \tag{2.3.14}$$

The KS Hamiltonian is given by $\hat{H}_S = \hat{T} + \hat{V}_S[n]$ where $\hat{T}$ is the single-particle kinetic energy operator. The ground state energy of the system can be solved self-consistently using the set of equations known as Kohn-Sham (KS) equations: [Kohn and Sham, 1965]

$$\int dr n(r) = N, \tag{2.3.15}$$

$$\hat{H}_S[n]|\psi_i\rangle = \varepsilon_i|\psi_i\rangle, \tag{2.3.16}$$

$$\hat{H}_S[n] = -\frac{1}{2}\nabla^2 + V(r) + V_{XC}[n(r)] + \int dr' \frac{n(r')}{|r - r'|}, \tag{2.3.17}$$

$$n(r) = \sum_i \theta(\mu - \varepsilon_i)\psi_i^*(r)\psi_i(r), \tag{2.3.18}$$

where $\psi_i(r)$ is the single-particle wavefunction obtained as the solution of the non-interacting system with the corresponding eigenvalue ε_i. The obtained single-particle solutions via the Kohn-Sham (KS) equations are called Kohn-Sham (KS) orbitals. In practice, the exact XC potential which contains the many-body physics of the system has to be approximated and a good approximation is required to obtain the solution discussed in the next section.

A detailed formalism to extend DFT to finite-temperature i.e., thermal density functional theory is presented in Refs.[Pittalis et al., 2011, Pribram-Jones et al., 2014, Pribram-Jones et al., 2016, Pribram-Jones and Burke, 2016, Burke et al., 2016, Smith et al., 2016, Smith et al., 2018, Harding et al., 2022].

2.3.1 Exchange-Correlation Functionals

The construction of exchange-correlation (XC) functionals has been an active field of research over the last few decades [Burke, 2012]. The accuracy and complexity of such functionals is well categorized and is informally referred to as the rungs on "Jacobs ladder" based on the complexity and higher order approximations involved for the evaluation shown in Fig. 2.3.1 [Perdew and Schmidt, 2001].

One of the simplest and widely used approximation is the local density approximation or LDA. The LDA is based on the assumption that the density of the systen can be treated locally as uniform electron gas (UEG). The XC energy is written as

$$E_{XC}^{LDA}[n] = \int drn(r)e_{XC}^{UEG}[n(r)], \tag{2.3.19}$$

where $e_{XC}^{UEG}[n(r)]$ is the energy density of the UEG [Martin, 2020, Varsano, 2006]. This term can be split into a simple analytic form for exchange and a numerical approximation for the correlation part as

$$e_{X}^{UEG}[n(r)] = -\frac{3}{4}\left[\frac{3n}{\pi}\right]^{1/3}, \tag{2.3.20}$$

$$e_{C}^{UEG}[n(r)] = \frac{a_1}{1 + a_2 r_s^{1/2} + a_3 r_s}, \tag{2.3.21}$$

where $a_1 = -0.1423$, $a_2 = 1.0529$ and $a_3 = 0.3334$ are constants that have been obtained from highly accurate QMC data for the UEG [Ceperley and Alder, 1980]. In the high-density limit, Gell-Mann *et. al.* [Gell-Mann and Brueckner, 1957] obtained $e_C(r_s) = 0.0622\log(r_s) - 0.094 + \mathcal{O}(r_s)$. Carr and Maradudin [Carr and Maradudin, 1964] further extended this with an additional term in the series: $e_C(r_s) = 0.0622\log(r_s) - 0.094 + 0.018 r_s \log(r_s) + a r_s + \mathcal{O}(r_s^2)$. At low density, the calculations of the correlation energy becomes difficult as the electrons become localized [Mahan, 2013]. In the low density limit, the system is expected to exhibit Wigner crystal phase [Wigner, 1934] and has the form $e_C(r_s) = a/(r_s) + b/(r_s^{3/2}) + c/(r_s^2) + \ldots$ where a, b, ... are constants [Sun et al., 2010]. Various approximations for the correlation term have resulted in several XC functionals [Perdew and Zunger, 1981, Perdew and Wang, 1992, Vosko et al., 1980]. The LDA works actually surprisingly well for systems far from uniform assuming it is only based on the uniform electron gas. Still, more accurate approximations are required for more quantitative accuracy for van der Waals interactions, or insulating systems involving band gaps.

Another widely used approximation constitutes the generalized gradient approximation or GGA. The XC energy is written as

$$E_{XC}^{GGA}[n(r)] = \int drn(r)e_{XC}^{GGA}[n(r), \nabla n(r)], \tag{2.3.22}$$

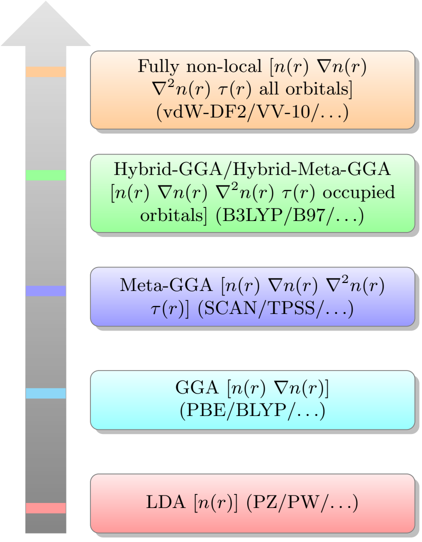

Figure 2.3.1: Jacob's ladder of XC functionals with some of the most common DFT functionals [Perdew and Zunger, 1981, Perdew and Wang, 1992, Perdew et al., 1996a, Becke, 1988, Lee et al., 1988, Sun et al., 2015, Tao et al., 2003, Becke, 1997, Lee et al., 2010, Vydrov and Van Voorhis, 2010] within each rung of the ladder [Perdew and Schmidt, 2001]. The arrow represents the increasing chemical accuracy. $n(r)$ is the electronic density and $\tau(r) = \sum_i^{occ.} \frac{1}{2} |\nabla \psi_i(r)|^2$ is the kinetic energy density for the occupied orbitals.

where e_{XC}^{GGA} is given by an analytic function of the density and the gradient of the density involving free parameters obtained using sum rules. The GGA in general provides better total energies for the atoms and molecules and also improves the band gap problem imposed by LDA for the insulators. PBE [Perdew et al., 1996a] is a popular choice of the GGA range of XC functionals and provides reasonable accuracy for the calculations involving bond-lengths and bond-angles but still underestimates the band gaps. Further improvements to GGA can be included with the additional use of kinetic energy density $\left(\nabla^2 n(r)\right)$ which are known as meta-GGA which vastly improves the evaluation at a higher computatational cost. With the combination of Hartree-Fock exchange and the rest of the contribution arising from *ab-initio* or empirical methods, hybrid class of functionals are constructed. HSE [Heyd et al., 2003] is a popular choice for metallic systems with the XC energy given by

$$E_{XC}^{HSE}[n(r)] = \alpha_m E_X^{SR}[n(r)] + (1 - \alpha_m) E_X^{SR}[n(r)] + E_X^{LR}[n(r)] + E_C[n(r)], \tag{2.3.23}$$

where α_m is the mixing fraction. The electron-electron interaction is separated into short-range (SR) and long-range (LR) parts for the exchange terms only. The first term in Eq. (2.3.23) contains the short-range Hartree-Fock exact exchange. The second term contains the short-range exchange contribution evaluated using PBE. The third and the final terms contain the long-range exchange contribution and the correlation energy evaluated using PBE respectively.

The range of XC functionals discussed in this section have been very successful in modeling a variety of systems but lack the thermal XC effects of including temperature. This becomes important in the warm dense regime as $\theta \approx 1$ and requires the construction of accurate finite-temperature XC functionals.

2.3.2 Finite-Temperature Exchange-Correlation Functionals

By replacing the XC energy $E_{XC}(r_s, \theta)$ of the system with the XC free energy $f_{XC}(r_s, \theta)$, the input can be used in DFT and DFT-MD for perfoming simulations at finite-temperature for the electrons. To construct a finite-temperature version of the LDA requires parametrization of the free energy with respect to density, temperature and spin.

Ebeling *et al.* [Ebeling et al., 1981, Ebeling and Richert, 1982, Ebeling and Richert, 1985b, Ebeling and Richert, 1985a] produced a Padé aprroximation for the f_{XC} which has been used for studying non-ideal plasmas and correctly reproduced the ground state and high temperature limit. Furthermore, Ichimaru and coworkers [Tanaka et al., 1985, Tanaka and Ichimaru, 1986] obtained the interaction energy V (per particle) for the UEG using linear response theory via static structure factor in Singwi, Tosi, Land, and Sjölander (STLS) approximation [Singwi et al., 1968] at finite-temperature

$$V = \frac{1}{2}\int_{k<\infty} \frac{dk}{(2\pi)^3}\left[S(k) - 1\right]\frac{4\pi}{k^2}. \tag{2.3.24}$$

Perrot and Dharma-wardhana [Perrot and Dharma-wardana, 1984, Perrot and Dharma-wardana, 2000, Dharma-wardana and Perrot, 2000] obtained a parametrization based on classical mapping. They introduced a modified temperature T_m such that $T_m = \sqrt{T^2 + T_e^2}$ and assumed an interpolation between the ground state and classical high temperature regimes. The mapping is such that the ground state correlation energy of the electron gas is recovered by mapping a classical sytem at an effective temperature T_e. The free energy paramaterization was obtained by performing simulations of the uniform electron gas in the region $\theta = 0 - 10$ and $r_s = 1 - 10$ and fitted to a functional form.

Karasiev *et al.* [Karasiev et al., 2014b] obtained a parametrization for the free energy using restricted path integral Monte Carlo (RPIMC) data for the uniform electron gas from Brown *et al.* [Brown et al., 2013a] hereafter refered to as *KSDT*. It was shown to exhibit deviations in E_{XC} of up to 10% [Schoof et al., 2015] and is the motivation behind *GDSMFB* [Groth et al., 2017c] explored in further detail in chapter 4. The expression for the free energy and the constants are given below:

$$f_{XC}(r_s, \theta) = -\frac{1}{r_s}\frac{a_{HF}(\theta) + b(\theta)r_s^{1/2} + c(\theta)r_s}{1 + d(\theta)r_s^{1/2} + e(\theta)r_s}, \tag{2.3.25}$$

$$a_{HF}(\theta) = 0.610887\tanh(\theta^{-1})\frac{0.75 + 3.04363\theta^2 - 0.09227\theta^3 + 1.7035\theta^4}{1 + 8.31051\theta^2 + 5.1105\theta^4}, \tag{2.3.26}$$

$$b(\theta) = \tanh(\theta^{-1/2})\frac{b_1 + b_2\theta^2 + b_3\theta^4}{1 + b_4\theta^2 + b_5\theta^4}, \tag{2.3.27}$$

$$c(\theta) = \left[c_1 + c_2\exp(\frac{-c_3}{\theta})\right]e(\theta), \tag{2.3.28}$$

$$d(\theta) = \tanh(\theta^{-1/2})\frac{d_1 + d_2\theta^2 + d_3\theta^4}{1 + d_4\theta^2 + d_5\theta^4}, \qquad (2.3.29)$$

$$e(\theta) = \tanh(\theta^{-1})\frac{e_1 + e_2\theta^2 + e_3\theta^4}{1 + e_4\theta^2 + e_5\theta^4}, \qquad (2.3.30)$$

where $a_{HF}(\theta)$ represents the Hartree-Fock limit as parametrized in Ref. [Perrot and Dharma-wardana, 1984] and $\{b_i, c_i, d_i, e_i\}$ are constants [Karasiev et al., 2014b]. Instead of utilizing the expression for the interacting energy, the following equation is used to calculate the XC energy

$$E_{xc}(r_s,\theta) = f_{xc}(r_s,\theta) = \theta\frac{f_{xc}(r_s,\theta)}{\partial\theta}|_{r_s}, \qquad (2.3.31)$$

and fitted to the E_{XC} data by Brown *et.al.* [Brown et al., 2013a]. Furthermore, Karasiev *et.al.* have constructed a finite-temperature GGA XC free-energy functional (KDT16) and shown the thermal effects on the pressure of alumimum and deuterium Hugoniot [Karasiev et al., 2018b, Karasiev et al., 2019a]. The recently constructed thermal hybrid functional (KDT0) [Mihaylov et al., 2020] based on previously developed KSDT and KDT16 offers improvements to the static calculations of band structure and band gaps across various temperature regimes. At low temperature, it reduces to the ground state hybrid PBE0 approximation [Perdew et al., 1996b, Adamo and Barone, 1999].

Groth and coworkers [Dornheim et al., 2016b, Groth et al., 2017c] obtained a parametrization for the free energy hereafter refered to as *GDSMFB*. The f_{XC} is obtained from PIMC data for the interaction energy using

$$f^{\xi}_{XC}(r_s,\theta) = \frac{1}{r_s^2}\int_0^{r_s} dr'_s r'_s V^{\xi}(r'_s,\theta), \qquad (2.3.32)$$

$$V^{\xi}(r_s,\theta) = 2f^{\xi}_{XC}(r_s,\theta) + r_s\frac{\partial f^{\xi}_{XC}(r_s,\theta)}{\partial r_s}|_{\theta}. \qquad (2.3.33)$$

f^0_{XC} and f^1_{XC} are fitted using the Padé fit

$$f(x) = \frac{\sum_{i=0}^{m\geq 0} a_i x^i}{1 + \sum_{j=0}^{n\geq 1} b_j x^j} = \frac{a_0 + a_1 x + a_2 x^2 + \ldots + a_m x^m}{1 + b_1 x + b_2 x^2 + \ldots + b_n x^n}, \qquad (2.3.34)$$

where $\{a_i, b_i\}$ are constants.

In the high density limit, the Hartree-Fock limit is obtained, $\lim_{r_s\to 0} f^{HF}_{\mathrm{XC}}(r_s,\theta) = \frac{a^{HF}(\theta)}{r_s}$. At the ground state limit, $\lim_{\theta\to 0} f^{HF}_{\mathrm{XC}}(r_s,\theta) = -\frac{1}{2}\varepsilon^{Ry}(r_s)$ where ε^{Ry} is the ground-state parameterization for the exchange correlation energy obtained by Ebeling *et al.* [Ebeling et al., 1981, Ebeling and Richert, 1982, Ebeling and Richert, 1985b, Ebeling and Richert, 1985a] using a Padé aprroximation in Rydberg atomic units given by

$$\varepsilon^{Ry}(r_s) = \frac{0.913}{r_s} + 0.1244\log(1 + \frac{2.117 r_s^{1/2}}{1 + 0.3008 r_s^{1/2}}). \qquad (2.3.35)$$

In the high-temperature limit, the Debye-Hückel result is obtained, $\lim_{\theta\to\infty} f^{HF}_{\mathrm{XC}}(r_s,\theta) =$

$-\frac{1}{3^{1/2}} r_s^{-3/2}\theta^{-1/2}$. The XC energy is calculated using Eq. (2.3.31). The XC free energy at arbitrary spin polarization is obtained using [Groth et al., 2017c, Groth et al., 2017b]

$$f_{XC}(r_s,\theta,\xi) = f^0_{XC}(r_s,\theta^0) + \left[f^1_{XC}(r_s,\theta^0, 2^{-2/3}) - f^0_{XC}(r_s,\theta^0)\right] \Phi(r_s,\theta^0,\xi), \tag{2.3.36}$$

where $\xi = (N^{\uparrow} - N^{\downarrow})/(N^{\uparrow} + N^{\downarrow})$ is the spin polarization and $\theta^0 = \theta(1+\xi)^{2/3}$. The interpolation function is given by

$$\Phi(r_s,\theta,\xi) = \frac{(1+\xi)^{\alpha(r_s,\theta)} + (1-\xi)^{\alpha(r_s,\theta)} - 2}{2^{\alpha(r_s,\theta)} - 2}, \tag{2.3.37}$$

$$\alpha(r_s,\theta) = 2 - h(r_s)e^{-\theta\lambda(r_s,\theta)}, \tag{2.3.38}$$

$$h(r_s) = \frac{2/3 + h_1 r_s}{1 + h_2 r_s}, \tag{2.3.39}$$

$$\lambda(r_s,\theta) = \lambda_1 + \lambda_2\theta r_s^{1/2}, \tag{2.3.40}$$

where $\{h_i, \lambda_i\}$ are constants. The parametrization for the free energy (KSDT/GDSMFB) are available as finite-temperature XC functionals for a suite of DFT codes via a library of XC functionals (LIBXC) [Marques et al., 2012, Lehtola et al., 2018] package or can be incorporated into DFT simulations using the parametrized form.

2.3.3 Density Functional Theory-Molecular Dynamics

Density functional theory is combined with molecular dynamics (DFT-MD) to perform simulations at finite-temperature. The Born-Oppenheimer approximation is used to seperate the electronic system from the ionic. The ionic and the electron motion are decoupled, hence this combination allows for inexpensive computations compared to PIMC. Electrons can be treated at finite temperature by extending the KS Ansatz through the Mermin formulation, for which traditionally ground state (T=0) XC functionals are mostly used. Recent developments in finite-temperature XC functionals have been successfully used for the equation of state calculations using DFT-MD [Karasiev et al., 2016, Karasiev et al., 2018a, Karasiev et al., 2019b, Ramakrishna et al., 2020]. The grand potential is minimized with respect to the minimizing density i.e. equilibrium density and there exists a functional which is a finite-temperature analog of the Hohenberg-Kohn functional [Hohenberg and Kohn, 1964, Mermin, 1965]. The temperature is included in a self-consistency cycle at a finite-temperature where the free energy is minimized instead of the energy.

With electronic smearing, the occupancy of the KS states is given by a smooth function. The temperature for the electrons is set to finite-temperature by the method of electronic smearing especially for metallic systems. This improves the convergence with respect to the sampling of the Brillouin zone in metals. At T=0, the Fermi-Dirac distribution is step-like and the degenerate states at the Fermi level leads to convergence issues while sampling. By smearing or allowing fractional occupation, the problem can be mitigated. Fictitious smearing

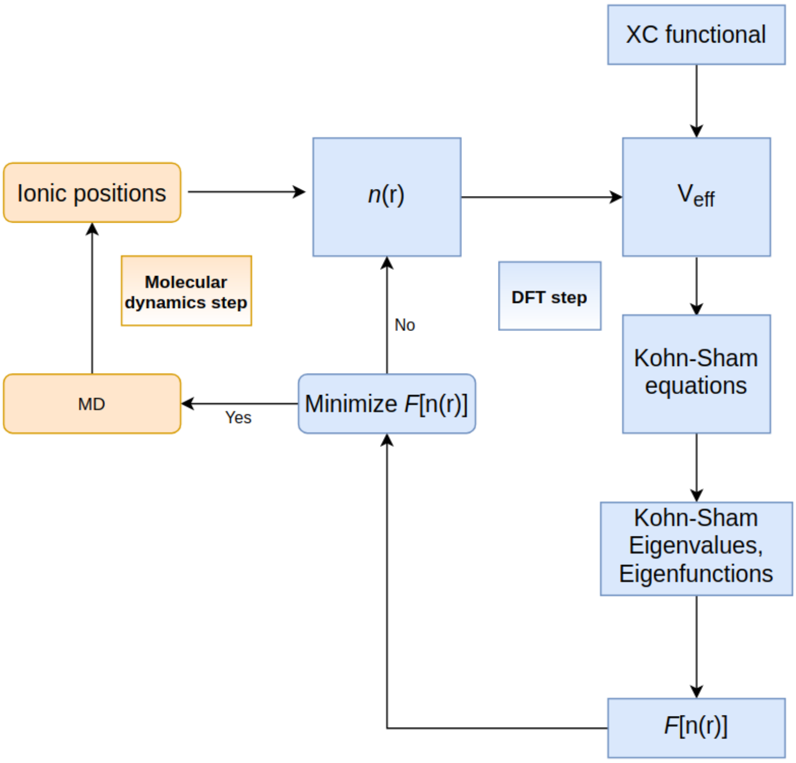

Figure 2.3.2: DFT-MD workflow represented in a flowchart.

choices include Gaussian smearing, usually employed for the calculations involving density of states. Other popular alternatives include Methfessel-Paxton [Methfessel and Paxton, 1989] or Marzari-Vanderbilt [Marzari et al., 1999] methods. The sampling in the Brillouin zone can influence the computed energy of the system. A common approach is to sample the reciprocal space at only the gamma-point (Γ). This saves a lot of computation time and works well for large system sizes. At large densities relevant in WDM, more k-points are required to sample the Brillouin zone. Monkhorst-Pack scheme [Monkhorst and Pack, 1976] can be utilized to generate a discrete grid of k-points for improving the convergence. See section 4.1 for the influence of k-point sampling.

The workflow of a typical DFT-MD simulation is shown in Fig. 2.3.2 [Graziani et al., 2014]. The DFT step consists of solving the KS equations self-consistently to minimize the free energy functional. In an MD step, the ions are moved for a finite time step by integrating Newton's equations using the Verlet algorithm [Verlet, 1967] and the resulting forces between the atoms are computed based on the electronic potential energy surface provided by the solution of the KS equations [Feynman, 1939, Hellmann, 2015]. The iteration has to be perfomed until the energy is converged. The self-consistent cycle is repeated for the new ionic positions. Periodic boundary conditions are employed for the simulation box. The temperature of the ions can be adjusted with the help of a thermostat, typically Nosé-Hoover [Nosé, 1984b, Nosé, 1984a] in the canonical ensemble.

2.3.4 Kubo-Greenwood Formula

In WDM, linear response calculations using *ab-initio* methods can be computed using relatively inexpensive (computationally) methods like the Kubo-Greenwood formula [Kubo, 1957, Greenwood, 1958] hereafter refered to as KG. The linear response quantities are computed only in the optical limit ($q \to 0$) under this scheme. Using the extended Mermin ansatz discussed in section 2.1.3 , it can be further extended to finite wavenumbers [Plagemann et al., 2012, Witte et al., 2017a]. The KG results in WDM have generally been applied to plasma and high energy densities and not in the calculations involving bound or partially bound state systems. Due to the approximations made in the derivation of KG, certain many body effects (that are usually collected in LFCs or XC kernels) are missing. In addition, KS eigenfunctions and eigenvalues are used, which are strongly dependent of the XC functional. KG on KS eigenfunctions and eigenvalues yields reasonable, if not accurate results which justifies their use on systems under certain conditions, but conceptually this procedure is wrong. These restrictions produce inconsistent results in the linear response, see section 3.2. The electrical conductivity can be evaluated from the wavefunctions evaluated from DFT using KG by computing the dynamic Onsager coefficients [Mazevet et al., 2010, Calderin et al., 2017]

$$\begin{aligned}\mathcal{L}_{ij}(\omega) = (-1)^{i+j}\frac{2\pi}{3V}\sum_{n,m,k,\alpha} |\langle \psi_{S_{n,k}} | \nabla_\alpha | \psi_{S_{m,k}} \rangle|^2 (\varepsilon_{m,k}-\mu)^{i-1}(\varepsilon_{n,k}-\mu)^{j-1} \\ \times \frac{f(\varepsilon_{m,k})-f(\varepsilon_{n,k})}{\varepsilon_{n,k}-\varepsilon_{m,k}}\delta(\varepsilon_{n,k}-\varepsilon_{m,k}-\omega),\end{aligned} \tag{2.3.41}$$

where V is the volume of the simulation cell, μ is the chemical potential, $f(\varepsilon)$ is the Fermi-Dirac distribution, $\alpha = x, y, z$, and $\psi_{S_{n,k}}$ are the KS orbitals at band n and wavevector k with corresponding energies $\varepsilon_{n,k}$ [Di Paola et al., 2020]. The electrical conductivity is given by the term $\mathcal{L}_{11}(\omega)$. As the summation is time consuming and too expensive for each time step of a DFT-MD simulation, it is instead performed for snapshots of the simulation.
The real part of the conductivity in Eq. (2.3.41) can be used to extract the imaginary part of the dielectric function using the relation $\Im[\varepsilon(\omega)] = \Re[\sigma(\omega)]/\varepsilon_0\omega$ and the real part of the dielectric function is in turn calculated using the Kramer-Kronig relation.

$$\Re[\varepsilon(q,\omega)] = 1 + \mathcal{P}\int_{-\infty}^{+\infty}\frac{d\omega'}{2\pi}\frac{\Im[\varepsilon(q,\omega')]}{\omega'-\omega}. \tag{2.3.42}$$

2.4 Time-Dependent Density Functional Theory

Time-dependent density functional theory (TDDFT) extends DFT to study the dynamics and phenomena of coupled electron-ion systems subject to time-dependent external fields. TDDFT can describe electronic excitations in solids including plasmons and excitons. DFT is a ground state theory and to study excited states requires an extension of the time-dependent Schrödinger equation. This follows from the Runge-Gross theorem [Runge and Gross, 1984] akin to the KS scheme by introducing an external KS potential $V_S(r,t)$ to a non-interacting electronic system that reproduces the time-dependent density $n(r,t)$ of the interacting system. The time-dependent KS equations take the following form

$$i\frac{\partial \psi_{S_j}(r,t)}{\partial t} = \left[-\frac{\nabla^2}{2} + V_S\left[n(r,t)\right]\right]\psi_{S_j}(r,t). \tag{2.4.1}$$

The occupied time-dependent KS orbitals determine the density of the interacting system

$$n(r,t) = \sum_j |\psi_{S_j}(r,t)|^2. \tag{2.4.2}$$

The KS potential similar to Eq. (2.3.14) is instead expressed as

$$V_S(r,t) = V_{ext}(r,t) + V_H(r,t) + V_{XC}(r,t). \tag{2.4.3}$$

The first term is the external potential, the second term is the Hartree potential, and the final term is the exchange correlation (XC) potential containing the many-body effects. The determination of XC potential in this formalism is not straightforward compared to DFT due to causality and can instead be represented as a functional derivative of an action functional (A_{XC}) derived from the Keldysm formalism [Keldysh et al., 1965, Varsano, 2006] as

$$V_{XC}\left[n(r,t)\right] = \frac{\partial A_{XC}}{\partial n(r,t')}\,|_{n(r,t)}, \tag{2.4.4}$$

where t' is the Keldysh pseudo time. The Keldysh formalism describes the evolution of a quantum mechanical system subjected to time-dependent external field or a systematic approach to study non-equilibrium systems. The exact expression for V_{XC} is unknown and the quality of calculations depend on the approximation for this term. The exchange-correlation kernel f_{XC} in TDDFT is given by

$$f_{XC}(r,r',\omega) = \frac{\partial V_{XC}\left[n(r,\omega)\right]}{\partial n(r',\omega)}\,|_{\delta V_{ext}=0}. \tag{2.4.5}$$

Compared to DFT where good approximations exist for V_{XC}, the simplest approximation in TDDFT is given by the adiabatic local density approximation (ALDA) or time-dependent local density approximation (TDLDA) where a static LDA functional is used for the dynamical properties [Onida et al., 2002]

$$V_{XC}^{ALDA}(r,\omega) = V_{XC}\left[n(r)\right]|_{n=n(t)}, \tag{2.4.6}$$

by using the approximation that the time-dependent functional is local in time which works for systems where the variation in temporal scale is negligible. Thus f_{XC} under ALDA is not frequency dependent. The kernel can now be written as

$$f_{XC}^{ALDA}(r,t,r',t') = \delta(r-r')\delta(t-t')\frac{\partial V_{XC}^{LDA}[n]}{\partial n}\,|_{n=n(r,t)}. \tag{2.4.7}$$

ALDA has issues as $q \rightarrow 0$, f_{XC}^{ALDA} does not diverge but approaches a constant missing the long range $1/q^2$ dependence and fails to describe excitonic effects. There has been extensive work on the construction of f_{XC} kernels especially long-range kernels for determination of optical properties [Botti et al., 2004, Sharma et al., 2011, Sottile et al., 2003, Reining et al., 2002, Ullrich, 2011].

The linear response of the system is measured by perturbing it with a time-dependent external potential $\delta W(r,t)$ which induces a time dependent density that is related to the perturbed potential [Ullrich, 2011]

$$\delta n(r,\omega) = \int dr' \chi(r,r'\omega)\delta W(r',\omega), \tag{2.4.8}$$

where $\chi(r,r',\omega)$ is the density-density response function of the system. Using the KS scheme, the induced density can be related to the potential via

$$\delta n(r,\omega) = \int dr' \chi_S(r,r'\omega)\delta V_S(r',\omega), \tag{2.4.9}$$

where δV_S contains the external, Hartree and the XC potential. The response function using the KS scheme is obtained by applying first-order perturbation theory to KS equations in terms of ground state eigenvalues (ε_j) and eigenfunctions (ψ_j) using

$$\chi_S(\mathbf{r},\mathbf{r}',\omega) = \lim_{\eta\to 0^+} \sum_{jk} \left(f_k - f_j\right) \frac{\psi_j(\mathbf{r})\psi_j^*(\mathbf{r}')\psi_k(\mathbf{r})\psi_k^*(\mathbf{r}')}{\omega - (\varepsilon_j - \varepsilon_k) + i\eta}, \tag{2.4.10}$$

where f_j is the KS orbital occupation numbers and η the Lorentzian broadening. Using Eqns. (2.4.8) and (2.4.9), the Dyson equation for the interacting density-density response function using the XC kernel is given by

$$\chi(r,r'\omega) = \chi_S(r,r,'\omega) + \int dr_1 dr_2 \chi_S(r,r_1,\omega)\left[\frac{1}{|r_1 - r_2|} + f_{XC}(r_1,r_2,\omega)\right]\chi(r_2,r',\omega). \tag{2.4.11}$$

The poles of Eq. (2.4.11) determine the excitiation energies of the system. Hence the knowledge of f_{XC} and χ_S allows to determine the full solution of Eq. (2.4.11). The Dyson equation connecting the interacting and non-interacting polarization functions in matrix formalism is written as

$$\chi = \left[1 - \chi_0(V + f_{xc})^{-1}\right]\chi_0. \tag{2.4.12}$$

The inverse of the dielectric function is a measure of the screening using the ratio of the total to the applied potential using

$$\varepsilon^{-1}(r,r,'\omega) = \frac{\delta V_{tot}(r,\omega)}{\delta V(r',\omega)}. \tag{2.4.13}$$

The dielectric matrix is now related to the polarizability using

$$\varepsilon^{-1}(r,r,'\omega) = \delta(r-r') + \int dr' V(r,r')\chi(r,r,'\omega). \tag{2.4.14}$$

The dynamically screened Coulomb interaction which takes into account the screening important for excitonic calculations is calculated using

$$W(r,r',\omega) = \int dr_1 V(r,r_1)\varepsilon^{-1}(r_1,r,'\omega). \tag{2.4.15}$$

The random phase approximation (RPA)[1] calculations are performed by setting the exchange-correlation kernel $f_{XC} \to 0$ in the density response function

$$\chi(q,\omega) = \frac{\chi_S^0(q,\omega)}{1-[V(q)-f_{XC}(q,\omega)]\chi_S^0(q,\omega))}. \tag{2.4.16}$$

Here χ_S^0 refers to the free density response function computed using the single particle KS states using Eq. (2.4.10) [Marques and Gross, 2004]. The dielectric function in RPA is obtained using

$$\varepsilon_{RPA}^{-1} = 1 + V(1-\chi_0 V)^{-1}\chi_0, \tag{2.4.17}$$

$$\varepsilon_{RPA} = 1 - \chi_0 V. \tag{2.4.18}$$

A simple way to construct an f_{XC} kernel with long-range behavior is to set [Ullrich, 2011]

$$f_{XC}(r,r') = -\frac{\alpha}{4\pi|\mathbf{r}-\mathbf{r}'|}, \tag{2.4.19}$$

and then performing a Fourier transformation, which is capable of accounting for the bound excitons using TDDFT. A simple long-range kernel using a parameter (α,β) dependent form $f_{XC}(q) = -\alpha/q^2$ in the static limit and $f_{XC}(q,\omega) = -(\alpha+\beta\omega^2)/q^2$ in the dynamical limit was developed which could capture the bound exciton with less comptational cost [Botti et al., 2004, Sottile et al., 2003] and outperformed ALDA. Due to the strong dependence of (α,β) on the material, the kernel is not so effective and simple to use until the development of a parameter free *bootstrap* kernel by Sharma *et. al* [Sharma et al., 2011] which effectively reproduces the bound exciton and computationally less expensive compared to the use of Bethe Salpeter equation discussed in section 2.6 .

The inverse of the dielectric function and the XC kernel are related by [Sharma et al., 2011]

$$\varepsilon^{-1}(q,\omega) = 1 + \chi_S^0(q,\omega)V(q)\left[1-(V(q)+f_{XC}(q,\omega))\chi_S^0(q,\omega)\right]^{-1}. \tag{2.4.20}$$

The bootstrap kernel is approximated by

$$f_{XC}^{boot}(q,\omega) = -\frac{\varepsilon^{-1}(q,\omega=0)V(q)}{\varepsilon_0^{00}(q,\omega=0)-1} = \frac{\varepsilon^{-1}(q,\omega=0)}{\chi_0^{00}(q,\omega=0)}, \tag{2.4.21}$$

where $\varepsilon_0(q,\omega)$ is the RPA dielectric function. The superscript in the denominator term indicates the evaluation with the reciprocal lattice vector components $G = G' = 0$. Equation (2.4.21) ensures the following conditions:

a) The long wavelength behavior $f_{XC}(q \to 0) = \alpha/q^2$,

---

[1] Not to be confused with the Lindhard dielectric function/RPA based on plasma theory introduced in section 2.1.1. RPA calculation in TDDFT formalism here simply means the lack of an XC kernel.

b) In the static limit $\omega \to 0$, the bootstrap kernel agrees closely with the RPA static dielectric constants.

Equation (2.4.20) is first solved by setting $f_{XC} \to 0$ to obtain ε^{-1} and then *bootstrapped* in Eq. (2.4.21) to obtain new f_{XC} and the self-consistency procedure is repeated for the two equations in the static limit. The procedure requires no external parameters and the computational cost is minimal as the expensive calculation involving χ_S^0 is only performed once.

2.5 GW Approximation

Using the second quantization formalism, the Green's function is introduced in this section. A single-particle Green's function describes the propagation of a single particle through the system containing the information on the momentum distribution and the ground state energy of the system. It is defined in coordinate and time space as

$$G(r_1, t_1, r_2, t_2) = -i\langle\varphi_N| T\left[a_H(r_1, t_1)a_H^\dagger(r_2, t_2)\right] |\varphi_N\rangle, \tag{2.5.1}$$

where φ_N is the N-electron ground state vector of the interacting system in the Heisenberg picture satisfying the Schrödinger equation $\hat{H}|\varphi_N\rangle = E|\varphi_N\rangle$ [Martin et al., 2016, Varsano, 2006]. The creation and annihilation field operators are given by $a_H^\dagger$ and a_H respectively defined as

$$\begin{aligned} a_H(r, t) &= e^{i\hat{H}t}a(r)e^{-i\hat{H}t} \\ a_H^\dagger(r, t) &= e^{-i\hat{H}t}a^\dagger(r)e^{i\hat{H}t}, \end{aligned} \tag{2.5.2}$$

and obeying the anti-commutation rules

$$\begin{aligned} a_H(r), a_H^\dagger(r') &= \delta(r - r') \\ a_H(r), a_H(r') = a_H^\dagger(r), a_H^\dagger(r') &= 0. \end{aligned} \tag{2.5.3}$$

T is the time-ordering operator such that

$$T\left[a_H(r_1, t_1)a_H^\dagger(r_2, t_2)\right] = \begin{cases} a_H(r_1, t_1)a_H^\dagger(r_2, t_2), & \text{if } t_1 > t_2 \\ -a_H(r_2, t_2)a_H^\dagger(r_1, t_1), & \text{if } t_1 < t_2. \end{cases} \tag{2.5.4}$$

The Green's function $G(r_1, t_1, r_2, t_2)$ describes the probability amplitude of the propagation of an electron (hole) from position r_2 at time t_2 to position r_1 at time t_1 given $t_1 > t_2$ ($t_2 > t_1$). By introducing the complete set of the eigenstates of the Hamiltonian, for the $(N + 1)$ and $(N - 1)$ particle systems and performing a Fourier transform, the Green's function in frequency space can be obtained as

$$G(r_1, r_2, \omega) = \sum_i \frac{F_i(r_1)F_i^*(r_2)}{\omega - \varepsilon_i + i\eta \,\mathrm{sign}(\varepsilon_i - \mu)}, \tag{2.5.5}$$

with μ the chemical potential of the system and ε_i are the single particle excitation energies such that

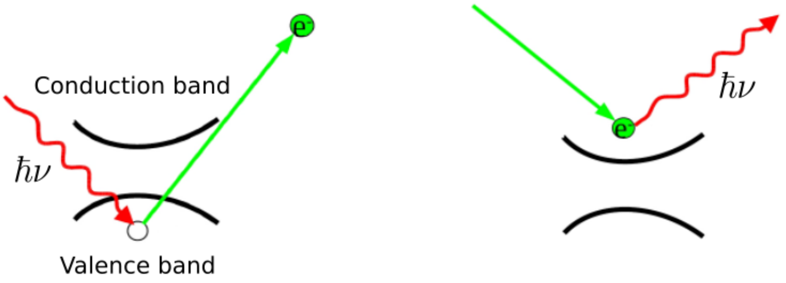

Figure 2.5.1: Single particle excitations correspond to the poles of single particle Green's functions in the GW approximation.

$$\varepsilon_i = \begin{cases} E_i^{N+1} - E_N^N, & \text{for} \quad \varepsilon_i \geq \mu \\ E_N^N - E_i^{N-1}, & \text{for} \quad \varepsilon_i < \mu. \end{cases} \tag{2.5.6}$$

where the subscript i indicates the label of the states of the N+1 (N−1) system for the total energies. The notation is made to distinguish the possible eigenstates of the system corresponding to the ionization energy (removal) and affinity (addition) of the system. By removing (adding) a particle the system gets excited in a combination of eigenstates with one less particle (one more particle).

The amplitudes are given by

$$F_i(r) = \begin{cases} \langle \varphi_N | a(r) | \varphi_{N+1,i} \rangle & \text{for} \quad \varepsilon_i \geq \mu \\ \langle \varphi_{N-1,i} | a(r) | \varphi_N \rangle & \text{for} \quad \varepsilon_i < \mu. \end{cases} \tag{2.5.7}$$

From Eq. 2.5.5, the Green's function essentially contains poles at the addition/removal eneries of the electron and describes energies of the quasiparticle excitations between valence and conduction bands depicted in Fig. 2.5.1. The resulting switching on of the interaction leads to a change in the single particle energies $E_i \rightarrow E_i + \Sigma$ where Σ is the self-energy operator. The self-energy can be treated as the potential felt by the addition or removal of an electron from the interacting system. The self-energy can be defined using the equation of motion of a single particle Green's function using the two particle Green's function

$$G(r_1, t_1, r_2, t_2) = G_H(r_1, t_1, r_2, t_2) + \int dr_3 dr_4 dt_3 dt_4 G_H(r_1, t_1, r_3, t_3)\Sigma(r_3, t_3, r_4, t_4)G(r_4, t_4, r_2, t_2), \tag{2.5.8}$$

where G_H is the Hartree Green's function of the non-interacting system, given by the solution of

$$[\omega - \hat{h}(r_1)]G(r_1, r_2, \omega) = \delta(r_1 - r_2), \tag{2.5.9}$$

where $\hat{h}(r)$ is the one-electron Hamiltonian $\hat{h}(r) = -\nabla_r^2/2 + V_{ext}(r) + V_H(r)$ with V_{ext} and V_H the external potential and the Hartree potential respectively. The self-energy term contains all the exchange and correlation many-body effects expressed in

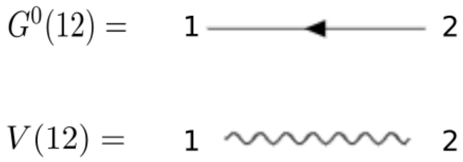

Figure 2.5.2: Feynman diagram representation of the Green's function and the interaction.

$$[\omega - \hat{h}(r_1)]G(r_1, r_2, \omega) = \delta(r_1 - r_2) + \int dr \Sigma(r_1, r, \omega) G(r, r_2, \omega). \tag{2.5.10}$$

Hedin's equations for self-consistency provides a systemic way to construct the self-energy using the screened Coulomb potential instead of the bare potential. It consists of a set of five equations [Hedin, 1965, Hedin and Lundqvist, 1970]

$$P(12) = -i \int d(34) G(1,3) G(4,1^+) \Gamma(34,2), \tag{2.5.11}$$

$$W(12) = V(12) + \int d(34) W(1,3) P(34) V(4,2), \tag{2.5.12}$$

$$\Sigma(12) = i \int d(34) G(14) W(1^+3) \Gamma(42,3), \tag{2.5.13}$$

$$G(12) = G^0(12) + \int d(34) G^0(13) \Sigma(34) G(42), \tag{2.5.14}$$

$$\Gamma(12,3) = \delta(12)\delta(13) + \int (d4567) \frac{\Sigma(12)}{G(45)} G(46) G(75) \Gamma(67,3), \tag{2.5.15}$$

where P is the polarization function or the irreducible polarizability, W is the screened interaction and Γ is the vertex function. The notation $1 = (r_1, t_1, \sigma_1)$ is used for the position, time and the spin. When Γ is set to unity, P describes non-interacting electron-hole pairs, or the random phase approximation (RPA). The screened interaction W is dynamical due to the frequency dependence of P.

Handling diagrams is much simpler than manipulating long and complex mathematical expressions. The Feynman diagrams explicitly unravel the physical content which underlies the various terms. The Feynman diagrams general premise is to provide a simple set of rules to convert a drawing into a well-defined mathematical quantity. The Green's function $G(1,2)$ is defined by a line oriented between 2 and 1. The line is designed to differentiate between $G(1,2)$ and $G(2,1)$. Essentially from the picture, we create a particle in 2 and destroy it back in 1. Hence, the particle propagates between 2 and 1. The interaction $V(1,2)$ is represented by a wavy line and has no direction $V(1,2) = V(2,1)$ as the screened interaction between the particles is symmetric. The screened interaction W was earlier refered in the section 2.1.1 in Fig. 2.1.1 for the sum of all possible polarization diagrams. The graphical notation of the Feynman diagrams are shown in Fig. 2.5.2 [Stefanucci and Van Leeuwen, 2013].

GW approximation consists in solving the set of Hedin's equations self-consistently represented graphically in Fig. 2.5.3. A practical approach involves approximating the vertex Γ as a local and instanteneous function $\Gamma_{GW} = \delta(12)\delta(13)$, which makes the solution of four self-conistent Hedin's equations in Fig. 2.5.3 simpler [Gonze et al., 2009]. In the first iteration, one starts with self-energy Σ set to zero, and G is approximated with the Green's function, of an appropriate non-interacting system (G^0) i.e., the KS system substituted as

$$G_S(r,r') = \sum_j \frac{\psi_S(r)\psi_S^*(r')}{\omega - \varepsilon_{S_j} - i\eta \mathrm{sign}(\mu - \varepsilon_{S_j})}, \tag{2.5.16}$$

where ψ_S and ε_S are the KS orbitals and the eigenvalues respectively. The polarizability is given by $-iG^0(12)G^0(21^+)$ and the screened interaction $W = \varepsilon^{-1}(1,2)V(4,2)$ is obtained using the dielectric matrix of the KS system. W is usually calculated using RPA and calculations beyond the level of RPA has little impact on the self-energy [Verdozzi et al., 1995]. The new self-energy $\Sigma(12) = iG^0(12)W(1^+2)$ is built, and the Schrödinger equation is solved to obtain a new set of quasiparticle energies and amplitudes. The loop should be iterated self-consistently, but due to the computational cost, an approach $\mathrm{G^0W^0}$ in which only a single iteration is performed is commonly used for most applications. The quasiparticle energies are given by

$$E_{QP} = \varepsilon_S + Z\langle\psi_S|\Sigma - V_{XC}|\psi_S\rangle, \tag{2.5.17}$$

where $Z = \left[\langle\psi_S|\frac{\partial\Sigma}{\partial\varepsilon_S}|\psi_S\rangle\right]^{-1}$ is the renormalization factor. It is defined as the amount of single-particle behavior of the particle-like excitation in the electron gas and is a measure of the spectral weight the quasiparticle peak carries [Mahan, 2013, Golze et al., 2019]. As the excitations behave like particles, they are termed *quasiparticles*. The self-energy in the GW approximation is represented as a Feynman diagram in Fig. 2.5.4 up to the leading contributing terms in the second order. The first two terms comprise the Hartree-Fock self-energy. The third term describes a particle (hole) propagating with an interaction with a particle-hole pair. The last term describes the correction to the exchange term in the second order.

The GW approximation provides good results for the calculation of band structures and band gaps in close agreement with experimental results [Shishkin and Kresse, 2007]. For the calculation of absorption spectra, the GW approximation is not sufficient as it describes excitations with the addition or removal of electrons whereas absorption involves the number of particles to remain constant, an electron leaving the valence band and leaving an hole or an empty state. Such a process requires the use of two particle propagators containing information about the propagation of two particles (electron–hole pairs) to describe the many-body effects and needs the inclusion of the vertex function.

2.6 Bethe-Salpeter Equation

The two particle (electron-hole) excitations can be described using the Bethe-Salpeter equation (BSE) [Salpeter and Bethe, 1951] which includes the electron-hole interaction. The vertex function can be extended to higher orders using the Dyson equation, thus giving the Bethe-Salpeter equation for the vertex function.

The functional derivative of the self-energy with respect to the Green's function is given

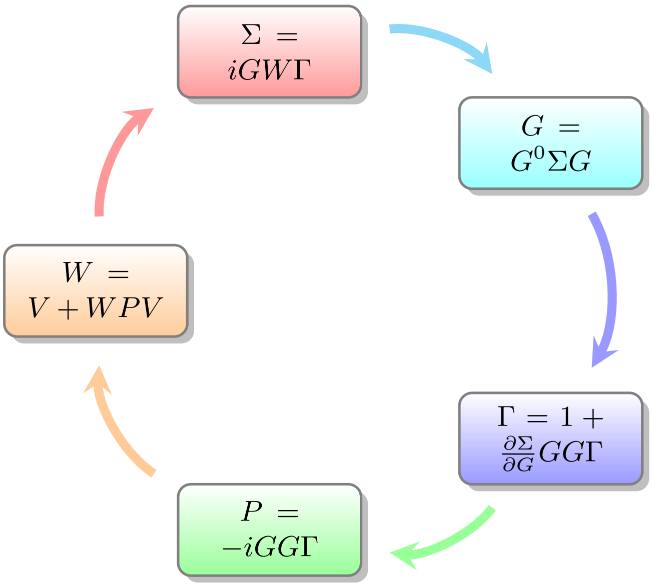

Figure 2.5.3: Solution of Hedin's equations in a self-consistency cycle.

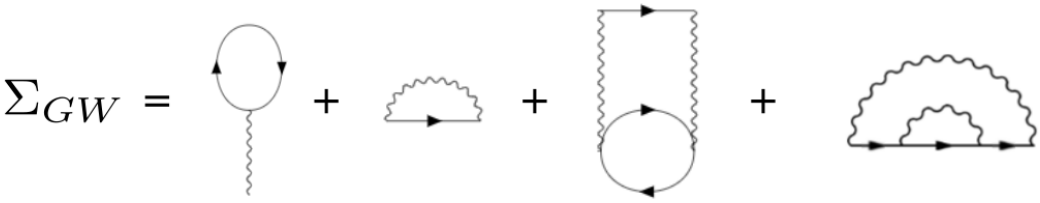

Figure 2.5.4: Feynman diagram of the GW self-energy in second-order Born approximation. The first two terms are the Hartree and Fock terms respectively. The third term is the first-order bubble diagram. The last term is the correction to the exchange in the second-order.

by [Onida et al., 2002, Strinati, 1988]

$$\frac{\partial \Sigma}{\partial G} = iW + iG\frac{\partial W}{\partial G}. \tag{2.6.1}$$

It is an alternative to saying that the self-energy can be graphically described by removing the Green's function line from the vertex diagram. Furthermore, ignoring the $iG(\partial W/\partial G)$ term which has a very small contribution, the functional derivative for the vertex in Hedin's equations [Eq. (2.5.15)] can be expressed as

$$\frac{\Sigma(12)}{G(45)} = \delta(14)\delta(25)W(1^+, 2). \tag{2.6.2}$$

The vertex for the Bethe-Salpeter equation is now given by

$$\Gamma(12, 3) = \delta(12)\delta(13) + i\int(d45)\frac{\partial\Sigma(12)}{\partial G(45)}G(14)G(52)\Gamma(45, 3). \tag{2.6.3}$$

The two-particle Green's functions is given by

$$G(12; 34) = G(13)G(24) \pm G(14)G(23) + \int d(1'2'3'4')G(11')G(3'3)K_r(1', 2'; 3', 4')G(4'4)G(22'). \tag{2.6.4}$$

The diagrammatic representation is shown in Fig. 2.6.1 with a square containing two incoming and two outgoing lines. The diagrammatic sum includes the product of two single-particle Green's function along with a kernel (K_r) containing all the two-particle Green's function diagrams of order greater than zero [Stefanucci and Van Leeuwen, 2013]. The two-particle density response function is given by

$$L(1, 2; 3, 4) = G(14)G(23) \pm \int d(1'2'3'4')G(11')G(3'3)K(1', 2'; 3', 4')L(4', 2; 2', 4). \tag{2.6.5}$$

By setting $1 = 3$ and $4 = 2$, Eq. (2.6.5) reduces to the polarizability (χ) form in Fig. 2.1.1. The relation between χ and L is $\chi(1, 2) = L(1, 2; 1^+, 2^+)$. The time ordering is important as $L(1, 2; 3, 4) = G_2(12; 34) - G(13)G(24)$ is calculated as the difference between two-particle and single-particle Green's function. The ambiguity is removed by shifting the time arguments of the starting points. The diagrammatic representation of L is shown in Fig. 2.6.2. The Dyson-like equation for the kernel (K) is given by

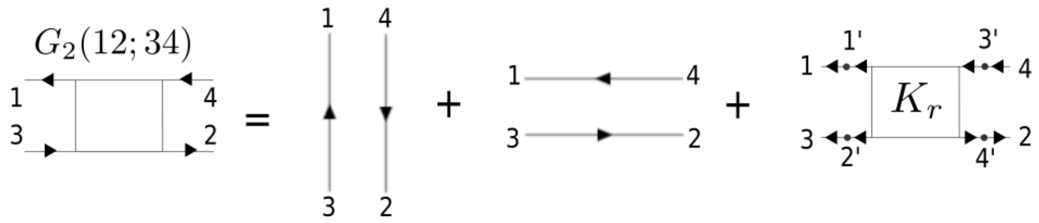

Figure 2.6.1: Feynman diagram representation of the two-particle Green's function.

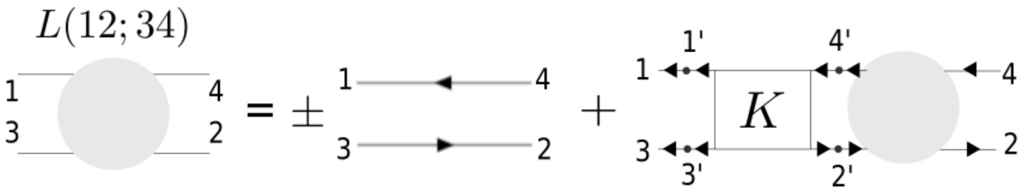

Figure 2.6.2: Feynman diagram representation of the two-particle density response function.

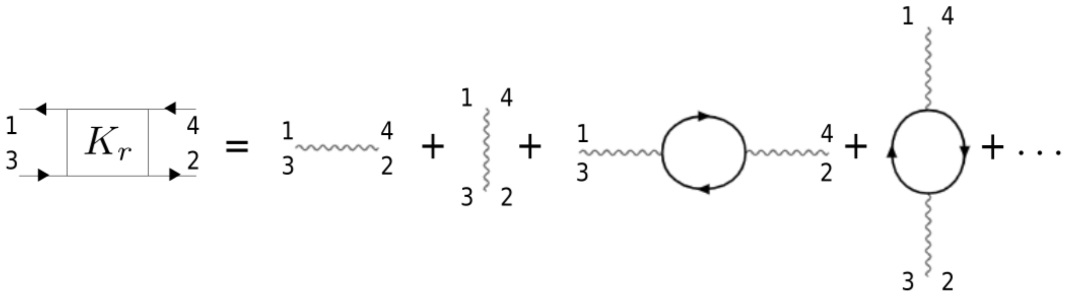

Figure 2.6.3: Feynman diagrams for the leading terms of the reducible kernel.

$$K_r(1,2;3,4) = K(1,2;3,4) + \int d(1'2'3'4')K(1,2';3,4')G(4'1)G(3'2')K_r(1',2;3',4). \qquad (2.6.6)$$

The reducible kernel is represented diagramatically in Fig. 2.6.3. In the lowest order approximation in interaction, the kernel reduces to

$$K = -i\delta(1,4)\delta(2,3)V(1,3) + i\delta(1,3)\delta(2,4)W(1,2). \qquad (2.6.7)$$

The first term in Eq. (2.6.7) is the exchange term and the second term is the self-energy variation with respect to the single particle Green's function. In terms of the GW approximation, it is the screened Coulomb interaction. Furthermore, only static screening is considered to simplify BSE time structure.

An electron in a valence band absorbs a photon and moves to the conduction band, leaving behind a hole in the valence band. The bound electron-hole pair form a quasiparticle known as *exciton* shown in Fig. 2.6.4. The approach to Bethe-Salpeter equation can be seen as a two-step process, where a first step involving the calculation of GW results in a sharp shift of the entire spectrum to higher energies and the subsequent inclusion of the electron-hole interaction redistributes oscillator strength to low energy peaks. Finally the peaks change, or creation of an additional peak in the quasiparticle gap. The description of the optical spectra of semiconductors and insulators is one of the most popular applications of the Bethe-Salpeter equation. The measured optical spectra of several systems with significiant excitonic features were found to be in good agreement with the experiments [Onida et al., 2002, Stefanucci and Van Leeuwen, 2013].

The constructed BSE Hamiltonian has to be diagonalized or inverted. Diagonalization has the advantage that it yields coefficients and transition energies which help interpret results. When taking into account several transitions, the Hamiltonian matrix can be too big and cause mem-

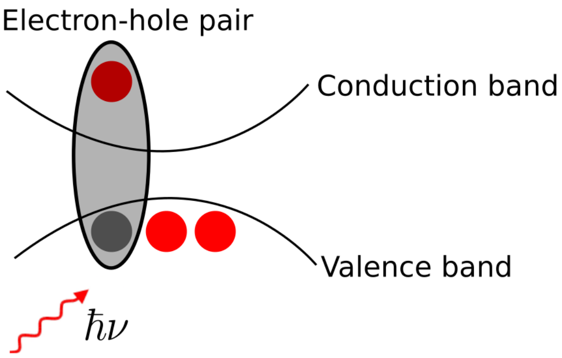

Figure 2.6.4: Two particle excitations correspond to the poles of two particle Green's functions. Electron in the conduction band and the hole left behind in the valence band form a bound exciton.

ory issues, since at least half of the matrix has to be stored in memory for the diagonalization. An alternative is the iterative inversion introduced by Haydock [Haydock, 1980] implemented in several *ab-initio* codes [Gonze et al., 2020, Marini et al., 2009]. In the iterative approach a matrix vector product must be performed at each iteration step, and the memory of the full matrix is not required. In general, iterative methods are very good for massive parallelization, even better than diagonalization. The calculation of matrix elements of W is the most time consuming component of the BSE. The use of Cholesky factorization with singular value decomposition has recently been demonstrated in reducing the computational cost at the same level of accuracy obtained using eigenvalue decomposition [Benner and Penke, 2020].

Calculation of optical spectra needs a much denser k-point sampling than for the corresponding ground-state computations. The explanation is that one is interested in more detailed knowledge of the electronic structure. The electron-hole interaction results in enhancing the low-energy structures which can be effectively captured by sampling enough k-points [Martin et al., 2016]. A good technique is to use a standard k-point grid, shifted by a fraction of the distance between k-points in an off-symmetry direction. All points are non-equivalent in this case, which corresponds to a better sampling in the Brillouin zone. The influence of k-point sampling on the spectrum of diamond is shown in Fig. 2.6.5. A k-point offset vector $(1/4, 1/2, 5/8)$ in lattice coordinates is used for the enhanced sampling in the Brillouin zone. The calculations are explored in further detail in section 3.2.

2.7 Conclusions

X-ray thomson scattering (XRTS) provides an effective diagonistics for warm dense matter. Traditionally, the inelastic scattering component of the XRTS spectra has been modeled using RPA based on plasma theory with the inclusion of local field corrections and collision frequencies built from quantum statistical approaches.

KS eigenvalues, which occur in the minimization of the density functional, do not bear a clear physical significance even though they can be regarded as well-defined approximations to the excitation energies. Particularly, they can be used as a good starting point for perturbative

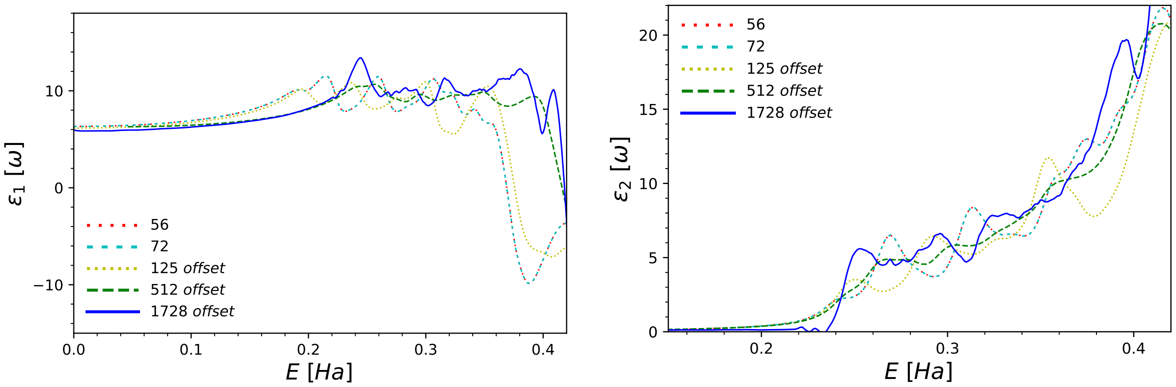

(a) (b)

Figure 2.6.5: Effect of *k*-point sampling on the a) Real and b) Imaginary part of the dielectric function of diamond in the optical limit.

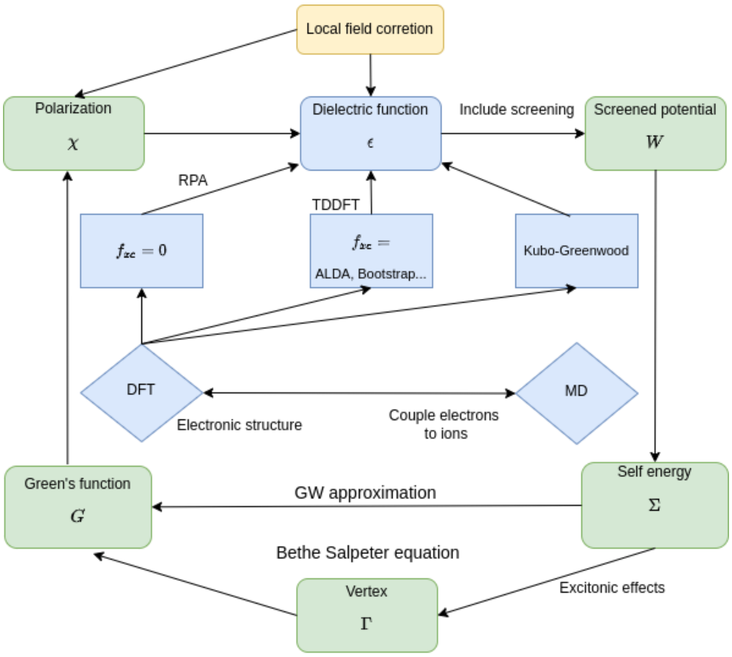

Figure 2.7.1: A flowchart of the procedure to obtain response function using density functional theory and many-body theoretical techniques.

self-energy calculations. GW calculations have been successfully carried out for real systems validating the experimental measurements.

The Bethe-Salpeter equation explains the electron-hole interaction (excitonic effects), through the functional derivative of the self-energy. The electron-hole interaction can be used in order to achieve improved response functions by adding the vertex corrections beyond the RPA, which is achieved in practice by solving the polarizability of the four-point propagator. Although computationally expensive, it generally leads to excellent absorption and energy-loss spectra of electrons. Calculations in TDDFT are computationally less expensive (with the two-point propagator) than the case with the Bethe-Salpeter method. The adiabatic local density approximation (ALDA) kernel for TDDFT has yielded promising results for finite systems, but has significant shortcomings in the definition of the absorption spectrum in solids, resulting in incorrect excitation energies, the absence of bound excitonic conditions, and substantial distortions of the spectral line shapes. The search for better TDDFT capabilities and kernels are therefore a subject of rising interest. Better exchange-correlation kernels for TDDFT in the ground state and an effective kernel for the warm dense matter regime can be developed in the future with the advancements and availability of local field correction data from PIMC simulations.

To conclude the section, a flowchart is presented in Fig. 2.7.1 showing the methodology involved in the evaluation of the response function. Based on *ab-initio* methods, DFT for ground state or DFT-MD (snapshots of ionic configurations) for higher temperatures are used for calculating the KS orbitals which are in turn used to calculate the response function based on the many-body theoretical techniques discussed so far.

3 Ab Initio Dielectric Response Function of Diamond and Other Relevant High-Pressure Phases of Carbon

Results of this chapter are published in
K. Ramakrishna et al.,
J. Phys.: Condensed Matter ***32****, 095401 (2020)*
S. Frydrych et al.,
Nature Communications ***11****, 2620 (2020)*
K. Voigt et al.,
Physics of Plasmas ***28****, 082701 (2021)*
D. Ranjan et al.,
Physics of Plasmas ***30****, 052702 (2023)*

Carbon is one of the most abundant elements in the universe. The wide array of allotropes and compounds formed is due to the ability to form hybrid bonds. Due to the extreme pressure and temperature conditions inside the planets, the material properties are drastically changed. Ross *et.al.* [Ross, 1981] predicted the occurance of diamond rain due to the demixing of the carbon and hydrogen atoms of methane under extreme conditions. Creating these conditions in the lab is possible using compression methods like laser driven shock waves such that nano-diamonds can indeed be observed [Kraus et al., 2017, Kraus et al., 2018, Schuster et al., 2020, Frydrych et al., 2020]. Recently, diamond formation is also observed in a doubly shocked epoxy sample additionally containing oxygen, nitrogen, and chlorine mixture indiciating complex chemical processes and kinetics plays an important role [Marshall et al., 2022]. Simulations can provide information a priori to the design of such experiments and are essential for the evaluation and analysis of the measurements [Kraus et al., 2018, Hartley et al., 2018]. For inertial confinement fusion (ICF), target design is important for its feasibility. Due to its high atomic density, low reactivity and high yield strength, diamond seems to be a promising candidate for the ablator material [Biener et al., 2006, Biener et al., 2009].

Carbon has a rich phase diagram based on the theoretical predictions under extreme conditions summarized in Fig. 3.0.1. Under ambient conditions of temperature and pressure, carbon manifests in two allotropes: graphite and diamond [Grumbach and Martin, 1996]. Diamond has a face centered cubic (FCC) structure and stable at conditions of low pressure and temperature. Graphite has an hexagonal strcuture (HCP) under ambient conditions. The individual layers in graphite are known as graphene [Geim, 2009] arranged in an honeycomb lattice. The BC8 (body centered cubic diamond) phase seen above 1000 GPa pressure is predicted to be harder than diamond. In ICF, this phase has to be avoided along the compression path. Apart from diamond, plastic materials are also interesting for ICF and the phase separation of carbon and hydrogen could lead to hydrodynamic instabilities reducing the implosion performance [Knudson et al., 2008, Biener et al., 2009, Hurricane et al., 2014].

Lonsdaleite or hexagonal diamond is a phase discovered for the first time in meteorite remnants in 1967 and has subsequently been recreated in the lab [Frondel and Marvin, 1967]. Based on theoretical predictions under ambient conditions, it is found to be metastable [Ferroir et al., 2010]. It is further reported in various laboratory experiments, but the occurance of the phase under ambient conditions is still debatable [Bundy and Kasper, 1967, Yagi et al., 1992, Utsumi et al., 2004, Németh et al., 2014, Kraus et al., 2016, Turneaure et al., 2017, McCulloch et al.,].

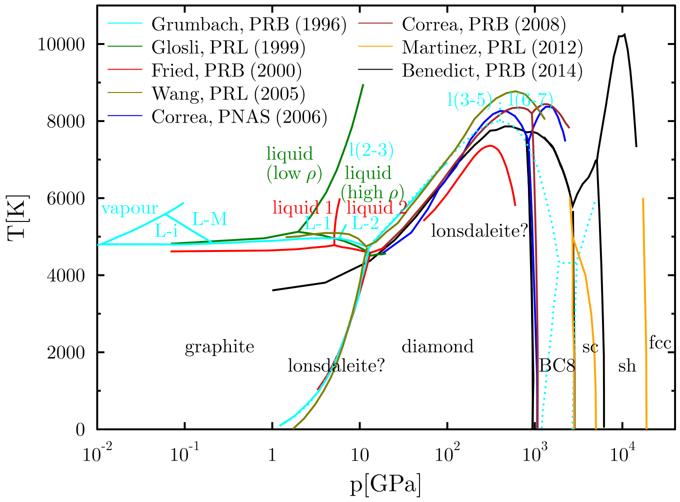

Figure 3.0.1: Carbon phase diagram based on the theoretical work over the last three decades [Grumbach and Martin, 1996, Glosli and Ree, 1999, Fried and Howard, 2000, Wang et al., 2005, Correa et al., 2006, Correa et al., 2008, Martinez-Canales et al., 2012, Benedict et al., 2014]. Data provided by Jan Vorberger.

The characterization of the electronic and ionic characteristics of carbon, its equation of state (EOS) and the related phase boundaries includes state-of-the-art methods such as density functional theory with molecular dynamics (DFT-MD) or path integral Monte Carlo (PIMC). A combination of DFT and many-body quantum statistics allows to include higher order correlations to be included such that the theoretical methods and predictive ability of dynamic structure factor (DSF) and equation of state is enhanced. The DSF is of particular interest, as it is an important quantity to assess the properties of high-pressure solids and fluids and warm dense matter (WDM) states. Improved DSF models in particular involve interactions between the electron–hole in semiconductors and insulators. This offers enhanced predictions for dielectric functions and conductivities, especially when combined with higher rungs of exchange correlation (XC) functionals to characterize the band gaps, thus leading to an improved description of the dielectric function or DSF. The determination of temperature based on the x-ray Thomson scattering (XRTS) data is therefore improved as a practical application.

3.1 Electronic Properties under High-Pressure

In this section, electronic structure calculations are performed on three different carbon phases: diamond, lonsdaleite and BC8. The crystal structure of the phases generated using VESTA [Momma and Izumi, 2011] are shown in Fig. 3.1.1. The calculations are performed using the *elk* code [Dewhurst, 2021] to obtain the optimal lattice parameters, density of states (DOS) and band gaps with the pressure varied. Furthermore, since the systems show interesting behavior with wide-band semidconducting to semimetallic nature in the pressure range, the choice of XC functionals and corrections to the band gap become important. The GW calculations are also performed to obtain accurate band gaps and are compared to a range of XC functionals.

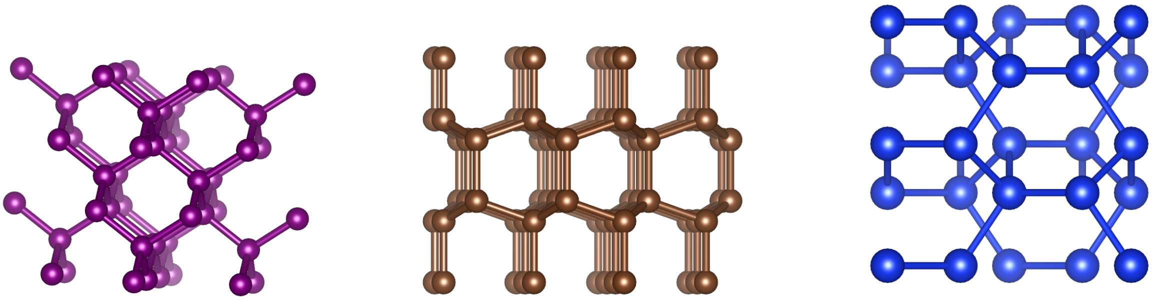
(a) Diamond (b) Lonsdaleite (c) BC8

Figure 3.1.1: Some of the crystal phases of carbon.

3.1.1 Diamond

Under ambient conditions, diamond has a face-centered cubic (FCC) structure with the space-group Fd$\bar{3}$m consisting of 2 atoms per primitive unit cell. The lattice parameters are $a = b = c$, $\alpha = \beta = \gamma = 90^0$. The electronic structure calculations are performed using the *elk* code [Dewhurst, 2021] on a 20×20×20 k-point mesh and 16 bands using a PBE XC functional [Perdew et al., 1996a] with Broyden mixing [Johnson, 1988]. The stated number of k-points and bands ensures the convergence with the use of an all-electron code. The XC functional is important for the reliability of the results as the electronic density fluctuations crucially determine the pressure and energy of the system at the considered high pressures. Martinez-Canales *et. al.* have successfully tested the PBE functional up to 1000 TPa for the carbon allotropes [Martinez-Canales et al., 2012].

The total energy obtained from DFT calcularions for various volumes are used in the Vinet equation of state (EOS) [Vinet et al., 1987, Vinet et al., 1989]

$$P(x) = 3B_0 \frac{(1-x)}{x^2} e^{\eta(1-x)}, \tag{3.1.1}$$

where $x = (V/V_0)^{1/3}$, $\eta = 1.5(B_0' - 1)$ with V_0 the equilibrium lattice volume. B_0 and $B_0' = (\partial B_0/\partial P)|_T$ are the bulk modulus and the pressure derivative of the bulk modulus respectively. The obtained equilibrium lattice parameter a_0 =3.569 Å is close to the experimental measurement 3.567 Å [Madelung, 2012].

The density of states (DOS) provides information on the location of the eigenvalues and their change with density or temperature. It is evaluated by a sum over the k-points

$$DOS(E) = \sum_k W_k \sum_i \gamma(E - \varepsilon_i), \tag{3.1.2}$$

where W_k is the weight associated with the k-point, γ is a broadening function, to account for the discreteness of the eigenvalues and ε_i are the KS eigenvalues. For normalization, the

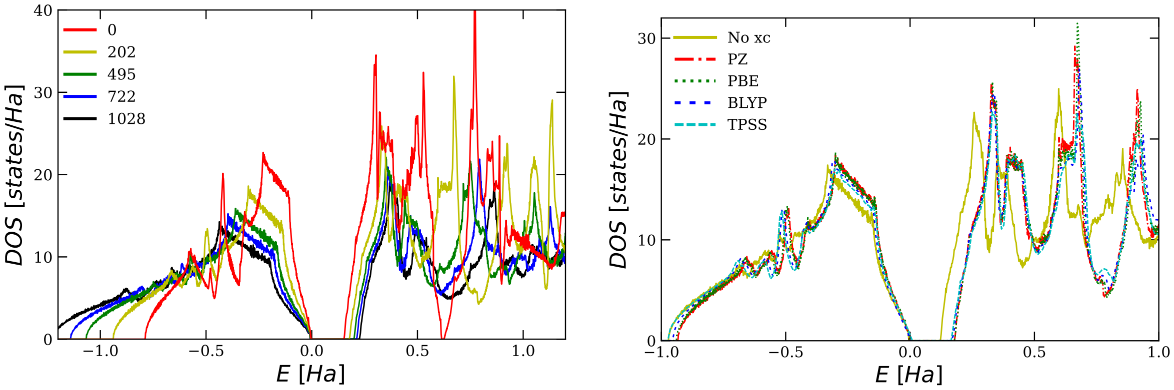

(a)

(b)

Figure 3.1.2: Density of states for diamond as a) function of pressure using PBE XC, b) at 202 GPa using various XC functionals. The pressures are in GPa and the valence band maximum is adjusted to zero. **K Ramakrishna and J Vorberger** 2020 J. Phys.: Condens. Matter **32** 095401.

Fermi energy is used in the case of metals and the valence band maximum in semiconductors [Seitsonen, 2000].

The electronic DOS at various pressures using the PBE XC functional are shown in Fig. 3.1.2(a). The valence band exhibits pressure broadening and an opening of the band gap is observed with increasing pressure. Figure 3.1.2(b) shows the DOS at 202 GPa using various XC functionals. With no XC included, the conduction band minimum is vastly underestimated whereas the valence states are better represented. The use of LDA (PZ) [Perdew and Zunger, 1981] or GGA (PBE) has very little differences to each other. The DOS using BLYP (GGA) [Becke, 1988, Lee et al., 1988] and TPSS (meta-GGA) [Tao et al., 2003] are computed using Quantum ESPRESSO [Giannozzi et al., 2009, Giannozzi et al., 2017] for 32 bands on a 20×20×20 *k*-point mesh using the tetrahedron method [Blöchl et al., 1994] for Brillouin zone integration. PBE, BLYP and TPSS agree with each other remarkably well. This also ensures the convergence of the calculations comparing an all-electron code and the use of pseudopotential.

With the choice of LDA or GGA XC functionals, the band gap in semiconductors and insulators is underestimated when compared with experiment [Perdew, 1985].

The fundamental band gap for an *N*-particle system is given by

$$E_G = (E_{N+1} - E_N) - (E_N - E_{N-1}), \tag{3.1.3}$$

where E_N is the ground state energy of *N*-particles. Let e_G denote the energy gap obtained from the exact KS equation for the *N*-particle ground state. The correction to the band gap is given by

$$E_G - e_G = \Delta = \frac{\partial E_{XC}}{\partial n(r)}|_{N+\delta} - \frac{\partial E_{XC}}{\partial n(r)}|_{N-\delta}. \tag{3.1.4}$$

The correction Δ is called the derivative disconinuity, due to the fact that E_N changes slope

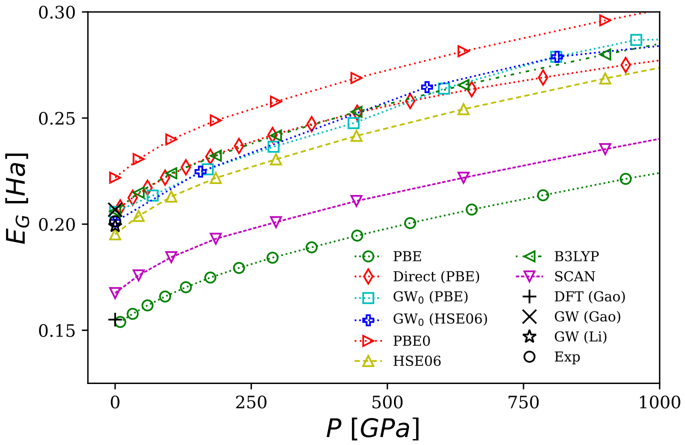

Figure 3.1.3: Band gap of diamond calculated using various XC functionals [Perdew et al., 1996a, Heyd et al., 2003, Becke, 1988, Lee et al., 1988, Sun et al., 2015, Perdew et al., 1996b] as function of pressure in DFT and within the GW approximation. The direct band gap is calculated using PBE. Theoretical data stems from Ref [Li et al., 2012, Gao, 2015]; Experimental data stems from Ref. [Peter and Cardona, 2010]. **K Ramakrishna and J Vorberger** 2020 J. Phys.: Condens. Matter **32** 095401.

at integer particle number [Martin et al., 2016]. Based on the derivative discontinuity in Eq. (3.1.4), improvements over LDA can be made with higher order XC functionals. Even with the knowledge of the exact XC functional, the fundamental band gap of the interacting system is not provided by the KS formalism [Sham and Schlüter, 1983, Perdew and Levy, 1983].

Based on the close agreement with experimental measurements, the GW method provides reliable band gaps [Shishkin and Kresse, 2007] discussed in section 2.5. The steps involve initial evaluation of the KS orbitals and eigenvalues obtained using DFT, followed by the setting up of the KS Green's function in Eq. (2.5.16). This leads to iteratively solving Eqns. (2.5.11)-(2.5.15) to obtain the self-energy and henceforth obtaining the corrections to the KS eigenvalues.

The correction is performed using the GW approximation implemented in VASP [Kresse and Hafner, 1993, Kresse and Joubert, 1999, Kresse and Furthmüller, 1996b, Kresse and Furthmüller, 1996a] with 64 bands on a $16\times16\times16$ *k*-point mesh centered around the Gamma point using the PBE XC functional with a hard carbon PAW pseudopotential and the energy cutoff set to 10 Ha. The core electrons are frozen for the purpose of the calculation while considering a core radius of $r_c = 1.5a_B$.

A significant number of empty bands is required for GW calculations. In the first step, a standard groundstate DFT calculation is performed to obtain the KS eigenvalues and eigenfunctions. In step two, a single-shot calculation refered to as G^0W^0 calculates the quasiparticle energies from a single GW iteration. The off-diagonal matrix elements of the self-energy are neglected.

With increasing pressure, the direct and the indirect band gaps widen almost linearly as shown in Fig. 3.1.3 corroborating the experimental evidence of the band gap opening under compression by Gamboa *et al.* [Fahy et al., 1987, Gamboa et al., 2016]. The band gap obtained using PBE is the smallest as expected and using advanced functionals further improves the band gap. The GW^0 results are in the range obtained by other simulations [Zhu et al., 2011, Li et al., 2012, Gao, 2015, Shi et al., 2020] and agree with experimental results [Peter and Cardona, 2010]. Hybrid functionals have been shown to provide reliable bandgaps [Paier et al., 2008, Hummer et al., 2009] for carbon allotropes espcecially HSE06 [Heyd et al., 2003, Paier et al., 2008]. Interestingly, the GW^0 corrections performed on PBE and HSE06 show no dependence on XC functionals.

The bulk diamond is characterized by a band gap renormalization induced by the electron–phonon interaction. This renormalization is important to the predictive power of *ab-initio* calculations when it comes to optical spectra [Cannuccia and Marini, 2011, Antonius et al., 2014]. For diamond, the direct band gap renormalization due to the electron-phonon coupling is shown to be 0.409 eV by Poncé *et. al.* [Poncé et al., 2014]. It is ignored considering the high pressures considered here [Zacharias and Giustino, 2016, Monserrat and Needs, 2014, Yang and Kawazoe, 2012, Cannuccia and Marini, 2011, Marini, 2008].

3.1.2 Lonsdaleite

Lonsdaleite is a carbon allotrope with the spacegroup P6$_3$/mmc. The lattice parameters are $a = b \neq c$, $\alpha = \beta = 90^0$, $\gamma = 120^0$. The unit cell volume is $(\sqrt{3}/2)a^2c$ with 4 atoms per unit cell. The basis vectors in lattice coordinates are given by the 4f Wyckoff positions $(\frac{1}{3}, \frac{2}{3}, z_1)$, $(\frac{2}{3}, \frac{1}{3}, \frac{1}{2} + z_1)$, $(\frac{2}{3}, \frac{1}{3}, -z_1)$, $(\frac{1}{3}, \frac{2}{3}, \frac{1}{2} - z_1)$ with the internal parameter z_1 [Mehl et al., 2017].

The DFT calculations are performed using the *elk* code [Dewhurst, 2021] for 16 bands on a 16×16×16 *k*-point mesh using PBE XC functional [Perdew et al., 1996a] with Broyden mixing [Johnson, 1988]. To account for the various pressure ranges, the muffin-tin radius is adjusted from 0.55 Å to 0.75 Å. Using the Vinet EOS, the equilibrium lattice constants $a = 2.524$ Å, $c = 4.128$ Å with $z_1 = 0.0625$ are obtained. While ideal hexagonal structures at ambient conditions have $z_1 = 1/16$ with $c/a = \sqrt{8/3}$, we have to relax the structure for each considered pressure to minimize the enthalpy and to obtain the lattice parameters as shown in Figs. 3.1.4(a) and 3.1.4(b).

The electronic DOS is shown in Fig. 3.1.5(a). With increasing pressure, the band gap closes in contrast to diamond. The band gap calculations are performed with a range of XC functionals and GW approximation. The band gap is shown as function of pressure in Fig. 3.1.5(b). The GW corrections are perfomed using VASP with a 16×16×16 *k*-point mesh centered around the Gamma point for 64 bands, and PBE XC functional. The kinetic energy cutoff for the wavefunctions is set to 40 Ha. A single shot G^{0}W^0 approach is used to reduce the computational cost also ignoring the off-diagonal elements of the self energy term. The indirect band gap, unlike in the cubic diamond case, is across the points $\Gamma \rightarrow K$ [Salehpour and Satpathy, 1990]. Under ambient conditions, the GW and the PBE band gaps are in good agreement with the available theoretical results [Zhu et al., 2011, Gao, 2015, De and Pryor, 2014]. Using advanced XC functionals, HSE06 and B3LYP, the results are comparable to the GW band gaps.

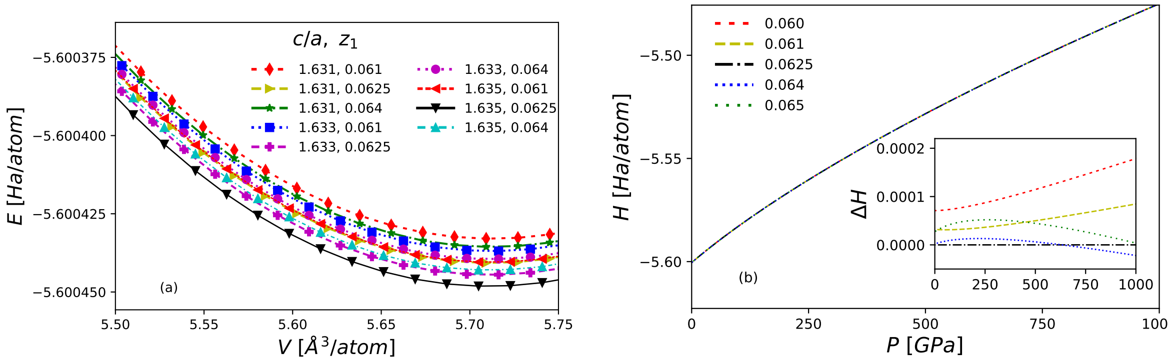

(a) (b)

Figure 3.1.4: a) Variation of the parameters c/a and z_1 for lonsdaleite, (b) Enthalpy vs pressure with respect to z_1 for lonsdaleite. The inset plot shows the relative enthalpies with respect to $z_1 = 0.0625$ vs pressure for $c/a = 1.635$. **K Ramakrishna and J Vorberger** 2020 J. Phys.: Condens. Matter **32** 095401.

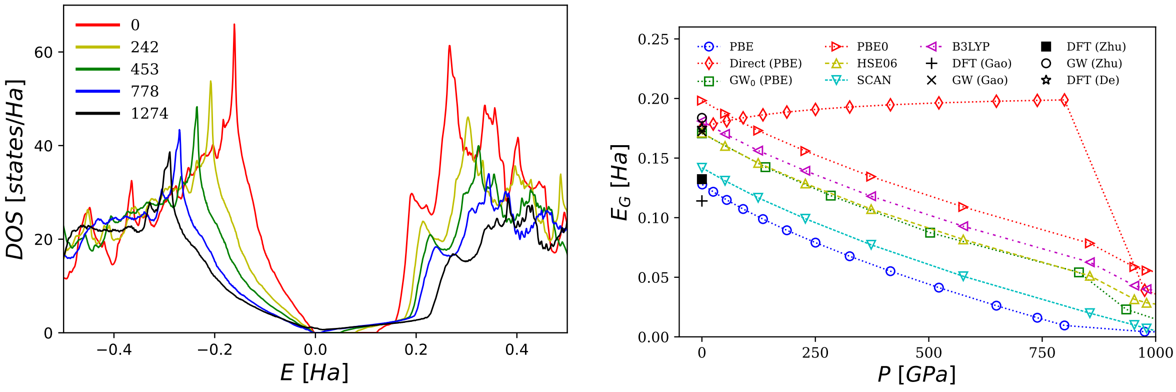

(a) (b)

Figure 3.1.5: a) Density of states for lonsdaleite as function of pressure. The pressures are in GPa and the valence band maximum is adjusted to zero, (b) Lonsdaleite band gap as function of pressure using DFT and GW. The direct band gap calculated using PBE is also shown. The density range covers 3.5 g/cm^3 to 6.9 g/cm^3. Theoretical data stems from Ref. [Zhu et al., 2011, De and Pryor, 2014, Gao, 2015]. **K Ramakrishna and J Vorberger** 2020 J. Phys.: Condens. Matter **32** 095401.

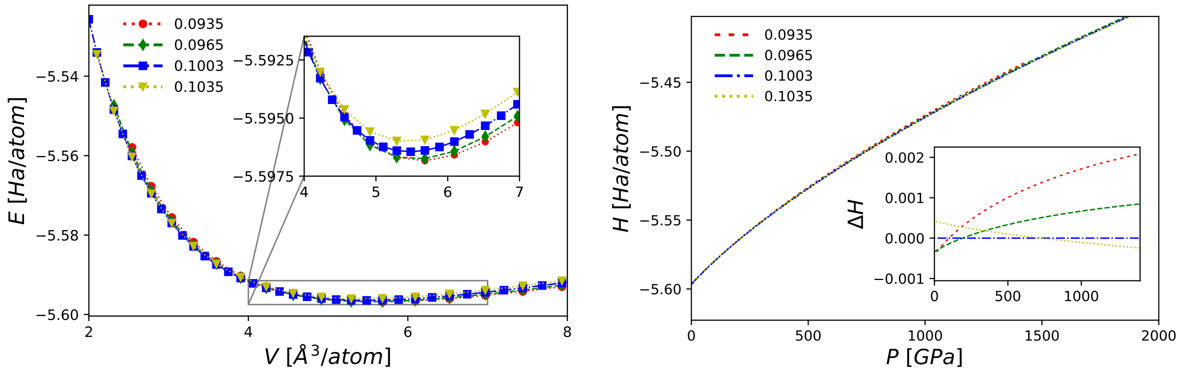

(a)

(b)

Figure 3.1.6: a) Variation of the parameter x_1 for BC8. The inset panel zooms at the region of the minimum, (b) Enthalpy vs pressure with respect to x_1 for BC8. The inset plot shows the relative enthalpies with respect to $x_1 = 0.1003$ vs pressure. $x_1 = 0.935$ suggested by Clark *et al.* is ideal for the formation of BC8 phase from diamond and at higher pressures the larger internal parameter is better suited [Clark, 1994]. **K Ramakrishna and J Vorberger** 2020 J. Phys.: Condens. Matter **32** 095401.

3.1.3 BC8

BC8 has a body-centered cubic structure with the spacegroup Ia$\bar{3}$ consisting of 8 atoms per unit cell with the unit cell volume $a_0^3/2$ where a_0 is the lattice constant. The lattice parameters are $a = b = c$, $\alpha = \beta = \gamma = 90^0$ [Benedict et al., 2014, Zhang et al., 2017]. The basis vectors in lattice coordinates are given by the 16c Wyckoff positions $(2x_1, 2x_1, x_1)$, $(\frac{1}{2}, 0, \frac{1}{2} - 2x_1)$, $(0, \frac{1}{2} - 2x_1, \frac{1}{2})$, $(\frac{1}{2} - 2x_1, \frac{1}{2}, 0)$, $(-2x_1, -2x_1, -2x_1)$, $(\frac{1}{2}, 0, \frac{1}{2} + 2x_1)$, $(0, \frac{1}{2} + 2x_1, \frac{1}{2})$, $(\frac{1}{2} + 2x_1, \frac{1}{2}, 0)$ with x_1 as a parameter [Mehl et al., 2017].

The DFT calculations are performed using the *elk* code [Dewhurst, 2021] for 32 bands on a 16×16×16 *k*-point mesh using PBE XC functional [Perdew et al., 1996a] with Broyden mixing [Johnson, 1988]. The internal parameter $x_1 = 0.0935$ compares favorably to the experimental value, 0.1003 ± 0.0008 widely used for the BC8 phase of silicon. Several DFT simulations involving BC8 phase have also used this parameter [Clark, 1994, Crain et al., 1994, Kasper and Richards, 1964]. Based on the enthalpy changes with respect to pressure as shown in Fig. 3.1.6(b) up to 2500 GPa, the parameter $x_1 = 0.1003$ is a suitable choice for the calculations involving the range of pressure. The lattice constant a_0=4.437 Å lies within the range of the values 4.425–4.477 Å obtained by Z. Li and Crain *et al.* [Li et al., 2015, Crain et al., 1994].

The electronic density of states calculated using the PBE XC functional with the *elk* code [Dewhurst, 2021] on a 16×16×16 *k*-point mesh for 32 bands is shown in Fig. 3.1.7. With increasing pressure, the band gap reduces in the inset plot and closes in the vicinity of 2900 GPa, where the simple cubic structure is the thermodynamically stable phase [Martinez-Canales et al., 2012]. The LDA and GW bandgaps reported by Z. Li and Zhu *et al.* [Li et al., 2015, Zhu et al., 2011] are large compared to our GGA (GW) values 0.9 (1.94) eV, which are comparable to early calculations by Johnston *et al.* [Johnston and Hoffmann, 1989].

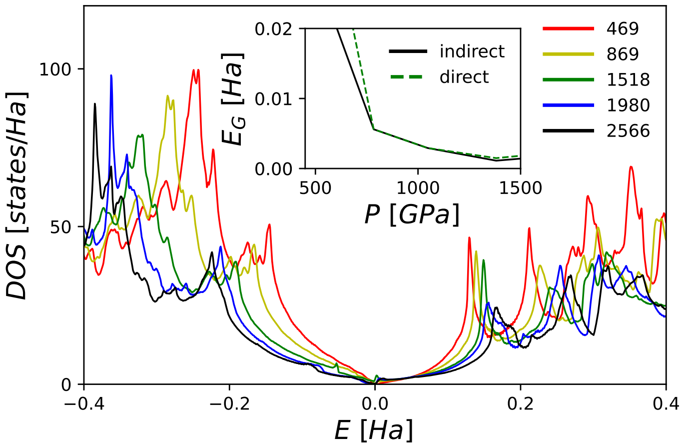

Figure 3.1.7: Density of states for BC8 as function of pressure. The inset plot shows the indirect and the direct band gaps calculated using the PBE XC functional. The pressures indicated are in GPa and the valence band maximum is adjusted to zero. **K Ramakrishna and J Vorberger** 2020 J. Phys.: Condens. Matter **32** 095401.

Using GGA XC, Correa *et al.* [Correa et al., 2006] obtained a bandgap of approximately 0.40 eV near the phase transition boundary from diamond at T=0 which may be compared to the 0.15 eV obtained here.

To summarize the section, the cold curves (energy vs volume) and the equation of state (EOS) for the carbon phases discussed in this section obtained using the Vinet equation of state [Vinet et al., 1987, Vinet et al., 1989] are shown in Figs. 3.1.8 and 3.1.9 respectively. The calculated equilibrium parameters are listed in Table 3.1.1 along with the available experimental results. The band gaps at equilibrium volume using GW^0 and various XC functionals are summarized in Table 3.1.2.

Table 3.1.1: Equilibrium lattice parameters, equilibrium volume per atom, bulk modulus, pressure derivative and static dielectric constants for various phases of carbon. The double row values shown for hexagonal diamond are for the lattice parameters, a=b and c. The static dielectric constant is computed using BSE. The values shown in parentheses are experimental data. [a] [Madelung, 2012]; [b] [Bundy and Kasper, 1967]; [c] [Van Vechten, 1969]; [d] [De and Pryor, 2014]. **K Ramakrishna and J Vorberger** 2020 J. Phys.: Condens. Matter **32** 095401.

phase	a_0 (Å)	V_0 (Å^3)	B_0 (GPa)	$B_0^{'}$	$\varepsilon_1(0)$
BC8	4.437	5.46	433.1	3.97	8.04
FCC	3.569 (3.567)^a	5.68	430.8	3.82	5.76 (5.9)^c
Hex.	2.524 (2.52)^b	5.69	430.9	3.87	6.25 (6.31)^b
	4.128 (4.12)^b				5.40 (5.79)^d

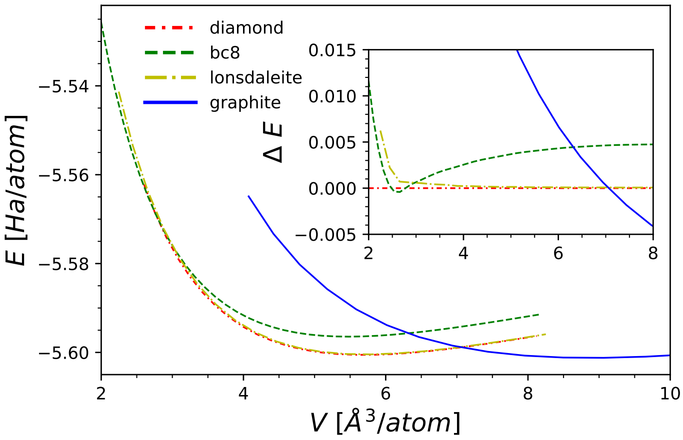

Figure 3.1.8: Cold curves for various phases of carbon. The inset panel shows the relative energies with respect to diamond vs volume, $\Delta E = E - E_d$. The diamond to BC8 crossover is observed around 2.8 Å^3/atom corresponding to pressure around 1000 GPa. **K Ramakrishna and J Vorberger** 2020 J. Phys.: Condens. Matter **32** 095401.

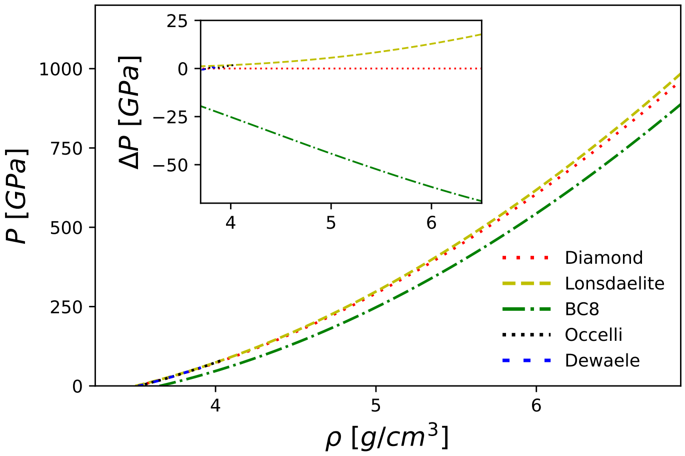

Figure 3.1.9: Equation of state for various carbon phases in comparison with experiments at room temperature (diamond only). Experimental data by Occelli [Occelli et al., 2003] and Dewaele [Dewaele et al., 2008] up to 4.0 g/cm^3. The inset panel shows the relative difference in pressures with respect to diamond vs density, $\Delta P = P - P_d$. **K Ramakrishna and J Vorberger** 2020 J. Phys.: Condens. Matter **32** 095401.

Table 3.1.2: Band gap (indirect) results in eV. GW^0 with HSE for the FCC phase and PBE for the other phases is used. [a] [Peter and Cardona, 2010]. **K Ramakrishna and J Vorberger** 2020 J. Phys.: Condens. Matter **32** 095401.

phase	GW	HSE06	PBE0	B3LYP	SCAN	PBE	Exp.
BC8	1.94	1.89	2.64	2.24	1.11	0.90	-
FCC	5.47	5.31	6.04	5.61	4.56	4.19	5.48[a]
Hex.	4.65	4.66	5.40	4.93	3.86	3.48	-

3.2 Linear Response under Ambient and High-Pressure Conditions

In this section, linear response calculations are perfomed on the KS orbitals obtained using DFT with a full-potential linearized augmented-plane wave (FLAPW) code implemented in *elk* [Dewhurst, 2021]. The KS eigenvalues and orbitals are later used for the RPA[1], TDDFT and BSE calculations discussed in sections 2.4 and 2.6. The Kubo-Greenwood formula (KG), Eq. (2.3.41) is used in the inbuilt VASP [Kresse and Hafner, 1993, Kresse and Joubert, 1999, Kresse and Furthmüller, 1996b, Kresse and Furthmüller, 1996a] subroutines to obtain the dielectric function.

The RPA is the first improvement to the Hartree–Fock approximation, representing a change in electron's self-energy due to dynamical screening [Pines and Bohm, 1952, Bohm and Pines, 1953, Stefanucci and Van Leeuwen, 2013]. It uses electronic states from DFT, but lacks the XC kernel as used in TDDFT due to setting $f_{\mathrm{XC}} \rightarrow 0$. The XC kernel used for the TDDFT calculations is the *bootstrap*, long range XC kernel implemented in the *elk* code [Dewhurst, 2021, Sharma et al., 2011]. The BSE solution provides a systematic description of electron–hole pair correlations including the quasiparticle "excitons" within the gap. This includes a two-step process where the quasiparticle electron states and wavefunctions calculated under the GW approximation are used to solve the BSE using a four-point polarization propagator in a Dyson-like equation [Martin et al., 2016]. The electron-hole pair interaction term is approximated by a Coulomb kernel along with a screened interaction term. The scaling is given by $\mathcal{O}(n^5)$, it is therefore the most computationally demanding method of all used here. Diagonalization scaling is given by $(N_c \times N_v \times N_k)^3$ where N_c, N_v and N_k denotes the number of conduction bands, valence bands, and k-points respectively. The BSE calculations in the optical limit are performed using the method of diagonalization in the *elk* code [Dewhurst, 2021]. The *exciting* code [Gulans et al., 2014, Sagmeister and Ambrosch-Draxl, 2009] is used for the finite-wavenumber BSE calculations.

---

[1] Not to be confused with the Lindhard dielectric function/RPA based on plasma theory introduced in section 2.1.1. RPA calculation in TDDFT formalism here simply means the lack of an XC kernel.

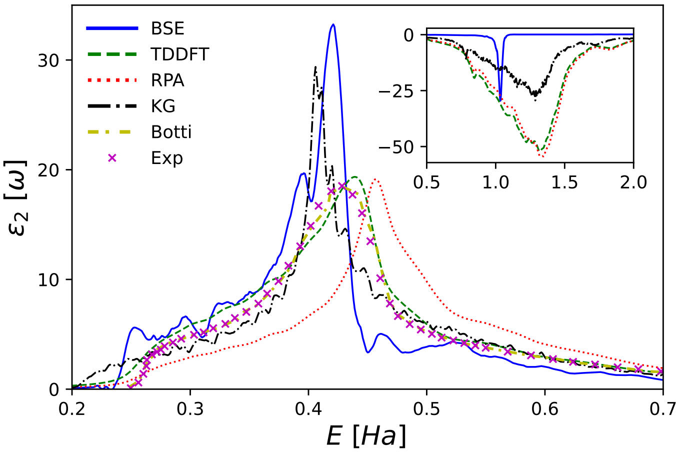

Figure 3.2.1: Imaginary part of the dielectric function of diamond in the optical limit at ambient conditions (ρ=3.509 g/cm^3) using various approaches. The inset plot shows the imaginary part of the inverse of the dielectric function including the plasmon peaks. In the inset, the curves obtained using TDDFT/RPA and KG are scaled, for the purpose of visualization. Botti Ref. [Botti et al., 2004]; Experimental data stems from Ref. [Palik, 1998]. **K Ramakrishna and J Vorberger** 2020 J. Phys.: Condens. Matter **32** 095401.

3.2.1 Diamond

The dielectric response function for diamond under ambient conditions evaluated using various approaches is shown in Fig. 3.2.1. As the band gap is large, excitonic effects are important and the BSE approach is required for an accurate calculation of absorption spectra. The BSE calculations are perfomed using a 12×12×12 k-point mesh with 8 empty states. The optical band gap can be deduced from the first peak of the imaginary part of the dielectric function (absorption curve). In some cases there can be a dark state with small oscillator intensities. In general, it is apparent that the onset of absorption happens softer and earlier for KG, RPA, and the TDDFT result than for the BSE or for the experimental result. The maximum in absorption ranges from 0.407 Ha for the KG model to 0.465 Ha in RPA. The experimental maximum is located at 0.427 Ha and is best reproduced by TDDFT closely followed by BSE. The oscillator intensity of BSE is quite large compared to the experimental result although the location of the absorption maxima is close to the experimental result. Such findings in the overestimation of the oscillator intensity are also reported in other calculations [Sakurai et al., 2017, Sharma et al., 2011, Benedict et al., 1998]. The narrow peak width in the BSE result indicates a more stable plasmon. Overall, the best match to the experimental result seems to be from the TDDFT method with the bootstrap kernel. The RPA deviation is understandable due to the lack of f_{XC} and therefore cannot capture bound excitons. When including the electron-hole pair interaction in the XC kernel, oscillator intensity shifts to lower energies. This effect is prominent for insulators and less for narrow-gap semiconductors [Benedict et al., 1998].

The response function is an important aspect for interpreting the high-pressure phase behavior, accessible via electron energy loss spectroscopy (EELS), x-ray Thomson scattering (XRTS),

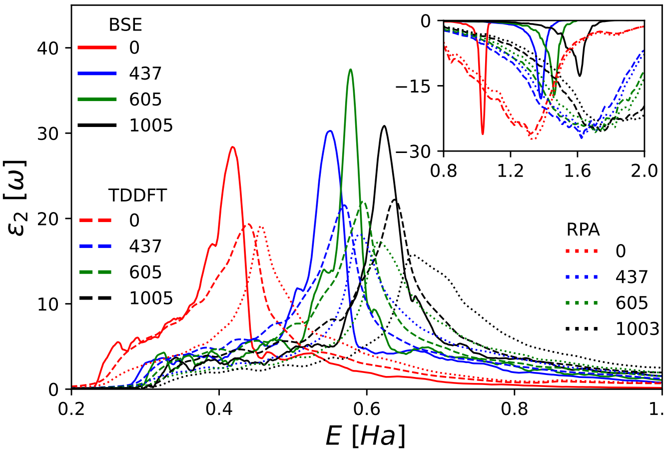

Figure 3.2.2: Imaginary part of the dielectric function of diamond in the optical limit for various pressures using BSE, TDDFT and RPA. The inset plot shows the imaginary part of the inverse of the dielectric function including the plasmon peaks. In the inset, the curves obtained using TDDFT and RPA are scaled for the purpose of visualization. All the pressures indicated are in GPa. The densities for these pressures are 3.51, 5.50, 6.00 and 7.00 g/cm^3 respectively. **K Ramakrishna and J Vorberger** 2020 J. Phys.: Condens. Matter **32** 095401.

x-ray Raman scattering (XRS) and other methods, also see sections 3.4 and 3.5. The absorption curve under high-pressure calculated using BSE, TDDFT and RPA are shown in Fig. 3.2.2. The maximum of the imaginary part of the dielectric function shifts to higher energies even faster than the edge, indicating a substantial shift in the absorption. At higher pressures, the broadening of the peaks is observed and the plasmons turn less stable. This can be explained using the Penn gap model in which the excitation energy of a collective excitation is a quadratic sum of the band gap energy and square of the plasma frequency calculated from the valence electron density. An interesting observation is a similar behaviour of different theories for higher pressures as for the zero pressure case of Fig. 3.2.1. The absorption peak at the highest energies is seen in the RPA results whereas BSE shows the highest absorption strength. The TDDFT spectra is similar to BSE albeit with lower oscillator strengths near the right exciton energies.

The imaginary part of the inverse dielectric function is also of paramount importance as it can be used to compute further quantities like the dynamic structure factor or the stopping power that are directly experimentally accessible. The predictions of different models for different densities in the optical limit are shown in the inset plots of Figures 3.2.1 & 3.2.2. The plasmon peak is given by the zero of the real part of the dielectric function that lies in the energy range of weak damping, describing the collective excitation of valence electrons across the band gap. There are more variations in the location, height and width of the plasmon peak compared to the imaginary part of the dielectric function due to nonlinear effects introduced by the Kramers-Kronig relation between the real and imaginary parts of the dielectric function. Hence, the imaginary part of the inverse dielectric function adds necessary information in addition to the imaginary part of the dielectric function. The plasmon peaks are located at the lowest energies in the BSE approximation whereas RPA and TDDFT predict similar plasmon

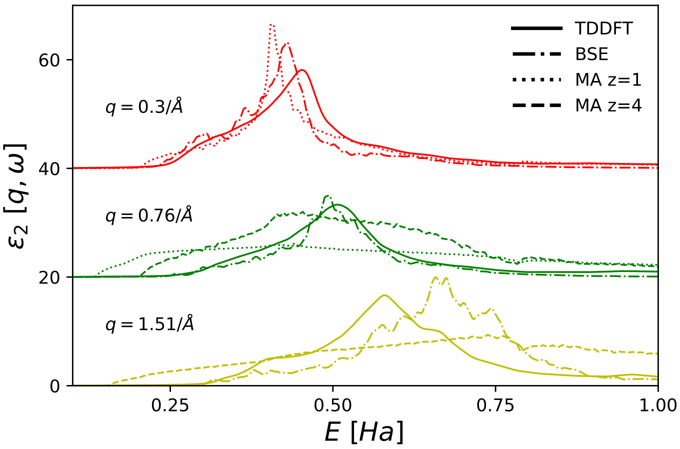

Figure 3.2.3: Imaginary part of the dielectric response function for diamond is calculated using TDDFT, BSE and MA at finite $\vec{q}$ for ρ=3.509 g/cm^3. The charge state $Z_i = 1$ is considered for $q = 0.3$/Å and 0.76/Å and $Z_i = 4$ is considered for $q = 0.76$/Å and 1.51/Å. **K Ramakrishna and J Vorberger** 2020 J. Phys.: Condens. Matter **32** 095401.

locations at higher energies. The plasmon width is smallest for the BSE and a lot greater for RPA/TDDFT. This is an indication of the BSE prediction for a stable quasiparticle. In the inset of Fig. 3.2.2, the plasmon peaks shift to higher energies as well as broaden with increase of pressure.

It is important to consider both the absorption and the energy-loss spectra (imaginary part of the inverse dielectric function). For energy-loss spectra, it is a good approximation to use the inverse of the dielectric function (ε^{-1}) with χ constructed from DFT rather than the updated ε^{-1} with GW eigenvalues. This seems contrary, especially when GW leads to improvement in the quasiparticle energies for large band gap systems. Starting with a GW calculation iterating Hedin's equations [Eqns. (2.5.11) - (2.5.15)] leads to P in the first iteration containing a vertex correction. Substituting P further in the self-energy term leads to an appearance of a second vertex and eventually the cancellation of the vertex in P and in the self-energy has been shown. Neglecting the vertex in both the W and in the self-energy in principle is a better approach [Onida et al., 2002].

It is of much interest to calculate the dielectric function at finite wavenumbers which is relevant for experiments as shown in Fig. 3.2.3. The q-points are complementary to the k-points using the relation $n_{k_i} \times q_i = N$ where n_{k_i} is the number of k-points along $\vec{x}$, q_i is the number of q-points along $\vec{x}$, N is an integer which is also a factor of n_{k_i} explained by the Monkhorst-Pack k-sampling [Monkhorst and Pack, 1976]. The TDDFT calculations are performed using an uniform 20×20×20 k-point mesh with 8 empty bands using the bootstrap kernel in the *elk* code [Dewhurst, 2021]. The BSE results stem from the *exciting* code [Gulans et al., 2014] using an uniform 12×12×12 k-point mesh with 16 empty bands.

A reduction of the peak height and a shift of the peak to higher energies in the imaginary part of the dielectric function is seen with an increase in momentum. The reduction in peak height as predicted by BSE is much more drastic in the considered q-range as the change in the TDDFT

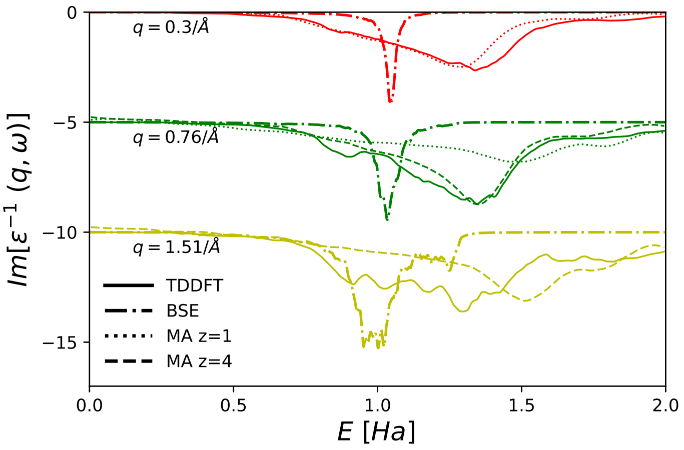

Figure 3.2.4: Imaginary part of the inverse of the dielectric function for diamond at ambient density ρ=3.509 g/cm^3 using TDDFT, BSE and MA at finite $\vec{q}$. The charge state $Z_i = 1$ is considered for $q = 0.3/Å$ and 0.76/Å and $Z_i = 4$ is considered for $q = 0.76/Å$ and 1.51/Å. **K Ramakrishna and J Vorberger** 2020 J. Phys.: Condens. Matter **32** 095401.

result. Further, the BSE peaks change their location more than the TDDFT peaks.

A wavenumber dependency of the dielectric function can also be obtained if a dynamic collision frequency is calculated from optical data (using Kubo-Greewood results) and then used in a Mermin dielectric function (MA) [Plagemann et al., 2012, Witte et al., 2017a]. Such a procedure leads to results different from both BSE and TDDFT, partly due to the different shape of KG in the optical limit and partly due to a different damping behaviour of the Mermin dielectric function with an increase in wavenumber as shown in Fig. 3.2.3. In the Mermin approach, an additional difficulty arises in having to choose a charge state Z_i i.e. the charge state of the ion, a choice that will have significant impact on the final result as the two curves for $q = 0.76$ Å^{-1} show. The extraction of an average charge state of an ion in the warm dense matter or high-pressure solid range is not trivial and most models for ionization states work for hot, low density plasmas. The most promising method seems to be the use of conductivity sum rule

$$\int_{-\infty}^{+\infty} \frac{d\omega}{\pi} \omega \Im[\varepsilon(q,\omega)] = \omega_{pl}^2, \tag{3.2.1}$$

where ω_{pl} is the plasma frequency and a split of the conductivity into Drude like free part and core part [Witte et al., 2017a, Bethkenhagen et al., 2020].

The dispersion of the plasmon subject to a change in wavenumber is shown in Fig. 3.2.4 with the imaginary part of the inverse of the response function calculated using various approaches at finite q. At small q, the behavior is similar to the optical limit. The excitation energy predicted by the BSE is too small. The KG+Mermin approach and TDDFT predict nearly the same peak location but slightly different peak widths. The free parameter of the ion charge state entering the KG+Mermin formulation is not known a priori [Fortmann et al., 2010]. At the highest $q = 1.51$ Å^{-1} considered here, the TDDFT and KG+Mermin results differ strongly in peak position and width indicating very different dispersion relations.

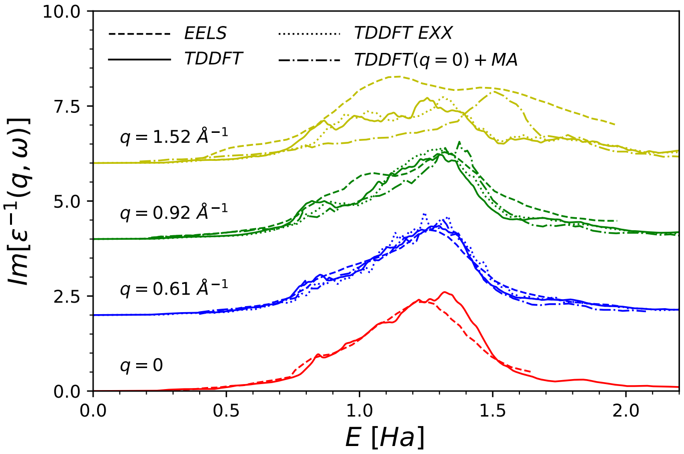

Figure 3.2.5: Imaginary part of the inverse dielectric function at various q for diamond at ambient conditions. Experimental data stems from Ref. [Daniels et al., 1970, Waidmann et al., 2000, Raether, 2006]. **K Ramakrishna and J Vorberger** 2020 J. Phys.: Condens. Matter **32** 095401.

The general functional form of the imaginary part of the inverse dielectric function as function of energy and wavenumber is also of interest as shown in Fig. 3.2.5. The experimental results are compared to the theoretical models using TDDFT with and without exact exchange (EXX) and the KG extension to finite q based on the Mermin dielectric function . For small q, the agreement is quite good. However, at large q, the peaks and distribution of weight deviate between experiment and theory thus giving a more complete picture of the challenges for theory.

3.2.2 Lonsdaleite

The dielectric function calculations based on TDDFT are performed using the bootstrap kernel within the *elk* code [Dewhurst, 2021] on a 12×12×12 k-point mesh and 24 empty states. The BSE calculations are done on a lower 8×8×8 k-point mesh and 16 empty states. As of now, no known experimental band gaps are reported for lonsdaleite. Due to large band gap, the screened Coulomb interaction is strong and the excitonic effects are still prominent at lower pressures. As the pressure is increased, contrary to the case of diamond, the band gap decreases until it finally closes in the vicinity of 1000 GPa.

The imaginary part of the response function using various methods along two orientations for the hexagonal lattice structure at $\vec{q} = 0$ is shown in panels a) and b) of Fig. 3.2.6. The TDDFT results at finite-q are shown in panels c) and d). The optical limit spectrum is well represented by BSE and TDDFT, while TDDFT doesn't quite resolve the prominent peaks in the BSE spectra along the two orientations. The maximum of the TDDFT spectra is located around the average of the twin peaks of the BSE result for the perpendicular case and closer to the first peak in the parallel case. Similar to the case of diamond, RPA predicts a blue shift in the maximum of the imaginary part of the dielectric function compared to BSE or TDDFT for the case parallel to z. Meanwhile, the KG calculation shows a red shift compared to BSE and TDDFT. In the case

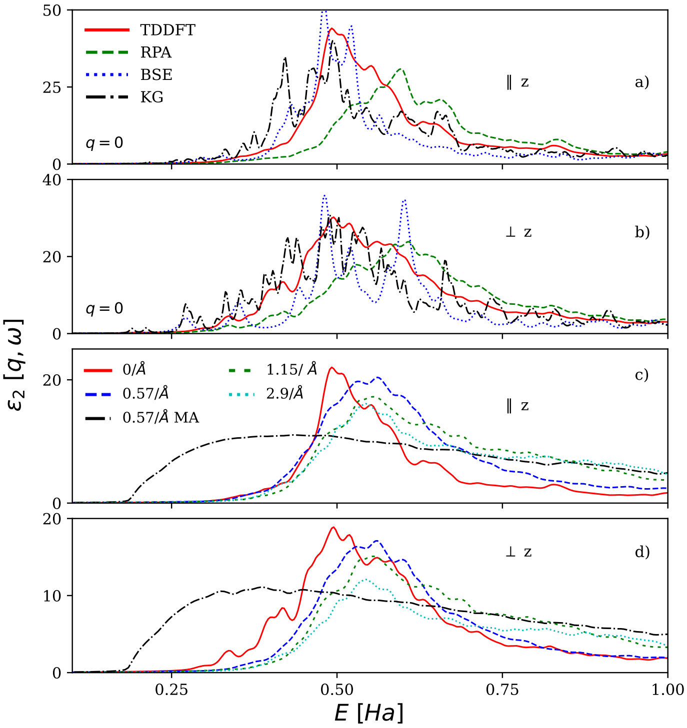

Figure 3.2.6: Imaginary part of the dielectric response function in panels a) and b) for lonsdaleite at 242 GPa using various approaches at $\vec{q}$=0. Comparison of TDDFT to KG+Mermin (MA) at finite $\vec{q}$ in panels c) and d). **K Ramakrishna and J Vorberger** 2020 J. Phys.: Condens. Matter **32** 095401.

perpendicular to the *z* axis, all differences are mitigated.

The finite-*q* results from TDDFT together with results from the Mermin response function using a collision frequency obtained using DFT is shown in panels c) and d) of Fig. 3.2.6. An ionization degree Z_i=1 as the fitting parameter is chosen for $|\vec{q}| = 0.57$ Å^{-1} to fit the Mermin ansatz (MA). The Mermin+DFT spectrum is almost uniform along both the directions in stark contrast to the TDDFT curves at $\vec{q} \neq 0$, as shown in Fig. 3.2.6. The differences between the two orientations parallel and orthogonal to *z*, respectively, observable in the optical limit (panels a) and b) in Fig. 3.2.6), vanish for the finite-*q* values as shown in panels c) and d).

The imaginary part of the inverse dielectric function for lonsdaleite at a pressure P=242 GPa is presented in Fig. 3.2.7. TDDFT and Mermin+DFT exhibit a difference in plasmon peak locations around 0.3–0.4 Ha, which is larger than in the FCC diamond case. Mermin+DFT also exhibit different structures near the peak parallel and perpendicular to *z* compared to TDDFT in Fig. 3.2.7.

To distinguish the phases in an inelastic x-ray scattering experiment would be advantageous. It is possible to distinguish lonsdaleite from diamond at high-pressure conditions either in the absorption spectrum or in the inelastic scattering spectrum by the characteristic positions of the respective absorption and plasmon peaks. Figure 3.2.8 shows the difference in absorption spectra and plasmon peaks in the optical limit and at finite-*q*. The differences in the *q* vector chosen for lonsdaleite and diamond are due to the differences arising from lattice structures and the *k*-point sampling considered.

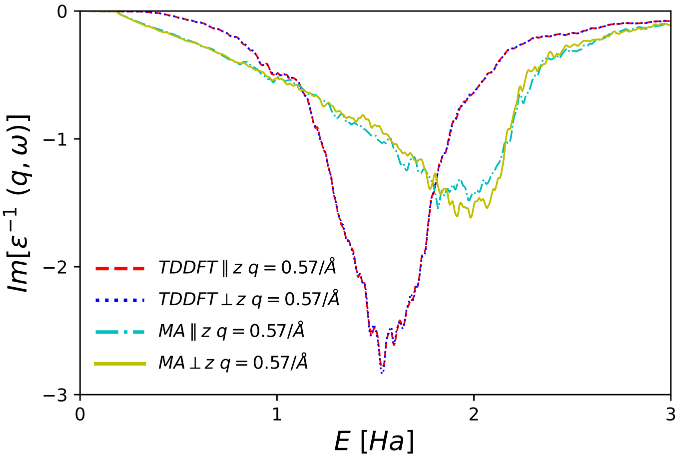

Figure 3.2.7: Imaginary part of the inverse of the dielectric function for lonsdaleite at 242 GPa using MA and TDDFT at $|\vec{q}| = 0.57Å^{-1}$. **K Ramakrishna and J Vorberger** 2020 J. Phys.: Condens. Matter **32** 095401.

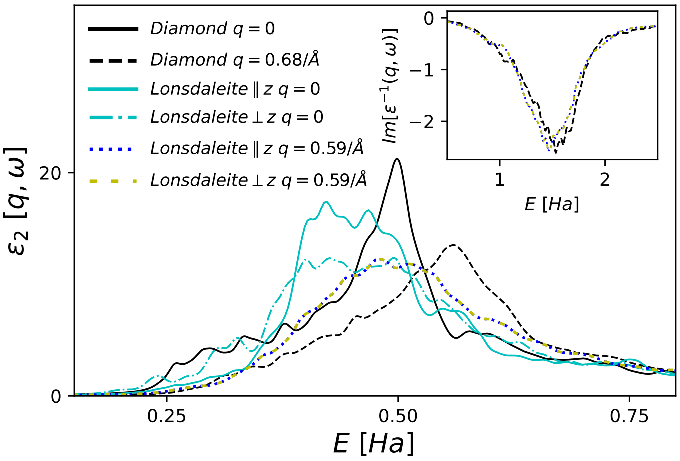

Figure 3.2.8: Comparison of the imaginary part of the TDDFT dielectric function for diamond and lonsdaleite at 292 GPa in the optical limit and at finite q. The inset panel shows the imaginary part of the inverse of the dielectric function at $|\vec{q}| = 0.68$ Å^{-1} for diamond and $|\vec{q}| = 0.59$ Å^{-1} for lonsdaleite (black–diamond, blue/yellow–lonsdaleite). **K Ramakrishna and J Vorberger** 2020 J. Phys.: Condens. Matter **32** 095401.

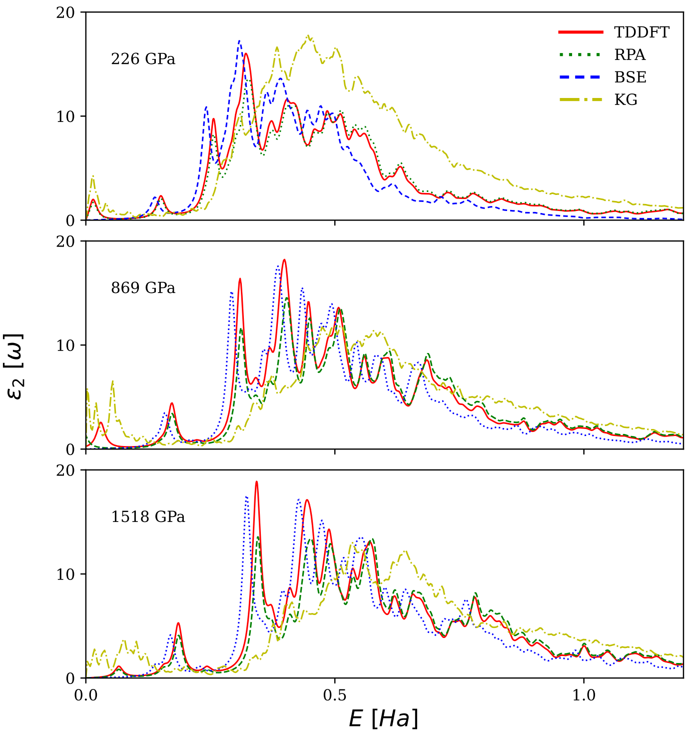

Figure 3.2.9: Imaginary part of the dielectric function of BC8 in the optical limit for various pressures using BSE, TDDFT, RPA and the Kubo-Greenwood formula. **K Ramakrishna and J Vorberger** 2020 J. Phys.: Condens. Matter **32** 095401.

3.2.3 BC8

The TDDFT spectra is obtained using the bootstrap kernel [Sharma et al., 2011] within the *elk* code [Dewhurst, 2021] for a 4×4×4 *k*-point mesh and 28 empty states. For the BSE calculations, the number of empty states is reduced up to 18 to reduce the computational cost. Due to the close proximity of the band edges for small pressures, a smaller *k*-point mesh is sufficient for convergence, see Fig. 3.2.9. The spectra in the optical limit obtained using RPA, TDDFT and BSE exhibit close resemblance albeit with different peak locations for the different pressures in Fig. 3.2.9. The KG results have an absorption peak near $\omega = 0$ due to the nature of the semi-metallicity prediction from DFT which is clearly absent from BSE spectra even at higher pressures. A shift of the main absorption peak to higher energies is seen in the KG results compared to the other methods considered. The agreement between the various methods with the exception of KG is quite remarkable, especially in hindsight after having analyzed the diamond and lonsdaleite phases.

The imaginary part of the inverse dielectric function obtained using various approaches is shown in Fig. 3.2.10. The spectra obtained using RPA and TDDFT do not show the twin peaks of the BSE and predict a very broad feature instead. A broad peak at a different location is seen in the KG results. A shift to higher energies for higher pressures is observed in the plasmon peaks obtained using TDDFT and BSE, whereas the KG result shows the opposite behaviour for the case of the highest pressure. Similar to the case of diamond, the BSE curve predicts the most stable plasmon excitation with a rather narrow peak and large intensity.

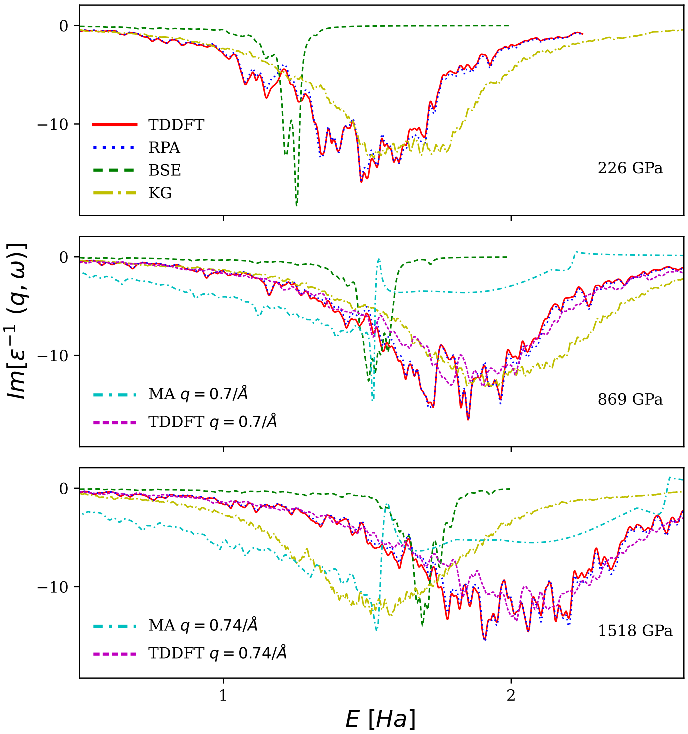

Figure 3.2.10: Imaginary part of the inverse of the dielectric function of BC8 at various pressures using BSE, TDDFT, RPA and the Kubo-Greenwood formula. The TDDFT, RPA, and KG curves are scaled fivefold and the finite-q MA curve is scaled tenfold. All curves in the optical limit except the specially marked MA and TDDFT curves. **K Ramakrishna and J Vorberger** 2020 J. Phys.: Condens. Matter **32** 095401.

For finite-q, a comparison between the MA approach and TDDFT at pressures of 869 GPa and 1518 GPa is also shown in Fig. 3.2.10. The collision frequency used in MA is taken from the optical limit of TDDFT. Due to the small magnitude of $\vec{q}$, the TDDFT results in the optical limit are very similar to the finite-q vector considered. However, the MA approach shows drastically different behavior with the peak location at smaller energy and the magnitude reduced.

3.3 Linear Response under Warm Dense Matter Conditions

A similar analysis can be performed for a warm dense state of carbon (P=150 GPa, T=6000 K) as presented in Fig. 3.3.1. In particular, TDDFT can also be used on DFT-MD snapshots in the WDM regime. The system size should be as large as possible. This is more important in particular for the TDDFT & RPA results that seem more dependent on the system size. A down shift of the plasmon energy with increase in temperature analogue to the closing of the band gap due to temperature effects is observed. Note that at conditions of P=150 GPa and T=6000 K, the influence of finite-temperature XC functional (GDSMFB) and adiabatic approximation (ALDA) built on finite-temperature local density approximation are negligible for carbon and carbon-hydrogen mixtures considered.

The TDDFT calculations for N=64 are performed using the *bootstrap* ker-

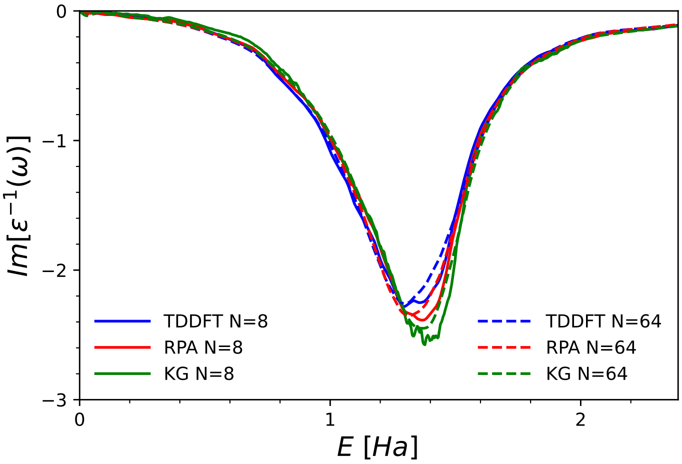

Figure 3.3.1: Imaginary part of the inverse dielectric function for diamond at WDM conditions (P=150 GPa, T=6000 K) in the optical limit. **K Ramakrishna and J Vorberger** 2020 J. Phys.: Condens. Matter **32** 095401.

nel [Sharma et al., 2011] in the *elk* code [Dewhurst, 2021] with a 3×3×3 *k*-point mesh applying PBE for the XC potential. For the system size N=8, a denser 6×6×6 *k*-point mesh is employed. Contrary to the KG result, the TDDFT result depends strongly on the system size. The RPA calculations are also performed using the *elk* code [Dewhurst, 2021] on a similar *k*-point mesh size. The KG results stem from calculations using VASP [Kresse and Hafner, 1993, Kresse and Joubert, 1999, Kresse and Furthmüller, 1996b, Kresse and Furthmüller, 1996a]. N=64 particles is the maximum size choosen due to the computational cost of all-electron calculations.

The influence of the XC kernel in TDDFT is shown in Fig. 3.3.2. The long-range contribution (LRC) kernel [Botti et al., 2005] is computed using Quantum ESPRESSO [Giannozzi et al., 2009, Giannozzi et al., 2017] and yambo [Marini et al., 2009] using an uniform 4×4×4 *k*-point mesh with 144 bands and an energy cutoff of 40 Ha with a PBE pseudopotential. Marzari-Vanderbuilt (MV) smearing [Marzari et al., 1999] of 0.019 Ha is used for the electronic temperature due to the presence of the band gap from the DFT calculations. The LRC kernel uses free parameters (α, β) in the dynamical XC kernel [Botti et al., 2005]

$$f_{\mathrm{XC}}^{LRC}(q,\omega) = -\frac{1}{q^2}(\alpha + \beta\omega^2), \tag{3.3.1}$$

where α and β are fitted to reproduce the experimental spectra for diamond under ambient conditions. For calculations under WDM conditions, fitting the values for α and β is not trivial, also due to lack of experimental spectra. Using a a self-consistency procedure [Sharma et al., 2011] employed in bootstrap kernel, the free parameters can be avoided and the XC kernel is still valid for conditions beyond the ideal solid regime. In metals, the adiabatic LDA (ALDA) kernel describes very well the plasmon dispersion but for insulators and semiconductors fails to capture the excitonic effects, see section 2.4. The ALDA kernel for TDDFT is computed using *elk* [Dewhurst, 2021] with an uniform 2×2×2 *k*-point mesh for N=64 and a denser 8×8×8 *k*-point mesh for N=8. For N=8, the ALDA and the bootstrap kernels converge

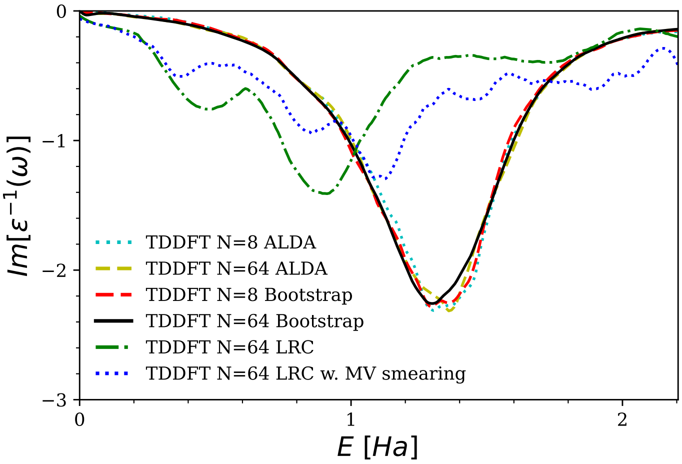

Figure 3.3.2: Change in the imaginary part of the inverse dielectric function of diamond at $P = 150$ GPa and $T = 6000$ K with system size and different XC kernels in TDDFT. **K Ramakrishna and J Vorberger** 2020 J. Phys.: Condens. Matter **32** 095401.

quite well, whereas at N=64, the ALDA has the peak blue shifted compared to the bootstrap kernel. For these conditions, the excitonic effects diminish and the ALDA kernel agrees with the bootstrap kernel as expected. The slight shift in the energies near the peak is attributed to the screening effects considered in the bootstrap kernel.

The demixing of a carbon-hydrogen (C-H) mixture is important for the understanding of planetary behavior and the inelastic response functions evaluated from *ab-initio* methods are important for modeling and analyzing XRTS experiments, see section 3.4. Fig. 3.3.3(a) shows the imaginary part of the inverse dielectric function at q= 1.13 Å^{-1} for a C-H mixture under WDM conditions (P=150 GPa, T=6000 K). The response functions are evaluated using the ALDA kernel for TDDFT in yambo [Marini et al., 2009] using the KS orbitals evaluated using Quantum ESPRESSO [Giannozzi et al., 2009, Giannozzi et al., 2017]. For the CH curve in Fig. 3.3.3(a), the simulations are perfomed for 64 carbon and 64 hydrogen atoms in a supercell using a 2×2×2 k-point mesh and 192 bands obtained from DFT-MD snapshots. The response function for carbon (C) is evaluated using the bootstrap kernel as previously discussed for a system size N=64. The response function for hydrogen (H) is evaluated for N=256 using 384 bands on a 2×2×2 k-point mesh. The plasmon peak of the CH is located in between the peaks of carbon and hydrogen with the carbon component dominating the linear response. Furthermore, stoichiometric components of the mixture can be evaluated by weighting the linear response of the constituent parts and thus possible demixing is visible in the inelastic scattering signal. Fig. 3.3.3(b) shows the imaginary part of the inverse dielectric function at q= 1.13 Å^{-1} for a C_x-H_y mixture. The location of the plasmon peaks are dominated by the constituent weight of the carbon or the hydrogen components in the mixture. The carbon component in the mixture has more contribution to the linear response compared to hydrogen as there are more electrons attached to the carbon atom. This is evident in the linear response, see the overlap of the curves for the C_3H and C_9H mixtures to pure carbon. The dynamic structure factor for a warm dense C-H mixture at q= 0.94 Å^{-1} is shown in Fig. 3.3.4. When convoluted with the ex-

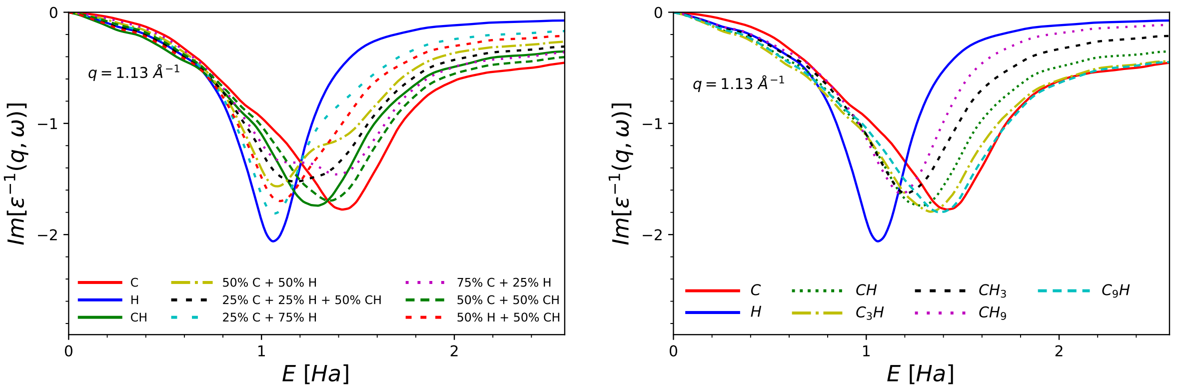

(a)

(b)

Figure 3.3.3: Imaginary part of the inverse dielectric function at warm dense matter conditions (P=150 GPa, T=6000 K) at q= 1.13 Å^{-1} for a) C-H mixture with stoichiometric components, b) C_x-H_y mixture.

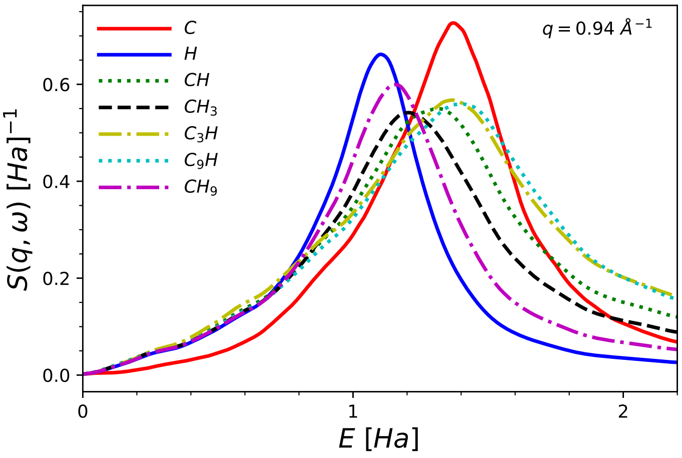

Figure 3.3.4: Dynamic structure factor at warm dense matter conditions (P=150 GPa, T=6000 K) at q= 0.94 Å^{-1} for a C_x-H_y mixture.

perimental instrument function, it is possible to distinguish between the specta of fully mixed C-H and the isolated spectra of carbon and hydrogen. The experimental resolution available in current XRTS diagnostics could pave way to study the demixing and possibly characterize the formation of metallic hydrogen [Ranjan et al., 2023]. The method in turn could also be applied for studying other mixtures like hydrogen-helium relevant for understanding the planetary interiors of jupiter and saturn.

The change in plasmon energy for a C-H mixture with wavenumber is shown in Fig. 3.3.5. The calculations at WDM conditions are perfomed using TDDFT with an ALDA kernel. The ambient carbon results computed are using the bootstrap kernel. The experimental results shown for ambient diamond are from XRTS measurements by Gamboa *et al.* [Gamboa et al., 2016]. A weak quadratic dispersion for the ambient diamond can be seen from the TDDFT and experimental results. Calculations for carbon at WDM conditions with N=8 and N=64 demonstate the finite size effects with the larger supercell resulting in a reduction of the plasmon energy

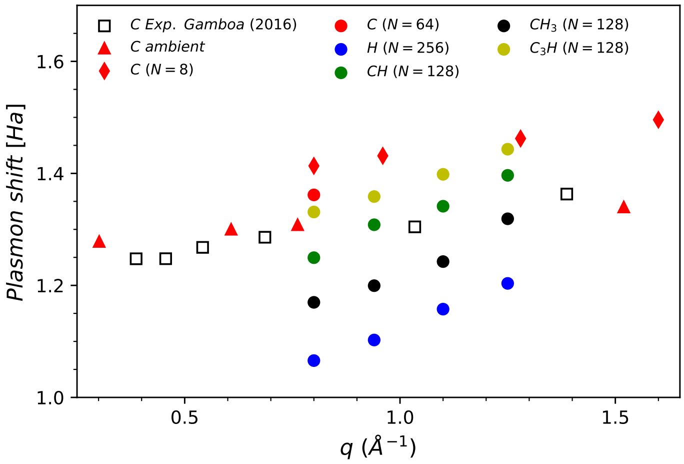

Figure 3.3.5: Plasmon position in carbon (C), hydrogen (H) and carbon-hydrogen mixtures (CH, CH_3, C_3H) as function of the wavenumber evaluated using TDDFT. The system sizes are indicated in the brackets. Experimental data obtained via XRTS is taken from Gamboa *et al.* [Gamboa et al., 2016].

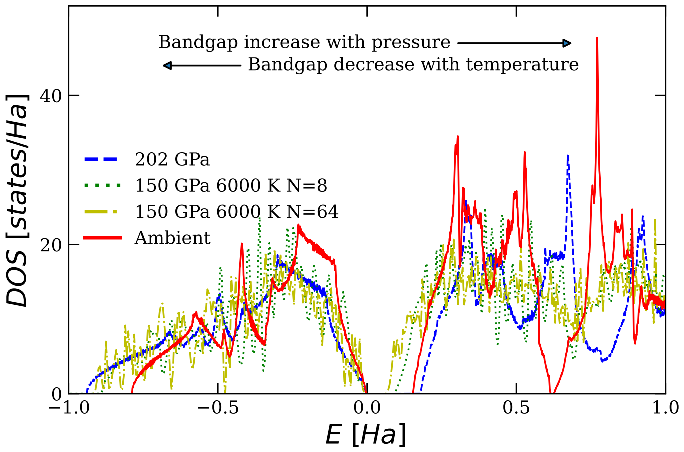

Figure 3.3.6: Density of states for diamond under ambient, compressed and WDM conditions. The valence band maximum is adjusted to zero.

by $\sim$0.05 Ha. The results for C-H mixtures are only shown in the range 0.8 Å^{-1} to 1.25 Å^{-1} relevant for the experimental conditions of the XRTS setup. At $q = 0.8$ Å^{-1}, the difference in plasmon energy ($\sim$0.3 Ha) between carbon and hydrogen species shows the importance of the wavenumber for the XRTS setup to characterize the demixing.

In Fig. 3.3.6, the density of states (DOS) is computed at ambient, compressed and warm dense matter conditions. The band gap is determined from the difference in the energies between the edges of the conduction and the valence band. With increasing pressure at ambient temperature, the band gap of diamond increases as previously discussed in section 3.2.1. With the change in temperature, the band gap decreases due to thermal effects. At the WDM conditions (P=150 GPa, T=6000 K), the system is below the melting curve, see Fig. 3.0.1, also the DOS for diamond indicates a presence of band gap. The change in band gap with respect to pressure is more elevated than the change with respect to temperature. Correa *et al.* [Correa et al., 2006] report a band gap of 6.8 eV at 1100 GPa at T=0 within the range of the values obtained using advanced XC functionals in Fig. 3.1.3. The band gap reduces to 3.6±0.5 eV at the melting temperature (6750 K). Thus, diamond remains an insulator in the solid phase and the metal-insulator transition occurs only upon melting. The effect of the system size can also be seen on the DOS as discussed for the evaluation of response function using DFT-MD snapshots. With N=64, the band gap is lower as expected for the conditions. Evaluating with a smaller size N=8 leads to a higher band gap and hence the system size is important for effective evaluation of properties under extreme conditions.

3.4 X-ray Thomson Scattering

In section 2.2, the theoretical description of the XRTS for obtaining diagnostics is briefly discussed. In this section, the focus is on direct comparison of the *ab-initio* results to experimental measurements and on supporting the analysis of WDM x-ray scattering experiments using the theoretical methods discussed in chapter 2.

The change in the location of the plasmon in the optical limit with density for diamond is shown in Fig. 3.4.1. The increase in the plasmon energy predicted by all the methods is in agreement with the XRTS measurements. BSE predicts the lowest values, about 30% lower than the TDDFT, RPA, KG, and available experimental results. The KG and TDDFT results nicely agree with the whole range of the experimental measurements [Gamboa et al., 2016]. The differences between KG and TDDFT arise as the pressure reaches 900 GPa (ρ=6.75 g/cm^3), close to the proposed transition to the BC8 phase. The differences in theoretical results at ambient conditions arises from the implemenation of scissor correction in TDDFT which incorporates the correct band gap [Sato et al., 2012, Waidmann et al., 2000, Azzolini et al., 2017].

The change in plasmon energy for diamond with wavenumber is shown in Fig. 3.4.2. The BSE results are ignored, as the plasmon shift with respect to density shown in Fig. 3.4.1 is too small and the same trend is seen with respect to the change in wavenumber. The experimental EELS measurements along different lattice directions stem from Waidman *et al.* [Waidmann et al., 2000]. The EELS measurements are able to resolve the dispersion along different orientations absent in the XRTS measurements. The XRTS measure-

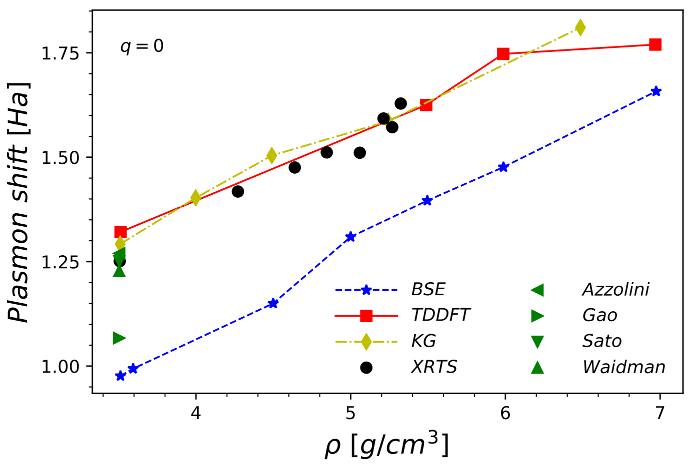

Figure 3.4.1: Plasmon position in diamond in the optical limit as function of the density. Experimental data obtained via XRTS is taken from Gamboa *et al.* [Gamboa et al., 2016], electron-energy loss spectroscopy (EELS) data by Sato *et al.* [Sato et al., 2012] and Waidmann *et al.* [Waidmann et al., 2000], BSE calculations for ambient conditions by Gao [Gao, 2015], TDDFT calculations at ambient conditions by Azzolini *et al.* [Azzolini et al., 2017]. **K Ramakrishna and J Vorberger** 2020 J. Phys.: Condens. Matter **32** 095401.

ments are basically an arithmetic means of the EELS results with a weak quadratic dispersion [Gamboa et al., 2016]. The TDDFT and TDDFT+Mermin results agree in the optical limit and at small wavenumbers. The TDDFT+Mermin results are strongly quadratic and deviates largely from the XRTS measurements with increasing wavenumbers. Good agreement with XRTS measurments over a wide range can be reached using RPA or TDDFT with different classes of approximations–with or without long range kernel (RPA vs TDDFT) and comparing PBE XC versus exact exchange (EXX) [Görling, 1996]. Comparing the RPA and TDDFT curves with PBE XC, the long range kernel lowers the plasmon energies. Azzolini *et al.* [Azzolini et al., 2017] also report a flat plasmon dispersion similar to the TDDFT results. The use of EXX improves the TDDFT results especially at higher wavenumbers. This is attributed to the improvements in screening taken care by EXX and hybrid functionals like HSE [Heyd et al., 2003].

Thus far, the XRTS measurements correspond to diamond at ambient and compressed conditions. Moving on to the WDM regime, *ab-initio* methods have been successfully applied to model the XRTS experiments [Baczewski et al., 2016, Witte et al., 2017a, Witte, 2019, Mo et al., 2018, Frydrych, 2018, Frydrych et al., 2020]. The schematic of the experimental setup is shown in Fig. 3.4.3. Polystyrene $(C_8H_8)_n$ samples are shock compressed with two laser beams and probed by x-rays with a photon energy of 8.18 KeV and a pulse duration of 50 fs. The scattered x-rays are collected by the forward (FXRTS) and backward (BXRTS) spectrometers at $\theta_f = 17°$, $k_f = 1.23/\text{Å}$ and $\theta_b = 124°$, $k_b = 7.3/\text{Å}$ respectively shown in Fig. 3.4.4. Based on hydrodynamic simulations using the HELIOS code [MacFarlane et al., 2006], the thermodynamic conditions of the sample are estimated to be T=5000 ± 500 K, P=150 ± 15 GPa as the second shock reaches the sample. The inelastic scattering spectra recorded by the FXRTS is

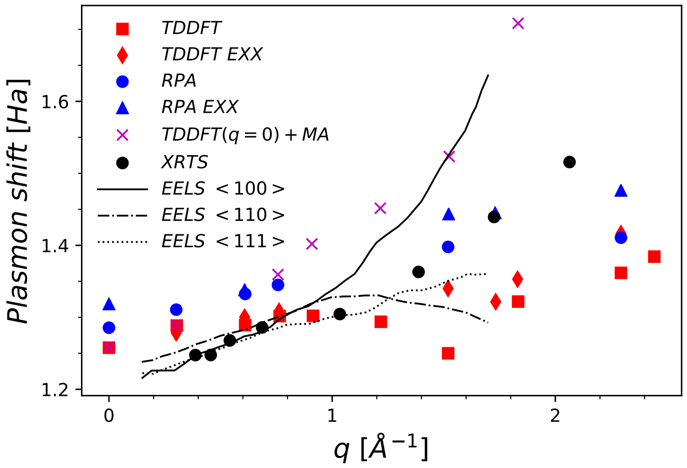

Figure 3.4.2: Plasmon position in diamond at ambient density as function of the wavenumber. Experimental data obtained via XRTS is taken from Gamboa *et al.* [Gamboa et al., 2016], EELS data by Waidmann *et al.* [Waidmann et al., 2000]. **K Ramakrishna and J Vorberger** 2020 J. Phys.: Condens. Matter **32** 095401.

expected to be dominated by the carbon component in the CH mixture.

TDDFT is used to model the inelastic carbon signal corresponding to the thermodynamic conditions (P=150 GPa, ρ=4.1 g/cm^3) at $\vec{q} = 1.23$/Å. The TDDFT calculations are performed in *elk* [Dewhurst, 2021] using the bootstrap kernel with a PBE XC for the potential. The inelastic TDDFT spectra is subtracted from the measured signal to obtain the elastic component of the forward scattering shown in Fig. 3.4.4b.

At the time of measurement, the samples contain a mixture of polystyrene in various states as well as diamond. The proportion of elastic and inelastic scattering in the measured spectra in forward direction is determined by a fit (see Fig. 3.4.5). The TDDFT spectra for diamond is also compared with the polystyrene spectra obtained using KG + Mermin Ansatz (MA) from DFT-MD snpshots. For the inelastic spectra, the diamond signal calculated with TDDFT is used, but with the intensity scaled. The elastic scattered component is modeled using a Gaussian curve. Subsequently the inelastic signal scaled by the fit is subtracted from the measured signal, so that only the elastic scatter signal remains [Frydrych, 2018].

The results are also in good agreement with the recorded x-ray diffraction (XRD) data and shows the formation of nanodiamonds induced by the second shock wave [Kraus et al., 2017, Schuster et al., 2020]. Contrary to the XRD method, the demixing values for the C-H separation obtained using XRTS do not depend on the crystalline structures in the experiment. The close resemblance of XRTS with XRD suggests that the observed carbon clusters seen consists mostly of diamond, which is not embedded in a significant amount of liquid carbon [Frydrych et al., 2020].

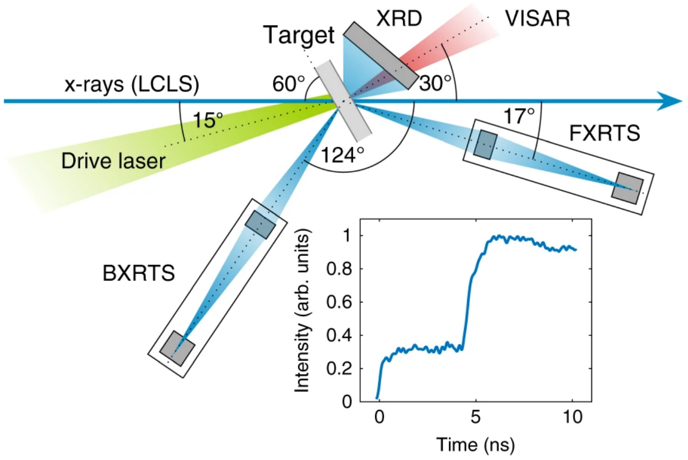

Figure 3.4.3: Experimental setup showing the compression of the polystyrene sample using a drive laser and the measurements using XRTS and XRD. Reprinted figure from **S. Frydrych** *et al.*, Demonstration of X-ray Thomson scattering as diagnostics for miscibility in warm dense matter. Nat Commun **11**, 2620 (2020) [Frydrych et al., 2020] licensed under CC-BY-4.0.

3.5 X-ray Raman Scattering

X-Ray Raman scattering (XRS) also known as non-resonant inelastic x-ray scattering (NRIXS) probes the electronic transitions similar to the x-ray absorption spectroscopy (XAS). The inelastic scattering process of the excitations of the core electrons into unoccupied states can be well understand with XRS. An important advantage of XRS over other methods is that transitions other than dipole can be switched on by varying the magntitude and the direction of the momentum transfer. Due to the high penetrative capability of the hard x-rays, XRS has an advantage over EELS for the investigation of samples under high-pressure. The electronic transition can be approximated as a dipole transition in XAS, while higher order quadrupole transitions are accesible via XRS based on the q-vector relating the incident and the scattered x-rays.

Using first order perturbation theory, the double differential scattering cross section for a scattering from ground state $|i\rangle$ with energy E_i to a final state $|f\rangle$ with energy E_f is given by [Schülke, 2007]

$$\frac{d^2\sigma}{d\Omega^2 d\hbar\omega} = \left(\frac{d\sigma}{d\Omega}\right) S(q,\omega), \tag{3.5.1}$$

where $\frac{d\sigma}{d\Omega}$ is the Thomson scattering cross section. The dynamic structure factor is given by

$$S(q,\omega) = \sum_f |\langle i| \sum_n e^{(-i\mathrm{q.r_n})} |f\rangle|^2 \delta(E_i - E_f + \omega), \tag{3.5.2}$$

where $q = (q_1 - q_2)$ is the momentum transfer. The initial state $|i\rangle$ is approximated by a Slater determinant composed of single-electron orbitals φ_i of the core electrons and other occupied orbitals ψ_j. The final state $|f\rangle$ is represented by a transition of a core electron φ_n to an unocccupied Bloch orbital ψ_k with the same spin. The matrix element in Eq. (3.5.2) reduces

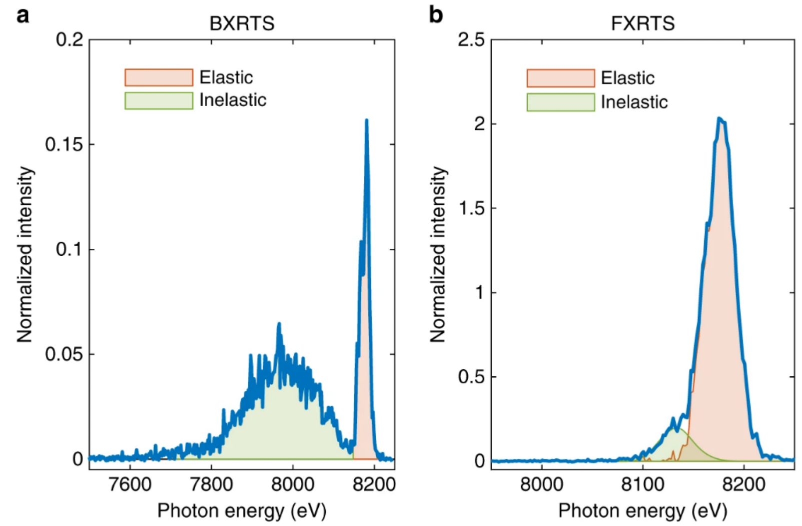

Figure 3.4.4: Scattered x-ray spectra recorded using the a) Backward and b) Forward spectrometers. Reprinted figure from **S. Frydrych** *et al.*, Demonstration of X-ray Thomson scattering as diagnostics for miscibility in warm dense matter. Nat Commun **11**, 2620 (2020) [Frydrych et al., 2020] licensed under CC-BY-4.0.

to

$$\langle i|\sum_n e^{(-i\mathbf{q}.\mathbf{r}_n)}|f\rangle = \int d^3r\psi_k^*(r)e^{(-i\mathbf{q}.\mathbf{r})}\varphi_n(r). \tag{3.5.3}$$

Using the periodicty of the Bloch orbital ψ_k and writing $r = R_n + r'$

$$\langle i|\sum_n e^{(-i\mathbf{q}.\mathbf{r}_n)}|f\rangle = e^{-i(\mathbf{q}+\mathbf{k}).\mathbf{R}_n}\int d^3r'\psi_k^*(r')e^{(-i\mathbf{q}.\mathbf{r}')}\varphi_n(r'). \tag{3.5.4}$$

Expanding the exponential in the matrix element of Eq. (3.5.4) as $e^{i\mathbf{q}.\mathbf{r}} = 1 + i\mathbf{q}.\mathbf{r} + (i\mathbf{q}.\mathbf{r})^2/2 + \ldots$ helps in better understanding of the transition processes. For small momentum transfers $\mathbf{q}.\mathbf{a}_\mathbf{c} \ll 1$, where a_c is the radius of the core orbital, the first term has no contribution due to orthogonality and the second term dominates with the dipole transitions permitted. For large momentum transfers, the contribution of the non-dipole transition terms increases. The double differential scattering cross section can be represented in a tensor form as

$$\frac{d^2\sigma}{d\Omega^2 d\hbar\omega} = \left(\frac{d\sigma}{d\Omega}\right) q.T(\omega).q, \tag{3.5.5}$$

with the tensor given by

$$T(\omega) = \sum_{unocc.}\int d^3r\psi_i(r)r\varphi_f^*(r)\int d^3r\psi_f^*(r)r\varphi_i(r)\delta(E_i - E_f),$$

.

The XRS simulations are performed using the FDMNES code [Joly, 2001, Bunău and Joly, 2009]. From the unit cell positions, the code evaluates the non-equivalent and equivalent atoms with the symmetry operation relating them to each other. A cluster is formed around each non-equivalent and absorbing atom based on the chosen radius of the cluster. The final states are

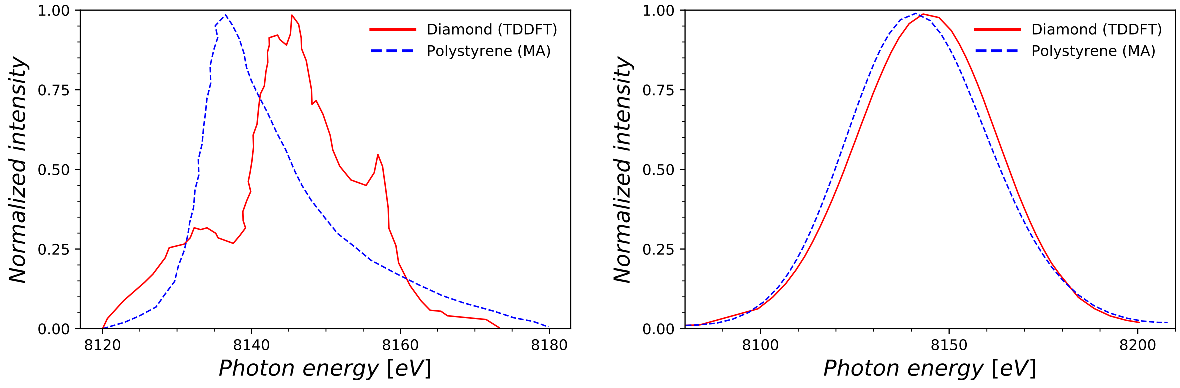

(a)

(b)

Figure 3.4.5: a) Inelastic scattering spectra for diamond and polystyrene calculated with TDDFT ($\vec{q} = 1.28$/Å) and KG+Mermin ($\vec{q} = 1.21$/Å) respectively, b) Inelastic scattering spectra after folding with the detector function with a Gaussian curve of halfwidth 34 eV. The data is taken from Ref. [Frydrych, 2018].

calculated for each cluster. The Poisson equation is solved to get the Coulomb potential from the superposed first guess atomic density, the XC potential is evaluated using an LDA Perdew-Wang formulation [Perdew and Wang, 1992]. The constructed potential is used to solve the Schrödinger equation to obtain the electronic structure which can be the final states when there is a transition. The Schrödinger equation is solved using a finite difference method that uses the full potential and the final states $|f\rangle$ are calculated. The finite difference method consists of constructing a space grid and discretizing the Schrödinger equation on the points of the grid. Although the method is computationally expensive but provides an accurate description of the electronic structure in both occupied and non occupied states and thus of the absorption-scattering phenomena. The matrix elements governing the transition depending on the polarization condition are evaluated based on the electronic structure. The absorption coefficient is calculated by applying the Fermi golden rule $\sum_f |\langle i|\hat{\mathcal{O}}|f\rangle|^2\delta(E_i - E_f + \omega)$ to get the matrix elements of the cross section. $\hat{\mathcal{O}}$ is the field operator classically describing the electron–photon interaction given by

$$\hat{\mathcal{O}} = \vec{\mathcal{E}}.\vec{r}(1 + \frac{i}{2}\vec{k}.\vec{r}), \tag{3.5.6}$$

where $\vec{r}$ is the position from the absorbing ion, $\vec{\mathcal{E}}$ the polarization of the photon and $\vec{k}$ its wavevector [Bunău and Joly, 2009].

Figure 3.5.1(a) and 3.5.1(b) shows the variation of XRS with a change in cluster radius and finite size effects. A cluster size of radius 5.0 Å and above ensures the convergence for N=4 and N=8 atoms. With increase in cluster radius, the computational demands increase as the final states calculated inside a sphere increase using the finite difference method. Figure 3.5.2(a) shows the XRS spectra for diamond under ambient conditions comparing the theoretical predictions with the experimental results. The simulations are performed using the FDMNES code [Joly, 2001, Bunău and Joly, 2009] for an ideal diamond lattice in an unit cell consisting of 8 atoms. The transition matrix is evaluated for $|\vec{q}| = 5.94$/Å up to angular momentum *l*=2. The selected *q* vector in the experiment is carefully chosen to avoid the position of the maxima of the Compton peak in the vicinity of the binding energy of the core electrons. The obtained experimental spectra [Voigt et al., 2021] shows good agreement with the theoretical predictions. The deconvolved experimetal data is obtained from deconvolution of the instrument function from the scattering spectrum. The Compton background represented using an exponential function is substracted in the vicinity of the K-edge. The dip around 300 eV is associated with the second band gap of diamond separating the lower set of conduction bands from the next set of higher level conduction bands. Transitions to these higher states from the valence bands involve energies exceding 20 eV. Figure. 3.5.2(b) shows the presence of a second band gap between the valence band edge and the higher conduction band [Painter et al., 1971, Sokolov et al., 2003]. At a moderate momentum transfer of 5.94/Å, the spectra is significantly dominated by dipole allowed transitions. This is observable in Fig. 3.5.3b where the calculated spectra are essentially identical after scaling the curve from Fig. 3.5.3a. Hence, XRS is a good alternative to soft XAS at moderate *q* values. With the intensity of XRS scaling quadratically with *q*, and larger momentum transfers resulting in more count rates, the method is highly beneficial [Galambosi et al., 2007].

To simulate the high temperature XRS spectra for carbon, DFT-MD simulations in combination with XRS simulations are performed to understand the expected changes in the XRS signal of heated and compressed diamond. VASP [Kresse and Hafner, 1993, Kresse and Joubert, 1999, Kresse and Furthmüller, 1996b, Kresse and Furthmüller, 1996a] is used to perform density functional molecular dynamics (DFT-MD) to obtain the equilibrated ionic configurations. The simulations are performed using a Nosé-Hoover thermostat [Nosé, 1984b, Hoover, 1985] using a PBE functional [Perdew et al., 1996a]. The MD simulations ran on a timestep of duration 0.2 fs up to a total of 2 ps or more until equilibration. The system consists of 8 atoms sampled using $2\times2\times2$ Monkhorst-Pack mesh [Monkhorst and Pack, 1976] with a hard carbon PAW pseudopotential and the energy cutoff set to 900 eV. The number of bands were consistently increased at higher temperatures to achieve the convergence. The equilibrated snapshots obtained using DFT-MD are used to perform the XRS calculations using FDMNES. Eight random ionic configurations are chosen, which are subsequently used to compute the XRS spectra for high temperatures.

Figure 3.5.4 shows the simulated spectra for isochorically heated diamond for a range of temperatures from 0.5 to 7.5 eV with additional calculations for various pressure conditions from 150 GPa to 437 GPa corresponding to densities 4.41–5.5 g/cm^3. The simulations for compressed conditions are performed based on the lattice parameters obtained using the Vinet equation of state [Vinet et al., 1987, Vinet et al., 1989] for diamond under ambient temperature. The increase in pressure results in reduction of the peak intensities and a shift of the spectral features to higher energies. This is expected as the diamond's indirect and direct band gap increases with pressure. At temperatures above 0.5 eV, isochorically heated diamond is in the liquid regime, refer Fig. 3.0.1 and Fig. 3.3.6. Comparing the 0.5 eV spectra under ambient and compressed pressure conditions, the increase of the peak intensities towards higher energies can also be observed in the results of the averaged XRS simulations with the ionic configurations obtained from DFT-MD, as explained above. With further increase in

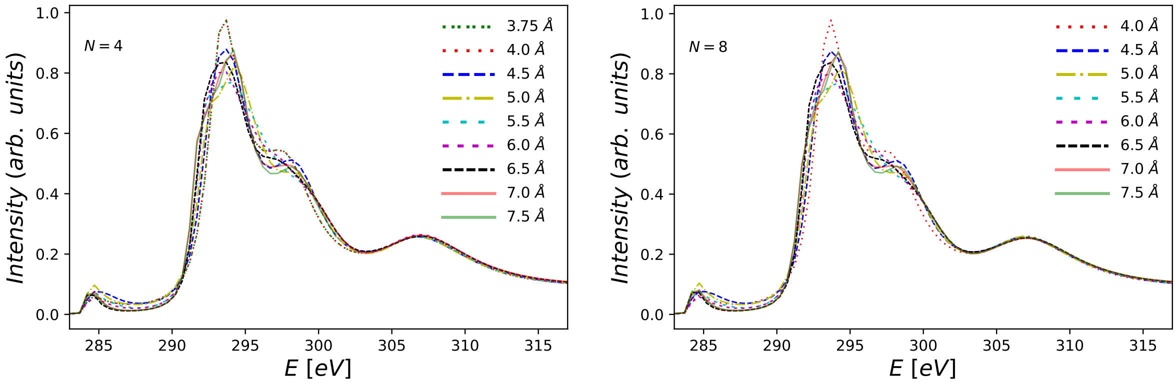

(a) (b)

Figure 3.5.1: X-ray Raman spectra for ambient diamond at $|\vec{q}| = 5.94/\text{Å}$ with a variation in the cluster radius. The simulation data is shown for diamond in an unit cell with a) 4 atoms and b) 8 atoms.

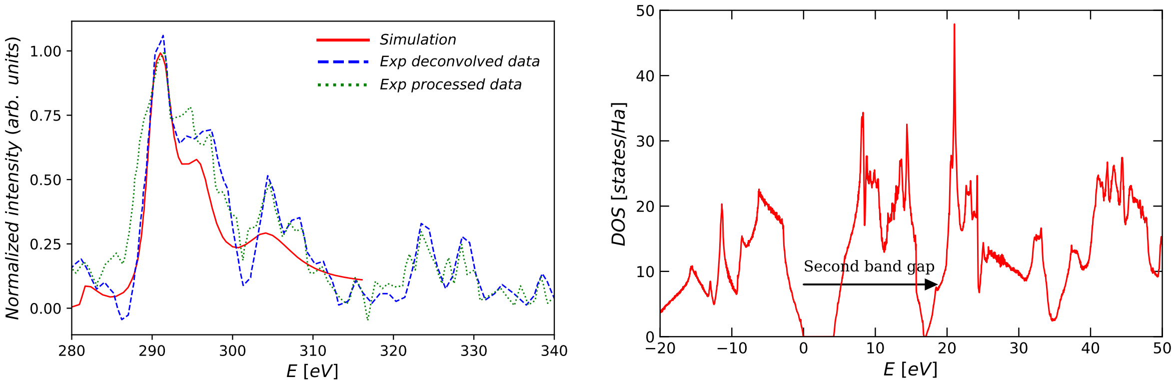

(a) (b)

Figure 3.5.2: a) Measured x-ray Raman spectra [Voigt et al., 2021] for diamond under ambient conditions at $|\vec{q}| = 5.94/\text{Å}$. The simulation data is shown for an unit cell consisting of 8 atoms. The carbon *K*-edge is located at ≈285 eV, b) Density of states for diamond at ambient conditions. The valence band maximum is adjusted to zero. Reprinted figure with permission from **K. Voigt** *et al.*, Physics of Plasmas **28** (8), 082701 (2021). Copyright 2021 by the AIP Publishing.

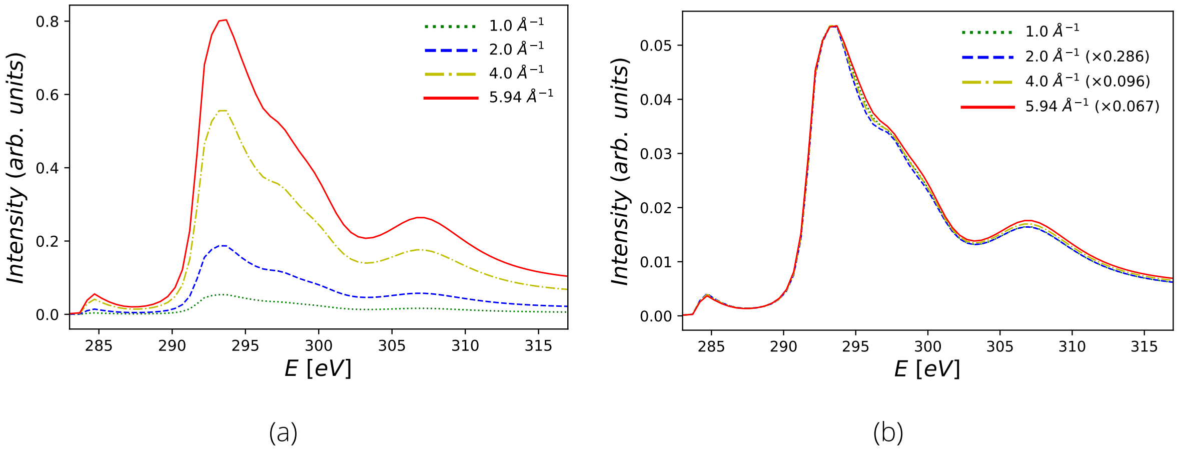

(a)

(b)

Figure 3.5.3: X-ray Raman spectra for diamond at ambient conditions for a) Various wavenumbers, b) Normalized with respect to 1.0 Å^{-1}. The scaling factor is indicated in the brackets.

temperature >0.5 eV, the phase is purely in the liquid regime and this is evident in the absence of the peak structures which are present under the cases of solid and warm dense conditions (~0.5 eV). The peak intensities in the liquid regime from 1.0 eV to 7.5 eV are further reduced compared to the solid phases and remain more or less uniform.

3.6 Conclusions

The electronic density of states, the band gap, and the dielectric response function as a function of pressure for various phases of carbon, namely diamond, lonsdaleite, and BC8 are calculated. In particular, the wavenumber dependence of the dielectric function is emphasized in order to provide high quality predictions for the dynamic structure and XRTS signals of these phases under high-pressure. The influence of different XC functionals on the band gaps and eigenvalues and thus on the response functions are also investigated. These results can provide a theoretical reference for future experiments on band gaps and optical properties for the various phases of carbon at high pressures.

BSE is the theory including the most advanced approximations and is expected to provide the quantitatively best results. Meanwhile TDDFT can reproduce the excitonic effects of the BSE reasonably well at a fraction of the computational cost and also at finite wavenumbers. The standard Kubo-Greenwood approach and its extension to finite wavenumbers via the extended Mermin Ansatz are compared to RPA, TDDFT and BSE. Available experimental data for diamond have been compared to the results of the simulations. For lonsdaleite and BC8 phase, experimental data under high-pressure are very sparse and only comparisons with different theoretical methods were possible.

For WDM conditions, TDDFT and RPA give different results to KG, and particular care is needed to eliminate finite size effects. The influence of the XC kernel in TDDFT is also investigated and is important for obtaining accurate results based on the WDM regime.

The location of the plasmon position in diamond under ambient conditions is well modeled

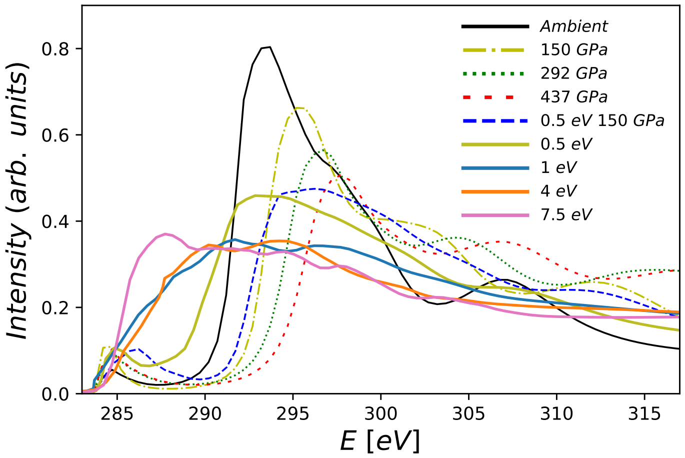

Figure 3.5.4: Calculated x-ray Raman spectra for compressed and ischorically heated diamond at $|\vec{q}| = 5.94/\text{Å}$. The spectrum for ambient conditions is shown in black for comparison. Various pressure conditions ranging from 150 GPa to 437 GPa (ρ=4.41–5.5 g/cm^3) and different temperature conditions ranging from 0.5 eV to 7.5 eV are investigated. Reprinted figure with permission from K. Voigt *et al.*, Physics of Plasmas **28** (8), 082701 (2021). Copyright 2021 by the AIP Publishing.

using TDDFT compared to other methods and in good agreement with the XRTS measurements. The approach using TDDFT to compute the inelastic-scattering spectra is a viable tool for experiments involving carbon and carbon bearing mixtures e.g. with attention to the formation of diamond [Kraus et al., 2017, Ramakrishna and Vorberger, 2019, Frydrych et al., 2020, Schuster et al., 2020]. The formation of diamond under WDM conditions is experimentally observed in polystyrene and polycrystalline graphite [Kraus et al., 2017, Frydrych et al., 2020, Schuster et al., 2020]. The simulations performed under this work further presents a scope to understand the complicated XRTS signals for understading the demixing of the carbon-hydrogen species. The demixing occurs at the predicted metallic hydrogen conditions and XRTS can be used in conjuction with LR-TDDFT predictions to obtain reliable diagnostics. The developed method is suitable especially considering the WDM regime for carbon-hydrogen mixtures in the recent experimental campaigns [Kraus et al., 2017, Frydrych et al., 2020] where carbon component is still strongly bounded and using RPA with plasma theory fails even combined with Mermin Ansatz providing unrealistic plasmon properties. The many-component species involved further complicates the use of the free-electron model of the RPA plasma theory including local-field corrections. The formation of metallic hydrogen is experimentally predicted to occur at these conditions, (see chapter 4) for the Equation of State. As comparable XRS measurements can be performed at XFEL sources in the future for low-Z materials, XRS is a viable tool for understanding the electronic structure i.e. changes in the chemical bonding and characterizing phase behavior in WDM regime.

4 Influence of Finite-Temperature Exchange-Correlation Effects in Hydrogen

Results of this chapter are published in
M. Bonitz et al.,
Physics of Plasmas ***27****, 042710 (2020)*
K. Ramakrishna et al.,
Phys. Rev. B ***101****, 195129 (2020)*

The success of density functional theory (DFT) regarding the description of materials was facilitated by the availability of accurate exchange-correlation (XC) functionals, which, however, cannot be obtained within DFT itself and have to be supplied as input. While the exact functional is, in general, not known, this quantity can often be reasonably approximated on the basis of the properties of the uniform electron gas (UEG) [Loos and Gill, 2016, Dornheim et al., 2018a]. The key quantity is given by the XC energy of the UEG, which, at zero temperature, was accurately computed by Ceperley and Alder [Ceperley and Alder, 1980]. These data were subsequently used as input for different parametrizations [Vosko et al., 1980, Perdew and Zunger, 1981, Perdew and Wang, 1992] of the XC energy $E_{\mathrm{XC}}(r_s)$, which allow for DFT calculations on the level of the local density approximation (LDA). These results further constitute the basis for more advanced functionals like the PBE [Perdew et al., 1996a].

While the generalization of DFT to finite-temperature was introduced over 50 years ago by Mermin [Mermin, 1965], most results pertaining to warm dense matter (WDM) have been obtained on the basis of the *zero-temperature approximation* e.g., Refs. [Mazevet et al., 2005, Mattsson et al., 2010, Schöttler and Redmer, 2018, Witte et al., 2017b, Baczewski et al., 2016, Whitley et al., 2015]), i.e., using XC functionals that were designed for the ground-state. Meanwhile, the assumption is questionable, as the thermal DFT formalism requires as input a parametrization of the XC free energy $f_{\mathrm{XC}}(r_s, \theta)$ that explicitly depends both on density and temperature [Gupta and Rajagopal, 1982, Smith et al., 2018]. Hence, replicating the success of ground state DFT at elevated temperatures requires an accurate description of the UEG in the WDM regime [Karasiev et al., 2016, Karasiev et al., 2019a, Luo et al., 2020, Ramakrishna et al., 2020, Mihaylov et al., 2020]. Perrot and Dharma-wardhana [Perrot and Dharma-wardana, 1984, Perrot and Dharma-wardana, 2000, Dharma-wardana and Perrot, 2000] introduced a classical mapping for the free energy parametrization and the overall accuracy is comparable to that obtained by Vashishta and Singwi [Vashishta and Singwi, 1972] and inferior to that given by the Singwi, Tosi, Land, and Sjölander (STLS) scheme [Singwi et al., 1968, Tanaka and Ichimaru, 1986].

As the overall accuracy of the free energy parametrizations was unknown, it has sparked a surge of new developments regarding quantum Monte Carlo (QMC) simulations of electrons in the WDM regime [Brown et al., 2013a, Blunt et al., 2014, Dornheim et al., 2015a, Malone et al., 2015, Dornheim et al., 2015b, Groth et al., 2016, Dornheim et al., 2016a, Malone et al., 2016, Dornheim et al., 2016b, Claes and Clark, 2017, Dornheim et al., 2017, Groth et al., 2017c, Dornheim et al., 2019]. Brown *et al.* [Brown et al., 2013a] presented the first path integral Monte Carlo (PIMC) results for the warm dense UEG, which were subsequently used as input for several parametrizations [Brown et al., 2013b, Sjostrom and Dufty, 2013, Karasiev et al., 2014b]. The Brown *et al.* [Brown et al., 2013a] data were obtained by imposing a restriction on the nodal structure of the thermal density matrix (*fixed node approximation*) [Ceperley, 1991] so that the quality of these data had remained unclear. Schoof *et al.* [Schoof et al., 2015] were able to unambiguously quantify the nodal errors by presenting an independent data set using the exact configuration PIMC method [Schoof et al., 2011]. It was found that the restricted PIMC data exhibit systematic deviations of up to 10%.

A set of unbiased PIMC data [Dornheim et al., 2016b] in the thermodynamic limit was used to construct a new parametrization *G*roth-*D*ornheim-*S*jostrom-*M*alone-*F*aulkes-*B*onitz (*GDSMFB*) of f_{XC} [Groth et al., 2017c]), which is employed throughout this work. The earlier parametrization by Karasiev *et al.* [Karasiev et al., 2014b] (KSDT) and also an improved version "corrKSDT" [Karasiev et al., 2018b] exhibits a comparable accuracy in the relevant WDM regime.

The investigation of gradient corrections by Sjostrom and Daligault [Sjostrom and Daligault, 2014] based on the the KSDT functional concludes that the finite-temperature XC effects start to matter at around T=10^4 K. The first thorough investigation of finite temperature XC effects was presented by Karasiev *et al.* [Karasiev et al., 2016], where the limits of the zero-temperature approximation were pointed out for a few different materials and quantities. Shortly thereafter, Karasiev *et al.* also presented a finite temperature GGA functional [Karasiev et al., 2018b] and reported a significant improvement in the principal Hugoniot of shocked deuterium [Karasiev et al., 2019a]. Recently, a thermal hybrid XC functional [Mihaylov et al., 2020] has been presented which could provide a significant improvement to static calculations of electronic band gap and band structure at temperatures within the WDM regime.

Yet, a detailed study of the impact of XC effects considering different relevant physical regimes (e.g., WDM, electron liquid, etc) was still missing, the aim is to fill this gap by carrying out extensive thermal DFT calculations of hydrogen and comparing different zero-temperature approximations to the GDSMFB functional [Groth et al., 2017c, Ramakrishna et al., 2020]. In this regard, hydrogen constitutes an obvious choice as it is the most abundant element in our universe and offers a plethora of interesting physical effects [McMahon et al., 2012] such as the liquid-liquid insulator-to-metal phase transition [Wigner and Huntington, 1935, Ashcroft, 1968, Weir et al., 1996, Dalladay-Simpson et al., 2016, Knudson et al., 2015, Celliers et al., 2018, Dias and Silvera, 2017, Eremets and Troyan, 2011]. Moreover, hydrogen-helium mixtures have been predicted to undergo temperature driven phase transition from a high temperature liquid (fully miscible) to a low temperature phase dominated with helium droplets. The experimental data on the phase diagram of hydrogen-helium mixtures are very scarce and the existing knowledge is based on simulations. Under the planetary interiors of jupiter and saturn, the interaction between hydrogen and helium leads to challenges in determining the equation of state (EOS) due to the miscibility [Schöttler and Redmer, 2018, Helled et al., 2020]. Further actively investigated questions regarding hydrogen at extreme conditions include ionization potential depression [Stransky, 2016, Saha, B. et al., 2002] and proton crystallization [Bonitz et al., 2005, Filinov et al., 2012].

The relative importance of thermal XC effects as a function of density (r_s) and temperature for

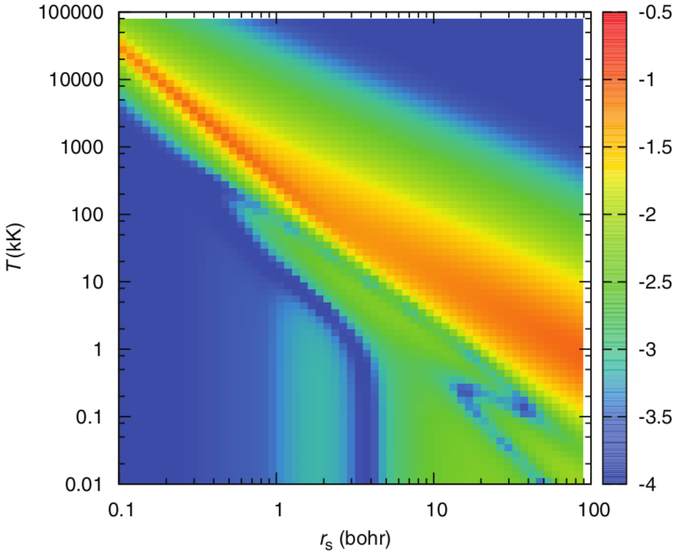

Figure 4.0.1: Map of the density-temperature plane showing the importance of the temperature dependence in finite-temperature XC free energy functional. The x-axis represents the density (r_s) in logarithmic scale. The y-axis represents the temperature ($\times 10^3$ K) in logarithmic scale. The color map shows the deviation [Eq. (4.0.1)] in logarithmic scale. Reprinted figure with permission from **V. V. Karasiev** *et al.*, Phys. Rev. E **93**, 063207 (2016). Copyright 2016 by the American Physical Society.

an uniform electron gas is shown in Fig. 4.0.1. The quantity is plotted as

$$\log_{10}\left(\frac{|f_{XC}(r_s,T)-e_{XC}(r_s)|}{|f_n(r_s,T)+e_{XC}(r_s)|}\right), \tag{4.0.1}$$

where f_{XC} is the XC free energy per particle, e_{XC} is the ground state XC energy per particle, and f_n is the non-interacting XC free energy per particle. The domain where the temperature dependence of the XC effects is most important is indicated by the yellow and orange regions. For example, a 10% change is expected in the XC free energy per particle at the onset of the red region in the map. It is clear that the finite-temperature XC is expected to be important at low temperature for large r_s (> 5). Also, in the large temperature limit, the importance vanishes as the system becomes increasingly ideal for large temperatures, and XC overall become unimportant [Karasiev et al., 2016].

The XC free energy per particle based on the GDSMFB parametrization [Eq. (2.3.25)] is plotted as a function of density and reduced temperature for a spin unpolarized case ($\xi = 0$) in Fig. 4.0.2(a). The spin polarization is given by $\xi = (N^{\uparrow}-N^{\downarrow})/(N^{\uparrow}+N^{\downarrow}) \in [0,1]$. Looking at a contour for a high density case, e.g., at $r_s = 1.0$, the influence of thermal XC has a maximum around $\theta = 0.5$ ($\approx 3\times10^5$ K), also evident in Fig. 4.0.1. Similarly, for a low density case, e.g., at $r_s = 14$, the XC free energy is small but the significance of thermal XC is spread over a wide range of reduced temperatures in Fig. 4.0.2(b), seen in the wide heat map (orange-red) around 10^4 K in Fig. 4.0.1. These effects are further explored in detail in the following sections for various density and temperature ranges. The spin dependency of the XC free energy is plotted as a function of density and reduced temperature in Fig. 4.0.2(c). For a spin polarized (ferromagnetic) case

($\xi = 1$), as the temperature increases, the f_{XC} of the polarized case increases relative to the unpolarized case.

A detailed phase diagram of hydrogen is shown in 4.0.3. The blue dotted lines are the phases between the solid molecular phases and the melt line from Refs. [Goncharov et al., 2011, Howie et al., 2015, Eremets et al., 2016]. The vertical yellow line is a proposed phase line distinguishing the semiconducting and semimetallic solid phases [Eremets et al., 2019]. The grey region is a hypothetical transition to an atomic solid phase stable beyond 500 GPa still not reached within the experimental means. The solid phases comprises crystal structure of various symmetries with same of the phases yet to be experimentally determined, so far the theoretical predictions are restricted to the stability of the phases at thermodynamic conditions from DFT and QMC simulations [Pickard and Needs, 2007, Geneste et al., 2012, Azadi et al., 2014, Drummond et al., 2015]. At high temperature, the insulator-metal transition is shown by the red curve before the existence of an intermediate semiconducting fluid state.

4.1 Computational Details

The DFT-MD simulations are performed using the CP2K code [Hutter et al., 2014]. The Kohn-Sham (KS) equations are solved using the Gaussian plane waves (GPW) method with the basis set consisting of Gaussians along with additional plane waves as auxiliary basis. The auxiliary basis is of the form $\psi(\vec{r}) = R_i(r)Y_{l_i,m_i}(\theta,\varphi)$, with $R_i(r)$ denoting the radial part and $Y_{l,m}$ denoting the angular part. The electron-proton potential is approximated using Goedecker-Teter-Hutter pseudopotentials [Goedecker et al., 1996] of LDA form with a cutoff radius of $r_c = 0.2\,\mathrm{a}_B$. The standard T=0 LDA XC functional is hereafter referred to as PZ (Perdew-Zunger) [Perdew and Zunger, 1981] and the parametrized temperature dependent LDA form of the XC functional as GDSMFB [Groth et al., 2017c]. The GDSMFB functional is accessed in the CP2K code using the library of exchange-correlation functionals (LIBXC) [Lehtola et al., 2018, Marques et al., 2012].

The convergence tests in terms of energy are performed using full DFT-MD simulations by varying the system parameters: *system size*, *basis set*, *k-point sampling* and *plane wave energy cutoff*. Simulations are run up to 10000 steps and the equilibrated snapshots are averaged to obtain the statistics: pressure/energy of the system. Full scale DFT-MD simulations although expensive are considered in this work for achieving the convergence involving a broad range of system parameters.

The right basis set is important for obtaining accurate results, while staying within reasonable limits for the computational demand [Ferrario et al., 2007]. The best accuracy with sufficient speed can be obtained when using the double-zeta valence polarized (DZVP) basis set for the computation of the pressure as summarized in Fig. 4.1.1(a) for the PZ functional. Computationally more expensive basis sets can be ignored as the pressure results are converged to ≈0.3%. DZV/DZVP basis sets have been previously utilized in the simulations of warm dense hydrogen and hydrogen-helium mixtures [Li et al., 2017b, Liu et al., 2018]. The plane wave energy cutoff is set between 450-800 Ry and the Gaussian basis set cutoff is set to 90–180 Ry

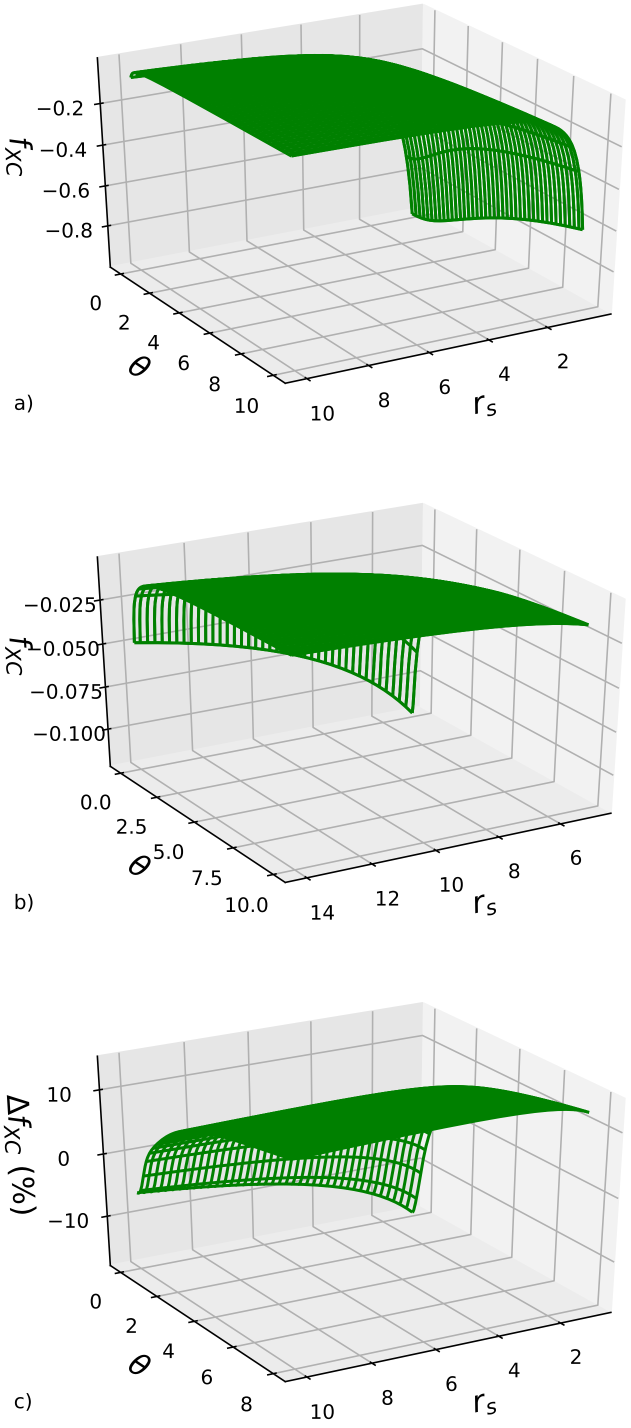

Figure 4.0.2: Exchange-correlation free energy per particle (f_{XC}) as a function of density (r_s) and reduced temperature (θ) for a) a spin unpolarized case, b) a spin unpolarized case at low densities $r_s = 5.0 - 14.0$ and small reduced temperatures, c) a spin polarized case. The change in the XC free energy is given by $\left[\frac{f_{XC}(r_s,\theta,\xi=1)-f_{XC}(r_s,\theta,\xi=0)}{f_{XC}(r_s,\theta,\xi=0)} \times 100\%\right]$.

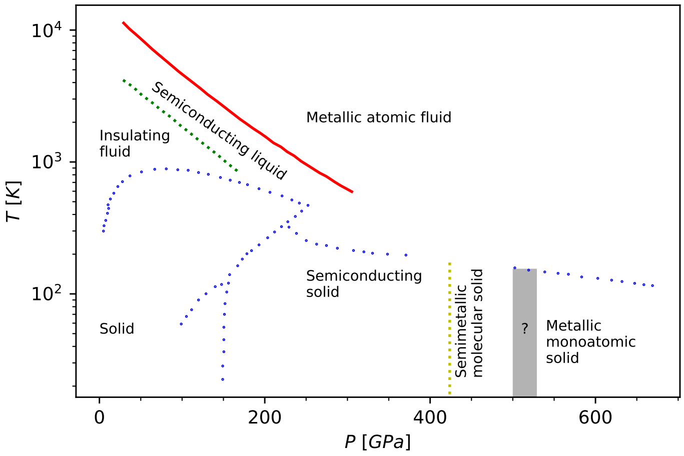

Figure 4.0.3: Phase diagram of hydrogen at high temperatures and pressures. Republished with permission of AIP Publishing from Phase diagram of hydrogen at extreme pressures and temperatures; updated through 2019, Low Temperature Physics **46**, 97 (2020) [Goncharov, 2020]. Permission conveyed through Copyright Clearance Center, Inc.

depending on the density and the temperature of the system.

With the DZVP basis set chosen, the choice of the system size is tested next. The smallest system size considered for the DFT-MD simulations (N=32) shows finite size effects at a range of densities and temperatures and the minimum size required for sufficient accuracy is given by N=256 as shown in Figure 4.1.1(b). Due to high computational demands required, which is explicitly mentioned in those cases, a sytem size N=32 is used for cases of small/large densities. Lorenzen *et al.* [Lorenzen et al., 2010] also observed a similar effect of the system size on the EOS for dense hydrogen. The effect is seen in Fig. 4.1.1(b) for $r_s = 3.0$ with a pressure variation of 4.7% with the change in system size from N=32 to N=256. At $r_s = 4.0$, the pressure variation with the same change in system size is 2.5%. At much lower densities ($r_s \geq 10$) a system size of N=32 or N=108 only is feasible for simulations due to bigger simulation boxes requiring more plane waves.

The computed energy and pressure of the system can be influenced by the choice of *k*-point sampling. At $r_s = 3.0$, T=15625 K, no dependence on *k*-point sampling is observed based on the system size for obtaining the convergence as shown in Fig. 4.1.1(c). With a small system size of N=32, the pressure difference between gamma-point sampling and the usage of *k*-points are negligible but the pressures obtained are comparatively higher than the values reported by Hu *et al.* and Wang *et al.* respectively [Hu et al., 2011, Wang and Zhang, 2013]. The pressure difference between gamma-point sampling and $3 \times 3 \times 3$ is < 0.1% for N=108. Higher *k*-point sampling has a smaller effect for bigger supercells as the case of N=256 particles demonstrates where the change in pressure is still < 0.1% going from gamma-point sampling to a $3 \times 3 \times 3$ grid of *k*-points. A system size of N=256 sampled at the gamma-point is considered based on the aforementioned reasons.

To account for the large kinetic energies of the protons at higher temperatures, the simulation time step needs to be varied. It ranges in between 0.02 fs for the highest temperatures and 0.1 fs for the lowest temperatures considered. At least 10000 time steps for the simulations are considered until the system had equilibrated and then further time steps of 4000–5000 are considered for obtaining the statistics. A Fermi occupation of the bands/eigenvalues is used to set the electronic temperature [Mermin, 1965, Gupta and Rajagopal, 1982] along with a Nosé-Hoover thermostat to control the ionic temperature in the canonical ensemble [Nosé, 1984b, Nosé, 1984a]. The simulation box consisted of an hexagonal cell (a=b, c=1.63a) under periodic boundary conditions and the cell size varied depending on the density. The simulations cover the density range from $r_s = 0.8137\ldots14$ for a wide range of temperatures T=250–400000 K. Simulations of temperature ranges beyond 400000 K are at present computationally too expensive using KS DFT formalism. Alternatives include orbital-free DFT [Karasiev et al., 2013, Karasiev et al., 2014c, Zhang et al., 2016, Luo et al., 2020], an extended KS formalism [Zhang et al., 2016], a stochastic-deterministic scheme [White and Collins, 2020], and Spectral Quadrature DFT (SQDFT) [Suryanarayana et al., 2018] for large-scale parallel KS DFT calculations which, however, are beyond the scope of this work.

4.2 High-Pressure Fluid

This section focuses on the finite-temperature XC effects on the equation of state (EOS) in the high-pressure fluid regime ($r_s < 2.0$) for $T \leq 10000$ K and a comparison is made to the available *ab-initio* results. While nuclear quantum effects (NQE) have been shown to influence the EOS at lower temperatures and the liquid-liquid phase transition (LLPT) [Morales et al., 2010b, Morales et al., 2013], they are not considered in this work as the focus is on the thermal XC effects on the electrons.

The simulations are performed for a system size N=256 and the *k*-point sampling is performed only at the gamma-point. Figure 4.2.1 shows the EOS at 1000 K computed with various XC functionals and *ab-initio* methods. In the PVT diagram, the LLPT can be recognized [Morales et al., 2010b] by its characteristic signature $(\partial P/\partial \rho)|_T = 0$. CEIMC gives a very clear signature of the LLPT. The DFT-MD results, which can be calculated for a finer grid of points and have to utilize a dense *k*-point grid near the transition region, show a slightly lower transition pressure [Lorenzen et al., 2010].

The incorporation of finite-temperature XC has no significant change in the EOS as the reduced temperatures are low at these densities, $0.003 < \theta < 0.004$. At T=1000 K, the LDA results (PZ/GDSMFB) are in the range obtained by Alavi *et al.* [Alavi et al., 1995]. Since LDA fails to capture the molecular dissociation correctly, the effect of finite-temperature XC on the LLPT can be ignored. There are obviously differences to the pressure isotherms obtained with different XC functionals, in particular in the molecular region. The most accurate EOS under these conditions is provided by the CEIMC method, and the next best approach would be DFT-MD if higher rungs of XC functionals, especially non-local density functionals, are used. Indeed, several papers recently reported a higher transition pressure comparable to and even above CEIMC when using functionals featuring van-der-Waals corrections [Knudson et al., 2015, Lu et al., 2019, Hinz et al., 2020].

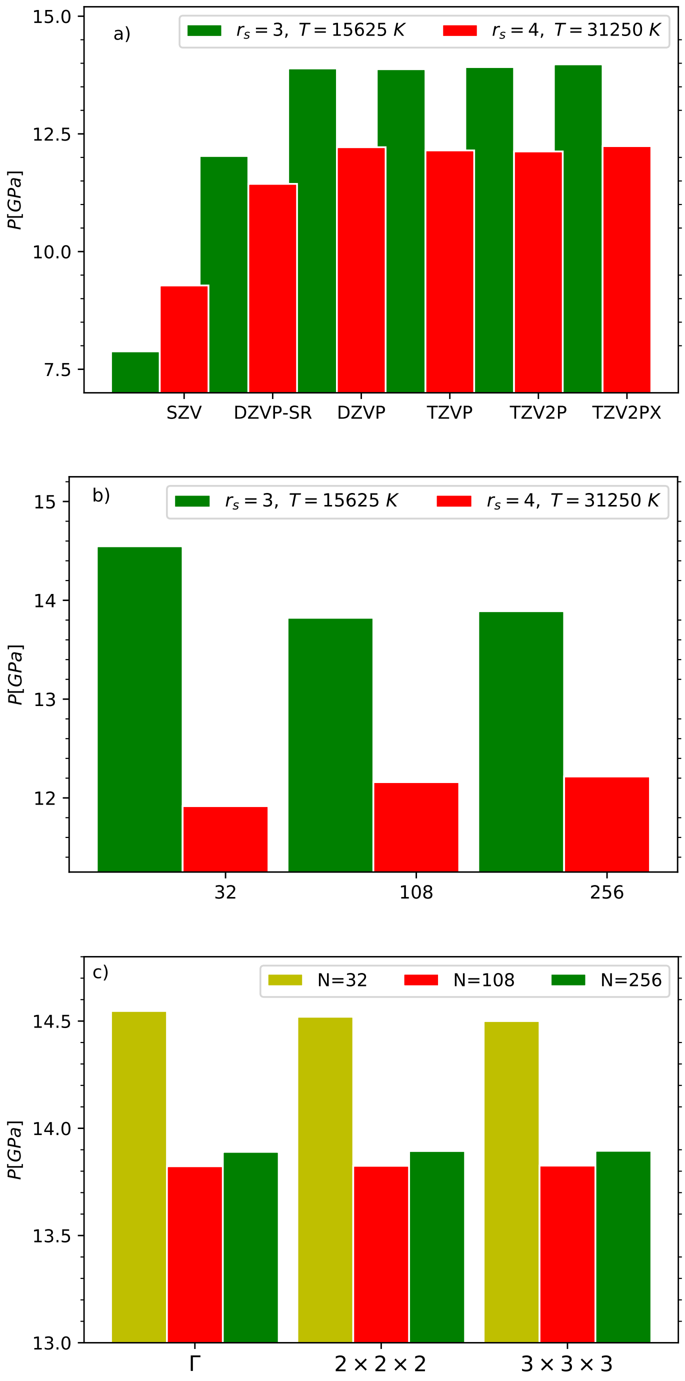

Figure 4.1.1: Pressure variation with respect to a) the basis set at $r_s = 3.0$, T=15625 K. The error bars are too small to be shown; b) system size for the DZVP basis set at $r_s = 3.0$, T=15625 K and $r_s = 4.0$, T=31250 K; c) *k*-point sampling for the DZVP basis set at $r_s = 3.0$, T=15625 K for a system size of 32, 108 and 256. Reprinted figure with permission from **K. Ramakrishna** *et al.*, Phys. Rev. B **101**, 195129 (2020). Copyright 2020 by the American Physical Society.

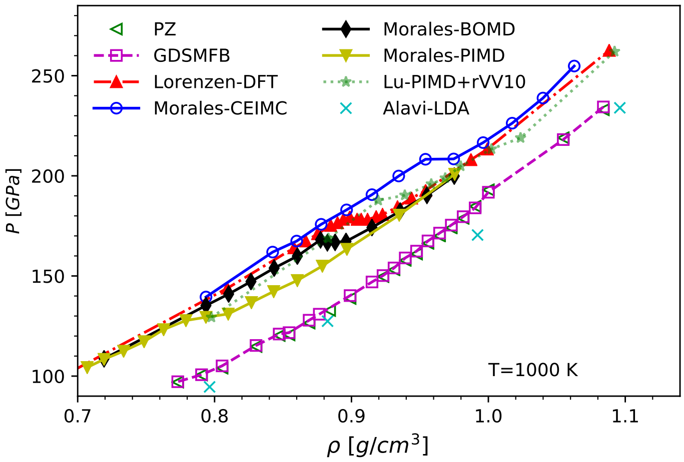

Figure 4.2.1: EOS at T=1000 K using various XC functionals and *ab-initio* methods. Lorenzen Ref. [Lorenzen et al., 2010]; Morales Ref. [Morales et al., 2010b]; Lu Ref. [Lu et al., 2019]; Alavi Ref. [Alavi et al., 1995]. PZ and GDSMFB results of this work. Reprinted figure with permission from **K. Ramakrishna** *et al.*, Phys. Rev. B **101**, 195129 (2020). Copyright 2020 by the American Physical Society.

The computed EOS in comparison to QMC and Born-Oppenheimer moleclar dynamics (BOMD) at temperatures 6000 K, 8000 K and 10000 K are shown in Figs. 4.2.2(a)-4.2.2(c). The relative difference in pressure shown in the inset plot is given by

$$\frac{(P_{GDSMFB} - P)}{P_{GDSMFB}} \times 100\%. \tag{4.2.1}$$

The LDA (PZ) results and the BOMD results obtained by Morales *et al.* using PBE consistently exhibit deviations from each other with smallest deviations for the lowest r_s (highest densities) where the system is metallic [Morales et al., 2010a]. A divergence is observed between the CEIMC method and the PBE results of Morales *et al.* with increasing r_s, where the CEIMC data more closely agree with the LDA results [Morales et al., 2010a]. A possible explanation for this trend would be a systematic bias in the CEIMC data due to the employed LDA based trial wave function in this approach, although this cannot be resolved on the basis of the data obtained here. In Fig. 4.2.2(a), the close agreement for lower densities ($r_s > 1.4$) between the PZ/GDSMFB results and QMC as well as PBE-BOMD data obtained by Mazzola *et al.* [Mazzola et al., 2018] and Vorberger *et al.* [Vorberger et al., 2007] are shown. The GDSMFB results in a higher pressure compared to PZ by 0.2 – 0.5% at these conditions, which is reasonable as $\theta \approx 0.01 - 0.03$. A similar trend can also be observed in Fig. 4.3.2 discussed in section 4.3 where the pressure difference is positive for similar densities at low temperatures.

For completeness, as it is not really related to the influence of thermal XC effects, the phase diagram of hydrogen at high densities including the LLPT is shown in Fig. 4.2.3. The LDA (PZ/GDSMFB) results are not included in the diagram as they fail to capture the LLPT and the EOS is inconsistent with the other XC functionals and experimental results [Mazzola et al., 2018, Morales et al., 2010a, Pierleoni et al., 2016, Pierleoni et al., 2018, Lorenzen et al., 2010, Tamblyn and Bonev, 2010, Zaghoo et al., 2016, Knudson et al., 2015,

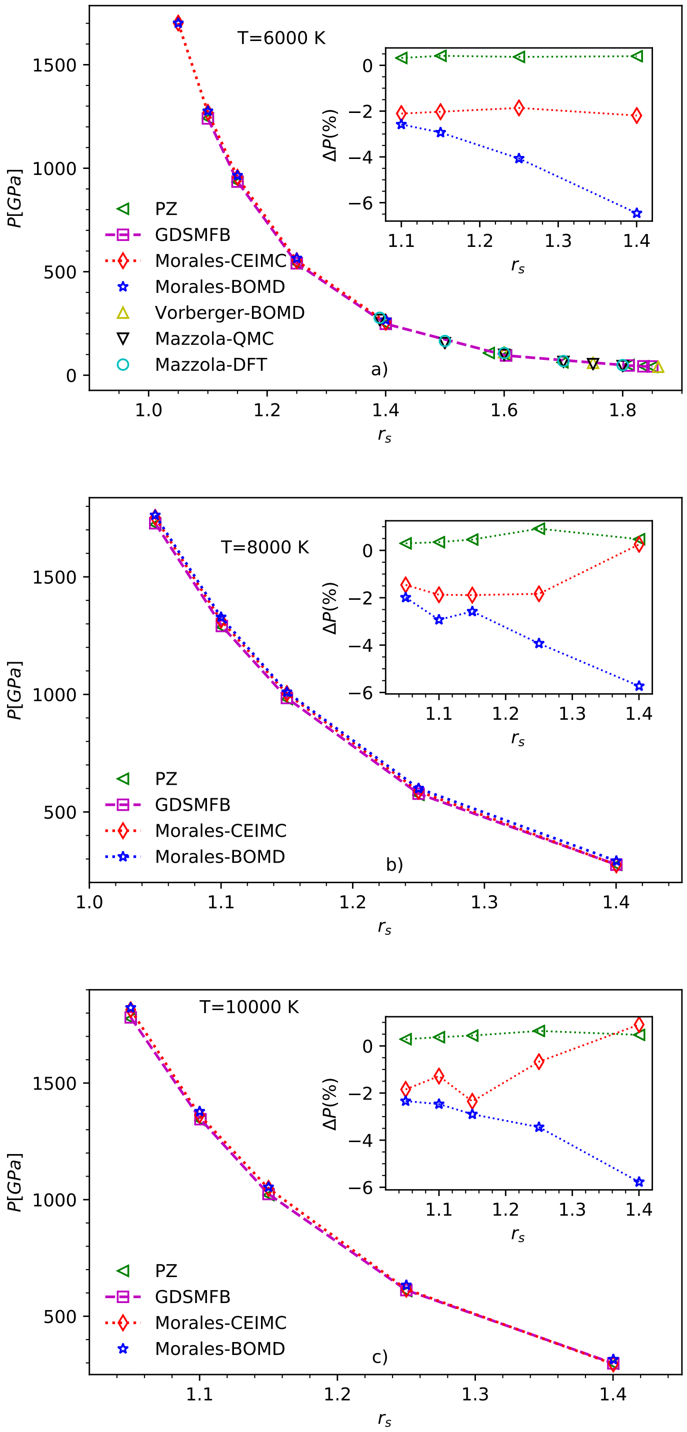

Figure 4.2.2: EOS at a) T=6000 K, b) T=8000 K, and c) T=10000 K comparing our results with the previous results obtained using PIMC and DFT. The inset plot shows the relative difference (Eq. 4.2.1) in pressure with respect to the finite-temperature case. Morales Ref. [Morales et al., 2010a]; Vorberger Ref. [Vorberger et al., 2007]; Mazzola Ref. [Mazzola et al., 2018]. Reprinted figure with permission from **K. Ramakrishna** *et al.*, Phys. Rev. B **101**, 195129 (2020). Copyright 2020 by the American Physical Society.

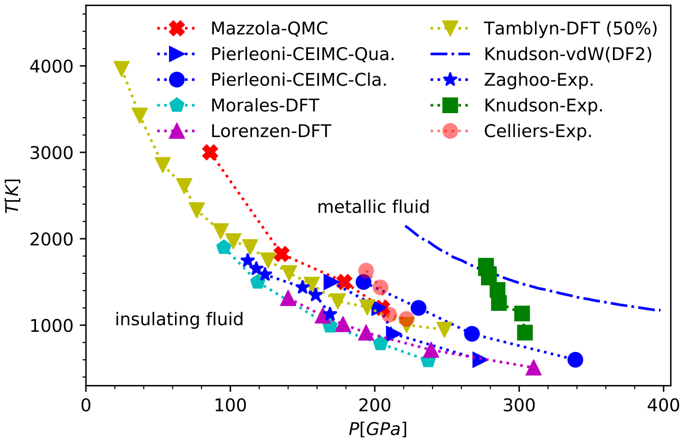

Figure 4.2.3: Phase diagram of hydrogen at high densities. Mazzola Ref. [Mazzola et al., 2018]; Morales Ref. [Morales et al., 2010a]; Pierleoni Ref. [Pierleoni et al., 2016, Pierleoni et al., 2018]; Lorenzen Ref. [Lorenzen et al., 2010]; Tamblyn Ref. [Tamblyn and Bonev, 2010]; Zaghoo Ref. [Zaghoo et al., 2016]; Knudson Ref. [Knudson et al., 2015]; Celliers Ref. [Celliers et al., 2018]. Reprinted figure with permission from **K. Ramakrishna** *et al.*, Phys. Rev. B **101**, 195129 (2020). Copyright 2020 by the American Physical Society.

Celliers et al., 2018]. The Pierleoni *et al.* data are shown both for quantum and classical protons [Pierleoni et al., 2016, Pierleoni et al., 2018]. The figure nicely demonstrates the wide spread of the predictions of the LLPT in the high-pressure fluid of hydrogen and the associated problems with the treatment of exchange and correlation in this correlated system.

4.3 Warm Dense Matter

In this section, the warm dense matter regime is explored, where thermal XC effects are expected to be important. The DFT-MD simulations need good convergence with respect to the simulation parameters. In section 4.1, the choice of the DZVP basis set is reasoned based on the computational cost and the accuracy for $r_s = 3.0 - 4.0$. The pseudopotential was further optimized using ATOM within the CP2K code that ensures even at the highest densities that there is no overlap of cores. In particular, the core radius was lowered even further to 0.1 a_B for high densities. At lower r_s (< 1.0), the basis set and the energy cutoff for the plane waves are important. A cutoff of 500 Ry and above with the DZVP basis set ensures the convergence in pressure calculations. Figure. 4.3.1 shows the energy cutoff for $r_s = 0.8137$ (5.0 g/cm^3) using various basis sets with PZ XC for 32 atoms at two different temperatures. The simulation parameters are well optimized at the higher densities considered for simulations, ensuring the consistent quality of the calculation across the whole range of WDM.
The equation of state for $r_s = 0.8137 \ldots 1.4$ corresponding to densities in the range of $5.0 \ldots 0.98$ g/cm^3 are compared in Figs. 4.3.2(a)-4.3.2(c). Overall, the agreement between LDA-BOMD of different sources and PIMC is reasonable. The PZ/GDSMFB results are consistently closest to PIMC of all DFT-MD data at the highest temperatures. However, the re-

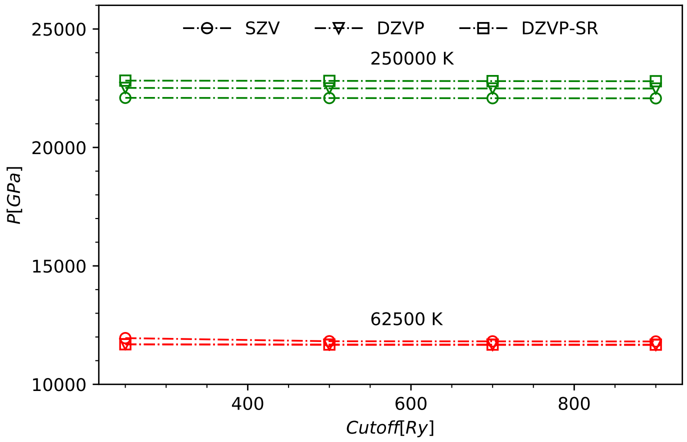

Figure 4.3.1: The convergence of pressure with respect to the plane wave energy cutoff and basis sets [single-zeta valence (SZV), double-zeta valence polarization (DZVP), double-zeta valence polarization short-range (DZVP-SR)] at 62500 K and 250000 K for $r_s = 0.8137$. Reprinted figure with permission from **K. Ramakrishna** *et al.*, Phys. Rev. B **101**, 195129 (2020). Copyright 2020 by the American Physical Society.

sults deviate from the data by Wang *et. al* [Wang and Zhang, 2013] at lower temperatures for $r_s = 0.8137$ shown in Fig. 4.3.2(a). At high densities and temperatures, the computational cost of the mixed Gaussian plane wave method increases hence the choice of N=32 for all of the simulations shown in this section. Also, the k-point sampling is performed only at the Gamma-point. The resulting finite-size effects have been demonstrated for lower temperatures at $r_s = 3.0$, where the obtained pressures are higher for smaller system sizes. Wang *et al.* [Wang and Zhang, 2013] use a system size ranging from 8–512 atoms sampled at the gamma-point with the KS DFT simulations restricted to $T < T_F$ for $\rho > 0.5$ g/cm^3. The finite-size effects do not necessarily constitute a problem, as the focus is on the pressure differences due to the use of the GDSMFB functional instead of PZ. For this difference, finite size effects are expected to cancel as has been reported for *ab-initio* PIMC calculations of the static local field correction [Dornheim et al., 2019, Groth et al., 2017a].

Thus, the relative difference in the total pressure calculated using

$$\frac{(P_{PZ} - P_{GDSMFB})}{P_{PZ}} \times 100\%. \tag{4.3.1}$$

shown in the inset plots in Fig. 4.3.2 is in good agreement with the KS DFT and orbital-free DFT results obtained by Karasiev *et al.* [Karasiev et al., 2016]. Danel *et al.* [Danel et al., 2016] estimated the temperature dependence in the XC functional based on a local density approximation, using an expression for the excess free energy by Ichimaru *et al.* [Ichimaru et al., 1987]. The electronic pressure variation with respect to temperature and density is shown in Fig. 4.3.3, obtained by subtracting the ideal ion pressure from the total pressure. A similar procedure is also used by Karasiev *et al.* [Karasiev et al., 2016]. The ionic excess pressure as can be obtained for instance by integrating over the pair correlation function, has not been subtracted [Kremp et al., 2006]. While density decreases, the relative difference in electronic pres-

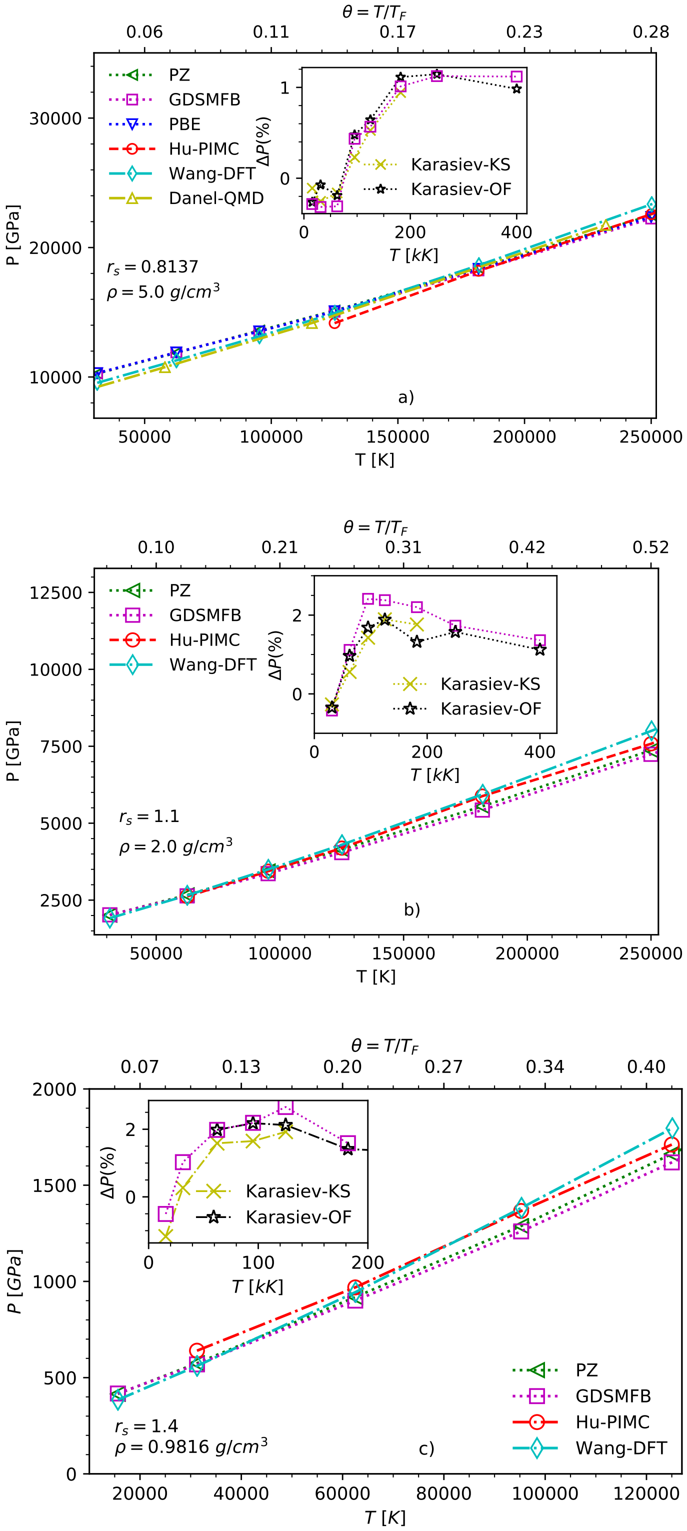

Figure 4.3.2: EOS at a) $r_s = 0.8137$, b) $r_s = 1.1$, c) $r_s = 1.4$. The previously obtained results using PIMC and DFT are also shown for comparison. The inset plot shows the relative difference (Eq. 4.3.1) in total pressure for the finite-temperature case with respect to the LDA case. Hu Ref. [Hu et al., 2011]; Wang (LDA) Ref. [Wang and Zhang, 2013]; Danel (LDA) Ref. [Danel et al., 2016]; Karasiev Ref. [Karasiev et al., 2016]. Reprinted figure with permission from **K. Ramakrishna** *et al.*, Phys. Rev. B **101**, 195129 (2020). Copyright 2020 by the American Physical Society.

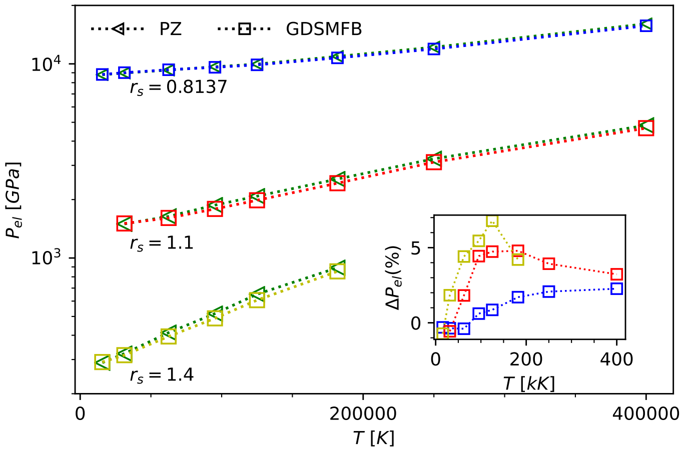

Figure 4.3.3: The electronic pressure as a function of temperature at various densities. The inset plot shows the relative difference (Eq. 4.3.1) in electronic pressure for the finite-temperature (GDSMFB) case with respect to the LDA (PZ) case. Reprinted figure with permission from **K. Ramakrishna** *et al.*, Phys. Rev. B **101**, 195129 (2020). Copyright 2020 by the American Physical Society.

sure at a fixed temperature increases as the temperature effects on the electronic correlations are more prominent as the Fermi temperature decreases with density. As the density decreases from $r_s = 0.8137$ to $r_s = 1.4$, at 125000 K, θ changes from 0.14 to 0.42 and a large deviation in the electronic pressure is noted. At $r_s = 0.8137$, notable deviations in the electronic pressure begin to appear at temperatures above 400000 K which, however, is beyond the scope of this work based on KS DFT.

Summarizing, the new simulation results further corroborate the observations by Karasiev *et al.* [Karasiev et al., 2016], and stress the importance of finite-temperature XC effects for DFT simulations in the WDM regime.

4.4 Moderately Coupled Plasma and Electron Liquid Regime

With increasing r_s (i.e., decreasing density), electronic correlations become more important and the system will eventually form an electron liquid [Giuliani and Vignale, 2005, Ichimaru and Utsumi, 1981, Utsumi and Ichimaru, 1981, Dornheim et al., 2018b, Groth et al., 2019, Dornheim et al., 2020b] for $r_s \gtrsim 10$. A natural realization of the 2D electron liquid is given by the localization of the electrons at the surface of elemental metals [Tamm, 1932]. In metals, 3D electron liquids can be found if the Fermi surface of the conducting electrons is spherical to facilitate the movement of electrons as free particles [Tamm, 1932, Giuliani and Vignale, 2005]. Controlling the amount of dopants in semiconductors also facilitates it. Although these exotic conditions are rather difficult to realize experimentally at present, they offer the valuable opportunity to study the nontrivial interplay of temperature and Coulomb coupling ($\Gamma = 1/(ak_BT)$) with quantum diffraction and exchange effects. The emergence of a collective excitonic mode for large r_s based on ground-state many-body theory was predicted by Takada [Takada, 2016],

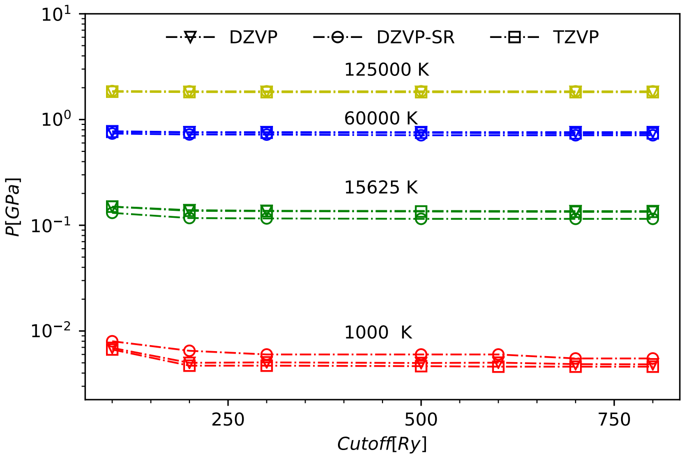

Figure 4.4.1: The convergence of pressure with respect to the plane wave energy cutoff and basis sets at various temperatures for $r_s = 14.0$. Reprinted figure with permission from **K. Ramakrishna** *et al.*, Phys. Rev. B **101**, 195129 (2020). Copyright 2020 by the American Physical Society.

which was recently substantiated by more accurate *ab-initio* PIMC calculations at finite-temperature [Dornheim et al., 2018b, Groth et al., 2019]. An exciting opportunity for future research is the possibility of an experimental detection of the associated negative dispersion relation of the dynamic structure factor [Dornheim et al., 2018b].

The thermal XC effects are more pronounced even at low temperatures for lower densities. The energy cutoff for $r_s = 14.0$ using various basis sets with PZ exchange correlation for 32 atoms at four different temperatures is shown in Fig. 4.4.1. A cutoff of 500 Ry and above ensures the convergence in pressure calculations. At high temperatures, the differences between the basis sets reduce irrespective of the energy cutoff. At low temperatures, triple-zeta valence polarization (TZVP) basis set fares marginally well with respect to DZVP, but is computationally expensive. The choice of DZVP basis set with the energy cutoff and other parameters discussed in section 4.1 is also justified at far lower densities.

The EOS for $r_s = 2.0 \ldots 14$ corresponding to densities in the range $9.8 \times 10^{-4} \ldots 0.34$ g/cm^3 is shown in Fig. 4.4.2(a). The system size is N=256 except at $r_s \geq 10$ where the system size is reduced to N=32 due to the large simulation box required at these low densities. The *k*-point sampling is performed only at the gamma-point. The EOS using PZ/GDSMFB fits well with the PIMC and DFT-MD data of Hu *et al.* and Wang *et al.*, respectively across a gamut of temperatures for the densities considered [Hu et al., 2011, Wang and Zhang, 2013]. The relative difference in total pressure between PZ and GDSMFB is shown in Fig. 4.4.2(b).

At intermediate temperatures, ΔP exhibits a sign change, which is shifted to larger temperatures for increasing density. This is again a consequence of the r_s dependence of the reduced temperature θ, which decreases with r_s. Such a sign change has been reported for the pressure in previous DFT calculations [Karasiev et al., 2012, Sjostrom and Daligault, 2014, Karasiev et al., 2016]. A similar behaviour was found in QMC calculations for the XC part of the kinetic energy of the UEG [Militzer and Pollock, 2002].

The relative difference in pressure is more pronounced in the range $r_s = 5.0 \ldots 10.0$, with

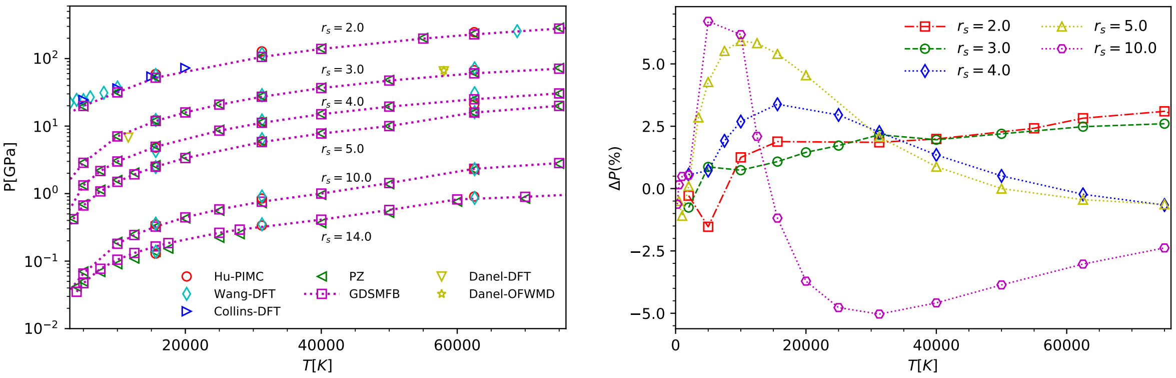

(a) (b)

Figure 4.4.2: a) EOS at $r_s = 2.0 - 14.0$. The previously obtained results using PIMC and DFT are also shown in comparison, b) Relative difference (Eq. 4.3.1) in total pressure for the finite-temperature case with respect to LDA at $r_s = 2.0 - 10.0$. Hu Ref. [Hu et al., 2011]; Wang Ref. [Wang and Zhang, 2013]; Collins Ref. [Collins et al., 2001]; Danel Ref. [Danel et al., 2016]. Reprinted figure with permission from **K. Ramakrishna** *et al.*, Phys. Rev. B **101**, 195129 (2020). Copyright 2020 by the American Physical Society.

positive differences at low temperatures and negative differences at higher temperatures being of a similar magnitude. The maximum changes for $r_s = 10.0$ are observed in a broad range of reduced temperatures of $\theta = 0.6 - 6.0$. For comparison, we mention that the positive maximum deviation for $r_s = 5.0$ is found for $\theta = 0.3 - 0.7$, whereas the negative maximum deviation extends to temperatures beyond the depicted range. At moderately coupled regime $r_s = 2.0 \ldots 3.0$, the onset of the significant changes begin near the maximum of the temperature considered in Fig. 4.4.2(b). This can be observed in Fig. 4.4.3(a), where the temperature is held constant and the relative difference in total pressure is evaluated with the change in density and the electron degeneracy. The positive pressure difference is maximal for the density range $r_s = 2.0 \ldots 3.0$ in the vicinity of $\theta \sim 1$ and $\Gamma \sim 2$. In order to achieve pressure/energy convergence for very low densities, e.g., $r_s = 14.0$, the plane wave energy cutoff needs to be increased up to 800 Ry. Then, agreement with Hu *et al.* and Wang *et al.*, respectively, across a range of temperatures is found[Hu et al., 2011, Wang and Zhang, 2013]. Due to the large simulation box, the sampling is performed only at the gamma-point for a system size set to N=32. As before, finite size effects should be unimportant as the interest is in the relative differences in total pressure.

The relative difference in total pressure across a wide range of temperature at $r_s = 14.0$ is shown in Fig. 4.4.3(b). The maximum relative differences can be seen at the reduced temperatures $\theta = 1.18$ and $\theta = 5.90$, respectively. These deviations exceed 20% and, thus, are even more pronounced than for the previously considered WDM regime.

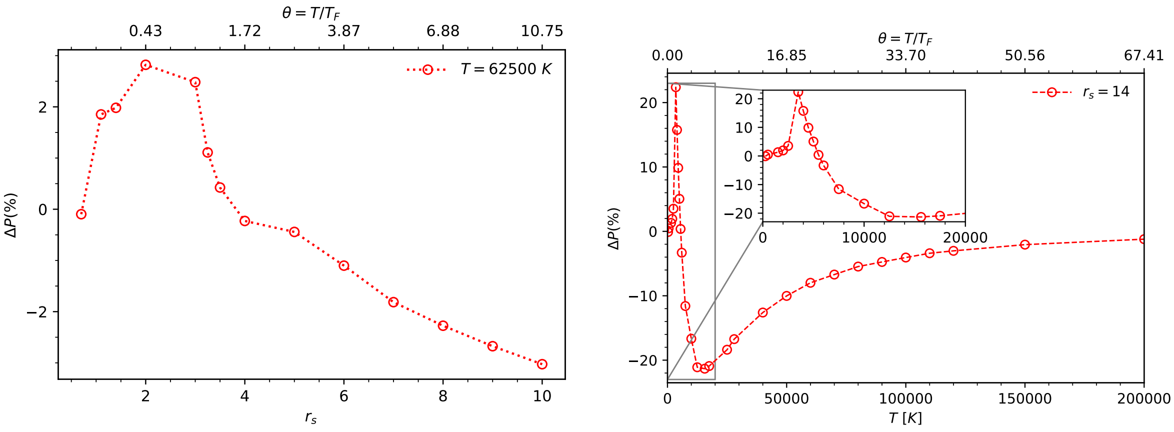

(a) (b)

Figure 4.4.3: a) Relative difference (Eq. 4.3.1) in total pressure for the finite-temperature case with respect to LDA with the change in density ($\leftarrow r_s$) and electron degeneracy at T=62500 K, b) Relative difference in total pressure for the finite-temperature case with respect to LDA at $r_s = 14$. Reprinted figure with permission from **K. Ramakrishna** *et al.*, Phys. Rev. B **101**, 195129 (2020). Copyright 2020 by the American Physical Society.

4.5 Density of States

The density of states (DOS) is computed for $r_s = 2.0$ simulating N=256 atoms sampled at the gamma-point using Eq. (3.1.2). A set of 5 independent equilibrated configurations from different simulation runs are averaged to obtain the corresponding DOS. In Figs. 4.5.1(a)-4.5.1(d), the DOS is shown for a range of temperatures and compared to the ground-state GGA calculations by Collins *et al.* [Collins et al., 2001]. At T=2000 K, the system is still insulating with a band gap shown in Fig. 4.5.1(a) while the results from Collins *et al.* show a slight increase in the DOS near the Fermi level. At a slightly higher temperature of T=5000 K, the system is metallic and our results match the trend obtained by Collins *et al.* Between T=2000 K and T=5000 K, the DOS is hardly influenced by finite-temperature XC effects as the reduced temperature is still low. At T=15625 K ($\theta = 0.107$), the results follow the trend seen by Collins *et al.*, with the $\sqrt{E}$ feature of the 3D electron gas clearly visible at 62500 K ($\theta = 0.43$). Noticeable differences between the DOS computed with the PZ (T=0) functional and the GDSMFB finite-temperature functional start to appear at these two temperatures, which are still below the regime where the maximum change in finite-temperature XC effects can be observed.

4.6 Electronic Density

Figure 4.6.1(a)-4.6.1(b) shows snapshots of an electronic density isosurface computed using PZ and GDSMFB for $r_s = 2.0$, T=62500 K (i.e., $\theta = 0.43$, which is located in the WDM regime) and for the same ionic configuration. The snapshot has been obtained by performing DFT-MD simulations with the PZ functional until the system equilibrated and a random ionic configuration is chosen, which is subsequently used to compute the density with the different XC

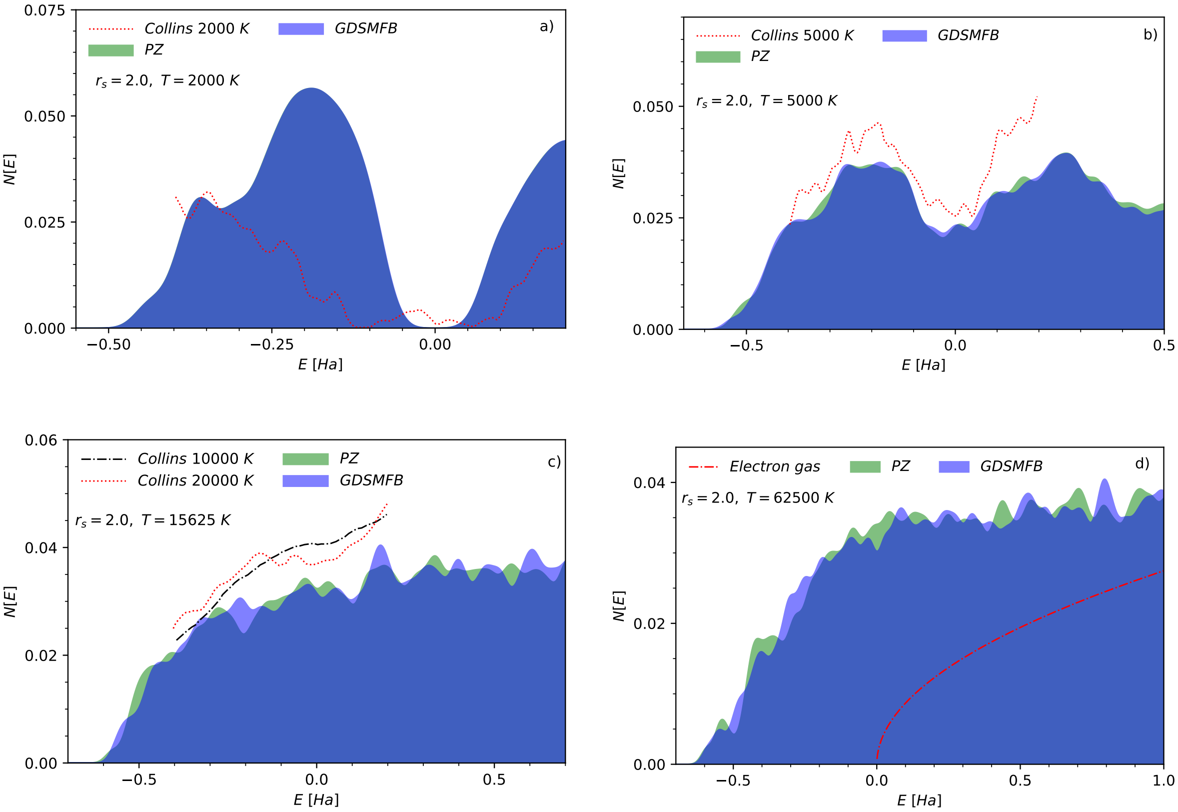

Figure 4.5.1: The density of states at $r_s = 2.0$ and a) T=2000 K, b) T=5000 K, c) T=15625 K, and d) T=62500 K using LDA and the finite-temperature case. The Fermi energy is set to zero. The green and the blue areas represent DOS calculated using PZ and GDSMFB respectively. The overlap between them is indicated by the dark blue area. The density of states for a 3D electron gas is shown only at T=62500 K. Collins Ref. [Collins et al., 2001]. Reprinted figure with permission from **K. Ramakrishna** *et al.*, Phys. Rev. B **101**, 195129 (2020). Copyright 2020 by the American Physical Society.

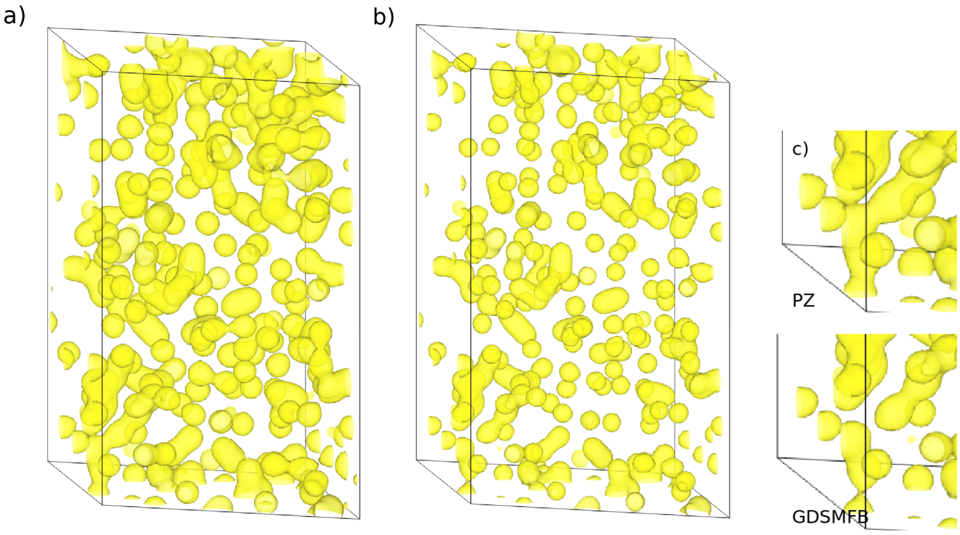

Figure 4.6.1: Snapshot of an electronic density isosurface for $r_s = 2.0$, T=62500 K ($\theta = 0.43$) using a) PZ and b) GDSMFB for the same ionic configuration with N=256. Panel c) shows magnified insets for PZ (top) and GDSMFB (bottom) for the bottom left corner of the respective simulation cells. Reprinted figure with permission from **K. Ramakrishna** *et al*., Phys. Rev. B **101**, 195129 (2020). Copyright 2020 by the American Physical Society.

functionals. A large system size of N=256 sampled at the gamma-point in an hexagonal super cell ensures the convergence at high densities. The visualization of the results are generated using VESTA [Momma and Izumi, 2011].

The two panel snapshots a) and b) from Fig. 4.6.1 has a similar structure, with the electronic isosurfaces centered around the ions. Still, distinct systematic differences exist, which can be seen especially well in Fig. Fig. 4.6.1(c) displaying a magnified section around the bottom left corner of the simulation cell. Using the PZ functional (top), there tends to be a substantial overlap between the electronic orbitals around individual atoms; on the other hand, the GDSMFB functional (bottom) results in a slightly reduced overlap. The thermal wavelength $\lambda \sim 1/\sqrt{T}$ decreases with increasing temperature, and thus the electronic orbitals are less extensive. Ultimately this leads to convergence in the high temperature limit of standard point-like particles. This phenomenon can not be reliably captured by the PZ functional, which was built strictly on the basis of ground state data for the uniform electron gas and the extension of the electronic isosurfaces is significantly overestimated.

Fig. 4.6.2 shows snapshots of an electronic density isosurface computed using PZ and GDSMFB for $r_s = 2.0$, T=15625 K ($\theta = 0.107$) and for the same ionic configuration. The influence of finite temperature XC results in a change of 2% in the total pressure but there appears to be negligible impact on the electronic density.

The inclusion of finite-temperature XC effects in a thermal DFT simulation of a warm dense matter system is critical to capturing the related physics, although the impact may be comparatively low on average quantities such as total or electronic pressure (3%, refer Fig. 4.4.3). For example, local electronic density fluctuations are important for the measurement of response functions and hence the prediction of structure factors as measured, e.g. through x-ray scattering [Falk, 2018, Graziani et al., 2014].

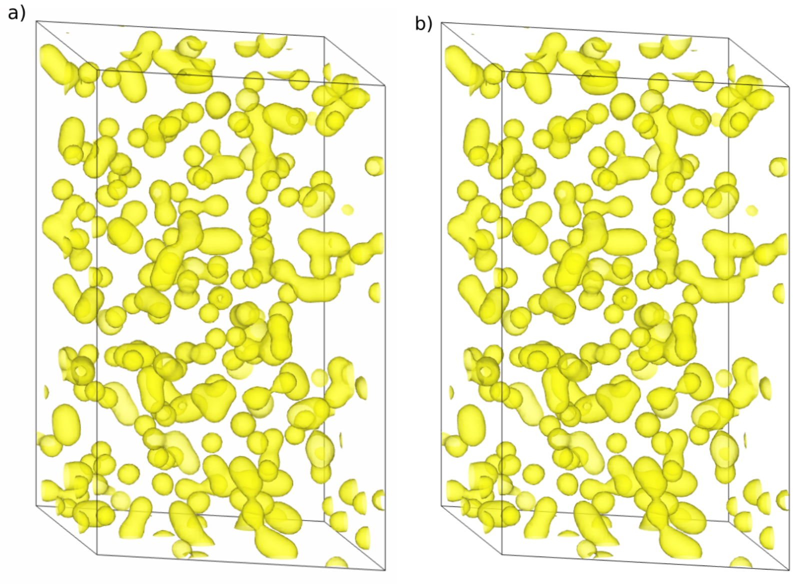

Figure 4.6.2: Snapshot of an electronic density isosurface for $r_s = 2.0$, T=15625 K ($\theta = 0.107$) using a) PZ and b) GDSMFB for the same ionic configuration with N=256.

4.7 Conclusions

In summary, the impact of finite-temperature XC effects on the results of DFT simulations of hydrogen over a vast range of conditions has been studied in detail. More specifically, extensive DFT calculations have been carried out using the ground-state functional by Perdew and Zunger (PZ) [Perdew and Zunger, 1981] and the finite temperature analogue GDSMFB [Groth et al., 2017c]. This allows to unambiguously quantify the impact of finite-temperature XC for different quantities and in different physical regimes for hydrogen.

The electronic temperature effects do not play a significant role for the description of the LLPT, as the reduced temperature is small, $\theta \lesssim 0.01$. An improved agreement between simulation and experiments will most likely require to further ascend Jacob's ladder of XC functionals [Perdew and Schmidt, 2001], but in the ground state. In the warm dense matter regime, temperature-effects in the XC functional become more important, the deviations in the electronic pressure clearly exceeding 5%. These deviations are non monotonous with respect to temperature, and a sign change is found in the pressure difference, which is shifted to larger temperatures with increasing density. The further development of XC functionals to consistently take into account thermal excitations is of central importance to achieve predictive capability for DFT calculations in the WDM regime.

In addition, the finite-temperature DFT results for hydrogen in the electron liquid regime have been presented. At these conditions, electronic XC effects are even more important for an accurate description, and, consequently, the temperature-dependence of the XC functional is crucial. The pressure differences between the PZ and GDSMFB functionals is seen to be exceeding 20% at $r_s = 14.0$ in the vicinity of the Fermi temperature. This could be of high importance for the future investigation of interesting phenomena such as the possible emergence of an incipient excitonic mode, which might occur at even lower densities [Takada, 2016].

Finally, other physical properties of hydrogen like the density of states, and the electronic density in coordinate space have been considered. Regarding the DOS, the finite-temperature XC effects do indeed significantly influence the DFT results in the WDM regime, as it is expected. The simulation results for the electronic isosurfaces in coordinate space are even more remarkable, as the PZ XC functional is not capable to describe the reduction of electronic overlap at finite temperature.

Possible topics for future research include the consideration of other materials and mixtures such as helium, hydrogen-helium, carbon-hydrogen and the investigation of transport properties like the electrical conductivity and the diffusion coefficient for hydrogen in warm dense matter regime.

5 Ab Initio Modeling of Plasmons in Aluminum under Ambient and Extreme Conditions

Results of this chapter are published in
T. Dornheim et al.,
Phys. Rev. Lett. ***125****, 235001 (2020)*
K. Ramakrishna et al.,
Phys. Rev. B ***103****, 125118 (2021)*

A coherent framework for modeling the properties of plasmons in the matter in the spectrum from ambient to warm dense conditions is of vital importance for both improving our fundamental understanding of extreme states of matter and facilitating the diagnosis of scattering experiments. While the properties of plasmons with standard techniques of solid-state physics are well comprehended from an experimental and theoretical perspective under ambient conditions, capturing them both in experiment and theory becomes challenging under warm dense conditions. Because both classical and quantum effects in the warm dense matter system have to be considered into account, well-established methods of plasma physics and condensed-matter physics break down. Therefore, understanding plasmons under warm dense conditions is based on an interplay of theory and experiment.

Plasmons provide information on the collective excitations of the material in the form of longitudinal oscillations. Such measurements can be carried out using various techniques such as x-ray Thomson scattering (XRTS) [Glenzer and Redmer, 2009, Glenzer et al., 2007], electron energy-loss spectroscopy (EELS) [Egerton, 2008] or inelastic x-ray scattering (IXS) at synchrotrons [Mao et al., 2001]. Diamond anvil cells or (laser generated) shocks can produce high pressures. The combination of high power lasers and powerful x-ray sources creates pressures on the order of a few Megabar and temperatures up to a few electronvolts enabling one to study astrophysical phenomena under laboratory conditions [Bostedt et al., 2016, Tschentscher et al., 2017, Falk, 2018]. This allows one to access the dynamic structure factor (DSF) via XRTS [Glenzer and Redmer, 2009]. By fitting the XRTS signal to the theoretical DSF models, important plasma parameters such as density and temperature are then determined. Local field corrections, possibly with additional collision frequencies within an extended Mermin approach [Fortmann et al., 2010], as been a tool for quick computational evaluation of the DSF for the plasma parameters. More accurate modeling techniques such as the Kubo-Greenwood formalism (KG) [Kubo, 1957, Greenwood, 1958] based on DFT-MD simulations or TDDFT capture electron-ion correlations at a more rigorous level but are significantly expensive computationally [Plagemann et al., 2012, Baczewski et al., 2016, Magyar et al., 2016, Witte et al., 2017a, Witte et al., 2018, Ramakrishna and Vorberger, 2019, Ramakrishna et al., 2021, Mo et al., 2020].

In this chapter, an assessment of several state-of-the-art modeling techniques to predict plasmon properties, both under ambient and warm dense conditions is made. Examples are given for properties such as dynamic structure factor, plasmon dispersion and plasmon width and compared to measurements on aluminum accessible via XRTS for different dispersion angles and sample conditions. The numerical modeling techniques tested include dielectric models based on static local field corrections (LFC) obtained using path integral Monte Carlo (PIMC) data for the uniform electron gas (UEG) at ground state [Corradini et al., 1998] and finite temperature [Dornheim et al., 2019, Dornheim et al., 2020a]. They also include linear response time-dependent density functional theory (TDDFT) as well as adiabatic exchange-correlation approximations (ALDA).

5.1 Computational Details

The linear response calculations involving random phase approximation (TDDFT-RPA)[1], local field corrections (TDDFT-LFC) and time-dependent density functional theory (TDDFT-XC) computations are performed using a full-potential linearised augmented-plane wave code implemented in the *elk* code [Dewhurst, 2021] for ambient conditions. The TDDFT calculations are performed using the adiabatic local density approximation (ALDA) for the f_{XC} kernel. The TDDFT-RPA calculations are performed by setting the exchange-correlation kernel $f_{XC} \to 0$ in the density response function

$$\chi^{GG'}(q,\omega) = \frac{\chi_S^{GG'}(q,\omega)}{1 - [V(q) + f_{XC}(q,\omega)]\chi_S^{GG'}(q,\omega)}. \tag{5.1.1}$$

Here $\chi_S^{GG'}$ refers to the free density response function computed using the single particle KS states using Eq. (2.4.10) [Marques and Gross, 2004]. $V(q) = 4\pi\delta(G - G')/(|(G+q)(G'+q)|)$ is the Coulomb potential with G, G' being the reciprocal lattice vectors. The DSF is computed given by the macroscopic response functions which are obtained using $\chi(q,\omega)$ by setting $G = 0,\ G' = 0$. By default, Adler-Wiser local field effects [Adler, 1962, Wiser, 1963] for ideal lattice conditions are used. The correlation between the electrons beyond the mean field level are represented by the XC kernel defined as

$$f_{XC}(q,\omega) = \chi_S^{-1}(q,\omega) - \chi^{-1}(q,\omega) - V(q), \tag{5.1.2}$$

related to the XC potential V_{XC} via $f_{XC}(q,\omega) = \delta V_{XC}(q,\omega)/\delta n(q,\omega)$ and to the local field corrections of dielectric models via $f_{XC}(q,\omega) = -V(q)G(q,\omega)$, where $V(q) = 4\pi/q^2$.

The local field corrections (TDDFT-LFC) in this work are incorporated by setting the term f_{XC} in the expression for the density response function in Eq. (5.1.2) to Eq. (2.1.31) [Corradini et al., 1998]. Due to the static limit of the local field corrections, the correction term is substituted in Eq. (5.1.2) as $f_{XC} = G(q, r_s)$ at ground state and as $f_{XC} = G(q, r_s, \theta)$ at finite-temperature where $\theta = K_B T/E_F$ is the degeneracy parameter.

The DFT calculations for ambient conditions (T=300 K) are performed using the *elk* code [Dewhurst, 2021] on a 40×40×40 k-point mesh on 80 bands with Perdew-Zunger XC functional [Perdew and Zunger, 1981]. The electronic smearing is of Fermi-Dirac type and set to 0.01 Ha. Fig. 5.1.1 shows the influence of the XC functional (PZ/PBE) in the evaluation of dynamic structure factor using TDDFT. LDA and PBE give very similar results hence LDA (PZ) XC functional is considered in the calculations.

---

[1] Due to the many approximations involved, it is careful to note the distinction between TDDFT-RPA and RPA in the following sections. Without the TDDFT prefix, RPA generically refers to response functions calculated using model dielectric functions. With the TDDFT prefix it refers to LR-TDDFT calculations in which $G(q) = f_{XC} = 0$. Similarly, this distinction also applies to the response functions involving local field correction: TDDFT-LFC and RPA-LFC where $G(q) = f_{XC}$=CDOP [Corradini et al., 1998].

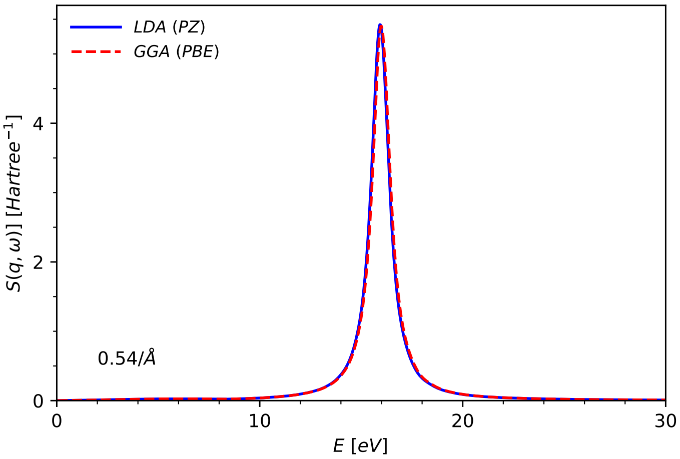

Figure 5.1.1: Dynamic structure factor evaluated using TDDFT (f_{XC}=ALDA) for aluminum in atomic units under ambient conditions at 0.54 Å^{-1} using PZ and PBE XC functionals.

Simulations involving large system sizes at high temperatures and pressures are computationally expensive using a full-potential linearised augmented-plane wave hence VASP [Kresse and Hafner, 1993, Kresse and Joubert, 1999, Kresse and Furthmüller, 1996b, Kresse and Furthmüller, 1996a] is used to perform density functional molecular dynamics (DFT-MD) to obtain the equilibrated ionic configurations used for the calculation of the response function using TDDFT. PAW pseudopotentials [Blöchl, 1994] with three electrons considered valence and a core radius of $r_c = 1.7$ a_B are used throughout. The plane wave cutoff was set to 350 eV and the convergence in each self-consistency cycle was set to 10^{-5}. The Mermin formulation [Mermin, 1965] of thermal density functional theory and Fermi occupation of the eigenvalues is considered. The first Brillouin zone was sampled on a 2×2×2 grid of *k*-points. The number of bands varied with the temperature up to 1050 for the highest electron temperature of T=12 eV for an N=32 supercell. LDA as well as PBE are considered for the exchange correlation. The thermostat in the NVT ensemble was of Nose-Hoover type [Nosé, 1984b, Hoover, 1985]. Ionic time steps of $\Delta t = 0.2$ fs were taken.

The TDDFT calculations at extreme conditions are performed for large system sizes using yambo [Marini et al., 2009] package with the KS wavefunctions generated from Quantum ESPRESSO [Giannozzi et al., 2009, Giannozzi et al., 2017]. The KS wavefunctions as input to yambo [Marini et al., 2009] are generated for a supercell containing 32 aluminum atoms using the Quantum ESPRESSO electronic structure code [Giannozzi et al., 2009, Giannozzi et al., 2017]. The LDA norm-conserving pseuopotentials generated with the OPIUM package [opi, 2018] are adopted for the TDDFT calculations. 11 valence electrons are considered for the psuedopotential, while the $1s^2$ core is ignored. The plane-wave cutoff to represent the KS wave functions is set to 70 Ry. Electronic occupations are generated using a Methfessel-Paxton smearing [Methfessel and Paxton, 1989] where the number of bands at an electronic temperature of 12 eV is set to 1050. The Brillouin zone was sampled using 3×3×3 Monkhorst-Pack mesh throughout.

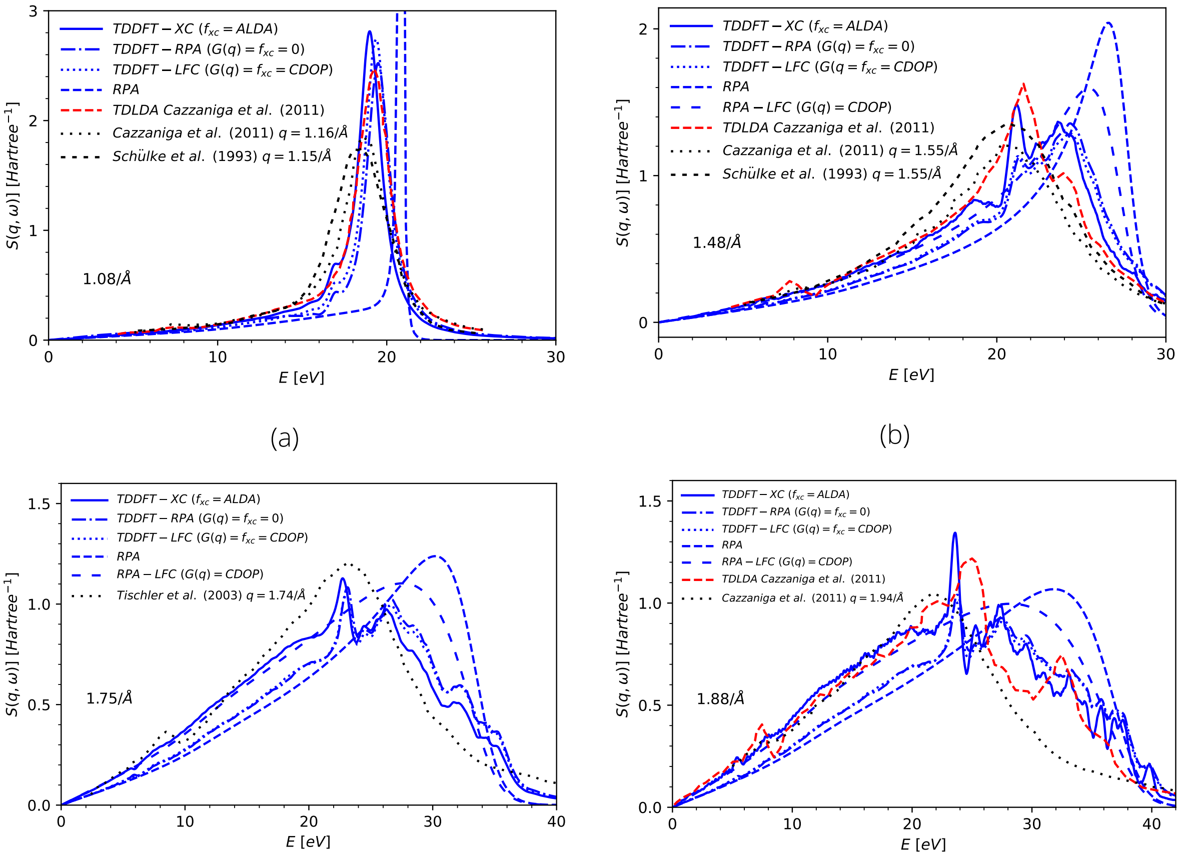

(a)

(b)

(c)

(d)

Figure 5.2.1: Dynamic structure factor for aluminum ($r_s = 2.07$, $\rho = 2.7$ g/cm^3) in atomic units under ambient conditions at a) $q = 1.08$/Å, b) $q = 1.48$/Å, c) $q = 1.75$/Å, d) $q = 1.88$/Å. Experimental data in black stems from Ref. [Cazzaniga et al., 2011, Schülke et al., 1993, Tischler et al., 2003]. Theoretical data in red stems from Ref. [Cazzaniga et al., 2011]. TDDFT-RPA/TDDFT-XC/LFC/RPA/RPA-LFC results of this work are shown in blue. Reprinted figure with permission from **K. Ramakrishna** *et al.*, Phys. Rev. B **103**, 125118 (2021). Copyright 2021 by the American Physical Society.

5.2 Ambient Conditions

Solid aluminum under ambient conditions has the space group $Fm\bar{3}m$ in the cubic face centered phase (FCC) with lattice constant 4.05 Å and density 2.7 g/cm^3. With a Wigner-Seitz radius of 2.07 atomic units and a density of states similar to the free electron gas, the RPA should be able to adequately explain plasmon dispersion [Ashcroft and Mermin, 1976].

5.2.1 Dynamic Structure Factor

In Fig. 5.2.1(a)-(d), the dynamic structure factor at ambient conditions for a range of wavenumbers is shown. The calculations are shown here in comparison to the nearest set of q-vectors available from the literature.

The discussion starts with panel a) at a wavenumber 1.08/Å for which the system is clearly dominated by collective effects, and the sharp plasmon carries bulk of the spectral weight. The peak of the free electron RPA result is roughly 2 eV above both experiments and all of the TDDFT calculations. That the TDDFT-RPA result gives a plasmon peak that is more consistent with these results suggests that deviations from a free electron model due to the lattice are a critical feature of the density response. In fact, the TDDFT-XC and TDDFT-LFC results both agree well with TDDFT-RPA, suggesting that XC effects and LFCs do not matter as much as capturing deviations from the dielectric model due to band structure effects at this value of $\vec{q}$. These results stem from the same initial set of KS orbitals and thus capture the deviations from a free electron model in the same way.

Surprisingly, TDDFT-XC calculations by Cazzaniga *et al.* [Cazzaniga et al., 2011] yielded an identical peak location, but a rather smaller peak height. This means that in the energy range of the plasmon, imaginary part of the response function by Cazzaniga *et al.* is about 10% larger than the TDDFT calculations obtained here. The main difference between these results and those of Cazzaniga *et al.* is that here the results are obtained using an all-electron code and Cazzaniga *et al.* use a norm-conserving pseudopotential.

The shape and location of the experimentally determined plasmon peaks for this wavenumber are even more dissimilar. The two different experimental results are in good agreement with each other [Cazzaniga et al., 2011, Schülke et al., 1993]. However, they are another factor of 1.5 smaller than Cazzaniga's and therefore only 60% as high as our results. Its location is lower by another eV. The differences become considerably more evident when the wavenumbers under consideration are not identical.

There are several plausible explanations for the discrepancy between experiment and theory. Cazzaniga *et al.* noted that the use of an adiabatic XC kernel might be one, and they report an improvement in the agreement from GW calculations by incorporating lifetimes. However, even this method does not give good agreement between experiment for all wavenumbers and theory. A non-local dynamical kernel as suggested by Panholzer *et al.* might give improvements [Panholzer et al., 2018]. However, there is also always the possibility that the KS orbitals and therefore the XC functional are not good enough when they are to be used to calculate the KS response function. Increasing the wavenumber of the perturbation as shown in panels b) to d) leads to a broadening of the plasmon peak and finally to a mix of collective and single-particle effects which all contribute to the DSF. As was the case in panel a), the TDDFT peaks occur at lower energies than for the RPA. The influence of the LFC is best visible at large q when compared to the free electron RPA, with lower intensities at the peaks and a shift towards lower energies at small q. In the TDDFT results, the difference between no LFC and different types of LFCs (ALDA or CDOP) is less distinct, still the same trend of redshift remains. The effect of LFCs in aluminum has been determined experimentally by Larson *et al.* [Larson et al., 1996] for q up to 4.37/Å and the experimental results suggest a stronger impact than theoretical LFC predictions for large wavenumbers.

The TDDFT results deviate from the experimental results in Fig. 5.2.1(c)-(d). The TDDFT curves start to show a double peak structure still absent in the experimental curves displayed here, though the maximum intensity is now in better agreement with the theoretical results. The overall peak position in the TDDFT results remains shifted to higher energies as compared

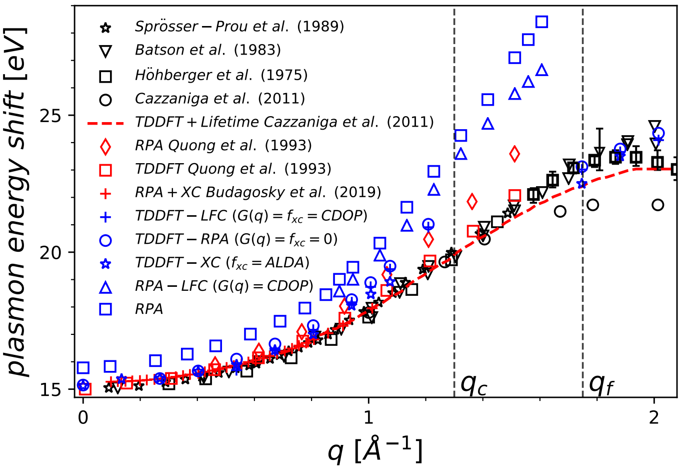

Figure 5.2.2: Aluminum plasmon dispersion under ambient conditions. The critical and the Fermi wavevectors are indicated by the vertical lines. Experimental data in black symbols stems from Ref. [Sprösser-Prou et al., 1989, Batson and Silcox, 1983, Cazzaniga et al., 2011, Höhberger et al., 1975]. Theoretical data shown in red symbols are taken from Ref. [Cazzaniga et al., 2011, Budagosky and Krasovskii, 2019, Lee and Chang, 1994, Quong and Eguiluz, 1993]. TDDFT-RPA/TDDFT-XC/LFC/RPA-LFC/RPA results of this work are indicated with blue symbols. Reprinted figure with permission from **K. Ramakrishna** *et al.*, Phys. Rev. B **103**, 125118 (2021). Copyright 2021 by the American Physical Society.

to the experimental and Cazzaniga's theoretical results. The disagreement is considerably more concerning. when considering the higher number of *k*-points, bands, and the number of explicitly treated electrons that are taken into account as compared to the earlier published results.

Usually, a two peak structure, as it seems to emerge from TDDFT at the higher wavenumbers in Fig. 5.2.1, is associated with plasmon and double plasmon excitations. It is already accounted for by the non-interacting electron-hole bubble along with the band structure and does not need higher order Coulomb correlations to appear. However, it seems that our TDDFT calculations overestimate the double plasmon excitations as in experiments they appear only at larger wavenumbers.

Inclusion of many-body effects, in the form of vertex correction for the irreducible polarizability is found to improve the agreement with the experimental measurements at large q [Fleszar et al., 1995]. The inclusion of a nonlocal and dynamical XC kernel in TDDFT is further shown to improve the DSF in some metals and semiconductors including the double-plasmon excitation [Panholzer et al., 2018, Sternemann et al., 2005, Huotari et al., 2008, Petri et al., 1976]. Sturm *et al.* [Sturm and Gusarov, 2000, Pandey et al., 1974] demonstrated that at large wavenumbers and at higher energies, dynamical correlations in f_{XC} are more important than band structure effects in the description of the DSF.

5.2.2 Plasmon Dispersion

The plasmon dispersion under ambient conditions is shown in Fig. 5.2.2. The plasmon is stable up to the critical wavenumber (q_c) with a quadratic dispersion feature and a flattering feature is observed for $q > q_c$. The wavenumber at which the dispersion merges into the continuum of the single-particle excitations is given by q_c [Pines, 2018b, Ichimaru, 1982]. For very small wavenumbers, in the optical limit, the Landau damping is very small [Landau, 1946] and the decay of the plasmon is mainly due to band structure effects [Ichimaru, 1982]. Electron-electron interactions play a stronger role with increasing wavenumber. For wavenumbers above q_c, a plasmon cannot be defined based on many-particle dielectric theories [Hamann et al., 2020], hence a shift based on the location of the peak of the DSF is given, see Fig. 5.2.1.

For large wavenumbers, the experimental results obtained by Batson [Batson and Silcox, 1983] and Höhberger [Höhberger et al., 1975] *et al.* agree with our results. In this case, one should not speak of a plasmon anymore. The observed feature is better described by a shift of the peak of the DSF that is now dominated by single-particle excitations. The results of Batson [Batson and Silcox, 1983] *et al.* show a flattening in the plasmon dispersion curve only for larger q as shown in 5.2.2.

The inclusion of different LFCs (TDDFT-LFC, CDOP), and XC kernels (TDDFT-XC) results in a lowering of the plasmon shift at intermediate and large wavenumbers. The influence of the TDDFT XC kernel compared to RPA in the lowering of the plasmon shift is also observed in the theoretical results of Quong *et al.* and Cazzaniga *et al.* [Quong and Eguiluz, 1993, Cazzaniga et al., 2011]. Further improvements to the ALDA kernel can be achieved by considering an exact-exchange kernel (EXX) [Marques et al., 2006]. The inclusion of lifetime effects in TDDFT lowers the shift further as shown by Cazzaniga *et al.* [Cazzaniga et al., 2011]. However, the experimental results at large wavenumbers by Cazzaniga *et al.* [Cazzaniga et al., 2011] seem to contradict the results of Sprösser [Sprösser-Prou et al., 1989], Batson [Batson and Silcox, 1983], and Höhberger [Höhberger et al., 1975]. This mainly illustrates the difficulty of extracting peak positions from DSF at large wavenumbers.

5.2.3 Plasmon Lifetimes

The full width at half maximum (FWHM) of the plasmon is shown in Fig. 5.2.3. This quantity reflects the strength of plasmon damping as can be extracted from the Lorentz profile of the weakly damped plasmon at small wavenumbers. It can also be determined by finding the zeros of the complex dielectric function $\varepsilon[q, \omega(q) - i\gamma(q)]$ [Ichimaru, 1982, Hamann et al., 2020] in which the imaginary parts correspond to inverse lifetimes.

As the FWHMs computed using TDDFT depend on the Lorentzian broadening (η), see Eqn. 2.4.10, it is necessary to consider how to extract this quantity consistently. This is done by extrapolating the value of the FWHM for multiple values of η to the $\eta \rightarrow 0$ limit [Li et al., 2017a]. Fig. 5.2.4a) shows the influence of the Lorentzian broadening (η) in the evaluation of the FWHM at $q = 0.54$ Å^{-1} and Fig. 5.2.4b) shows the influence of the Lorentzian broadening in the evaluation of dynamic structure factor using TDDFT.

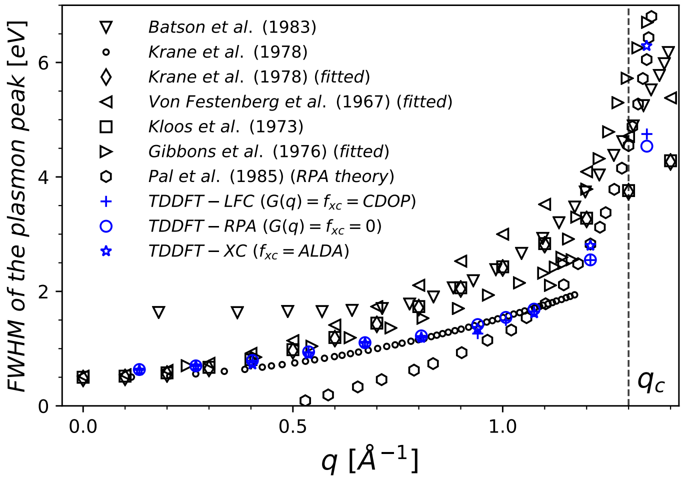

Figure 5.2.3: Aluminum plasmon peak FWHM under ambient conditions. The critical wavevector is indicated by the vertical line. Experimental and theoretical data in black symbols stems from Ref. [Krane, 1978, Batson and Silcox, 1983, Festenberg, 1967, Kloos, 1973, Gibbons et al., 1976, Pal and Tripathy, 1985]. TDDFT-RPA/TDDFT-XC/LFC results of this work are indicated with blue symbols. Reprinted figure with permission from **K. Ramakrishna** *et al.*, Phys. Rev. B **103**, 125118 (2021). Copyright 2021 by the American Physical Society.

The data in Fig. 5.2.3 is shown up to the wavenumbers near q_c where a stable plasmon feature is obtained from $S(q, \omega)$. The width calculated within TDDFT-RPA and TDDFT-XC has a flat feature for $q < 1.0$/Å and then grows rapidly with increasing q which can also be seen in the experimental measurements [Krane, 1978, Kloos, 1973, Batson and Silcox, 1983, Festenberg, 1967]. The inclusion of LFC increases the width for q above q_c and has negligible impact for small q where the width is dominated by the band structure as calculated in the DFT calculations. This is exemplified by the good agreement of TDDFT-RPA and TDDFT-XC for $q < 1.0$/Å. Significant deviations between the two emerge near q_c when the LFC has an increasing impact. However, the deviations between TDDFT-RPA and TDDFT-XC for the plasmon dispersion starts to appear at much smaller wavenumbers.

While our calculated plasmon dispersion curves are in good agreement with the results of Batson *et al.* [Batson and Silcox, 1983], the lifetimes given by Batson deviate from our results. Our plasmon lifetime results are in best agreement with the experimental results of Krane *et al.* [Krane, 1978] and, at small q, with the experimental results of Kloos *et al.* and Von Festenberg *et al.* [Kloos, 1973, Festenberg, 1967].

Any experimental measurement, e.g., via EELS, XRTS, gives a q-dependent scattering signal featuring a plasmon energy shift and a width associated with it. Information on both of these parameters are vital to benchmark (dynamic) LFCs, collision frequencies, and kernels in order to produce accurate TDDFT models. However, most experimental results available to us for ambient aluminum provide either the dispersion or the decay rates with the exception of Batson *et al.* [Batson and Silcox, 1983]. Thus, with the Batson data in its entirety not being consistent with our results and the lack of further consistent plasmon position and FWHM data from experiments, it yields an inconclusive, hence, very unsatisfactory picture. We are not

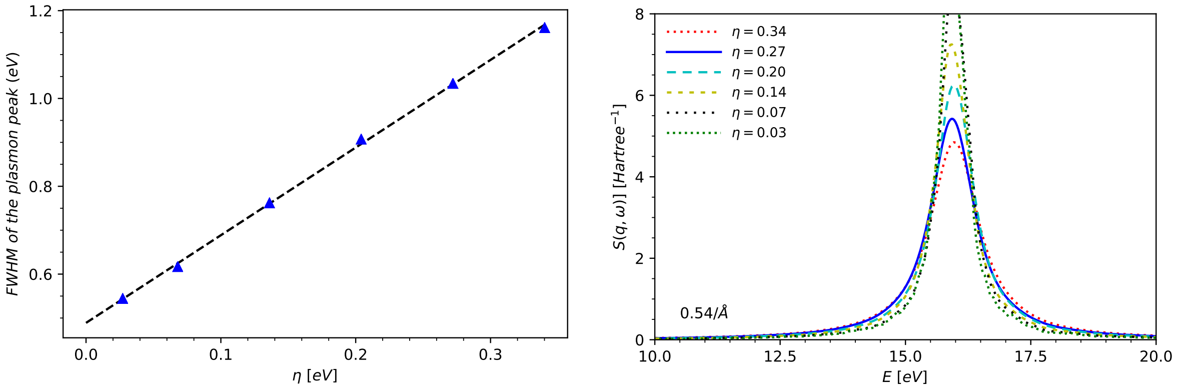

(a) (b)

Figure 5.2.4: a) FWHM of the plasmon peak evaluated using TDDFT (f_{XC}=ALDA) for aluminum under ambient conditions at $q = 0.54$ Å^{-1} for various values of Lorentzian broadening (η), b) Dynamic structure factor evaluated using TDDFT (f_{XC}=ALDA) for aluminum in atomic units under ambient conditions at $q = 0.54$ Å^{-1} for various values of Lorentzian broadening (η) in eV.

able to compare both plasmon position and FWHM of the plasmon peak to other theoretical predictions either due to a lack of data.

5.3 Extreme Conditions

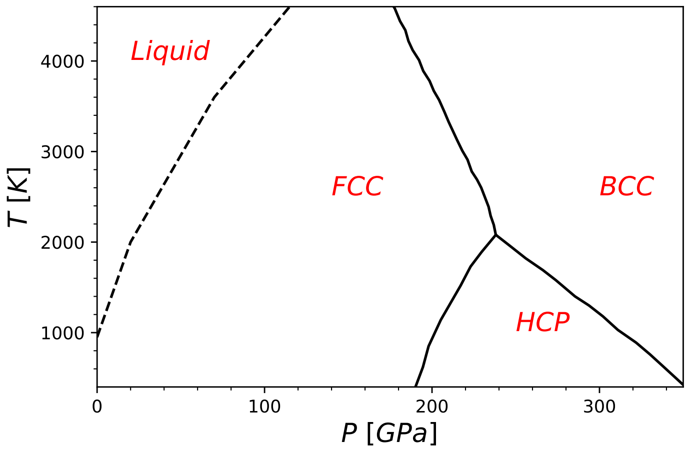

Figure 5.3.1: Phase diagram of aluminum. The melting curve is shown as dashed line. The data is taken from Ref. [Kudasov et al., 2013, Bouchet et al., 2009].

Measurements of the plasmon shift and width at extreme conditions of high-pressure and temperature are quite challenging. Solid aluminum foils can be heated to high temperatures by using isochoric heating with optical or x-ray pulses. The electronic response of WDM can be obtained by combining such a setup with x-ray and optical diagnostics [Sperling et al., 2015]. High-intensity laser pulses can be used to achieve higher densities and, consequently, higher

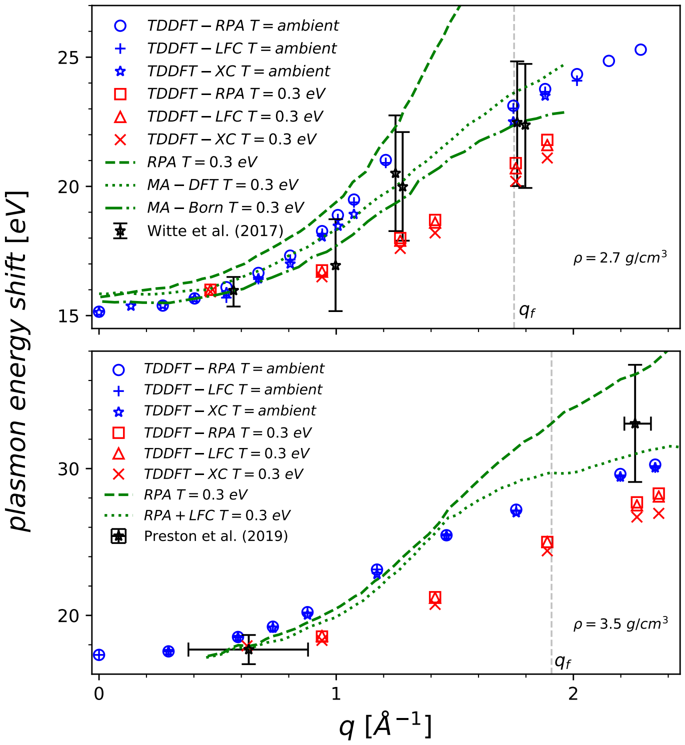

Figure 5.3.2: Aluminum plasmon dispersion under extreme conditions (T=0.3 eV) for densities 2.7 g/cm^3 (uncompressed-top panel) and 3.5 g/cm^3 (compressed-bottom panel). The Fermi wavevector is indicated by the vertical line. Experimental and theoretical data for RPA, MA, RPA+LFC stems from Ref. [Witte et al., 2017a, Preston et al., 2019]. TDDFT-RPA/TDDFT-XC/TDDFT-LFC results of this work are indicated with blue and red symbols. Reprinted figure with permission from **K. Ramakrishna** *et al.*, Phys. Rev. B **103**, 125118 (2021). Copyright 2021 by the American Physical Society.

pressures through isentropic or shock compression [Preston et al., 2019].

The phase diagram of aluminum at megabar pressures based on *ab-initio* calculations is shown in Fig. 5.3.1. The results indicate that with application of pressure, an FCC–HCP transition takes place followed by the transition to the BCC phase [Fiquet et al., 2019]. At very high pressures (>3.2 TPa), aluminum undergoes a transition to an Al16 structure with symmetry I4/mcm [Pickard and Needs, 2010]. The melting curve for aluminum pressure obtained using *ab-initio* molecular dynamics simulations considering N=512 atoms is also shown [Bouchet et al., 2009]. At ambient pressure, the melting of aluminum takes place at ≈1000 K [Boehler and Ross, 1997, Hänström and Lazor, 2000].

5.3.1 Plasmon dispersion

In Fig. 5.3.2, the plasmon dispersion is shown for densities 2.7 g/cm^3 (uncompressed) and 3.5 g/cm^3 (compressed) at ambient temperature and at T=0.3 eV. At these conditions, the temperature should have negligible impact on the plasmon dispersion, because it depends primarily on the electron density when the Fermi energy exceeds the temperature (i.e., for

ρ (g/cm^3)	T (eV)	q (Å^{-1})	LFC	T-LFC
2.7	1.0	3.02	0.79	0.79
2.7	3.0	3.02	0.79	0.79
2.7	6.0	3.02	0.79	0.76
2.7	8.0	1.89	0.33	0.34
2.7	8.0	2.36	0.53	0.51
2.7	8.0	2.83	0.72	0.67
2.7	8.0	3.02	0.79	0.74
2.7	12.0	0.47	0.02	0.02
2.7	12.0	0.94	0.08	0.09
2.7	12.0	1.42	0.19	0.20
2.7	12.0	1.89	0.33	0.34
2.7	12.0	2.36	0.53	0.48
2.7	12.0	2.83	0.72	0.63
3.5	0.3	2.83	0.63	0.63
3.5	0.3	3.02	0.70	0.70

Table 5.3.1: Local field corrections (LFC) and finite-temperature local field corrections (T-LFC) for aluminum at 2.7 and 3.5 g/cm^3 for various temperatures and q-vectors. Reprinted table with permission from **K. Ramakrishna** *et al.*, Phys. Rev. B **103**, 125118 (2021). Copyright 2021 by the American Physical Society.

small θ). However, the quadratic term in Eq. (2.1.24) is generally temperature dependent. The influence of any finite-temperature LFC (T-LFC), $G(q, r_s, \theta)$, can be readily assessed based on the density, temperature and the momentum vector of the system, see Table 5.3.1. Due to extremely small $\theta = 0.02 - 0.025$, temperature effects can be ignored in $G(q, r_s, \theta) \to G(q, r_s)$. To this end, we also perform a comparison with RPA and TDDFT results computed at ambient temperature.

When the static LFC is included, the plasmon dispersion is reduced at large wavenumbers and approaches the results obtained with TDDFT akin to the LFC approximation used for the XC kernel in TDDFT. Within the RPA, we also investigated the effect of treating the electrons within an all-electron formalism rather than a pseudopotential-based formalism. We found that including the core electrons on a system size up to N=32 yields only an insignificant deviation on the shift from those calculated with the use of a pseudopotential, see Fig. 5.3.4 in section 5.3.3.

We compare our data for the uncompressed case at T=0.3 eV with both the experimental measurements (black symbols) and the theoretical plasma physics models (green curves) of Witte *et al.* [Witte et al., 2017a]. For small wavenumbers, all our TDDFT results agree well with the experimental and other curves, which is mainly an indication that the density is correct. At larger wavenumbers, deviations are apparent which are caused by differing temperatures and different levels of approximations. Due to the large error bars, it is not possible to outright discard any theory with the exception of the pure RPA (green dashed). However, it seems that within the TDDFT results, there is no indication of the temperature being as extracted by Witte *et al.* [Witte et al., 2017a]. The T=0.3 eV results (red) seem consistently on the lower end of error bars of the measurements. A better agreement is reached when considering the ions at ideal lattice positions and not in a molten state (blue symbols). This seems reasonable, as the time frame of the measurements is in the 100 fs range and, hence, too short for the onset of any significant ion motion. This highlights the problem of the model-dependent temperature extraction in such experiments [Mo et al., 2018, Mo et al., 2020].

The available data set is restricted to two measurements, i.e., at small and large q for the compressed case. The data agree well with the experimental measurement at small q indicating the density determination seems reasonable. The TDDFT results are much lower than the experimental results at large q due to the strong influence of the ions, which are in a liquid state, at the elevated temperature. Ignoring the ionic temperature (ideal lattice at ambient temperatures), the simulations are in better agreement with the experimental plasmon shift. The transition from a quadratic dispersion to a flat feature can be observed at a smaller q when compared to ambient density (uncompressed). RPA+LFC theory and TDDFT results indicate an increased damping with an increase in density (top versus lower panels in Fig. 5.3.2, but the experimental data remain inconclusive.

In summary, both XRTS measurements are in much better agreement with the ambient data than the results obtained at T = 0.3 eV[Mo et al., 2018]. Thus, temperature measurements via XRTS, if not done via detailed balance, are always model dependent. LR-TDDFT is significantly more capable than any other theory of including electron-electron as well as electron-ion correlations in the computation of collective effects and structure factors when employing suitable XC kernels or LFCs, respectively.

5.3.2 Plasmon Lifetimes

In Fig. 5.3.3, the plasmon width is shown for a density of 2.7 g/cm^3 and temperatures of 0.3 and 6.0 eV. The data is compared to the available experimental results of Witte *et al.* and the calculations involving plasma theory [Witte et al., 2017a, Witte et al., 2018]. At T=0.3 eV, the experimental data nicely agrees with the *ab-initio* results for the cold case. The width resulting from TDDFT in the cold case features a similar trend than the free electron gas where both methods agree for small wavenumbers. At T=0.3 eV, the width is obtained from the linear response calculations involving DFT-MD snapshots. Here, the TDDFT results feature larger widths for small q but the data still lies within the large error bars of the experimental results at large q.

A similar trend can be observed for the case of T=6 eV as presented in the bottom panel of Fig. 5.3.3. The cold TDDFT results (ambient) fit the experimentally determined width much better than the TDDFT data at elevated temperatures where the width is increased strongly due to the liquid structure of the ions. Remarkably, the cold data is in much better agreement with the XRTS measurements than results at 0.3 eV and 6 eV data. Apart from the model-dependent temperature determination as mentioned above, this hints at the fact that the experimental time scales are too short to allow an equilibrium of the coupled electron-ion system to be established.

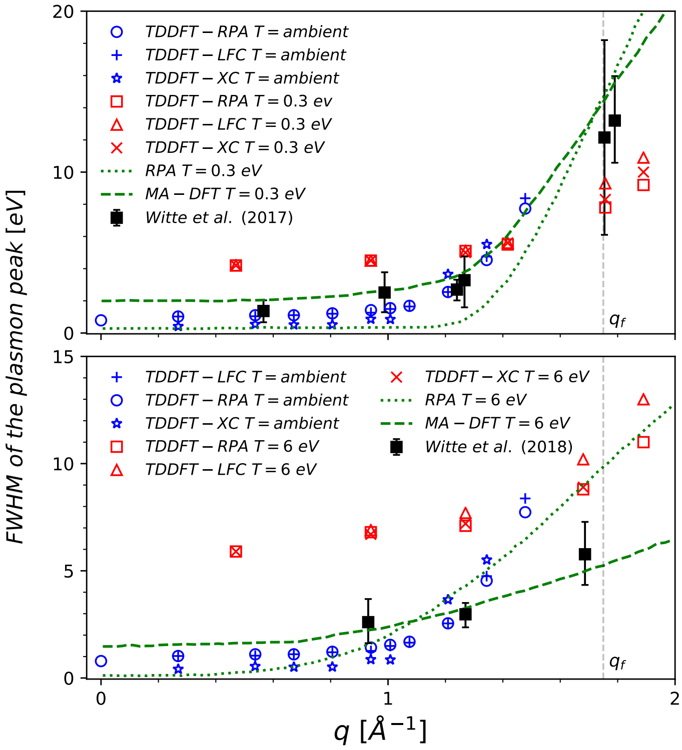

Figure 5.3.3: Aluminum plasmon peak FWHM under extreme conditions for 2.7 g/cm^3 at T=0.3 eV (top) and T=6 eV (bottom). The Fermi wavevector is indicated by the vertical line. Experimental and theoretical data for RPA, MA stems from Ref. [Witte et al., 2017a, Witte et al., 2018]. Reprinted figure with permission from **K. Ramakrishna** *et al.*, Phys. Rev. B **103**, 125118 (2021). Copyright 2021 by the American Physical Society.

5.3.3 Temperature Dependence of the Dynamic Structure Factor

The convergence with respect to the number of bands and *k*-points is important for accuracy and to balance computational cost. The dynamic structure factor for aluminum at 2 eV and 6 eV using 32 atoms for 600 and 750 bands respectively is shown with respect to the *k*-points and the number of electrons considered in the pseudopotential in Fig. 5.3.4. The results are well converged with respect to the *k*-points and the AE (all electron) pseudopotential results in lowering of the peak intensity and an increase in the intensity to higher energies at the shoulder for T=6 eV at energies near 10 eV. In Fig. 5.3.5, the influence of the XC functional (PZ/PBE) is shown in the evaluation of dynamic structure factor from snapshots obtained using MD simulations. LDA and PBE give very similar results for a variety of quantities like the band structure, the density of states, the electron-phonon coupling [Waldecker et al., 2016], and the dynamic structure factor [Dornheim et al., 2020a]. As the discrepancies due to the XC functional is minimal, LDA (PZ) is considered for the calculations.

In Fig. 5.3.6, the dynamic structure factor of aluminum for various temperatures is shown. Panels a) to c) clearly shows the dispersion and change in lifetime of the plasmon. In the TDDFT results, the plasmon peak locations at a specific *q* are independent of temperature as long as the plasmon dominates the spectrum in panels a) and b). This is in contrast to the

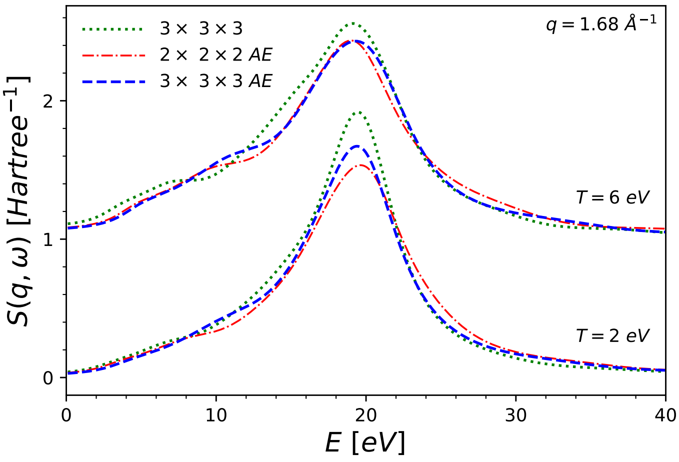

Figure 5.3.4: Dynamic structure factor for aluminum (2.7 g/cm^3) in atomic units at T=2 eV and T=6 eV with respect to *k*-points and the number of electrons considered in the pseudopotential. AE refers to the use of an all electron pseudopotential (11 electrons ignoring the $1s^2$ core) compared to the 3 valence electrons otherwise. Reprinted figure with permission from **K. Ramakrishna** *et al.*, Phys. Rev. B **103**, 125118 (2021). Copyright 2021 by the American Physical Society.

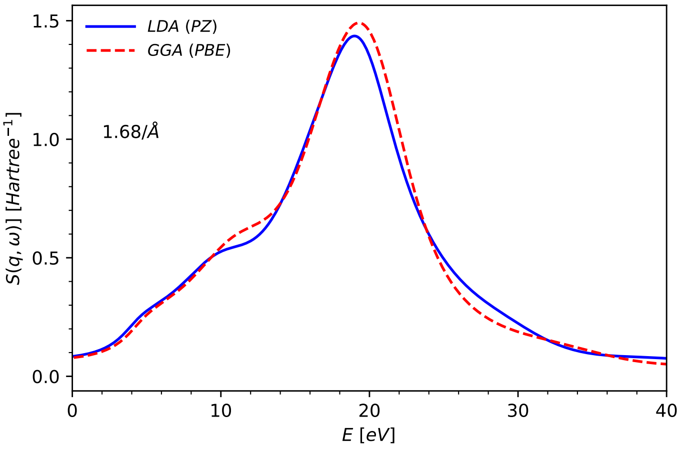

Figure 5.3.5: Dynamic structure factor evaluated using TDDFT (f_{xc}=ALDA) for aluminum in atomic units for 1.68 $Å^{-1}$ at 6 eV using PZ and PBE XC functionals. Reprinted figure with permission from **K. Ramakrishna** *et al.*, Phys. Rev. B **103**, 125118 (2021). Copyright 2021 by the American Physical Society.

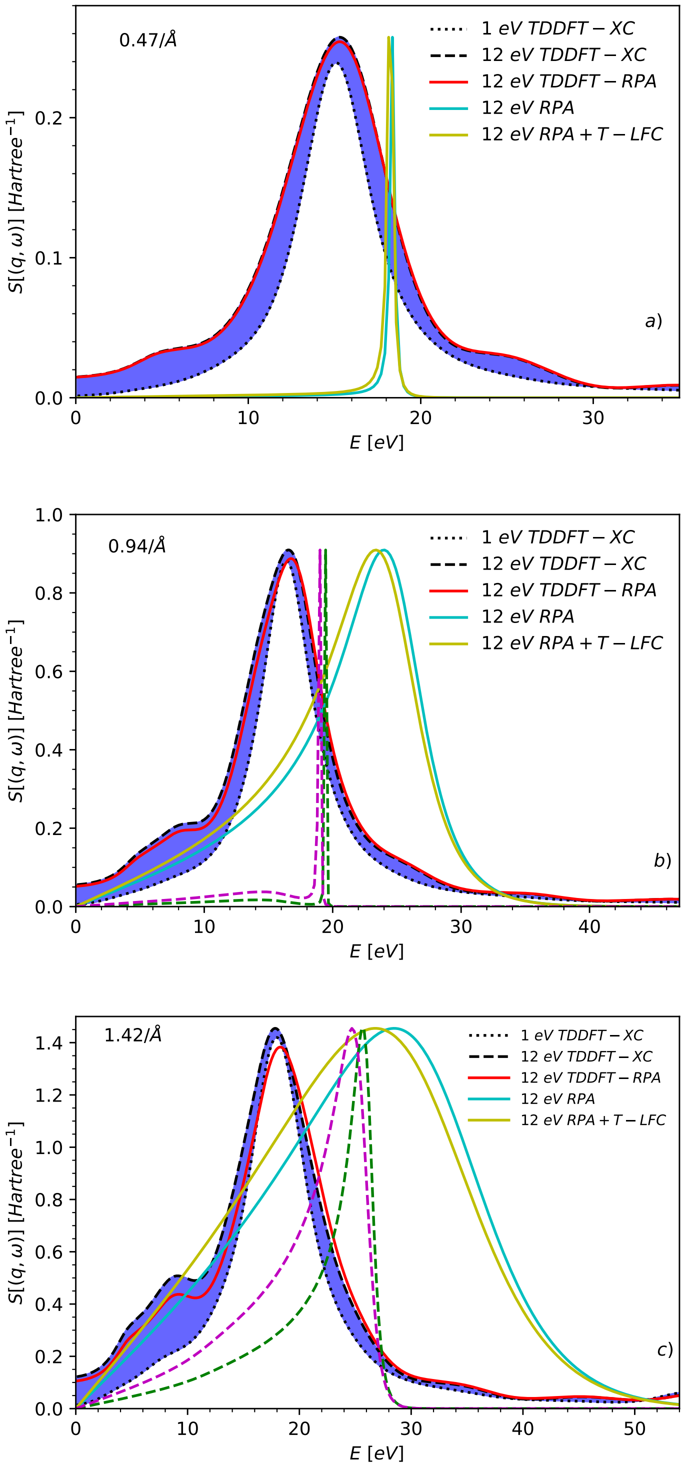

Figure 5.3.6: Dynamic structure factor for aluminum in atomic units at a) $q = 0.47$ Å^{-1}, b) $q = 0.94$ Å^{-1}, c) $q = 1.42$ Å^{-1} for various temperatures. The TDDFT-RPA results are shown only at 12 eV. The TDDFT-XC results are shown from 1 to 12 eV in the blue area (black curves for 1 and 12 eV) and are broadening with temperature. The purple and green dashed lines are the RPA and RPA+T-LFC results at 1 eV respectively. The RPA results are normalized with respect to the TDDFT-XC results at 12 eV to allow plotting them at the same scale. Reprinted figure with permission from **K. Ramakrishna** *et al.*, Phys. Rev. B **103**, 125118 (2021). Copyright 2021 by the American Physical Society.

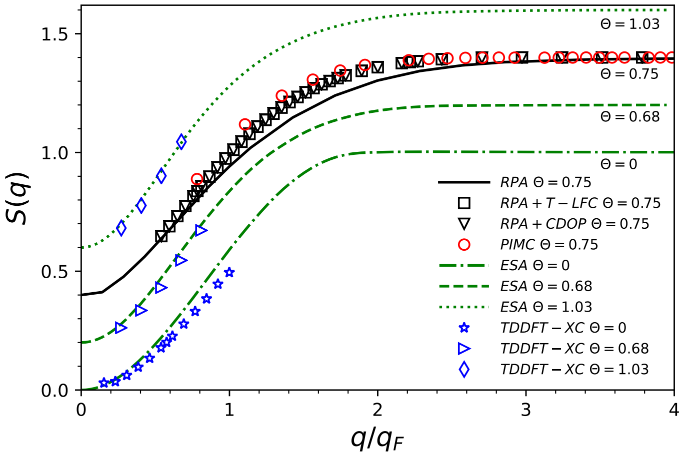

Figure 5.3.7: Static structure factor for aluminum ($r_s = 2.07$) computed using PIMC and RPA including LFCs at $\theta = 0.75$ (T=8.77 eV). The ESA results are shown for $\theta = 0$, $\theta = 0.68$ (T=8 eV) and $\theta = 1.03$ (T=12 eV). The TDDFT-XC results are shown from ambient to T=12 eV for q/q_F up to ~1.0. Reprinted figure with permission from **K. Ramakrishna** *et al.*, Phys. Rev. B **103**, 125118 (2021). Copyright 2021 by the American Physical Society.

Lindhard-RPA calculation (cyan and olive curves, respectively, for with and without LFCs), in which the plasmon's energy varies dramatically with temperature (panel b). The width of the plasmon peak naturally increases with temperature. At large wavenumbers, as single-particle effects begin to influence the structure factor seen in panel c), temperature effects also cause a change in the position of the peak as predicted by TDDFT too.

A downshift of the intensities to lower frequencies is obtained with the inclusion of LFCs. A slight increase of the peak height at large q is observed in panel c) with the TDDFT results.

At large q and at high temperatures, the influence of finite-temperature LFC (T-LFC) is apparent, at T=12 eV with deviations occuring from ground state LFC in the energy range 0-10 eV. The local field corrections for aluminum for various temperatures and wavenumbers are given in Table. 5.3.1. Determining temperature from plasmon peak and width is highly model based, and that the applied theory should be used with great care.

5.3.4 Static Structure Factor

In Fig. 5.3.7, the electronic static structure factor for aluminum ($r_s = 2.07$) is shown for several values of the degeneracy temperature θ within different theories. The PIMC results (red circles) are compared with the RPA calculations including static local field corrections at finite temperature (T-LFC) and ground state (CDOP). The TDDFT-XC results (blue symbols) are also shown for comparison in the range up to 12 eV for $q/q_F \lesssim 1.0$. Only the contribution of the valence electrons are considered for the TDDFT-XC results. The TDDFT-XC results are only considered up to this range as at higher wavenumbers there are other excitations (L-edge, specifically with $L_{2,3}$ and L_1) which do not occur in an electron gas considered in PIMC simulations. The static structure factor is obtained using DSF according to

$$S(q) = \int_{-\infty}^{\infty} S(q,\omega) d\omega. \tag{5.3.1}$$

The curves in green have been obtained using the effective static approximation (ESA) [Dornheim et al., 2020a], which has been shown to yield highly accurate results for $S(q)$ over the entire WDM regime, with a typical systematic error of ∼0.1% as compared to PIMC additionally at a fraction of the computational cost. The agreement between the static structure from both PIMC and ESA and the integrated TDDFT spectra is quite satisfactory and serves as a benchmark of the quality of the TDDFT spectra.

5.4 Conclusions

The capabilities of LR-TDDFT in calculating plasmon dispersion, lifetimes and the DSF for the simple metal aluminum at ambient (FCC lattice) and extreme conditions (high-pressure fluid) are well demonstrated. Starting with the use of a simple first-principle approximation (TDDFT-RPA), a variety of XC kernels in the LR-TDDFT equations: ALDA, static T=0 LFCs (CDOP), and temperature-dependent LFCs (T-LFC), the latter two based on QMC simulations. The obtained results are compared to other TDDFT results and to plasma physics theories using the Mermin dielectric function and several different collision frequencies. Additionally, also compared to experimental values where they were accessible.

The analysis are based on a small number of complete data sets for aluminum at room temperature, including plasmon lifetimes and plasmon dispersion some of which are newly presented here. There is almost no consistent case in this dataset where two theories (or experiments) agree in plasmon position and lifetime at the same time. Even more concerning is the fact that TDDFT calculations that should produce very similar results based on the published set of parameters and methods fail to do so. Although this is true for aluminum at room temperature, the situation is actually worse for warm dense, or high temperature aluminum, which has greater error bars and uncertainties due to experimental difficulties and computational challenges. The effect of LFCs experimentally determined at ambient conditions show that the inclusion is of much importance for strongly correlated low dimensional systems and in materials exhibiting anisotropic dielectric properties [Inaoka et al., 2014, Sato and Terauchi, 2022]. Since such spectra are also used for temperature and density determination of the created states, this has important implications for the evaluation of experimental spectra from XRTS and other experiments. While this is less of a concern for states in ambient conditions or in solids at high-pressure, it is an issue for WDM states. In theory, XRTS is one of the few methods capable of obtaining such fundamental parameters, which are then used as reference to subsequent simulation techniques. As a result, we need not only accurate and reliable methods for calculating the dynamic structure, but also fast methods for fitting spectra [Dornheim et al., 2022]. The findings clearly show that reliable approaches, such as LR-TDDFT, are in desperate need of development or enhancement possibly through the inclusion of effective local field corrections and advanced exchange-correlation kernels compared to ALDA.

6 Conclusions and Perspectives

Results of this chapter are published in
K. Ramakrishna et al.,
Phys. Rev. B ***107****, 115131 (2023)*
T. Dornheim et al.,
Physics of Plasmas ***30****, 032705 (2023)*

In chapter 4, the influence of finite-temperature exchange correlation (XC) effects based on the *GDSMFB* parametrization on the equation of state (EOS) of hydrogen has been rigorously demonstrated. The inclusion of finite temperature XC effects in a warm dense matter system is vital to capture the related physics, although the impact may be comparatively low on average quantities such as electronic pressure or density of states. The local electronic density fluctuations are important for the measurement of response functions and hence the prediction of structure factors as measured through x-ray scattering. The calculations in this work are mainly restricted to the computation of static quantities. Furthermore, dynamical properties like electrical and thermal conductivities relevant for astrophysical modeling of the planetary systems can be effectively evaluated [Helled et al., 2020].

In this work, predictive capabilities for modeling warm dense matter is approached in a systematic way based on *first-principles* methods. An improved understanding of the linear response under warm dense conditions is viable only if the linear response under ambient conditions is well understood with regard to the experimental results leading to a systematic approach for the extreme conditions.

Linear-response TDDFT (LR-TDDFT) based on the assessment of the exchange correlation (XC) kernel in the evaluation of the density response function is successful in capturing the essential physics as demonstrated in Chapter 3 and 5 for carbon and aluminum respectively. The adiabatic local density approximation (ALDA) has been revealed to give good results for the study of plasmons in solids, and metals in particular. Moreover, it constitutes a substantial improvement over the more simple RPA (f_{XC}=0) [Botti et al., 2007, Onida et al., 2002]. ALDA is also successful in general for treating non-metallic systems particularly for inelastic spectra in the small q limit but not for absorption in the optical limit. ALDA fails to capture the bound excitons in materials like diamond demonstrated in Chapter 3 [Giuliani and Vignale, 2005]. Instead, the bootstrap kernel [Sharma et al., 2011] for TDDFT, and higher rungs of XC functionals, especially hybrid functionals are well suited for carbon based materials. The evaluation of the dynamic structure factor (DSF) with ALDA for simple metals can be further improved with the inclusion of non-local and non-adiabatic effects for e.g. using the 2*p*2*h* kernel by Panholzer *et al.* [Panholzer et al., 2018]. The novel kernel provides details on the dynamic behavior of the uniform electron gas including the feature of the double plasmon behavior observed in simple metals not captured by the ALDA kernel.

An alternative method to LR-TDDFT is real-time propagation in time-dependent density functional theory (RT-TDDFT) [Yabana and Bertsch, 1996, Bertsch et al., 2000]. RT-TDDFT has evolved into a computationally powerful simulation approach for studying non-equilibrium electron dynamics. It is distinct from LR-TDDFT and it enables one to go beyond the linear-response regime. As in LR-TDDFT, the response function computed using RT-TDDFT captures collective effects that aren't captured in the standard approach using the Kubo-

Greenwood (KG) formula. For certain regimes of electronic excitation, and large systems, RT-TDDFT can be computationally more efficient than LR-TDDFT for calculating optical properties [Tussupbayev et al., 2015].

The formulation describes how an external electric field $\boldsymbol{E}(\omega)$ gives rise to an induced electric current

$$\boldsymbol{J}(\omega) = \boldsymbol{\sigma}(\omega)\,\boldsymbol{E}(\omega)\,, \tag{6.0.1}$$

where the constant of proportionality can be identified as the electrical conductivity $\boldsymbol{\sigma}(\omega)$. This is formulated in the frequency domain with both the current and the electric field being vectors, while the conductivity is a tensor. The induced current can be computed on the atomistic level by using RT-TDDFT. By applying an electric field $\boldsymbol{E}(t) = -(1/c)(\partial \boldsymbol{A}/\partial t)$, where $\boldsymbol{A}$ is the impressed vector potential and c is the speed of light, we obtain the induced time-dependent current density

$$\boldsymbol{j}(r,t) = \Im[\sum_{i}^{N} \varphi^{*}_{S_{n,k}}(r,t)\nabla\varphi_{S_{n,k}}(r,t)] + n(r,t)\boldsymbol{A}_S(r,t)/c. \tag{6.0.2}$$

When integrated over the spatial coordinates, it yields a time-dependent electric current $\boldsymbol{J}(t)$. By taking the Fourier transform we obtain Ohm's law in the frequency domain as denoted in Eq. (6.0.1). The time-dependent current density is obtained by solving the time-dependent Kohn-Sham (KS) equations

$$\hat{H}_S\varphi_{S_{n,k}}(r,t) = i\frac{\partial}{\partial t}\varphi_{S_{n,k}}(r,t)\,, \tag{6.0.3}$$

for the KS orbitals $\varphi_{S_{n,k}}(r,t)$. Here, the effective Hamiltonian is given by

$$\hat{H}_S = \frac{1}{2}\left[-i\nabla + \frac{1}{c}\boldsymbol{A}_S(r,t)\right]^2 + V_S(r,t) \tag{6.0.4}$$

where $V_S(,t) = V_{ext}(r,t) + V_H(r,t) + V_{XC}(r,t)$ is the KS potential involving the sum of the external, the Hartree, and XC potentials, while the effective vector potential $\boldsymbol{A}_S(r,t) = \boldsymbol{A}(r,t) + \boldsymbol{A}_{XC}(r,t)$ comprises the sum of the external vector potential and the XC contribution.

The following RT-TDDFT results are obtained from the all-electron full-potential linearized augmented plane wave (FP-LAPW) method [Singh and Nordstrom, 2006] as implemented in the *elk* [Dewhurst, 2021] and *exciting* [Gulans et al., 2014, Pela and Draxl, 2021] codes.

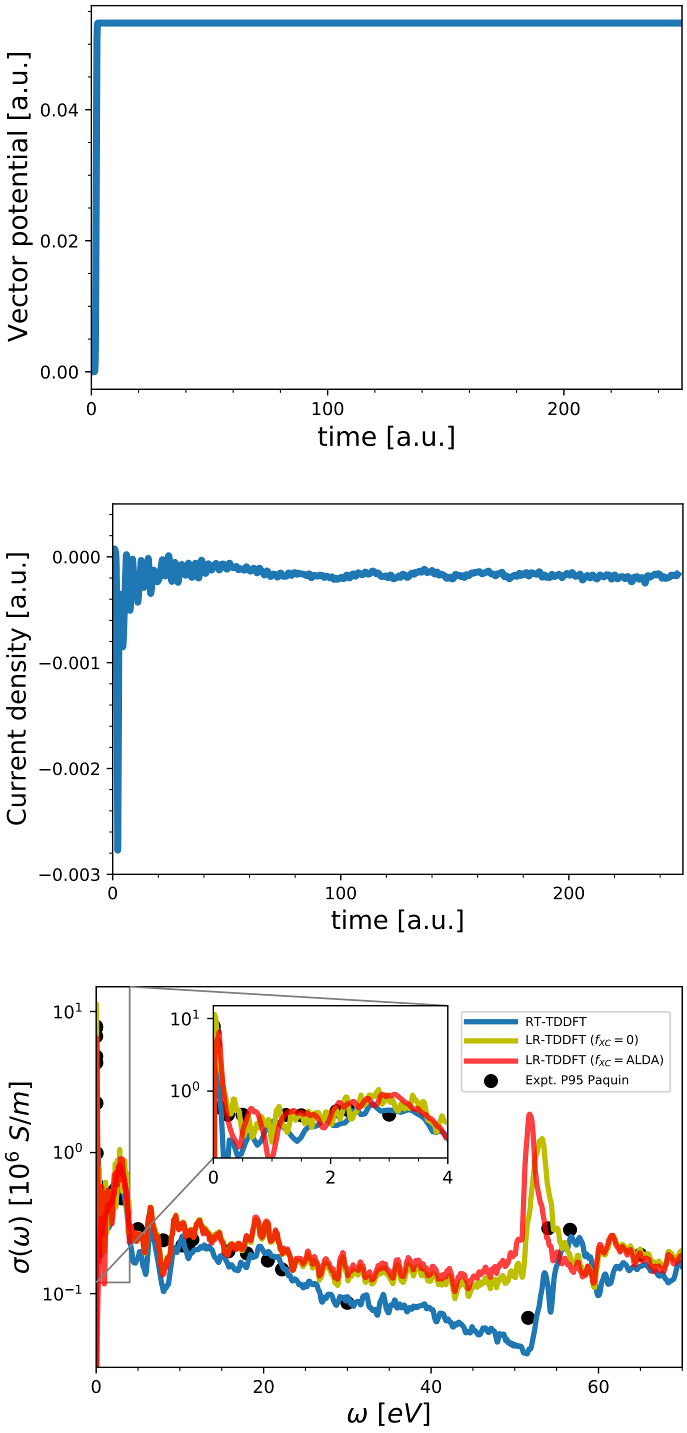

Figure 6.0.1: a) Sigmoidal pulse in the $\vec{z}$ direction vs time, b) Induced current density vs time, c) Dynamical electrical conductivity of iron computed using LR-TDDFT (RPA-yellow, ALDA - red) and RT-TDDFT (blue) at ambient conditions. Experimental data stems from Ref. [Paquin, 1995].

A sigmoidal pulse of vector amplitude 0.1 a.u. (atomic units) is applied with a peak time 2 a.u. having a full-width half maximum (FWHM) of 0.5 a.u. for a total simulation time up to t =250 a.u with a time-step Δt =0.02 a.u . Here we adopt Hartree atomic units, i.e., $\hbar = e = m_e = a_0 = 1$. The aforementioned pulse parameters are applied in the $\vec{z}$ direction shown in Fig. 6.0.1a). The induced current density along $\vec{z}$ is shown in Fig. 6.0.1b). The total duration of the real-time propagation is essential to obtain a smaller resolution in the frequency space while also ensuring the current density reaches a steady state with time. The spectral energy resolution is inversely proportional to the total time propagation and the energy window of the simulation is inversely proportional to the FWHM of the pulse. The dynamical electrical conductivity obtained using the Fourier transform of the induced current density is shown in Fig. 6.0.1c) (blue). The results shown are for ferromagnetic body centered cubic (BCC) iron under ambient conditions (T=300 K). The RT-TDDFT result is overall in good agreement with the dynamical experimental results [Paquin, 1995] compared to LR-TDDFT (yellow and red curves) computed using RPA XC kernel ($f_{\mathrm{XC}} = 0$) and ALDA respectively. LR-TDDFT falls short of providing an accurate description across the entire frequency domain. Especially, the feature at $\sim$55 eV which stems from *3p* to conduction band transitions is missing in the LR-TDDFT results. The influence of XC kernel (ALDA vs RPA) has negligible impact in the energy range considered except around $\sim$50 eV where the peak feature has a slight redshift. In essence, RT-TDDFT captures the electronic excitations much more effectively than LR-TDDFT which are especially important for strongly correlated and localized 3*d* electrons in iron.

The real-time formalism of time-dependent DFT is a powerful tool for computing transport properties in materials under extreme conditions. It offers a feasible alternative to current cutting-edge methodologies, such as evaluating the KG formula using DFT data. We anticipate that this technique will be widely utilized for interpreting forthcoming free-electron laser scattering experiments at facilities such as LCLS [Fletcher et al., 2015], and the European XFEL [Tschentscher et al., 2017]. This will also enable studying the non-linear response [Dornheim et al., 2020c, Dornheim et al., 2021] of materials under extreme conditions accessible through recent advances in free-electron lasers [Zastrau et al., 2021, Cerantola et al., 2021].

Bibliography

[opi, 2018] (2018). Opium - pseudopotential generation project. `http://opium.sourceforge.net/`.

[Adamo and Barone, 1999] Adamo, C. and Barone, V. (1999). Toward reliable density functional methods without adjustable parameters: The pbe0 model. *The Journal of chemical physics*, 110(13):6158–6170.

[Adler, 1962] Adler, S. L. (1962). Quantum theory of the dielectric constant in real solids. *Physical Review*, 126(2):413.

[Alavi et al., 1995] Alavi, A., Parrinello, M., and Frenkel, D. (1995). Ab initio calculation of the sound velocity of dense hydrogen: implications for models of jupiter. *Science*, 269(5228):1252–1254.

[Allen and Tildesley, 2017] Allen, M. P. and Tildesley, D. J. (2017). *Computer simulation of liquids*. Oxford university press.

[Andrade et al., 2018] Andrade, X., Hamel, S., and Correa, A. A. (2018). Negative differential conductivity in liquid aluminum from real-time quantum simulations. *The European Physical Journal B*, 91(10):229.

[Antonius et al., 2014] Antonius, G., Poncé, S., Boulanger, P., Côté, M., and Gonze, X. (2014). Many-body effects on the zero-point renormalization of the band structure. *Physical Review Letters*, 112(21):215501.

[Ashcroft, 1968] Ashcroft, N. W. (1968). Metallic hydrogen: A high-temperature superconductor? *Phys. Rev. Lett.*, 21:1748–1749.

[Ashcroft and Mermin, 1976] Ashcroft, N. W. and Mermin, N. D. (1976). *Solid State Physics*. Holt-Saunders.

[Atzeni and Meyer-ter Vehn, 2004] Atzeni, S. and Meyer-ter Vehn, J. (2004). *The Physics of Inertial Fusion: Beam-Plasma Interaction, Hydrodynamics, Hot Dense Matter*. Clarendon Press.

[Azadi et al., 2014] Azadi, S., Monserrat, B., Foulkes, W. M. C., and Needs, R. J. (2014). Dissociation of high-pressure solid molecular hydrogen: A quantum monte carlo and anharmonic vibrational study. *Phys. Rev. Lett.*, 112:165501.

[Azzolini et al., 2017] Azzolini, M., Morresi, T., Garberoglio, G., Calliari, L., Pugno, N. M., Taioli, S., and Dapor, M. (2017). Monte carlo simulations of measured electron energy-loss spectra of diamond and graphite: Role of dielectric-response models. *Carbon*, 118:299–309.

[Baczewski et al., 2021] Baczewski, A. D., Hentschel, T., Kononov, A., and Hansen, S. B. (2021). Predictions of bound-bound transition signatures in x-ray thomson scattering. *arXiv preprint arXiv:2109.09576*.

[Baczewski et al., 2016] Baczewski, A. D., Shulenburger, L., Desjarlais, M., Hansen, S., and Magyar, R. (2016). X-ray thomson scattering in warm dense matter without the chihara decomposition. *Physical review letters*, 116(11):115004.

[Baer et al., 2013] Baer, R., Neuhauser, D., and Rabani, E. (2013). Self-averaging stochastic kohn-sham density-functional theory. *Phys. Rev. Lett.*, 111:106402.

[Baldsiefen et al., 2017] Baldsiefen, T., Cangi, A., Eich, F. G., and Gross, E. K. U. (2017). Exchange-correlation approximations for reduced-density-matrix-functional theory at finite temperature: Capturing magnetic phase transitions in the homogeneous electron gas. *Phys. Rev. A*, 96:062508.

[Baldsiefen et al., 2015] Baldsiefen, T., Cangi, A., and Gross, E. K. U. (2015). Reduced-density-matrix-functional theory at finite temperature: Theoretical foundations. *Phys. Rev. A*, 92:052514.

[Batson and Silcox, 1983] Batson, P. E. and Silcox, J. (1983). Experimental energy-loss function, $Im[-\frac{1}{\epsilon}(q,\omega)]$, for aluminum. *Phys. Rev. B*, 27:5224–5239.

[Becke, 1988] Becke, A. D. (1988). Density-functional exchange-energy approximation with correct asymptotic behavior. *Phys. Rev. A*, 38:3098–3100.

[Becke, 1997] Becke, A. D. (1997). Density-functional thermochemistry. v. systematic optimization of exchange-correlation functionals. *The Journal of chemical physics*, 107(20):8554–8560.

[Benedict et al., 2014] Benedict, L. X., Driver, K. P., Hamel, S., Militzer, B., Qi, T., Correa, A. A., Saul, A., and Schwegler, E. (2014). Multiphase equation of state for carbon addressing high pressures and temperatures. *Physical Review B*, 89(22):224109.

[Benedict et al., 1998] Benedict, L. X., Shirley, E. L., and Bohn, R. B. (1998). Theory of optical absorption in diamond, si, ge, and gaas. *Physical Review B*, 57(16):R9385.

[Benner and Penke, 2020] Benner, P. and Penke, C. (2020). Efficient and accurate algorithms for solving the bethe-salpeter eigenvalue problem for crystalline systems.

[Bertsch et al., 2000] Bertsch, G. F., Iwata, J.-I., Rubio, A., and Yabana, K. (2000). Real-space, real-time method for the dielectric function. *Physical Review B*, 62(12):7998.

[Bethkenhagen et al., 2020] Bethkenhagen, M., Witte, B. B., Schörner, M., Röpke, G., Döppner, T., Kraus, D., Glenzer, S. H., Sterne, P. A., and Redmer, R. (2020). Carbon ionization at gigabar pressures: An ab initio perspective on astrophysical high-density plasmas. *Physical Review Research*, 2(2):023260.

[Biener et al., 2009] Biener, J., Ho, D., Wild, C., Woerner, E., Biener, M., El-dasher, B., Hicks, D., Eggert, J., Celliers, P., Collins, G., et al. (2009). Diamond spheres for inertial confinement fusion. *Nuclear Fusion*, 49(11):112001.

[Biener et al., 2006] Biener, J., Mirkarimi, P. B., Tringe, J. W., Baker, S. L., Wang, Y., Kucheyev, S. O., Teslich, N. E., Wu, K. J. J., Hamza, A. V., Wild, C., et al. (2006). Diamond ablators for inertial confinement fusion. *Fusion science and technology*, 49(4):737–742.

[Blanchet et al., 2020] Blanchet, A., Torrent, M., and Clerouin, J. (2020). Requirements for very high temperature kohn-sham density functional simulations and how to bypass them.

[Blöchl, 1994] Blöchl, P. E. (1994). Projector augmented-wave method. *Physical review B*, 50(24):17953.

[Blöchl et al., 1994] Blöchl, P. E., Jepsen, O., and Andersen, O. K. (1994). Improved tetrahedron method for brillouin-zone integrations. *Phys. Rev. B*, 49:16223–16233.

[Blunt et al., 2014] Blunt, N. S., Rogers, T. W., Spencer, J. S., and Foulkes, W. M. C. (2014). Density-matrix quantum monte carlo method. *Phys. Rev. B*, 89:245124.

[Boehler and Ross, 1997] Boehler, R. and Ross, M. (1997). Melting curve of aluminum in a diamond cell to 0.8 mbar: implications for iron. *Earth and Planetary Science Letters*, 153(3-4):223–227.

[Bohm and Gross, 1949] Bohm, D. and Gross, E. P. (1949). Theory of plasma oscillations. a. origin of medium-like behavior. *Phys. Rev.*, 75:1851–1864.

[Bohm and Pines, 1951] Bohm, D. and Pines, D. (1951). A collective description of electron interactions. i. magnetic interactions. *Phys. Rev.*, 82:625–634.

[Bohm and Pines, 1953] Bohm, D. and Pines, D. (1953). A collective description of electron interactions: Iii. coulomb interactions in a degenerate electron gas. *Physical Review*, 92(3):609.

[Böhme et al., 2022] Böhme, M., Moldabekov, Z., Vorberger, J., and Dornheim, T. (2022). Electronic density response of warm dense hydrogen: Ab initio path integral monte carlo simulations. *arXiv preprint arXiv:2203.01797*.

[Bonitz, 2016] Bonitz, M. (2016). *Quantum kinetic theory*, volume 412. Springer.

[Bonitz et al., 2020] Bonitz, M., Dornheim, T., Moldabekov, Z. A., Zhang, S., Hamann, P., Kählert, H., Filinov, A., Ramakrishna, K., and Vorberger, J. (2020). Ab initio simulation of warm dense matter. *Physics of Plasmas*, 27(4):042710.

[Bonitz et al., 2005] Bonitz, M., Filinov, V. S., Fortov, V. E., Levashov, P. R., and Fehske, H. (2005). Crystallization in two-component coulomb systems. *Phys. Rev. Lett.*, 95:235006.

[Bostedt et al., 2016] Bostedt, C., Boutet, S., Fritz, D. M., Huang, Z., Lee, H. J., Lemke, H. T., Robert, A., Schlotter, W. F., Turner, J. J., and Williams, G. J. (2016). Linac coherent light source: The first five years. *Rev. Mod. Phys.*, 88:015007.

[Botti et al., 2005] Botti, S., Fourreau, A., Nguyen, F., Renault, Y.-O., Sottile, F., and Reining, L. (2005). Energy dependence of the exchange-correlation kernel of time-dependent density functional theory: A simple model for solids. *Physical Review B*, 72(12):125203.

[Botti et al., 2007] Botti, S., Schindlmayr, A., Del Sole, R., and Reining, L. (2007). Time-dependent density-functional theory for extended systems. *Reports on Progress in Physics*, 70(3):357.

[Botti et al., 2004] Botti, S., Sottile, F., Vast, N., Olevano, V., Reining, L., Weissker, H.-C., Rubio, A., Onida, G., Del Sole, R., and Godby, R. (2004). Long-range contribution to the exchange-correlation kernel of time-dependent density functional theory. *Physical Review B*, 69(15):155112.

[Bouchet et al., 2009] Bouchet, J., Bottin, F., Jomard, G., and Zérah, G. (2009). Melting curve of aluminum up to 300 gpa obtained through ab initio molecular dynamics simulations. *Physical Review B*, 80(9):094102.

[Brown et al., 2013a] Brown, E. W., Clark, B. K., DuBois, J. L., and Ceperley, D. M. (2013a). Path-integral monte carlo simulation of the warm dense homogeneous electron gas. *Physical review letters*, 110(14):146405.

[Brown et al., 2013b] Brown, E. W., DuBois, J. L., Holzmann, M., and Ceperley, D. M. (2013b). Exchange-correlation energy for the three-dimensional homogeneous electron gas at arbitrary temperature. *Phys. Rev. B*, 88:081102.

[Budagosky and Krasovskii, 2019] Budagosky, J. A. and Krasovskii, E. E. (2019). All-electron product basis set: Application to plasmon anisotropy in simple metals. *Phys. Rev. B*, 99:245149.

[Bunău and Joly, 2009] Bunău, O. and Joly, Y. (2009). Self-consistent aspects of x-ray absorption calculations. *Journal of Physics: Condensed Matter*, 21(34):345501.

[Bundy and Kasper, 1967] Bundy, F. and Kasper, J. (1967). Hexagonal diamond-a new form of carbon. *The Journal of Chemical Physics*, 46(9):3437–3446.

[Burke, 2012] Burke, K. (2012). Perspective on density functional theory. *The Journal of chemical physics*, 136(15):150901.

[Burke et al., 2016] Burke, K., Smith, J. C., Grabowski, P. E., and Pribram-Jones, A. (2016). Exact conditions on the temperature dependence of density functionals. *Physical Review B*, 93(19):195132.

[Calderin et al., 2017] Calderin, L., Karasiev, V. V., and Trickey, S. B. (2017). Kubo–greenwood electrical conductivity formulation and implementation for projector augmented wave datasets. *Computer Physics Communications*, 221:118–142.

[Cangi and Pribram-Jones, 2015] Cangi, A. and Pribram-Jones, A. (2015). Efficient formalism for warm dense matter simulations. *Phys. Rev. B*, 92:161113.

[Cannuccia and Marini, 2011] Cannuccia, E. and Marini, A. (2011). Effect of the quantum zero-point atomic motion on the optical and electronic properties of diamond and trans-polyacetylene. *Physical review letters*, 107(25):255501.

[Car and Parrinello, 1985] Car, R. and Parrinello, M. (1985). Unified approach for molecular dynamics and density-functional theory. *Phys. Rev. Lett.*, 55:2471–2474.

[Carr and Maradudin, 1964] Carr, W. J. and Maradudin, A. A. (1964). Ground-state energy of a high-density electron gas. *Phys. Rev.*, 133:A371–A374.

[Cazzaniga et al., 2011] Cazzaniga, M., Weissker, H.-C., Huotari, S., Pylkkänen, T., Salvestrini, P., Monaco, G., Onida, G., and Reining, L. (2011). Dynamical response function in sodium and aluminum from time-dependent density-functional theory. *Phys. Rev. B*, 84:075109.

[Celliers et al., 2018] Celliers, P. M., Millot, M., Brygoo, S., McWilliams, R. S., Fratanduono, D. E., Rygg, J. R., Goncharov, A. F., Loubeyre, P., Eggert, J. H., Peterson, J. L., Meezan, N. B., Le Pape, S., Collins, G. W., Jeanloz, R., and Hemley, R. J. (2018). Insulator-metal transition in dense fluid deuterium. *Science*, 361(6403):677–682.

[Ceperley, 1991] Ceperley, D. M. (1991). Fermion nodes. *Journal of Statistical Physics*, 63(5):1237–1267.

[Ceperley and Alder, 1980] Ceperley, D. M. and Alder, B. J. (1980). Ground state of the electron gas by a stochastic method. *Phys. Rev. Lett.*, 45:566–569.

[Cerantola et al., 2021] Cerantola, V., Rosa, A. D., Konôpková, Z., Torchio, R., Brambrink, E., Rack, A., Zastrau, U., and Pascarelli, S. (2021). New frontiers in extreme conditions science at synchrotrons and free electron lasers. *Journal of Physics: Condensed Matter*, 33(27):274003.

[Chihara, 1987] Chihara, J. (1987). Difference in x-ray scattering between metallic and non-metallic liquids due to conduction electrons. *Journal of Physics F: Metal Physics*, 17(2):295.

[Claes and Clark, 2017] Claes, J. and Clark, B. K. (2017). Finite-temperature properties of strongly correlated systems via variational monte carlo. *Phys. Rev. B*, 95:205109.

[Clark, 1994] Clark, S. (1994). Complex structures in tetrahedrally bonded semiconductors.

[Collins et al., 2001] Collins, L. A., Bickham, S. R., Kress, J. D., Mazevet, S., Lenosky, T. J., Troullier, N. J., and Windl, W. (2001). Dynamical and optical properties of warm dense hydrogen. *Phys. Rev. B*, 63:184110.

[Corradini et al., 1998] Corradini, M., Del Sole, R., Onida, G., and Palummo, M. (1998). Analytical expressions for the local-field factor $g(q)$ and the exchange-correlation kernel $K_{xc}(r)$ of the homogeneous electron gas. *Phys. Rev. B*, 57:14569–14571.

[Correa, 2018] Correa, A. A. (2018). Calculating electronic stopping power in materials from first principles. *Computational Materials Science*, 150:291–303.

[Correa et al., 2008] Correa, A. A., Benedict, L. X., Young, D. A., Schwegler, E., and Bonev, S. A. (2008). First-principles multiphase equation of state of carbon under extreme conditions. *Phys. Rev. B*, 78:024101.

[Correa et al., 2006] Correa, A. A., Bonev, S. A., and Galli, G. (2006). Carbon under extreme conditions: Phase boundaries and electronic properties from first-principles theory. *Proceedings of the National Academy of Sciences*, 103(5):1204–1208.

[Crain et al., 1994] Crain, J., Clark, S., Ackland, G., Payne, M., Milman, V., Hatton, P., and Reid, B. (1994). Theoretical study of high-density phases of covalent semiconductors. i. ab initio treatment. *Physical Review B*, 49(8):5329.

[Curchod et al., 2013] Curchod, B. F., Rothlisberger, U., and Tavernelli, I. (2013). Trajectory-based nonadiabatic dynamics with time-dependent density functional theory. *ChemPhysChem*, 14(7):1314–1340.

[Cytter et al., 2018] Cytter, Y., Rabani, E., Neuhauser, D., and Baer, R. (2018). Stochastic density functional theory at finite temperatures. *Phys. Rev. B*, 97:115207.

[Cytter et al., 2019] Cytter, Y., Rabani, E., Neuhauser, D., Preising, M., Redmer, R., and Baer, R. (2019). Transition to metallization in warm dense helium-hydrogen mixtures using stochastic density functional theory within the kubo-greenwood formalism. *Physical Review B*, 100(19):195101.

[Dalladay-Simpson et al., 2016] Dalladay-Simpson, P., Howie, R. T., and Gregoryanz, E. (2016). Evidence for a new phase of dense hydrogen above 325 gigapascals. *Nature*, 529(7584):63.

[Danel et al., 2016] Danel, J.-F., Kazandjian, L., and Piron, R. (2016). Equation of state of warm dense deuterium and its isotopes from density-functional theory molecular dynamics. *Phys. Rev. E*, 93:043210.

[Daniels et al., 1970] Daniels, J., Festenberg, C. v., Raether, H., and Zeppenfeld, K. (1970). Optical constants of solids by electron spectroscopy. In *Springer Tracts in Modern Physics, Volume 54*, pages 77–135. Springer.

[Davidson, 2003] Davidson, R. C. (2003). *Frontiers in High Energy Density Physics: the X-games of Contemporary Science*. National Academies Press, Washington, DC.

[De and Pryor, 2014] De, A. and Pryor, C. E. (2014). Electronic structure and optical properties of si, ge and diamond in the lonsdaleite phase. *Journal of Physics: Condensed Matter*, 26(4):045801.

[Dewaele et al., 2008] Dewaele, A., Datchi, F., Loubeyre, P., and Mezouar, M. (2008). High pressure–high temperature equations of state of neon and diamond. *Phys. Rev. B*, 77:094106.

[Dewhurst, 2021] Dewhurst, J. t. (2021). Elk, all-electron full-potential linearised augmented-plane wave (fp-lapw) code. `http://elk.sourceforge.net/`.

[Dharma-wardana and Perrot, 2000] Dharma-wardana, M. W. C. and Perrot, F. (2000). Simple classical mapping of the spin-polarized quantum electron gas: Distribution functions and local-field corrections. *Phys. Rev. Lett.*, 84:959–962.

[Di Paola et al., 2020] Di Paola, C., Macheda, F., Laricchia, S., Weber, C., and Bonini, N. (2020). First-principles study of electronic transport and structural properties of $cu_{12}sb_4s_{13}$ in its high-temperature phase. *Phys. Rev. Research*, 2:033055.

[Dias and Silvera, 2017] Dias, R. P. and Silvera, I. F. (2017). Observation of the wigner-huntington transition to metallic hydrogen. *Science*, 355(6326):715–718.

[Ding et al., 2015] Ding, F., Goings, J. J., Liu, H., Lingerfelt, D. B., and Li, X. (2015). Ab initio two-component ehrenfest dynamics. *The Journal of chemical physics*, 143(11):114105.

[Dornheim, 2018] Dornheim, T. (2018). *The Uniform Electron Gas atWarm Dense Matter Conditions - A Permutation Blocking Path Integral Monte Carlo Perspective*. PhD thesis, Christian-Albrechts-Universität zu Kiel.

[Dornheim et al., 2022] Dornheim, T., Böhme, M., Kraus, D., Döppner, T., Preston, T., Moldabekov, Z., and Vorberger, J. (2022). Accurate temperature diagnostics for matter under extreme conditions. *arXiv preprint arXiv:2206.12805*.

[Dornheim et al., 2021] Dornheim, T., Böhme, M., Moldabekov, Z. A., Vorberger, J., and Bonitz, M. (2021). Density response of the warm dense electron gas beyond linear response theory: Excitation of harmonics. *Phys. Rev. Research*, 3:033231.

[Dornheim et al., 2020a] Dornheim, T., Cangi, A., Ramakrishna, K., Böhme, M., Tanaka, S., and Vorberger, J. (2020a). Effective static approximation: A fast and reliable tool for warm-dense matter theory. *Phys. Rev. Lett.*, 125:235001.

[Dornheim et al., 2018a] Dornheim, T., Groth, S., and Bonitz, M. (2018a). The uniform electron gas at warm dense matter conditions. *Physics Reports*, 744:1–86.

[Dornheim et al., 2015a] Dornheim, T., Groth, S., Filinov, A., and Bonitz, M. (2015a). Permutation blocking path integral monte carlo: a highly efficient approach to the simulation of strongly degenerate non-ideal fermions. *New Journal of Physics*, 17(7):073017.

[Dornheim et al., 2017] Dornheim, T., Groth, S., Malone, F. D., Schoof, T., Sjostrom, T., Foulkes, W. M. C., and Bonitz, M. (2017). Ab initio quantum monte carlo simulation of the warm dense electron gas. *Physics of Plasmas*, 24(5):056303.

[Dornheim et al., 2016a] Dornheim, T., Groth, S., Schoof, T., Hann, C., and Bonitz, M. (2016a). Ab initio quantum monte carlo simulations of the uniform electron gas without fixed nodes: The unpolarized case. *Phys. Rev. B*, 93:205134.

[Dornheim et al., 2016b] Dornheim, T., Groth, S., Sjostrom, T., Malone, F. D., Foulkes, W. M. C., and Bonitz, M. (2016b). Ab initio quantum monte carlo simulation of the warm dense electron gas in the thermodynamic limit. *Phys. Rev. Lett.*, 117:156403.

[Dornheim et al., 2018b] Dornheim, T., Groth, S., Vorberger, J., and Bonitz, M. (2018b). Ab initio path integral monte carlo results for the dynamic structure factor of correlated electrons: From the electron liquid to warm dense matter. *Phys. Rev. Lett.*, 121:255001.

[Dornheim et al., 2023] Dornheim, T., Moldabekov, Z. A., Ramakrishna, K., Tolias, P., Baczewski, A. D., Kraus, D., Preston, T. R., Chapman, D. A., Böhme, M. P., Döppner, T., Graziani, F., Bonitz, M., Cangi, A., and Vorberger, J. (2023). Electronic density response of warm dense matter. *Physics of Plasmas*, 30(3). 032705.

[Dornheim et al., 2015b] Dornheim, T., Schoof, T., Groth, S., Filinov, A., and Bonitz, M. (2015b). Permutation blocking path integral monte carlo approach to the uniform electron gas at finite temperature. *The Journal of Chemical Physics*, 143(20):204101.

[Dornheim et al., 2020b] Dornheim, T., Sjostrom, T., Tanaka, S., and Vorberger, J. (2020b). Strongly coupled electron liquid: Ab initio path integral monte carlo simulations and dielectric theories. *Physical Review B*, 101(4):045129.

[Dornheim et al., 2020c] Dornheim, T., Vorberger, J., and Bonitz, M. (2020c). Nonlinear electronic density response in warm dense matter. *Phys. Rev. Lett.*, 125:085001.

[Dornheim et al., 2019] Dornheim, T., Vorberger, J., Groth, S., Hoffmann, N., Moldabekov, Z. A., and Bonitz, M. (2019). The static local field correction of the warm dense electron gas: An ab initio path integral monte carlo study and machine learning representation. *The Journal of Chemical Physics*, 151(19):194104.

[Drummond et al., 2015] Drummond, N. D., Monserrat, B., Lloyd-Williams, J. H., Ríos, P. L., Pickard, C. J., and Needs, R. J. (2015). Quantum monte carlo study of the phase diagram of solid molecular hydrogen at extreme pressures. *Nature communications*, 6(1):1–6.

[Ebeling and Richert, 1982] Ebeling, W. and Richert, W. (1982). Thermodynamic functions of nonideal hydrogen plasmas. *Annalen der Physik*, 494(5):362–370.

[Ebeling and Richert, 1985a] Ebeling, W. and Richert, W. (1985a). Plasma phase transition in hydrogen. *Physics Letters A*, 108(2):80–82.

[Ebeling and Richert, 1985b] Ebeling, W. and Richert, W. (1985b). Thermodynamic properties of liquid hydrogen metal. *physica status solidi (b)*, 128(2):467–474.

[Ebeling et al., 1981] Ebeling, W., Richert, W., Kraeft, W., and Stolzmann, W. (1981). Padé approximations for the thermodynamic functions of weakly interacting coulombic quantum systems. *physica status solidi (b)*, 104(1):193–202.

[Egerton, 2008] Egerton, R. F. (2008). Electron energy-loss spectroscopy in the tem. *Reports on Progress in Physics*, 72(1):016502.

[Eremets and Troyan, 2011] Eremets, M. and Troyan, I. (2011). Conductive dense hydrogen. *Nature materials*, 10(12):927.

[Eremets et al., 2016] Eremets, M., Troyan, I., and Drozdov, A. (2016). Low temperature phase diagram of hydrogen at pressures up to 380 gpa. a possible metallic phase at 360 gpa and 200 k. *arXiv preprint arXiv:1601.04479*.

[Eremets et al., 2019] Eremets, M. I., Drozdov, A. P., Kong, P., and Wang, H. (2019). Semimetallic molecular hydrogen at pressure above 350 gpa. *Nature Physics*, 15(12):1246–1249.

[Fabian et al., 2019] Fabian, M. D., Shpiro, B., Rabani, E., Neuhauser, D., and Baer, R. (2019). Stochastic density functional theory. *Wiley Interdisciplinary Reviews: Computational Molecular Science*, 9(6):e1412.

[Fahy et al., 1987] Fahy, S., Chang, K.-J., Louie, S. G., and Cohen, M. L. (1987). Pressure coefficients of band gaps of diamond. *Physical Review B*, 35(11):5856.

[Falk, 2018] Falk, K. (2018). Experimental methods for warm dense matter research. *High Power Laser Science and Engineering*, 6:e59.

[Farid et al., 1993] Farid, B., Heine, V., Engel, G., and Robertson, I. (1993). Extremal properties of the harris-foulkes functional and an improved screening calculation for the electron gas. *Physical Review B*, 48(16):11602.

[Ferrario et al., 2007] Ferrario, M., Ciccotti, G., and Binder, K. (2007). *Computer Simulations in Condensed Matter: From Materials to Chemical Biology. Volume 1*, volume 703. Springer.

[Ferroir et al., 2010] Ferroir, T., Dubrovinsky, L., El Goresy, A., Simionovici, A., Nakamura, T., and Gillet, P. (2010). Carbon polymorphism in shocked meteorites: Evidence for new natural ultrahard phases. *Earth and Planetary Science Letters*, 290(1-2):150–154.

[Festenberg, 1967] Festenberg, C. v. (1967). Zur dämpfung des al-15 ev-plasmaverlustes in abhängigkeit vom streuwinkel und der kristallitgröße. *Zeitschrift für Physik*, 207(1):47–55.

[Feynman, 1939] Feynman, R. P. (1939). Forces in molecules. *Phys. Rev.*, 56:340–343.

[Filinov et al., 2012] Filinov, V. S., Bonitz, M., Fehske, H., Fortov, V. E., and Levashov, P. R. (2012). Proton crystallization in a dense hydrogen plasma. *Contributions to Plasma Physics*, 52(3):224–228.

[Fiquet et al., 2019] Fiquet, G., Narayana, C., Bellin, C., Shukla, A., Estève, I., Ruoff, A. L., Garbarino, G., and Mezouar, M. (2019). Structural phase transitions in aluminium above 320 gpa. *Comptes Rendus Géoscience*, 351(2-3):243–252.

[Fleszar et al., 1995] Fleszar, A., Quong, A. A., and Eguiluz, A. G. (1995). Band-structure and many-body effects in the dynamical response of aluminum metal. *Physical review letters*, 74(4):590.

[Fletcher et al., 2015] Fletcher, L., Lee, H., Döppner, T., Galtier, E., Nagler, B., Heimann, P., Fortmann, C., LePape, S., Ma, T., Millot, M., et al. (2015). Ultrabright x-ray laser scattering for dynamic warm dense matter physics. *Nature photonics*, 9(4):274–279.

[Fortmann, 2014] Fortmann, C. (2014). Dynamical structure factor in high energy density plasmas and application to x-ray thomson scattering. In *Frontiers and Challenges in Warm Dense Matter*, pages 177–201. Springer.

[Fortmann et al., 2010] Fortmann, C., Wierling, A., and Röpke, G. (2010). Influence of local-field corrections on thomson scattering in collision-dominated two-component plasmas. *Physical Review E*, 81(2):026405.

[Fried and Howard, 2000] Fried, L. E. and Howard, W. M. (2000). Explicit gibbs free energy equation of state applied to the carbon phase diagram. *Phys. Rev. B*, 61:8734–8743.

[Frondel and Marvin, 1967] Frondel, C. and Marvin, U. B. (1967). Lonsdaleite, a hexagonal polymorph of diamond. *Nature*, 214(5088):587.

[Frydrych et al., 2020] Frydrych, S., Vorberger, J., Hartley, N. J., Schuster, A. K., Ramakrishna, K., Saunders, A. M., van Driel, T., Falcone, R. W., Fletcher, L. B., Galtier, E., Gamboa, E. J., Glenzer, S. H., Granados, E., MacDonald, M. J., MacKinnon, A. J., McBride, E. E., Nam, I., Neumayer, P., Pak, A., Voigt, K., Roth, M., Sun, P., Gericke, D. O., Döppner, T., and Kraus, D. (2020). Demonstration of x-ray thomson scattering as diagnostics for miscibility in warm dense matter. *Nature Communications*, 11(1):2620.

[Frydrych, 2018] Frydrych, S. A. (2018). *Entmischung von Elementen in warmer dichter Materie*. PhD thesis, Technische Universität Darmstadt.

[Galambosi et al., 2007] Galambosi, S., Soininen, J. A., Nygård, K., Huotari, S., and Hämäläinen, K. (2007). Symmetry of the 1*s* core exciton in diamond studied using x-ray raman scattering. *Phys. Rev. B*, 76:195112.

[Galassi et al., 2002] Galassi, M., Davies, J., Theiler, J., Gough, B., Jungman, G., Alken, P., Booth, M., Rossi, F., and Ulerich, R. (2002). *GNU scientific library*. Citeseer.

[Gamboa et al., 2016] Gamboa, E., Fletcher, L., Lee, H., MacDonald, M., Zastrau, U., Gauthier, M., Gericke, D., Vorberger, J., Granados, E., Hastings, J., et al. (2016). Band gap opening in strongly compressed diamond observed by x-ray energy loss spectroscopy. Technical report, SLAC National Accelerator Lab., Menlo Park, CA (United States).

[Gao, 2015] Gao, S.-P. (2015). Band gaps and dielectric functions of cubic and hexagonal diamond polytypes calculated by many-body perturbation theory. *physica status solidi (b)*, 252(1):235–242.

[Geim, 2009] Geim, A. K. (2009). Graphene: status and prospects. *science*, 324(5934):1530–1534.

[Gell-Mann and Brueckner, 1957] Gell-Mann, M. and Brueckner, K. A. (1957). Correlation energy of an electron gas at high density. *Phys. Rev.*, 106:364–368.

[Geneste et al., 2012] Geneste, G., Torrent, M., Bottin, F. m. c., and Loubeyre, P. (2012). Strong isotope effect in phase ii of dense solid hydrogen and deuterium. *Phys. Rev. Lett.*, 109:155303.

[Giannozzi et al., 2017] Giannozzi, P., Andreussi, O., Brumme, T., Bunau, O., Nardelli, M. B., Calandra, M., Car, R., Cavazzoni, C., Ceresoli, D., Cococcioni, M., et al. (2017). Advanced capabilities for materials modelling with quantum espresso. *Journal of Physics: Condensed Matter*, 29(46):465901.

[Giannozzi et al., 2009] Giannozzi, P., Baroni, S., Bonini, N., Calandra, M., Car, R., Cavazzoni, C., Ceresoli, D., Chiarotti, G. L., Cococcioni, M., Dabo, I., et al. (2009). Quantum espresso: a modular and open-source software project for quantum simulations of materials. *Journal of physics: Condensed matter*, 21(39):395502.

[Gibbons et al., 1976] Gibbons, P., Schnatterly, S., Ritsko, J., and Fields, J. (1976). Line shape of the plasma resonance in simple metals. *Physical Review B*, 13(6):2451.

[Giuliani and Vignale, 2005] Giuliani, G. and Vignale, G. (2005). *Quantum Theory of the Electron Liquid*. Cambridge University Press.

[Glenzer et al., 2007] Glenzer, S. H., Landen, O. L., Neumayer, P., Lee, R. W., Widmann, K., Pollaine, S. W., Wallace, R. J., Gregori, G., Höll, A., Bornath, T., Thiele, R., Schwarz, V., Kraeft, W.-D., and Redmer, R. (2007). Observations of plasmons in warm dense matter. *Phys. Rev. Lett.*, 98:065002.

[Glenzer and Redmer, 2009] Glenzer, S. H. and Redmer, R. (2009). X-ray thomson scattering in high energy density plasmas. *Reviews of Modern Physics*, 81(4):1625.

[Glosli and Ree, 1999] Glosli, J. N. and Ree, F. H. (1999). Liquid-liquid phase transformation in carbon. *Phys. Rev. Lett.*, 82:4659–4662.

[Goedecker et al., 1996] Goedecker, S., Teter, M., and Hutter, J. (1996). Separable dual-space gaussian pseudopotentials. *Phys. Rev. B*, 54:1703–1710.

[Golze et al., 2019] Golze, D., Dvorak, M., and Rinke, P. (2019). The gw compendium: A practical guide to theoretical photoemission spectroscopy. *Frontiers in chemistry*, 7:377.

[Goncharov, 2020] Goncharov, A. (2020). Phase diagram of hydrogen at extreme pressures and temperatures; updated through 2019. *Low Temperature Physics*, 46(2):97–103.

[Goncharov et al., 2011] Goncharov, A. F., Hemley, R. J., and Mao, H.-k. (2011). Vibron frequencies of solid h2 and d2 to 200 gpa and implications for the p–t phase diagram. *The Journal of chemical physics*, 134(17):174501.

[Gonze et al., 2009] Gonze, X., Amadon, B., Anglade, P.-M., Beuken, J.-M., Bottin, F., Boulanger, P., Bruneval, F., Caliste, D., Caracas, R., Côté, M., et al. (2009). Abinit: First-principles approach to material and nanosystem properties. *Computer Physics Communications*, 180(12):2582–2615.

[Gonze et al., 2020] Gonze, X., Amadon, B., Antonius, G., Arnardi, F., Baguet, L., Beuken, J.-M., Bieder, J., Bottin, F., Bouchet, J., Bousquet, E., et al. (2020). The abinit project: Impact, environment and recent developments. *Computer Physics Communications*, 248:107042.

[Görling, 1996] Görling, A. (1996). Density-functional theory for excited states. *Physical Review A*, 54(5):3912.

[Görling, 1996] Görling, A. (1996). Exact treatment of exchange in kohn-sham band-structure schemes. *Phys. Rev. B*, 53:7024–7029.

[Graziani et al., 2014] Graziani, F., Desjarlais, M., Redmer, R., and Trickey, S. (2014). *Frontiers and Challenges in Warm Dense Matter*. Lecture Notes in Computational Science and Engineering. Springer International Publishing.

[Greenwood, 1958] Greenwood, D. (1958). The boltzmann equation in the theory of electrical conduction in metals. *Proceedings of the Physical Society*, 71(4):585.

[Gross and Kohn, 1985] Gross, E. K. U. and Kohn, W. (1985). Local density-functional theory of frequency-dependent linear response. *Phys. Rev. Lett.*, 55:2850–2852.

[Groth et al., 2017a] Groth, S., Dornheim, T., and Bonitz, M. (2017a). Configuration path integral Monte Carlo approach to the static density response of the warm dense electron gas. *J. Chem. Phys.*, 147(16):164108.

[Groth et al., 2017b] Groth, S., Dornheim, T., and Bonitz, M. (2017b). Free energy of the uniform electron gas: Testing analytical models against first-principles results. *Contributions to Plasma Physics*, 57(3):137–146.

[Groth et al., 2017c] Groth, S., Dornheim, T., Sjostrom, T., Malone, F. D., Foulkes, W. M. C., and Bonitz, M. (2017c). Ab initio exchange-correlation free energy of the uniform electron gas at warm dense matter conditions. *Phys. Rev. Lett.*, 119:135001.

[Groth et al., 2019] Groth, S., Dornheim, T., and Vorberger, J. (2019). Ab initio path integral monte carlo approach to the static and dynamic density response of the uniform electron gas. *Phys. Rev. B*, 99:235122.

[Groth et al., 2016] Groth, S., Schoof, T., Dornheim, T., and Bonitz, M. (2016). Ab initio quantum monte carlo simulations of the uniform electron gas without fixed nodes. *Phys. Rev. B*, 93:085102.

[Grumbach and Martin, 1996] Grumbach, M. P. and Martin, R. M. (1996). Phase diagram of carbon at high pressures and temperatures. *Phys. Rev. B*, 54:15730–15741.

[Gulans et al., 2014] Gulans, A., Kontur, S., Meisenbichler, C., Nabok, D., Pavone, P., Rigamonti, S., Sagmeister, S., Werner, U., and Draxl, C. (2014). Exciting: a full-potential all-electron package implementing density-functional theory and many-body perturbation theory. *Journal of Physics: Condensed Matter*, 26(36):363202.

[Gupta and Rajagopal, 1982] Gupta, U. and Rajagopal, A. (1982). Density functional formalism at finite temperatures with some applications. *Physics Reports*, 87(6):259 – 311.

[Hamann et al., 2020] Hamann, P., Vorberger, J., Dornheim, T., Moldabekov, Z., and Bonitz, M. (2020). Ab initio results for the plasmon dispersion and damping of the warm dense electron gas.

[Hänström and Lazor, 2000] Hänström, A. and Lazor, P. (2000). High pressure melting and equation of state of aluminium. *Journal of alloys and compounds*, 305(1-2):209–215.

[Harding et al., 2022] Harding, B. P., Mauri, Z., and Pribram-Jones, A. (2022). Approximate bounds and temperature dependence of adiabatic connection integrands for the uniform electron gas. *The Journal of Chemical Physics*, 156(13):134104.

[Hartley et al., 2018] Hartley, N., Vorberger, J., Döppner, T., Cowan, T., Falcone, R., Fletcher, L., Frydrych, S., Galtier, E., Gamboa, E., Gericke, D., et al. (2018). Liquid structure of shock-compressed hydrocarbons at megabar pressures. *Physical review letters*, 121(24):245501.

[Haydock, 1980] Haydock, R. (1980). The recursive solution of the schrodinger equation. In *Solid state physics*, volume 35, pages 215–294. Elsevier.

[Hedin, 1965] Hedin, L. (1965). New method for calculating the one-particle green's function with application to the electron-gas problem. *Phys. Rev.*, 139:A796–A823.

[Hedin and Lundqvist, 1970] Hedin, L. and Lundqvist, S. (1970). Effects of electron-electron and electron-phonon interactions on the one-electron states of solids. In *Solid state physics*, volume 23, pages 1–181. Elsevier.

[Helled et al., 2020] Helled, R., Mazzola, G., and Redmer, R. (2020). Understanding dense hydrogen at planetary conditions. *Nature Reviews Physics*, 2(10):562–574.

[Hellmann, 2015] Hellmann, H. (2015). *Hans Hellmann: Einführung in Die Quantenchemie: Mit Biografischen Notizen von Hans Hellmann Jr.* Springer-Verlag.

[Heyd et al., 2003] Heyd, J., Scuseria, G. E., and Ernzerhof, M. (2003). Hybrid functionals based on a screened coulomb potential. *The Journal of chemical physics*, 118(18):8207–8215.

[Hinz et al., 2020] Hinz, J., Karasiev, V. V., Hu, S., Zaghoo, M., Mejía-Rodríguez, D., Trickey, S., and Calderín, L. (2020). Fully consistent density functional theory determination of the insulator-metal transition boundary in warm dense hydrogen. *Physical Review Research*, 2(3):032065.

[Höhberger et al., 1975] Höhberger, H., Otto, A., and Petri, E. (1975). Plasmon resonance in al, deviations from quadratic dispersion observed. *Solid State Communications*, 16(1):175–179.

[Hohenberg and Kohn, 1964] Hohenberg, P. and Kohn, W. (1964). Inhomogeneous electron gas. *Physical review*, 136(3B):B864.

[Höll et al., 2007] Höll, A., Bornath, T., Cao, L., Döppner, T., Düsterer, S., Förster, E., Fortmann, C., Glenzer, S., Gregori, G., Laarmann, T., et al. (2007). Thomson scattering from near-solid density plasmas using soft x-ray free electron lasers. *High Energy Density Physics*, 3(1-2):120–130.

[Hoover, 1985] Hoover, W. G. (1985). Canonical dynamics: Equilibrium phase-space distributions. *Phys. Rev. A*, 31:1695–1697.

[Howie et al., 2015] Howie, R. T., Dalladay-Simpson, P., and Gregoryanz, E. (2015). Raman spectroscopy of hot hydrogen above 200 gpa. *Nature materials*, 14(5):495–499.

[Hu et al., 2011] Hu, S. X., Militzer, B., Goncharov, V. N., and Skupsky, S. (2011). First-principles equation-of-state table of deuterium for inertial confinement fusion applications. *Phys. Rev. B*, 84:224109.

[Hubbard, 1957] Hubbard, J. (1957). The description of collective motions in terms of many-body perturbation theory. *Proceedings of the Royal Society of London. Series A. Mathematical and Physical Sciences*, 240(1223):539–560.

[Hummer et al., 2009] Hummer, K., Harl, J., and Kresse, G. (2009). Heyd-scuseria-ernzerhof hybrid functional for calculating the lattice dynamics of semiconductors. *Physical Review B*, 80(11):115205.

[Huotari et al., 2008] Huotari, S., Sternemann, C., Schülke, W., Sturm, K., Lustfeld, H., Sternemann, H., Volmer, M., Gusarov, A., Müller, H., and Monaco, G. (2008). Electron-density dependence of double-plasmon excitations in simple metals. *Physical Review B*, 77(19):195125.

[Hurricane et al., 2014] Hurricane, O., Callahan, D., Casey, D., Celliers, P., Cerjan, C., Dewald, E., Dittrich, T., Döppner, T., Hinkel, D., Hopkins, L. B., et al. (2014). Fuel gain exceeding unity in an inertially confined fusion implosion. *Nature*, 506(7488):343.

[Hutter et al., 2014] Hutter, J., Iannuzzi, M., Schiffmann, F., and VandeVondele, J. (2014). cp2k: atomistic simulations of condensed matter systems. *Wiley Interdisciplinary Reviews: Computational Molecular Science*, 4(1):15–25.

[Ichimaru, 1982] Ichimaru, S. (1982). Strongly coupled plasmas: high-density classical plasmas and degenerate electron liquids. *Reviews of Modern Physics*, 54(4):1017.

[Ichimaru et al., 1987] Ichimaru, S., Iyetomi, H., and Tanaka, S. (1987). Statistical physics of dense plasmas: Thermodynamics, transport coefficients and dynamic correlations. *Physics Reports*, 149(2-3):91–205.

[Ichimaru and Utsumi, 1981] Ichimaru, S. and Utsumi, K. (1981). Analytic expression for the dielectric screening function of strongly coupled electron liquids at metallic and lower densities. *Phys. Rev. B*, 24:7385–7388.

[Ichimuru, 2004] Ichimuru, S. (2004). Statistical plasma physics, volume ii: Condensed plasmas, vol. 2 of. *Frontiers in Physics*.

[Inaoka et al., 2014] Inaoka, T., Sugiyama, Y., and Sato, K. (2014). Exchange–correlation and temperature effects on plasmons in strongly correlated two-dimensional electron systems: Finite-temperature local-field-correction theory combined with angle-resolved raman spectroscopy. *physica status solidi (b)*, 251(5):980–990.

[Johnson, 1988] Johnson, D. D. (1988). Modified broyden's method for accelerating convergence in self-consistent calculations. *Phys. Rev. B*, 38:12807–12813.

[Johnston and Hoffmann, 1989] Johnston, R. L. and Hoffmann, R. (1989). Superdense carbon, c8: supercubane or analog of. gamma.-silicon? *Journal of the American Chemical Society*, 111(3):810–819.

[Joly, 2001] Joly, Y. (2001). X-ray absorption near-edge structure calculations beyond the muffin-tin approximation. *Phys. Rev. B*, 63:125120.

[Karasiev et al., 2019a] Karasiev, V., Hu, S., Zaghoo, M., and Boehly, T. (2019a). Exchange-correlation thermal effects in shocked deuterium: Softening the principal hugoniot and thermophysical properties. *Physical Review B*, 99(21):214110.

[Karasiev et al., 2016] Karasiev, V. V., Calderín, L., and Trickey, S. B. (2016). Importance of finite-temperature exchange correlation for warm dense matter calculations. *Phys. Rev. E*, 93:063207.

[Karasiev et al., 2013] Karasiev, V. V., Chakraborty, D., Shukruto, O. A., and Trickey, S. B. (2013). Nonempirical generalized gradient approximation free-energy functional for orbital-free simulations. *Phys. Rev. B*, 88:161108.

[Karasiev et al., 2018a] Karasiev, V. V., Dufty, J. W., and Trickey, S. (2018a). Nonempirical semilocal free-energy density functional for matter under extreme conditions. *Physical review letters*, 120(7):076401.

[Karasiev et al., 2018b] Karasiev, V. V., Dufty, J. W., and Trickey, S. B. (2018b). Nonempirical semilocal free-energy density functional for matter under extreme conditions. *Phys. Rev. Lett.*, 120:076401.

[Karasiev et al., 2019b] Karasiev, V. V., Hu, S. X., Zaghoo, M., and Boehly, T. R. (2019b). Exchange-correlation thermal effects in shocked deuterium: Softening the principal hugoniot and thermophysical properties. *Phys. Rev. B*, 99:214110.

[Karasiev et al., 2022] Karasiev, V. V., Mihaylov, D. I., and Hu, S. X. (2022). Meta-gga exchange-correlation free energy density functional to increase the accuracy of warm dense matter simulations. *Phys. Rev. B*, 105:L081109.

[Karasiev et al., 2014a] Karasiev, V. V., Sjostrom, T., Chakraborty, D., Dufty, J. W., Runge, K., Harris, F. E., and Trickey, S. (2014a). Innovations in finite-temperature density functionals. In *Frontiers and Challenges in Warm Dense Matter*, pages 61–85. Springer.

[Karasiev et al., 2014b] Karasiev, V. V., Sjostrom, T., Dufty, J., and Trickey, S. (2014b). Accurate homogeneous electron gas exchange-correlation free energy for local spin-density calculations. *Physical review letters*, 112(7):076403.

[Karasiev et al., 2014c] Karasiev, V. V., Sjostrom, T., and Trickey, S. (2014c). Finite-temperature orbital-free dft molecular dynamics: Coupling profess and quantum espresso. *Computer Physics Communications*, 185(12):3240 – 3249.

[Karasiev et al., 2012] Karasiev, V. V., Sjostrom, T., and Trickey, S. B. (2012). Comparison of density functional approximations and the finite-temperature hartree-fock approximation in warm dense lithium. *Phys. Rev. E*, 86:056704.

[Karasiev and Trickey, 2012] Karasiev, V. V. and Trickey, S. B. (2012). Issues and challenges in orbital-free density functional calculations. *Computer Physics Communications*, 183(12):2519–2527.

[Kasper and Richards, 1964] Kasper, J. and Richards, S. (1964). The crystal structures of new forms of silicon and germanium. *Acta Crystallographica*, 17(6):752–755.

[Keldysh et al., 1965] Keldysh, L. V. et al. (1965). Diagram technique for nonequilibrium processes. *Sov. Phys. JETP*, 20(4):1018–1026.

[Kloos, 1973] Kloos, T. (1973). Plasmaschwingungen in al, mg, li, na und k angeregt durch schnelle elektronen. *Zeitschrift für Physik A Hadrons and nuclei*, 265(3):225–238.

[Knudson et al., 2008] Knudson, M., Desjarlais, M., and Dolan, D. (2008). Shock-wave exploration of the high-pressure phases of carbon. *Science*, 322(5909):1822–1825.

[Knudson et al., 2015] Knudson, M. D., Desjarlais, M. P., Becker, A., Lemke, R. W., Cochrane, K. R., Savage, M. E., Bliss, D. E., Mattsson, T. R., and Redmer, R. (2015). Direct observation of an abrupt insulator-to-metal transition in dense liquid deuterium. *Science*, 348(6242):1455–1460.

[Kohn and Sham, 1965] Kohn, W. and Sham, L. J. (1965). Self-consistent equations including exchange and correlation effects. *Physical review*, 140(4A):A1133.

[Krane, 1978] Krane, K. J. (1978). Dispersion and damping of volume plasmons in polycrystalline aluminium and indium. *Journal of Physics F: Metal Physics*, 8(10):2133–2137.

[Kraus, 2012] Kraus, D. (2012). *Characterization of phase transitions in warm dense matter with X-ray scattering*. PhD thesis, Technische Universität Darmstadt.

[Kraus et al., 2018] Kraus, D., Hartley, N., Frydrych, S., Schuster, A., Rohatsch, K., Rödel, M., Cowan, T., Brown, S., Cunningham, E., Van Driel, T., et al. (2018). High-pressure chemistry of hydrocarbons relevant to planetary interiors and inertial confinement fusion. *Physics of Plasmas*, 25(5):056313.

[Kraus et al., 2016] Kraus, D., Ravasio, A., Gauthier, M., Gericke, D., Vorberger, J., Frydrych, S., Helfrich, J., Fletcher, L., Schaumann, G., Nagler, B., et al. (2016). Nanosecond formation of diamond and lonsdaleite by shock compression of graphite. *Nature communications*, 7:10970.

[Kraus et al., 2017] Kraus, D., Vorberger, J., Pak, A., Hartley, N., Fletcher, L., Frydrych, S., Galtier, E., Gamboa, E., Gericke, D., Glenzer, S., et al. (2017). Formation of diamonds in laser-compressed hydrocarbons at planetary interior conditions. *Nature Astronomy*, 1(9):606.

[Kremp et al., 2006] Kremp, D., Schlanges, M., and Kraeft, W.-D. (2006). *Quantum statistics of nonideal plasmas*, volume 25. Springer Science & Business Media.

[Kresse and Furthmüller, 1996a] Kresse, G. and Furthmüller, J. (1996a). Efficiency of ab-initio total energy calculations for metals and semiconductors using a plane-wave basis set. *Computational materials science*, 6(1):15–50.

[Kresse and Furthmüller, 1996b] Kresse, G. and Furthmüller, J. (1996b). Efficient iterative schemes for ab initio total-energy calculations using a plane-wave basis set. *Physical review B*, 54(16):11169.

[Kresse and Hafner, 1993] Kresse, G. and Hafner, J. (1993). Ab initio molecular dynamics for liquid metals. *Physical Review B*, 47(1):558.

[Kresse and Joubert, 1999] Kresse, G. and Joubert, D. (1999). From ultrasoft pseudopotentials to the projector augmented-wave method. *Physical review b*, 59(3):1758.

[Kritcher et al., 2020] Kritcher, A. L., Swift, D. C., Döppner, T., Bachmann, B., Benedict, L. X., Collins, G. W., DuBois, J. L., Elsner, F., Fontaine, G., Gaffney, J. A., et al. (2020). A measurement of the equation of state of carbon envelopes of white dwarfs. *Nature*, 584(7819):51–54.

[Kubo, 1957] Kubo, R. (1957). Statistical-mechanical theory of irreversible processes. i. general theory and simple applications to magnetic and conduction problems. *Journal of the Physical Society of Japan*, 12(6):570–586.

[Kubo, 1966] Kubo, R. (1966). The fluctuation-dissipation theorem. *Reports on progress in physics*, 29(1):255.

[Kudasov et al., 2013] Kudasov, Y. B., Surdin, O., Korshunov, A., Pavlov, V., Frolova, N., and Kuzin, R. (2013). Lattice dynamics and phase diagram of aluminum at high temperatures. *Journal of Experimental and Theoretical Physics*, 117(4):664–671.

[Landau, 1946] Landau, L. D. (1946). On the vibrations of the electronic plasma. *Zh. Eksp. Teor. Fiz.*, 10:25.

[Larder et al., 2019] Larder, B., Gericke, D., Richardson, S., Mabey, P., White, T., and Gregori, G. (2019). Fast nonadiabatic dynamics of many-body quantum systems. *Science Advances*, 5(11):eaaw1634.

[Larson et al., 1996] Larson, B. C., Tischler, J. Z., Isaacs, E. D., Zschack, P., Fleszar, A., and Eguiluz, A. G. (1996). Inelastic x-ray scattering as a probe of the many-body local-field factor in metals. *Phys. Rev. Lett.*, 77:1346–1349.

[LeBlanc et al., 2022] LeBlanc, J. P. F., Chen, K., Haule, K., Prokof'ev, N. V., and Tupitsyn, I. S. (2022). Dynamic response of the electron gas: Towards the exact exchange-correlation kernel. *arXiv preprint arXiv:2205.13595*.

[Lee et al., 1988] Lee, C., Yang, W., and Parr, R. G. (1988). Development of the colle-salvetti correlation-energy formula into a functional of the electron density. *Phys. Rev. B*, 37:785–789.

[Lee et al., 2010] Lee, K., Murray, É. D., Kong, L., Lundqvist, B. I., and Langreth, D. C. (2010). Higher-accuracy van der waals density functional. *Physical Review B*, 82(8):081101.

[Lee and Chang, 1994] Lee, K.-H. and Chang, K. J. (1994). First-principles study of the optical properties and the dielectric response of al. *Phys. Rev. B*, 49:2362–2367.

[Lehtola et al., 2018] Lehtola, S., Steigemann, C., Oliveira, M. J., and Marques, M. A. (2018). Recent developments in libxc — a comprehensive library of functionals for density functional theory. *SoftwareX*, 7:1 – 5.

[Levy, 1995] Levy, M. (1995). Excitation energies from density-functional orbital energies. *Phys. Rev. A*, 52:R4313–R4315.

[Li et al., 2017a] Li, P., Ren, X., and He, L. (2017a). First-principles calculations and model analysis of plasmon excitations in graphene and graphene/hbn heterostructure. *Phys. Rev. B*, 96:165417.

[Li et al., 2005] Li, X., Tully, J. C., Schlegel, H. B., and Frisch, M. J. (2005). Ab initio ehrenfest dynamics. *The Journal of chemical physics*, 123(8):084106.

[Li et al., 2012] Li, X.-Z., Gomez-Abal, R., Jiang, H., Ambrosch-Draxl, C., and Scheffler, M. (2012). Impact of widely used approximations to the g_0w_0 method: An all-electron perspective. *New Journal of Physics*, 14(2):023006.

[Li et al., 2017b] Li, Z.-G., Zhang, W., Fu, Z.-J., Dai, J.-Y., Chen, Q.-F., and Chen, X.-R. (2017b). Benchmarking the diffusion and viscosity of h-he mixtures in warm dense matter regime by quantum molecular dynamics simulations. *Physics of Plasmas*, 24(5):052903.

[Li et al., 2015] Li, Z.-Z., Lian, C.-S., Xu, J., Xu, L.-F., Wang, J.-T., and Chen, C. (2015). Computational prediction of body-centered cubic carbon in an all-s p 3 six-member ring configuration. *Physical Review B*, 91(21):214106.

[Lindhard, 1954] Lindhard, J. (1954). On the properties of a gas of charged particles. *Dan. Vid. Selsk Mat.-Fys. Medd.*, 28:8.

[Liu et al., 2018] Liu, L., Li, Z.-G., Dai, J.-Y., Chen, Q.-F., and Chen, X.-R. (2018). Quantum molecular dynamics study on the proton exchange, ionic structures, and transport properties of warm dense hydrogen-deuterium mixtures. *Phys. Rev. E*, 97:063204.

[Loos and Gill, 2016] Loos, P.-F. and Gill, P. M. W. (2016). The uniform electron gas. *Wiley Interdisciplinary Reviews: Computational Molecular Science*, 6(4):410–429.

[Lorenzen et al., 2010] Lorenzen, W., Holst, B., and Redmer, R. (2010). First-order liquid-liquid phase transition in dense hydrogen. *Phys. Rev. B*, 82:195107.

[Lu et al., 2019] Lu, B., Kang, D., Wang, D., Gao, T., and Dai, J. (2019). Towards the same line of liquid–liquid phase transition of dense hydrogen from various theoretical predictions$*.ChinesePhysicsLetters, 36(10):103102$.

[Luo et al., 2018] Luo, K., Karasiev, V. V., and Trickey, S. (2018). A simple generalized gradient approximation for the noninteracting kinetic energy density functional. *Physical Review B*, 98(4):041111.

[Luo et al., 2020] Luo, K., Karasiev, V. V., and Trickey, S. (2020). Towards accurate orbital-free simulations: A generalized gradient approximation for the noninteracting free energy density functional. *Physical Review B*, 101(7):075116.

[MacFarlane et al., 2006] MacFarlane, J., Golovkin, I., and Woodruff, P. (2006). Helios-cr–a 1-d radiation-magnetohydrodynamics code with inline atomic kinetics modeling. *Journal of Quantitative Spectroscopy and Radiative Transfer*, 99(1-3):381–397.

[Madelung, 2012] Madelung, O. (2012). *Semiconductors: group IV elements and III-V compounds*. Springer Science & Business Media.

[Magyar et al., 2016] Magyar, R. J., Shulenburger, L., and Baczewski, A. (2016). Stopping of deuterium in warm dense deuterium from ehrenfest time-dependent density functional theory. *Contributions to Plasma Physics*, 56(5):459–466.

[Mahan, 2013] Mahan, G. D. (2013). *Many-particle physics*. Springer Science & Business media.

[Malone et al., 2016] Malone, F. D., Blunt, N. S., Brown, E. W., Lee, D. K. K., Spencer, J. S., Foulkes, W. M. C., and Shepherd, J. J. (2016). Accurate exchange-correlation energies for the warm dense electron gas. *Phys. Rev. Lett.*, 117:115701.

[Malone et al., 2015] Malone, F. D., Blunt, N. S., Shepherd, J. J., Lee, D. K. K., Spencer, J. S., and Foulkes, W. M. C. (2015). Interaction picture density matrix quantum monte carlo. *The Journal of Chemical Physics*, 143(4):044116.

[Mao et al., 2001] Mao, H.-k., Kao, C., and Hemley, R. J. (2001). Inelastic x-ray scattering at ultrahigh pressures. *Journal of Physics: Condensed Matter*, 13(34):7847.

[Marini, 2008] Marini, A. (2008). Ab initio finite-temperature excitons. *Physical review letters*, 101(10):106405.

[Marini et al., 2009] Marini, A., Hogan, C., Grüning, M., and Varsano, D. (2009). Yambo: an ab initio tool for excited state calculations. *Computer Physics Communications*, 180(8):1392–1403.

[Marques et al., 2006] Marques, M., Ullrich, C. A., Nogueira, F., Rubio, A., Burke, K., and Gross, E. K. (2006). *Time-dependent density functional theory*. Springer Berlin.

[Marques and Gross, 2004] Marques, M. A. and Gross, E. K. (2004). Time-dependent density functional theory. *Annu. Rev. Phys. Chem.*, 55:427–455.

[Marques et al., 2012] Marques, M. A., Oliveira, M. J., and Burnus, T. (2012). Libxc: A library of exchange and correlation functionals for density functional theory. *Computer Physics Communications*, 183(10):2272 – 2281.

[Marshall et al., 2022] Marshall, M., Gorman, M., Polsin, D., Eggert, J., Ginnane, M., Rygg, J., Collins, G., and Leininger, L. (2022). Diamond formation in double-shocked epoxy to 150 gpa. *Journal of Applied Physics*, 131(8):085904.

[Martin, 2020] Martin, R. M. (2020). *Electronic structure: basic theory and practical methods*. Cambridge university press.

[Martin et al., 2016] Martin, R. M., Reining, L., and Ceperley, D. M. (2016). *Interacting Electrons: Theory and Computational Approaches*. Cambridge University Press.

[Martinez-Canales et al., 2012] Martinez-Canales, M., Pickard, C. J., and Needs, R. J. (2012). Thermodynamically stable phases of carbon at multiterapascal pressures. *Physical review letters*, 108(4):045704.

[Marzari et al., 1999] Marzari, N., Vanderbilt, D., De Vita, A., and Payne, M. (1999). Thermal contraction and disordering of the al (110) surface. *Physical review letters*, 82(16):3296.

[Mattsson et al., 2010] Mattsson, T. R., Lane, J. M. D., Cochrane, K. R., Desjarlais, M. P., Thompson, A. P., Pierce, F., and Grest, G. S. (2010). First-principles and classical molecular dynamics simulation of shocked polymers. *Phys. Rev. B*, 81:054103.

[Mazevet et al., 2005] Mazevet, S., Desjarlais, M. P., Collins, L. A., Kress, J. D., and Magee, N. H. (2005). Simulations of the optical properties of warm dense aluminum. *Phys. Rev. E*, 71:016409.

[Mazevet et al., 2010] Mazevet, S., Torrent, M., Recoules, V., and Jollet, F. (2010). Calculations of the transport properties within the paw formalism. *High Energy Density Physics*, 6(1):84–88.

[Mazzola et al., 2018] Mazzola, G., Helled, R., and Sorella, S. (2018). Phase diagram of hydrogen and a hydrogen-helium mixture at planetary conditions by quantum monte carlo simulations. *Phys. Rev. Lett.*, 120:025701.

[McCulloch et al.,] McCulloch, D. G., Wong, S., Shiell, T. B., Haberl, B., Cook, B. A., Huang, X., Boehler, R., McKenzie, D. R., and Bradby, J. E. Investigation of room temperature formation of the ultra-hard nanocarbons diamond and lonsdaleite. *Small*, n/a(n/a):2004695.

[McMahon et al., 2012] McMahon, J. M., Morales, M. A., Pierleoni, C., and Ceperley, D. M. (2012). The properties of hydrogen and helium under extreme conditions. *Rev. Mod. Phys.*, 84:1607–1653.

[Mehl et al., 2017] Mehl, M. J., Hicks, D., Toher, C., Levy, O., Hanson, R. M., Hart, G., and Curtarolo, S. (2017). The aflow library of crystallographic prototypes: part 1. *Computational Materials Science*, 136:S1–S828.

[Mermin, 1965] Mermin, N. D. (1965). Thermal properties of the inhomogeneous electron gas. *Phys. Rev.*, 137:A1441–A1443.

[Mermin, 1970] Mermin, N. D. (1970). Lindhard dielectric function in the relaxation-time approximation. *Physical Review B*, 1(5):2362.

[Methfessel and Paxton, 1989] Methfessel, M. and Paxton, A. T. (1989). High-precision sampling for brillouin-zone integration in metals. *Phys. Rev. B*, 40:3616–3621.

[Mihaylov et al., 2020] Mihaylov, D. I., Karasiev, V. V., and Hu, S. X. (2020). Thermal hybrid exchange-correlation density functional for improving the description of warm dense matter. *Phys. Rev. B*, 101:245141.

[Militzer and Pollock, 2002] Militzer, B. and Pollock, E. L. (2002). Lowering of the kinetic energy in interacting quantum systems. *Phys. Rev. Lett.*, 89:280401.

[Mo et al., 2018] Mo, C., Fu, Z., Kang, W., Zhang, P., and He, X. (2018). First-principles estimation of electronic temperature from x-ray thomson scattering spectrum of isochorically heated warm dense matter. *Physical review letters*, 120(20):205002.

[Mo et al., 2020] Mo, C., Fu, Z.-G., Zhang, P., Kang, W., Zhang, W., and He, X. T. (2020). First-principles method for x-ray thomson scattering including both elastic and inelastic features in warm dense matter. *Phys. Rev. B*, 102:195127.

[Momma and Izumi, 2011] Momma, K. and Izumi, F. (2011). *VESTA3* for three-dimensional visualization of crystal, volumetric and morphology data. *Journal of Applied Crystallography*, 44(6):1272–1276.

[Monkhorst and Pack, 1976] Monkhorst, H. J. and Pack, J. D. (1976). Special points for brillouin-zone integrations. *Physical review B*, 13(12):5188.

[Monserrat and Needs, 2014] Monserrat, B. and Needs, R. (2014). Comparing electron-phonon coupling strength in diamond, silicon, and silicon carbide: First-principles study. *Physical Review B*, 89(21):214304.

[Morales et al., 2013] Morales, M. A., McMahon, J. M., Pierleoni, C., and Ceperley, D. M. (2013). Nuclear quantum effects and nonlocal exchange-correlation functionals applied to liquid hydrogen at high pressure. *Physical review letters*, 110(6):065702.

[Morales et al., 2010a] Morales, M. A., Pierleoni, C., and Ceperley, D. M. (2010a). Equation of state of metallic hydrogen from coupled electron-ion monte carlo simulations. *Phys. Rev. E*, 81:021202.

[Morales et al., 2010b] Morales, M. A., Pierleoni, C., Schwegler, E., and Ceperley, D. M. (2010b). Evidence for a first-order liquid-liquid transition in high-pressure hydrogen from ab initio simulations. *Proceedings of the National Academy of Sciences*, 107(29):12799–12803.

[Moroni et al., 1992] Moroni, S., Ceperley, D. M., and Senatore, G. (1992). Static response from quantum monte carlo calculations. *Phys. Rev. Lett.*, 69:1837–1840.

[Moroni et al., 1995] Moroni, S., Ceperley, D. M., and Senatore, G. (1995). Static response and local field factor of the electron gas. *Phys. Rev. Lett.*, 75:689–692.

[Moses et al., 2009] Moses, E. I., Boyd, R. N., Remington, B. A., Keane, C. J., and Al-Ayat, R. (2009). The national ignition facility: Ushering in a new age for high energy density science. *Physics of Plasmas*, 16(4):041006.

[Németh et al., 2014] Németh, P., Garvie, L. A., Aoki, T., Dubrovinskaia, N., Dubrovinsky, L., and Buseck, P. R. (2014). Lonsdaleite is faulted and twinned cubic diamond and does not exist as a discrete material. *Nature communications*, 5:5447.

[Nettelmann et al., 2008] Nettelmann, N., Holst, B., Kietzmann, A., French, M., Redmer, R., and Blaschke, D. (2008). Ab initio equation of state data for hydrogen, helium, and water and the internal structure of jupiter. *The Astrophysical Journal*, 683(2):1217.

[Nosé, 1984a] Nosé, S. (1984a). A molecular dynamics method for simulations in the canonical ensemble. *Molecular physics*, 52(2):255–268.

[Nosé, 1984b] Nosé, S. (1984b). A unified formulation of the constant temperature molecular dynamics methods. *The Journal of chemical physics*, 81(1):511–519.

[Occelli et al., 2003] Occelli, F., Loubeyre, P., and LeToullec, R. (2003). Properties of diamond under hydrostatic pressures up to 140 gpa. *Nature materials*, 2(3):151.

[Ojanperä et al., 2012] Ojanperä, A., Havu, V., Lehtovaara, L., and Puska, M. (2012). Nonadiabatic ehrenfest molecular dynamics within the projector augmented-wave method. *The Journal of chemical physics*, 136(14):144103.

[Oliveira et al., 1990] Oliveira, L. N., Gross, E. K., and Kohn, W. (1990). Ensemble-density functional theory for excited states. *International Journal of Quantum Chemistry*, 38(S24):707–716.

[Onida et al., 2002] Onida, G., Reining, L., and Rubio, A. (2002). Electronic excitations: density-functional versus many-body green's-function approaches. *Reviews of modern physics*, 74(2):601.

[Paier et al., 2008] Paier, J., Marsman, M., and Kresse, G. (2008). Dielectric properties and excitons for extended systems from hybrid functionals. *Physical Review B*, 78(12):121201.

[Painter et al., 1971] Painter, G. S., Ellis, D. E., and Lubinsky, A. R. (1971). Ab initio calculation of the electronic structure and optical properties of diamond using the discrete variational method. *Phys. Rev. B*, 4:3610–3622.

[Pal and Tripathy, 1985] Pal, R. and Tripathy, D. (1985). Plasmon dispersion and linewidth in aluminium. *Pramana*, 24(6):905–910.

[Palik, 1998] Palik, E. D. (1998). *Handbook of optical constants of solids*, volume 3. Academic press.

[Pandey et al., 1974] Pandey, K., Platzman, P., Eisenberger, P., and Foo, E.-N. (1974). Plasmons in periodic solids. *Physical Review B*, 9(12):5046.

[Panholzer et al., 2018] Panholzer, M., Gatti, M., and Reining, L. (2018). Nonlocal and nonadiabatic effects in the charge-density response of solids: A time-dependent density-functional approach. *Phys. Rev. Lett.*, 120:166402.

[Paquin, 1995] Paquin, R. A. (1995). Properties of metals. *Handbook of optics*, 2:35–49.

[Pearson et al., 1993] Pearson, M., Smargiassi, E., and Madden, P. (1993). Ab initio molecular dynamics with an orbital-free density functional. *Journal of Physics: Condensed Matter*, 5(19):3221.

[Pela and Draxl, 2021] Pela, R. R. and Draxl, C. (2021). All-electron full-potential implementation of real-time tddft in exciting. *Electronic Structure*, 3(3):037001.

[Perdew, 1985] Perdew, J. P. (1985). Density functional theory and the band gap problem. *International Journal of Quantum Chemistry*, 28(S19):497–523.

[Perdew et al., 1996a] Perdew, J. P., Burke, K., and Ernzerhof, M. (1996a). Generalized gradient approximation made simple. *Physical review letters*, 77(18):3865.

[Perdew et al., 1996b] Perdew, J. P., Ernzerhof, M., and Burke, K. (1996b). Rationale for mixing exact exchange with density functional approximations. *The Journal of chemical physics*, 105(22):9982–9985.

[Perdew and Levy, 1983] Perdew, J. P. and Levy, M. (1983). Physical content of the exact kohn-sham orbital energies: Band gaps and derivative discontinuities. *Phys. Rev. Lett.*, 51:1884–1887.

[Perdew and Schmidt, 2001] Perdew, J. P. and Schmidt, K. (2001). Jacob's ladder of density functional approximations for the exchange-correlation energy. In *AIP Conference Proceedings*, volume 577, pages 1–20. AIP.

[Perdew and Wang, 1992] Perdew, J. P. and Wang, Y. (1992). Accurate and simple analytic representation of the electron-gas correlation energy. *Phys. Rev. B*, 45:13244–13249.

[Perdew and Zunger, 1981] Perdew, J. P. and Zunger, A. (1981). Self-interaction correction to density-functional approximations for many-electron systems. *Phys. Rev. B*, 23:5048–5079.

[Perrot and Dharma-wardana, 1984] Perrot, F. m. c. and Dharma-wardana, M. W. C. (1984). Exchange and correlation potentials for electron-ion systems at finite temperatures. *Phys. Rev. A*, 30:2619–2626.

[Perrot and Dharma-wardana, 2000] Perrot, F. m. c. and Dharma-wardana, M. W. C. (2000). Spin-polarized electron liquid at arbitrary temperatures: Exchange-correlation energies, electron-distribution functions, and the static response functions. *Phys. Rev. B*, 62:16536–16548.

[Peter and Cardona, 2010] Peter, Y. and Cardona, M. (2010). *Fundamentals of semiconductors: physics and materials properties*. Springer Science & Business Media.

[Petersilka et al., 1996] Petersilka, M., Gossmann, U. J., and Gross, E. K. U. (1996). Excitation energies from time-dependent density-functional theory. *Phys. Rev. Lett.*, 76:1212–1215.

[Petri et al., 1976] Petri, E., Otto, A., and Hanke, W. (1976). Anisotropy of plasmon dispersion in al: An electron correlation effect. *Solid State Communications*, 19(8):711–714.

[Pickard and Needs, 2010] Pickard, C. J. and Needs, R. (2010). Aluminium at terapascal pressures. *Nature materials*, 9(8):624–627.

[Pickard and Needs, 2007] Pickard, C. J. and Needs, R. J. (2007). Structure of phase iii of solid hydrogen. *Nature Physics*, 3(7):473–476.

[Pierleoni et al., 2018] Pierleoni, C., Holzmann, M., and Ceperley, D. M. (2018). Local structure in dense hydrogen at the liquid–liquid phase transition by coupled electron–ion monte carlo. *Contributions to Plasma Physics*, 58(2-3):99–106.

[Pierleoni et al., 2016] Pierleoni, C., Morales, M. A., Rillo, G., Holzmann, M., and Ceperley, D. M. (2016). Liquid–liquid phase transition in hydrogen by coupled electron–ion monte carlo simulations. *Proceedings of the National Academy of Sciences*, 113(18):4953–4957.

[Pines, 2018a] Pines, D. (2018a). *Elementary excitations in solids*. CRC Press.

[Pines, 2018b] Pines, D. (2018b). *Theory of Quantum Liquids: Normal Fermi Liquids*. CRC Press.

[Pines and Bohm, 1952] Pines, D. and Bohm, D. (1952). A collective description of electron interactions: Ii. collective vs individual particle aspects of the interactions. *Physical Review*, 85(2):338.

[Pittalis et al., 2011] Pittalis, S., Proetto, C., Floris, A., Sanna, A., Bersier, C., Burke, K., and Gross, E. K. (2011). Exact conditions in finite-temperature density-functional theory. *Physical review letters*, 107(16):163001.

[Plagemann et al., 2012] Plagemann, K., Sperling, P., Thiele, R., Desjarlais, M., Fortmann, C., Döppner, T., Lee, H., Glenzer, S. H., and Redmer, R. (2012). Dynamic structure factor in warm dense beryllium. *New Journal of Physics*, 14(5):055020.

[Poncé et al., 2014] Poncé, S., Antonius, G., Boulanger, P., Cannuccia, E., Marini, A., Côté, M., and Gonze, X. (2014). Verification of first-principles codes: Comparison of total energies, phonon frequencies, electron–phonon coupling and zero-point motion correction to the gap between abinit and qe/yambo. *Computational materials science*, 83:341–348.

[Preston et al., 2019] Preston, T. R., Appel, K., Brambrink, E., Chen, B., Fletcher, L. B., Fortmann-Grote, C., Glenzer, S. H., Granados, E., Göde, S., Konôpková, Z., Lee, H. J., Marquardt, H., McBride, E. E., Nagler, B., Nakatsutsumi, M., Sperling, P., Witte, B. B. L., and Zastrau, U. (2019). Measurements of the momentum-dependence of plasmonic excitations in matter around 1 mbar using an x-ray free electron laser. *Applied Physics Letters*, 114(1):014101.

[Pribram-Jones and Burke, 2016] Pribram-Jones, A. and Burke, K. (2016). Connection formulas for thermal density functional theory. *Phys. Rev. B*, 93:205140.

[Pribram-Jones et al., 2016] Pribram-Jones, A., Grabowski, P. E., and Burke, K. (2016). Thermal density functional theory: Time-dependent linear response and approximate functionals from the fluctuation-dissipation theorem. *Physical review letters*, 116(23):233001.

[Pribram-Jones et al., 2014] Pribram-Jones, A., Pittalis, S., Gross, E., and Burke, K. (2014). Thermal density functional theory in context. In *Frontiers and Challenges in Warm Dense Matter*, pages 25–60. Springer.

[Provorse and Isborn, 2016] Provorse, M. R. and Isborn, C. M. (2016). Electron dynamics with real-time time-dependent density functional theory. *International Journal of Quantum Chemistry*, 116(10):739–749.

[Quong and Eguiluz, 1993] Quong, A. A. and Eguiluz, A. G. (1993). First-principles evaluation of dynamical response and plasmon dispersion in metals. *Phys. Rev. Lett.*, 70:3955–3958.

[Raether, 2006] Raether, H. (2006). *Excitation of plasmons and interband transitions by electrons*, volume 88. Springer.

[Rahman, 1964] Rahman, A. (1964). Correlations in the motion of atoms in liquid argon. *Phys. Rev.*, 136:A405–A411.

[Ramakrishna et al., 2021] Ramakrishna, K., Cangi, A., Dornheim, T., Baczewski, A., and Vorberger, J. (2021). First-principles modeling of plasmons in aluminum under ambient and extreme conditions. *Phys. Rev. B*, 103:125118.

[Ramakrishna et al., 2020] Ramakrishna, K., Dornheim, T., and Vorberger, J. (2020). Influence of finite temperature exchange-correlation effects in hydrogen. *Phys. Rev. B*, 101:195129.

[Ramakrishna et al., 2023] Ramakrishna, K., Lokamani, M., Baczewski, A., Vorberger, J., and Cangi, A. (2023). Electrical conductivity of iron in earth's core from microscopic ohm's law. *Phys. Rev. B*, 107:115131.

[Ramakrishna and Vorberger, 2019] Ramakrishna, K. and Vorberger, J. (2019). Ab initio dielectric response function of diamond and other relevant high pressure phases of carbon. *Journal of Physics: Condensed Matter*, 32(9):095401.

[Ranjan et al., 2023] Ranjan, D., Ramakrishna, K., Voigt, K., Humphries, O. S., Heuser, B., Stevenson, M. G., Lütgert, J., He, Z., Qu, C., Schumacher, S., May, P. T., Amouretti, A., Appel, K., Brambrink, E., Cerantola, V., Chekrygina, D., Fletcher, L. B., Göde, S., Harmand, M., Hartley, N. J., Hau-Riege, S. P., Makita, M., Pelka, A., Schuster, A. K., Šmíd, M., Toncian, T., Zhang, M., Preston, T. R., Zastrau, U., Vorberger, J., and Kraus, D. (2023). Toward using collective x-ray Thomson scattering to study C–H demixing and hydrogen metallization in warm dense matter conditions. *Physics of Plasmas*, 30(5). 052702.

[Reining et al., 2002] Reining, L., Olevano, V., Rubio, A., and Onida, G. (2002). Excitonic effects in solids described by time-dependent density-functional theory. *Phys. Rev. Lett.*, 88:066404.

[Ross, 1981] Ross, M. (1981). The ice layer in uranus and neptune?diamonds in the sky? *Nature*, 292(5822):435–436.

[Runge and Gross, 1984] Runge, E. and Gross, E. K. U. (1984). Density-functional theory for time-dependent systems. *Phys. Rev. Lett.*, 52:997–1000.

[Sagmeister and Ambrosch-Draxl, 2009] Sagmeister, S. and Ambrosch-Draxl, C. (2009). Time-dependent density functional theory versus bethe–salpeter equation: an all-electron study. *Physical Chemistry Chemical Physics*, 11(22):4451–4457.

[Saha, B. et al., 2002] Saha, B., Mukherjee, P. K., and Diercksen, G. H. F. (2002). Energy levels and structural properties of compressed hydrogen atom under debye screening. *A&A*, 396(1):337–344.

[Sakurai et al., 2017] Sakurai, M., Chelikowsky, J. R., Louie, S. G., and Saito, S. (2017). Quasiparticle energies and dielectric functions of diamond polytypes. *Physical Review Materials*, 1(5):054603.

[Salehpour and Satpathy, 1990] Salehpour, M. and Satpathy, S. (1990). Comparison of electron bands of hexagonal and cubic diamond. *Physical Review B*, 41(5):3048.

[Salpeter and Bethe, 1951] Salpeter, E. E. and Bethe, H. A. (1951). A relativistic equation for bound-state problems. *Physical Review*, 84(6):1232.

[Sato et al., 2012] Sato, Y., Terauchi, M., Inami, W., and Yoshiasa, A. (2012). High energy-resolution electron energy-loss spectroscopy analysis of dielectric property and electronic structure of hexagonal diamond. *Diamond and Related Materials*, 25:40–44.

[Sato and Terauchi, 2022] Sato, Y. K. and Terauchi, M. (2022). Evaluation of exchange-correlation effects on the heat-shielding performance of carrier electrons in lab6 using momentum-transfer resolved electron energy-loss spectroscopy. *Journal of Applied Physics*, 131(6):063104.

[Saunders, 2018] Saunders, A. M.-A. (2018). *Using X-ray Thomson Scattering to Measure Plasma Conditions in Warm Dense Matter Experiments on the OMEGA Laser*. PhD thesis, University of California, Berkeley.

[Schoof et al., 2011] Schoof, T., Bonitz, M., Filinov, A., Hochstuhl, D., and Dufty, J. (2011). Configuration path integral monte carlo. *Contributions to Plasma Physics*, 51(8):687–697.

[Schoof et al., 2015] Schoof, T., Groth, S., Vorberger, J., and Bonitz, M. (2015). Ab initio thermodynamic results for the degenerate electron gas at finite temperature. *Phys. Rev. Lett.*, 115:130402.

[Schöttler and Redmer, 2018] Schöttler, M. and Redmer, R. (2018). Ab initio calculation of the miscibility diagram for hydrogen-helium mixtures. *Phys. Rev. Lett.*, 120:115703.

[Schöttler and Redmer, 2018] Schöttler, M. and Redmer, R. (2018). Simulations of h—he mixtures using the van der waals density functional. *Journal of Plasma Physics*, 84(4):755840401.

[Schülke, 2007] Schülke, W. (2007). *Electron dynamics by inelastic X-ray scattering*. Number 7. Oxford University Press.

[Schülke et al., 1993] Schülke, W., Schulte-Schrepping, H., and Schmitz, J. R. (1993). Dynamic structure of electrons in al metal studied by inelastic x-ray scattering. *Phys. Rev. B*, 47:12426–12436.

[Schuster et al., 2020] Schuster, A., Hartley, N., Vorberger, J., Döppner, T., van Driel, T., Falcone, R., Fletcher, L., Frydrych, S., Galtier, E., Gamboa, E., et al. (2020). Measurement of diamond nucleation rates from hydrocarbons at conditions comparable to the interiors of icy giant planets. *Physical Review B*, 101(5):054301.

[Seitsonen, 2000] Seitsonen, A. P. (2000). *Theoretical investigations into adsorption and co-adsorption on transition-metal surfaces as models to heterogenous catalysis*. PhD thesis, Technische Universität Berlin.

[Sham and Schlüter, 1983] Sham, L. J. and Schlüter, M. (1983). Density-functional theory of the energy gap. *Phys. Rev. Lett.*, 51:1888–1891.

[Sharma et al., 2011] Sharma, S., Dewhurst, J., Sanna, A., and Gross, E. (2011). Bootstrap approximation for the exchange-correlation kernel of time-dependent density-functional theory. *Physical review letters*, 107(18):186401.

[Shi et al., 2020] Shi, Z., Dao, M., Tsymbalov, E., Shapeev, A., Li, J., and Suresh, S. (2020). Metallization of diamond. *Proceedings of the National Academy of Sciences*, 117(40):24634–24639.

[Shishkin and Kresse, 2007] Shishkin, M. and Kresse, G. (2007). Self-consistent *gw* calculations for semiconductors and insulators. *Phys. Rev. B*, 75:235102.

[Singh and Nordstrom, 2006] Singh, D. J. and Nordstrom, L. (2006). *Planewaves, Pseudopotentials, and the LAPW method*. Springer Science & Business Media.

[Singwi et al., 1970] Singwi, K. S., Sjölander, A., Tosi, M. P., and Land, R. H. (1970). Electron correlations at metallic densities. iv. *Phys. Rev. B*, 1:1044–1053.

[Singwi et al., 1968] Singwi, K. S., Tosi, M. P., Land, R. H., and Sjölander, A. (1968). Electron correlations at metallic densities. *Phys. Rev.*, 176:589–599.

[Sjostrom and Daligault, 2014] Sjostrom, T. and Daligault, J. (2014). Gradient corrections to the exchange-correlation free energy. *Phys. Rev. B*, 90:155109.

[Sjostrom and Dufty, 2013] Sjostrom, T. and Dufty, J. (2013). Uniform electron gas at finite temperatures. *Phys. Rev. B*, 88:115123.

[Smith et al., 2016] Smith, J. C., Pribram-Jones, A., and Burke, K. (2016). Exact thermal density functional theory for a model system: Correlation components and accuracy of the zero-temperature exchange-correlation approximation. *Phys. Rev. B*, 93:245131.

[Smith et al., 2018] Smith, J. C., Sagredo, F., and Burke, K. (2018). Warming up density functional theory. In *Frontiers of Quantum Chemistry*, pages 249–271. Springer.

[Sokhotskii, 1873] Sokhotskii, Y. W. (1873). *On definite integrals and functions used in series expansions*. PhD thesis, St. Petersburg.

[Sokolov et al., 2003] Sokolov, A., Kurmaev, E., Leitch, S., Moewes, A., Kortus, J., Finkelstein, L., Skorikov, N., Xiao, C., and Hirose, A. (2003). Band dispersion of mgb2, graphite and diamond from resonant inelastic scattering. *Journal of Physics: Condensed Matter*, 15(12):2081.

[Sottile et al., 2003] Sottile, F., Olevano, V., and Reining, L. (2003). Parameter-free calculation of response functions in time-dependent density-functional theory. *Phys. Rev. Lett.*, 91:056402.

[Sperling et al., 2015] Sperling, P., Gamboa, E. J., Lee, H. J., Chung, H. K., Galtier, E., Omarbakiyeva, Y., Reinholz, H., Röke, G., Zastrau, U., Hastings, J., Fletcher, L. B., and Glenzer, S. H. (2015). Free-electron x-ray laser measurements of collisional-damped plasmons in isochorically heated warm dense matter. *Phys. Rev. Lett.*, 115:115001.

[Sprösser-Prou et al., 1989] Sprösser-Prou, J., vom Felde, A., and Fink, J. (1989). Aluminum bulk-plasmon dispersion and its anisotropy. *Phys. Rev. B*, 40:5799–5801.

[Stefanucci and Van Leeuwen, 2013] Stefanucci, G. and Van Leeuwen, R. (2013). *Nonequilibrium many-body theory of quantum systems: a modern introduction*. Cambridge University Press.

[Sternemann et al., 2005] Sternemann, C., Huotari, S., Vankó, G., Volmer, M., Monaco, G., Gusarov, A., Lustfeld, H., Sturm, K., and Schülke, W. (2005). Correlation-induced double-plasmon excitation in simple metals studied by inelastic x-ray scattering. *Phys. Rev. Lett.*, 95:157401.

[Stransky, 2016] Stransky, M. (2016). Monte carlo simulations of ionization potential depression in dense plasmas. *Physics of Plasmas*, 23(1):012708.

[Strinati, 1988] Strinati, G. (1988). Application of the green's functions method to the study of the optical properties of semiconductors. *La Rivista del Nuovo Cimento (1978-1999)*, 11(12):1–86.

[Sturm and Gusarov, 2000] Sturm, K. and Gusarov, A. (2000). Dynamical correlations in the electron gas. *Phys. Rev. B*, 62:16474–16491.

[Sun et al., 2010] Sun, J., Perdew, J. P., and Seidl, M. (2010). Correlation energy of the uniform electron gas from an interpolation between high-and low-density limits. *Physical Review B*, 81(8):085123.

[Sun et al., 2015] Sun, J., Ruzsinszky, A., and Perdew, J. P. (2015). Strongly constrained and appropriately normed semilocal density functional. *Phys. Rev. Lett.*, 115:036402.

[Suryanarayana et al., 2018] Suryanarayana, P., Pratapa, P. P., Sharma, A., and Pask, J. E. (2018). Sqdft: Spectral quadrature method for large-scale parallel o (n) kohn–sham calculations at high temperature. *Computer Physics Communications*, 224:288–298.

[Takada, 2016] Takada, Y. (2016). Emergence of an excitonic collective mode in the dilute electron gas. *Phys. Rev. B*, 94:245106.

[Tamblyn and Bonev, 2010] Tamblyn, I. and Bonev, S. A. (2010). Structure and phase boundaries of compressed liquid hydrogen. *Phys. Rev. Lett.*, 104:065702.

[Tamm, 1932] Tamm, I. (1932). Über eine mögliche art der elektronenbindung an kristalloberflächen. *Zeitschrift für Physik*, 76(11-12):849–850.

[Tanaka and Ichimaru, 1986] Tanaka, S. and Ichimaru, S. (1986). Thermodynamics and correlational properties of finite-temperature electron liquids in the singwi-tosi-land-sjölander approximation. *Journal of the Physical Society of Japan*, 55(7):2278–2289.

[Tanaka et al., 1985] Tanaka, S., Mitake, S., and Ichimaru, S. (1985). Parametrized equation of state for electron liquids in the singwi-tosi-land-sjölander approximation. *Physical Review A*, 32(3):1896.

[Tao et al., 2003] Tao, J., Perdew, J. P., Staroverov, V. N., and Scuseria, G. E. (2003). Climbing the density functional ladder: Nonempirical meta–generalized gradient approximation designed for molecules and solids. *Phys. Rev. Lett.*, 91:146401.

[Thiele et al., 2008] Thiele, R., Bornath, T., Fortmann, C., Höll, A., Redmer, R., Reinholz, H., Röpke, G., Wierling, A., Glenzer, S., and Gregori, G. (2008). Plasmon resonance in warm dense matter. *Physical Review E*, 78(2):026411.

[Tischler et al., 2003] Tischler, J. Z., Larson, B. C., Zschack, P., Fleszar, A., and Eguiluz, A. G. (2003). Interplay between inelastic x-ray scattering and ab initio density-response calculations: Insight into the electronic correlations in aluminum. *physica status solidi (b)*, 237(1):280–288.

[Tschentscher et al., 2017] Tschentscher, T., Bressler, C., Grünert, J., Madsen, A., Mancuso, A. P., Meyer, M., Scherz, A., Sinn, H., and Zastrau, U. (2017). Photon Beam Transport and Scientific Instruments at the European XFEL. *Appl. Sci.*, 7(6):592.

[Tully, 2012] Tully, J. C. (2012). Perspective: Nonadiabatic dynamics theory. *The Journal of chemical physics*, 137(22):22A301.

[Turneaure et al., 2017] Turneaure, S. J., Sharma, S. M., Volz, T. J., Winey, J., and Gupta, Y. M. (2017). Transformation of shock-compressed graphite to hexagonal diamond in nanoseconds. *Science advances*, 3(10):eaao3561.

[Tussupbayev et al., 2015] Tussupbayev, S., Govind, N., Lopata, K., and Cramer, C. J. (2015). Comparison of real-time and linear-response time-dependent density functional theories for molecular chromophores ranging from sparse to high densities of states. *Journal of chemical theory and computation*, 11(3):1102–1109.

[Ullrich, 2011] Ullrich, C. A. (2011). *Time-dependent density-functional theory: concepts and applications*. OUP Oxford.

[Utsumi and Ichimaru, 1981] Utsumi, K. and Ichimaru, S. (1981). Dielectric formulation of strongly coupled electron liquids at metallic densities. iv. static properties in the low-density domain and the wigner crystallization. *Phys. Rev. B*, 24:3220–3225.

[Utsumi et al., 2004] Utsumi, W., Okada, T., Taniguchi, T., Funakoshi, K.-i., Kikegawa, T., Hamaya, N., and Shimomura, O. (2004). In situ x-ray diffraction of graphite–diamond transformation using various catalysts under high pressures and high temperatures. *Journal of Physics: Condensed Matter*, 16(14):S1017.

[Van Vechten, 1969] Van Vechten, J. A. (1969). Quantum dielectric theory of electronegativity in covalent systems. i. electronic dielectric constant. *Physical Review*, 182(3):891.

[Varsano, 2006] Varsano, D. (2006). *First principles description of response functions in low dimensional systems*. PhD thesis, The University of the Basque Country.

[Vashishta and Singwi, 1972] Vashishta, P. and Singwi, K. S. (1972). Electron correlations at metallic densities. v. *Phys. Rev. B*, 6:875–887.

[Verdozzi et al., 1995] Verdozzi, C., Godby, R. W., and Holloway, S. (1995). Evaluation of *GW* approximations for the self-energy of a hubbard cluster. *Phys. Rev. Lett.*, 74:2327–2330.

[Verlet, 1967] Verlet, L. (1967). Computer "experiments" on classical fluids. i. thermodynamical properties of lennard-jones molecules. *Phys. Rev.*, 159:98–103.

[Vinet et al., 1989] Vinet, P., Rose, J. H., Ferrante, J., and Smith, J. R. (1989). Universal features of the equation of state of solids. *Journal of Physics: Condensed Matter*, 1(11):1941.

[Vinet et al., 1987] Vinet, P., Smith, J. R., Ferrante, J., and Rose, J. H. (1987). Temperature effects on the universal equation of state of solids. *Physical Review B*, 35(4):1945.

[Voigt et al., 2021] Voigt, K., Zhang, M., Ramakrishna, K., Amouretti, A., Appel, K., Brambrink, E., Cerantola, V., Chekrygina, D., Döppner, T., Falcone, R., et al. (2021). Demonstration of an x-ray raman spectroscopy setup to study warm dense carbon at the high energy density instrument of european xfel. *Physics of Plasmas*, 28(8):082701.

[Vorberger et al., 2007] Vorberger, J., Tamblyn, I., Militzer, B., and Bonev, S. A. (2007). Hydrogen-helium mixtures in the interiors of giant planets. *Phys. Rev. B*, 75(2):024206.

[Vosko et al., 1980] Vosko, S. H., Wilk, L., and Nusair, M. (1980). Accurate spin-dependent electron liquid correlation energies for local spin density calculations: a critical analysis. *Canadian Journal of physics*, 58(8):1200–1211.

[Vydrov and Van Voorhis, 2010] Vydrov, O. A. and Van Voorhis, T. (2010). Nonlocal van der waals density functional: The simpler the better. *The Journal of chemical physics*, 133(24):244103.

[Waidmann et al., 2000] Waidmann, S., Knupfer, M., Arnold, B., Fink, J., Fleszar, A., and Hanke, W. (2000). Local-field effects and anisotropic plasmon dispersion in diamond. *Physical Review B*, 61(15):10149.

[Waldecker et al., 2016] Waldecker, L., Bertoni, R., Ernstorfer, R., and Vorberger, J. (2016). Electron-phonon coupling and energy flow in a simple metal beyond the two-temperature approximation. *Phys. Rev. X*, 6:021003.

[Walter et al., 2008] Walter, M., Häkkinen, H., Lehtovaara, L., Puska, M., Enkovaara, J., Rostgaard, C., and Mortensen, J. J. (2008). Time-dependent density-functional theory in the projector augmented-wave method. *The Journal of chemical physics*, 128(24):244101.

[Wang and Zhang, 2013] Wang, C. and Zhang, P. (2013). Wide range equation of state for fluid hydrogen from density functional theory. *Physics of Plasmas*, 20(9):092703.

[Wang et al., 2005] Wang, X., Scandolo, S., and Car, R. (2005). Carbon phase diagram from ab initio molecular dynamics. *Phys. Rev. Lett.*, 95:185701.

[Wang and Carter, 2002] Wang, Y. A. and Carter, E. A. (2002). Orbital-free kinetic-energy density functional theory. In *Theoretical methods in condensed phase chemistry*, pages 117–184. Springer.

[Weir et al., 1996] Weir, S. T., Mitchell, A. C., and Nellis, W. J. (1996). Metallization of fluid molecular hydrogen at 140 gpa (1.4 mbar). *Phys. Rev. Lett.*, 76:1860–1863.

[White and Collins, 2020] White, A. J. and Collins, L. A. (2020). Fast and universal kohn-sham density functional theory algorithm for warm dense matter to hot dense plasma. *Phys. Rev. Lett.*, 125:055002.

[Whitley et al., 2015] Whitley, H. D., Sanchez, D. M., Hamel, S., Correa, A. A., and Benedict, L. X. (2015). Molecular dynamics simulations of warm dense carbon. *Contributions to Plasma Physics*, 55(5):390–398.

[Wigner, 1934] Wigner, E. (1934). On the interaction of electrons in metals. *Physical Review*, 46(11):1002.

[Wigner and Huntington, 1935] Wigner, E. and Huntington, H. (1935). On the possibility of a metallic modification of hydrogen. *The Journal of Chemical Physics*, 3(12):764–770.

[Wiser, 1963] Wiser, N. (1963). Dielectric constant with local field effects included. *Phys. Rev.*, 129:62–69.

[Witte et al., 2017a] Witte, B. B., Fletcher, L., Galtier, E., Gamboa, E., Lee, H., Zastrau, U., Redmer, R., Glenzer, S., and Sperling, P. (2017a). Warm dense matter demonstrating non-drude conductivity from observations of nonlinear plasmon damping. *Physical review letters*, 118(22):225001.

[Witte, 2019] Witte, B. B. L. (2019). *Many-particle physics calculation of the dynamic structure factor in warm dense matter*. PhD thesis, Universität Rostock.

[Witte et al., 2017b] Witte, B. B. L., Shihab, M., Glenzer, S. H., and Redmer, R. (2017b). Ab initio simulations of the dynamic ion structure factor of warm dense lithium. *Phys. Rev. B*, 95:144105.

[Witte et al., 2018] Witte, B. B. L., Sperling, P., French, M., Recoules, V., Glenzer, S. H., and Redmer, R. (2018). Observations of non-linear plasmon damping in dense plasmas. *Physics of Plasmas*, 25(5):056901.

[Yabana and Bertsch, 1996] Yabana, K. and Bertsch, G. F. (1996). Time-dependent local-density approximation in real time. *Phys. Rev. B*, 54:4484–4487.

[Yabana et al., 2006] Yabana, K., Nakatsukasa, T., Iwata, J.-I., and Bertsch, G. (2006). Real-time, real-space implementation of the linear response time-dependent density-functional theory. *physica status solidi (b)*, 243(5):1121–1138.

[Yagi et al., 1992] Yagi, T., Utsumi, W., Yamakata, M.-a., Kikegawa, T., and Shimomura, O. (1992). High-pressure in situ x-ray-diffraction study of the phase transformation from graphite to hexagonal diamond at room temperature. *Physical Review B*, 46(10):6031.

[Yang and Kawazoe, 2012] Yang, Y. and Kawazoe, Y. (2012). Characterization of zero-point vibration in one-component crystals. *EPL (Europhysics Letters)*, 98(6):66007.

[Yao et al., 2019] Yao, Y., Yost, D. C., and Kanai, Y. (2019). *k*-shell core-electron excitations in electronic stopping of protons in water from first principles. *Phys. Rev. Lett.*, 123:066401.

[Yost et al., 2017] Yost, D. C., Yao, Y., and Kanai, Y. (2017). Examining real-time time-dependent density functional theory nonequilibrium simulations for the calculation of electronic stopping power. *Physical Review B*, 96(11):115134.

[Zacharias and Giustino, 2016] Zacharias, M. and Giustino, F. (2016). One-shot calculation of temperature-dependent optical spectra and phonon-induced band-gap renormalization. *Physical Review B*, 94(7):075125.

[Zaghoo et al., 2016] Zaghoo, M., Salamat, A., and Silvera, I. F. (2016). Evidence of a first-order phase transition to metallic hydrogen. *Phys. Rev. B*, 93:155128.

[Zastrau et al., 2021] Zastrau, U., Appel, K., Baehtz, C., Baehr, O., Batchelor, L., Berghäuser, A., Banjafar, M., Brambrink, E., Cerantola, V., Cowan, T. E., et al. (2021). The high energy density scientific instrument at the european xfel. *Journal of synchrotron radiation*, 28(5).

[Zhang et al., 2017] Zhang, H., Liu, H., Wei, K., Kurakevych, O. O., Le Godec, Y., Liu, Z., Martin, J., Guerrette, M., Nolas, G. S., and Strobel, T. A. (2017). Bc8 silicon (si-iii) is a narrow-gap semiconductor. *Physical review letters*, 118(14):146601.

[Zhang et al., 2016] Zhang, S., Wang, H., Kang, W., Zhang, P., and He, X. (2016). Extended application of kohn-sham first-principles molecular dynamics method with plane wave approximation at high energy—from cold materials to hot dense plasmas. *Physics of Plasmas*, 23(4):042707.

[Zhu et al., 2011] Zhu, Q., Oganov, A. R., Salvadó, M. A., Pertierra, P., and Lyakhov, A. O. (2011). Denser than diamond: ab initio search for superdense carbon allotropes. *Physical Review B*, 83(19):193410.

List of Tables

3.1.1 Equilibrium lattice parameters, equilibrium volume per atom, bulk modulus, pressure derivative and static dielectric constants for various phases of carbon. The double row values shown for hexagonal diamond are for the lattice parameters, a=b and c. The static dielectric constant is computed using BSE. The values shown in parentheses are experimental data. [a] [Madelung, 2012]; [b] [Bundy and Kasper, 1967]; [c] [Van Vechten, 1969]; [d] [De and Pryor, 2014]. **K Ramakrishna and J Vorberger** 2020 J. Phys.: Condens. Matter **32** 095401. 55

3.1.2 Band gap (indirect) results in eV. GW^0 with HSE for the FCC phase and PBE for the other phases is used. [a] [Peter and Cardona, 2010]. **K Ramakrishna and J Vorberger** 2020 J. Phys.: Condens. Matter **32** 095401. 57

5.3.1 Local field corrections (LFC) and finite-temperature local field corrections (T-LFC) for aluminum at 2.7 and 3.5 g/cm^3 for various temperatures and q-vectors. Reprinted table with permission from **K. Ramakrishna** *et al.*, Phys. Rev. B **103**, 125118 (2021). Copyright 2021 by the American Physical Society. 115

List of Figures

1.0.1 The temperature and the density plane describing warm dense parameters. The x-axis corresponds to the electronic density in logarithmic scale. The y-axis corresponds to the temperature in logarithmic scale. The electronic parameters are fully defined by (r_s, θ). The coupling parameter Γ as it is given in the figure follows from (r_s, θ). Republished with permission of Elsevier from The uniform electron gas at warm dense matter conditions, Physics Reports **744**:1-86 (2018) [Dornheim et al., 2018a]. Permission conveyed through Copyright Clearance Center, Inc. 4

2.1.1 The bubble diagram and the diagramatic sum of the Feynman diagrams to obtain the RPA sum. 12

2.1.2 Static LFC of aluminum at four different temperatures. The static LFC data have been obtained from the machine-learning representation from Ref. [Dornheim et al., 2019]. Reprinted figure with permission from **K. Ramakrishna** *et al.*, Phys. Rev. B **103**, 125118 (2021). Copyright 2021 by the American Physical Society. 18

2.2.1 Comparison of the x-ray sources and the capability of probing the electron density. Republished with permission of Springer from Frontiers and Challenges in Warm Dense Matter (2014) [Fortmann, 2014]. Permission conveyed through Copyright Clearance Center, Inc. 20

2.2.2 A schematic cartoon of x-ray Thomson scattering illustrating the length of the scattering vector. The screening length (λ_s) and the length scale of the density fluctuations (λ^*) are also shown for comparison. 20

2.3.1 Jacob's ladder of XC functionals with some of the most common DFT functionals [Perdew and Zunger, 1981, Perdew and Wang, 1992, Perdew et al., 1996a, Becke, 1988, Lee et al., 1988, Sun et al., 2015, Tao et al., 2003, Becke, 1997, Lee et al., 2010, Vydrov and Van Voorhis, 2010] within each rung of the ladder [Perdew and Schmidt, 2001]. The arrow represents the increasing chemical accuracy. $n(r)$ is the electronic density and $\tau(r) = \sum_i^{occ.} \frac{1}{2}|\nabla\psi_i(r)|^2$ is the kinetic energy density for the occupied orbitals. 26

2.3.2 DFT-MD workflow represented in a flowchart. 30

2.5.1 Single particle excitations correspond to the poles of single particle Green's functions in the GW approximation. 36

2.5.2 Feynman diagram representation of the Green's function and the interaction. . . 37

2.5.3 Solution of Hedin's equations in a self-consistency cycle. 39

2.5.4 Feynman diagram of the GW self-energy in second-order Born approximation. The first two terms are the Hartree and Fock terms respectively. The third term is the first-order bubble diagram. The last term is the correction to the exchange in the second-order. 39

2.6.1 Feynman diagram representation of the two-particle Green's function. 40

2.6.2 Feynman diagram representation of the two-particle density response function. 41

2.6.3 Feynman diagrams for the leading terms of the reducible kernel. 41

2.6.4 Two particle excitations correspond to the poles of two particle Green's functions. Electron in the conduction band and the hole left behind in the valence band form a bound exciton. 42

2.6.5 Effect of *k*-point sampling on the a) Real and b) Imaginary part of the dielectric function of diamond in the optical limit. 43

2.7.1 A flowchart of the procedure to obtain response function using density functional theory and many-body theoretical techniques. 43

3.0.1 Carbon phase diagram based on the theoretical work over the last three decades [Grumbach and Martin, 1996, Glosli and Ree, 1999, Fried and Howard, 2000, Wang et al., 2005, Correa et al., 2006, Correa et al., 2008, Martinez-Canales et al., 2012, Benedict et al., 2014]. Data provided by Jan Vorberger. 48

3.1.1 Some of the crystal phases of carbon. 49

3.1.2 Density of states for diamond as a) function of pressure using PBE XC, b) at 202 GPa using various XC functionals. The pressures are in GPa and the valence band maximum is adjusted to zero. **K Ramakrishna and J Vorberger** 2020 J. Phys.: Condens. Matter **32** 095401. 50

3.1.3 Band gap of diamond calculated using various XC functionals [Perdew et al., 1996a, Heyd et al., 2003, Becke, 1988, Lee et al., 1988, Sun et al., 2015, Perdew et al., 1996b] as function of pressure in DFT and within the GW approximation. The direct band gap is calculated using PBE. Theoretical data stems from Ref [Li et al., 2012, Gao, 2015]; Experimental data stems from Ref. [Peter and Cardona, 2010]. **K Ramakrishna and J Vorberger** 2020 J. Phys.: Condens. Matter **32** 095401. 51

3.1.4 a) Variation of the parameters *c/a* and z_1 for lonsdaleite, (b) Enthalpy vs pressure with respect to z_1 for lonsdaleite. The inset plot shows the relative enthalpies with respect to $z_1 = 0.0625$ vs pressure for $c/a = 1.635$. **K Ramakrishna and J Vorberger** 2020 J. Phys.: Condens. Matter **32** 095401. 53

3.1.5 a) Density of states for lonsdaleite as function of pressure. The pressures are in GPa and the valence band maximum is adjusted to zero, (b) Lonsdaleite band gap as function of pressure using DFT and GW. The direct band gap calculated using PBE is also shown. The density range covers 3.5 g/cm^3 to 6.9 g/cm^3. Theoretical data stems from Ref. [Zhu et al., 2011, De and Pryor, 2014, Gao, 2015]. **K Ramakrishna and J Vorberger** 2020 J. Phys.: Condens. Matter **32** 095401. . . . 53

3.1.6 a) Variation of the parameter x_1 for BC8. The inset panel zooms at the region of the minimum, (b) Enthalpy vs pressure with respect to x_1 for BC8. The inset plot shows the relative enthalpies with respect to $x_1 = 0.1003$ vs pressure. $x_1 = 0.935$ suggested by Clark *et al.* is ideal for the formation of BC8 phase from diamond and at higher pressures the larger internal parameter is better suited [Clark, 1994]. **K Ramakrishna and J Vorberger** 2020 J. Phys.: Condens. Matter **32** 095401. 54

3.1.7 Density of states for BC8 as function of pressure. The inset plot shows the indirect and the direct band gaps calculated using the PBE XC functional. The pressures indicated are in GPa and the valence band maximum is adjusted to zero. **K Ramakrishna and J Vorberger** 2020 J. Phys.: Condens. Matter **32** 095401. 55

3.1.8 Cold curves for various phases of carbon. The inset panel shows the relative energies with respect to diamond vs volume, $\Delta E = E - E_d$. The diamond to BC8 crossover is observed around 2.8 Å^3/atom corresponding to pressure around 1000 GPa. **K Ramakrishna and J Vorberger** 2020 J. Phys.: Condens. Matter **32** 095401. 56

3.1.9 Equation of state for various carbon phases in comparison with experiments at room temperature (diamond only). Experimental data by Occelli [Occelli et al., 2003] and Dewaele [Dewaele et al., 2008] up to 4.0 g/cm^3. The inset panel shows the relative difference in pressures with respect to diamond vs density, $\Delta P = P - P_d$. **K Ramakrishna and J Vorberger** 2020 J. Phys.: Condens. Matter **32** 095401. 56

3.2.1 Imaginary part of the dielectric function of diamond in the optical limit at ambient conditions (ρ=3.509 g/cm^3) using various approaches. The inset plot shows the imaginary part of the inverse of the dielectric function including the plasmon peaks. In the inset, the curves obtained using TDDFT/RPA and KG are scaled, for the purpose of visualization. Botti Ref. [Botti et al., 2004]; Experimental data stems from Ref. [Palik, 1998]. **K Ramakrishna and J Vorberger** 2020 J. Phys.: Condens. Matter **32** 095401. 58

3.2.2 Imaginary part of the dielectric function of diamond in the optical limit for various pressures using BSE, TDDFT and RPA. The inset plot shows the imaginary part of the inverse of the dielectric function including the plasmon peaks. In the inset, the curves obtained using TDDFT and RPA are scaled for the purpose of visualization. All the pressures indicated are in GPa. The densities for these pressures are 3.51, 5.50, 6.00 and 7.00 g/cm^3 respectively. **K Ramakrishna and J Vorberger** 2020 J. Phys.: Condens. Matter **32** 095401. 59

3.2.3 Imaginary part of the dielectric response function for diamond is calculated using TDDFT, BSE and MA at finite $\vec{q}$ for ρ=3.509 g/cm^3. The charge state $Z_i = 1$ is considered for $q = 0.3$/Å and 0.76/Å and $Z_i = 4$ is considered for $q = 0.76$/Å and 1.51/Å. **K Ramakrishna and J Vorberger** 2020 J. Phys.: Condens. Matter **32** 095401. 60

3.2.4 Imaginary part of the inverse of the dielectric function for diamond at ambient density ρ=3.509 g/cm^3 using TDDFT, BSE and MA at finite $\vec{q}$. The charge state $Z_i = 1$ is considered for $q = 0.3$/Å and 0.76/Å and $Z_i = 4$ is considered for $q = 0.76$/Å and 1.51/Å. **K Ramakrishna and J Vorberger** 2020 J. Phys.: Condens. Matter **32** 095401. 61

3.2.5 Imaginary part of the inverse dielectric function at various q for diamond at ambient conditions. Experimental data stems from Ref. [Daniels et al., 1970, Waidmann et al., 2000, Raether, 2006]. **K Ramakrishna and J Vorberger** 2020 J. Phys.: Condens. Matter **32** 095401. 62

3.2.6 Imaginary part of the dielectric response function in panels a) and b) for lonsdaleite at 242 GPa using various approaches at $\vec{q}$=0. Comparison of TDDFT to KG+Mermin (MA) at finite $\vec{q}$ in panels c) and d). **K Ramakrishna and J Vorberger** 2020 J. Phys.: Condens. Matter **32** 095401. 63

3.2.7 Imaginary part of the inverse of the dielectric function for lonsdaleite at 242 GPa using MA and TDDFT at $|\vec{q}| = 0.57$Å^{-1}. **K Ramakrishna and J Vorberger** 2020 J. Phys.: Condens. Matter **32** 095401. 64

3.2.8 Comparison of the imaginary part of the TDDFT dielectric function for diamond and lonsdaleite at 292 GPa in the optical limit and at finite q. The inset panel shows the imaginary part of the inverse of the dielectric function at $|\vec{q}| = 0.68$ Å^{-1} for diamond and $|\vec{q}| = 0.59$ Å^{-1} for lonsdaleite (black–diamond, blue/yellow–lonsdaleite). **K Ramakrishna and J Vorberger** 2020 J. Phys.: Condens. Matter **32** 095401. 64

3.2.9 Imaginary part of the dielectric function of BC8 in the optical limit for various pressures using BSE, TDDFT, RPA and the Kubo-Greenwood formula. **K Ramakrishna and J Vorberger** 2020 J. Phys.: Condens. Matter **32** 095401. 65

3.2.10 Imaginary part of the inverse of the dielectric function of BC8 at various pressures using BSE, TDDFT, RPA and the Kubo-Greenwood formula. The TDDFT, RPA, and KG curves are scaled fivefold and the finite-q MA curve is scaled tenfold. All curves in the optical limit except the specially marked MA and TDDFT curves. **K Ramakrishna and J Vorberger** 2020 J. Phys.: Condens. Matter **32** 095401. 66

3.3.1 Imaginary part of the inverse dielectric function for diamond at WDM conditions (P=150 GPa, T=6000 K) in the optical limit. **K Ramakrishna and J Vorberger** 2020 J. Phys.: Condens. Matter **32** 095401. 67

3.3.2 Change in the imaginary part of the inverse dielectric function of diamond at $P = 150$ GPa and $T = 6000$ K with system size and different XC kernels in TDDFT. **K Ramakrishna and J Vorberger** 2020 J. Phys.: Condens. Matter **32** 095401. . . 68

3.3.3 Imaginary part of the inverse dielectric function at warm dense matter conditions (P=150 GPa, T=6000 K) at q= 1.13 Å^{-1} for a) C-H mixture with stoichiometric components, b) C_x-H_y mixture. 69

3.3.4 Dynamic structure factor at warm dense matter conditions (P=150 GPa, T=6000 K) at q= 0.94 Å^{-1} for a C_x-H_y mixture. 69

3.3.5 Plasmon position in carbon (C), hydrogen (H) and carbon-hydrogen mixtures (CH, CH_3, C_3H) as function of the wavenumber evaluated using TDDFT. The system sizes are indicated in the brackets. Experimental data obtained via XRTS is taken from Gamboa *et al.* [Gamboa et al., 2016]. 70

3.3.6 Density of states for diamond under ambient, compressed and WDM conditions. The valence band maximum is adjusted to zero. 70

3.4.1 Plasmon position in diamond in the optical limit as function of the density. Experimental data obtained via XRTS is taken from Gamboa *et al.* [Gamboa et al., 2016], electron-energy loss spectroscopy (EELS) data by Sato *et al.* [Sato et al., 2012] and Waidmann *et al.* [Waidmann et al., 2000], BSE calculations for ambient conditions by Gao [Gao, 2015], TDDFT calculations at ambient conditions by Azzolini *et al.* [Azzolini et al., 2017]. **K Ramakrishna and J Vorberger** 2020 J. Phys.: Condens. Matter **32** 095401. 72

3.4.2 Plasmon position in diamond at ambient density as function of the wavenumber. Experimental data obtained via XRTS is taken from Gamboa *et al.* [Gamboa et al., 2016], EELS data by Waidmann *et al.* [Waidmann et al., 2000]. **K Ramakrishna and J Vorberger** 2020 J. Phys.: Condens. Matter **32** 095401. . . 73

3.4.3 Experimental setup showing the compression of the polystyrene sample using a drive laser and the measurements using XRTS and XRD. Reprinted figure from **S. Frydrych** *et al.*, Demonstration of X-ray Thomson scattering as diagnostics for miscibility in warm dense matter. Nat Commun **11**, 2620 (2020) [Frydrych et al., 2020] licensed under CC-BY-4.0. 74

3.4.4 Scattered x-ray spectra recorded using the a) Backward and b) Forward spectrometers. Reprinted figure from **S. Frydrych** *et al.*, Demonstration of X-ray Thomson scattering as diagnostics for miscibility in warm dense matter. Nat Commun **11**, 2620 (2020) [Frydrych et al., 2020] licensed under CC-BY-4.0. . . . 75

3.4.5 a) Inelastic scattering spectra for diamond and polystyrene calculated with TDDFT ($\vec{q} = 1.28$/Å) and KG+Mermin ($\vec{q} = 1.21$/Å) respectively, b) Inelastic scattering spectra after folding with the detector function with a Gaussian curve of halfwidth 34 eV. The data is taken from Ref. [Frydrych, 2018]. 76

3.5.1 X-ray Raman spectra for ambient diamond at $|\vec{q}| = 5.94$/Å with a variation in the cluster radius. The simulation data is shown for diamond in an unit cell with a) 4 atoms and b) 8 atoms. 78

3.5.2 a) Measured x-ray Raman spectra [Voigt et al., 2021] for diamond under ambient conditions at $|\vec{q}| = 5.94$/Å. The simulation data is shown for an unit cell consisting of 8 atoms. The carbon K-edge is located at ≈285 eV, b) Density of states for diamond at ambient conditions. The valence band maximum is adjusted to zero. Reprinted figure with permission from **K. Voigt** *et al.*, Physics of Plasmas **28** (8), 082701 (2021). Copyright 2021 by the AIP Publishing. 78

3.5.3 X-ray Raman spectra for diamond at ambient conditions for a) Various wavenumbers, b) Normalized with respect to 1.0 $Å^{-1}$. The scaling factor is indicated in the brackets. 79

3.5.4 Calculated x-ray Raman spectra for compressed and ischorically heated diamond at $|\vec{q}| = 5.94/\text{Å}$. The spectrum for ambient conditions is shown in black for comparison. Various pressure conditions ranging from 150 GPa to 437 GPa (ρ=4.41–5.5 g/cm^3) and different temperature conditions ranging from 0.5 eV to 7.5 eV are investigated. Reprinted figure with permission from **K. Voigt** *et al.*, Physics of Plasmas **28** (8), 082701 (2021). Copyright 2021 by the AIP Publishing. 80

4.0.1 Map of the density-temperature plane showing the importance of the temperature dependence in finite-temperature XC free energy functional. The x-axis represents the density (r_s) in logarithmic scale. The y-axis represents the temperature ($\times 10^3$ K) in logarithmic scale. The color map shows the deviation [Eq. (4.0.1)] in logarithmic scale. Reprinted figure with permission from **V. V. Karasiev** *et al.*, Phys. Rev. E **93**, 063207 (2016). Copyright 2016 by the American Physical Society. 85

4.0.2 Exchange-correlation free energy per particle (f_{XC}) as a function of density (r_s) and reduced temperature (θ) for a) a spin unpolarized case, b) a spin unpolarized case at low densities $r_s = 5.0 - 14.0$ and small reduced temperatures, c) a spin polarized case. The change in the XC free energy is given by $\left[\frac{f_{XC}(r_s,\theta,\xi=1)-f_{XC}(r_s,\theta,\xi=0)}{f_{XC}(r_s,\theta,\xi=0)} \times 100\%\right]$. 87

4.0.3 Phase diagram of hydrogen at high temperatures and pressures. Republished with permission of AIP Publishing from Phase diagram of hydrogen at extreme pressures and temperatures; updated through 2019, Low Temperature Physics **46**, 97 (2020) [Goncharov, 2020]. Permission conveyed through Copyright Clearance Center, Inc. 88

4.1.1 Pressure variation with respect to a) the basis set at $r_s = 3.0$, T=15625 K. The error bars are too small to be shown; b) system size for the DZVP basis set at $r_s = 3.0$, T=15625 K and $r_s = 4.0$, T=31250 K; c) *k*-point sampling for the DZVP basis set at $r_s = 3.0$, T=15625 K for a system size of 32, 108 and 256. Reprinted figure with permission from **K. Ramakrishna** *et al.*, Phys. Rev. B **101**, 195129 (2020). Copyright 2020 by the American Physical Society. 90

4.2.1 EOS at T=1000 K using various XC functionals and *ab-initio* methods. Lorenzen Ref. [Lorenzen et al., 2010]; Morales Ref. [Morales et al., 2010b]; Lu Ref. [Lu et al., 2019]; Alavi Ref. [Alavi et al., 1995]. PZ and GDSMFB results of this work. Reprinted figure with permission from **K. Ramakrishna** *et al.*, Phys. Rev. B **101**, 195129 (2020). Copyright 2020 by the American Physical Society. 91

4.2.2 EOS at a) T=6000 K, b) T=8000 K, and c) T=10000 K comparing our results with the previous results obtained using PIMC and DFT. The inset plot shows the relative difference (Eq. 4.2.1) in pressure with respect to the finite-temperature case. Morales Ref. [Morales et al., 2010a]; Vorberger Ref. [Vorberger et al., 2007]; Mazzola Ref. [Mazzola et al., 2018]. Reprinted figure with permission from **K. Ramakrishna** *et al.*, Phys. Rev. B **101**, 195129 (2020). Copyright 2020 by the American Physical Society. 92

4.2.3 Phase diagram of hydrogen at high densities. Mazzola Ref. [Mazzola et al., 2018]; Morales Ref. [Morales et al., 2010a]; Pierleoni Ref. [Pierleoni et al., 2016, Pierleoni et al., 2018]; Lorenzen Ref. [Lorenzen et al., 2010]; Tamblyn Ref. [Tamblyn and Bonev, 2010]; Zaghoo Ref. [Zaghoo et al., 2016]; Knudson Ref. [Knudson et al., 2015]; Celliers Ref. [Celliers et al., 2018]. Reprinted figure with permission from **K. Ramakrishna** *et al*., Phys. Rev. B **101**, 195129 (2020). Copyright 2020 by the American Physical Society. 93

4.3.1 The convergence of pressure with respect to the plane wave energy cutoff and basis sets [single-zeta valence (SZV), double-zeta valence polarization (DZVP), double-zeta valence polarization short-range (DZVP-SR)] at 62500 K and 250000 K for $r_s = 0.8137$. Reprinted figure with permission from **K. Ramakrishna** *et al*., Phys. Rev. B **101**, 195129 (2020). Copyright 2020 by the American Physical Society. 94

4.3.2 EOS at a) $r_s = 0.8137$, b) $r_s = 1.1$, c) $r_s = 1.4$. The previously obtained results using PIMC and DFT are also shown for comparison. The inset plot shows the relative difference (Eq. 4.3.1) in total pressure for the finite-temperature case with respect to the LDA case. Hu Ref. [Hu et al., 2011]; Wang (LDA) Ref. [Wang and Zhang, 2013]; Danel (LDA) Ref. [Danel et al., 2016]; Karasiev Ref. [Karasiev et al., 2016]. Reprinted figure with permission from **K. Ramakrishna** *et al*., Phys. Rev. B **101**, 195129 (2020). Copyright 2020 by the American Physical Society. 95

4.3.3 The electronic pressure as a function of temperature at various densities. The inset plot shows the relative difference (Eq. 4.3.1) in electronic pressure for the finite-temperature (GDSMFB) case with respect to the LDA (PZ) case. Reprinted figure with permission from **K. Ramakrishna** *et al*., Phys. Rev. B **101**, 195129 (2020). Copyright 2020 by the American Physical Society. 96

4.4.1 The convergence of pressure with respect to the plane wave energy cutoff and basis sets at various temperatures for $r_s = 14.0$. Reprinted figure with permission from **K. Ramakrishna** *et al*., Phys. Rev. B **101**, 195129 (2020). Copyright 2020 by the American Physical Society. 97

4.4.2 a) EOS at $r_s = 2.0 - 14.0$. The previously obtained results using PIMC and DFT are also shown in comparison, b) Relative difference (Eq. 4.3.1) in total pressure for the finite-temperature case with respect to LDA at $r_s = 2.0 - 10.0$. Hu Ref. [Hu et al., 2011]; Wang Ref. [Wang and Zhang, 2013]; Collins Ref. [Collins et al., 2001]; Danel Ref. [Danel et al., 2016]. Reprinted figure with permission from **K. Ramakrishna** *et al*., Phys. Rev. B **101**, 195129 (2020). Copyright 2020 by the American Physical Society. 98

4.4.3 a) Relative difference (Eq. 4.3.1) in total pressure for the finite-temperature case with respect to LDA with the change in density (← r_s) and electron degeneracy at T=62500 K, b) Relative difference in total pressure for the finite-temperature case with respect to LDA at $r_s = 14$. Reprinted figure with permission from **K. Ramakrishna** *et al.*, Phys. Rev. B **101**, 195129 (2020). Copyright 2020 by the American Physical Society. 99

4.5.1 The density of states at $r_s = 2.0$ and a) T=2000 K, b) T=5000 K, c) T=15625 K, and d) T=62500 K using LDA and the finite-temperature case. The Fermi energy is set to zero. The green and the blue areas represent DOS calculated using PZ and GDSMFB respectively. The overlap between them is indicated by the dark blue area. The density of states for a 3D electron gas is shown only at T=62500 K. Collins Ref. [Collins et al., 2001]. Reprinted figure with permission from **K. Ramakrishna** *et al.*, Phys. Rev. B **101**, 195129 (2020). Copyright 2020 by the American Physical Society. 100

4.6.1 Snapshot of an electronic density isosurface for $r_s = 2.0$, T=62500 K ($\theta = 0.43$) using a) PZ and b) GDSMFB for the same ionic configuration with N=256. Panel c) shows magnified insets for PZ (top) and GDSMFB (bottom) for the bottom left corner of the respective simulation cells. Reprinted figure with permission from **K. Ramakrishna** *et al.*, Phys. Rev. B **101**, 195129 (2020). Copyright 2020 by the American Physical Society. 101

4.6.2 Snapshot of an electronic density isosurface for $r_s = 2.0$, T=15625 K ($\theta = 0.107$) using a) PZ and b) GDSMFB for the same ionic configuration with N=256. 102

5.1.1 Dynamic structure factor evaluated using TDDFT (f_{XC}=ALDA) for aluminum in atomic units under ambient conditions at 0.54 Å^{-1} using PZ and PBE XC functionals. 107

5.2.1 Dynamic structure factor for aluminum ($r_s = 2.07$, $\rho = 2.7$ g/cm^3) in atomic units under ambient conditions at a) $q = 1.08$/Å, b) $q = 1.48$/Å, c) $q = 1.75$/Å, d) $q = 1.88$/Å. Experimental data in black stems from Ref. [Cazzaniga et al., 2011, Schülke et al., 1993, Tischler et al., 2003]. Theoretical data in red stems from Ref. [Cazzaniga et al., 2011]. TDDFT-RPA/TDDFT-XC/LFC/RPA/RPA-LFC results of this work are shown in blue. Reprinted figure with permission from **K. Ramakrishna** *et al.*, Phys. Rev. B **103**, 125118 (2021). Copyright 2021 by the American Physical Society. 108

5.2.2 Aluminum plasmon dispersion under ambient conditions. The critical and the Fermi wavevectors are indicated by the vertical lines. Experimental data in black symbols stems from Ref. [Sprösser-Prou et al., 1989, Batson and Silcox, 1983, Cazzaniga et al., 2011, Höhberger et al., 1975]. Theoretical data shown in red symbols are taken from Ref. [Cazzaniga et al., 2011, Budagosky and Krasovskii, 2019, Lee and Chang, 1994, Quong and Eguiluz, 1993]. TDDFT-RPA/TDDFT-XC/LFC/RPA-LFC/RPA results of this work are indicated with blue symbols. Reprinted figure with permission from **K. Ramakrishna** *et al.*, Phys. Rev. B **103**, 125118 (2021). Copyright 2021 by the American Physical Society. 110

5.2.3 Aluminum plasmon peak FWHM under ambient conditions. The critical wavevector is indicated by the vertical line. Experimental and theoretical data in black symbols stems from Ref. [Krane, 1978, Batson and Silcox, 1983, Festenberg, 1967, Kloos, 1973, Gibbons et al., 1976, Pal and Tripathy, 1985]. TDDFT-RPA/TDDFT-XC/LFC results of this work are indicated with blue symbols. Reprinted figure with permission from **K. Ramakrishna** *et al.*, Phys. Rev. B **103**, 125118 (2021). Copyright 2021 by the American Physical Society. 112

5.2.4 a) FWHM of the plasmon peak evaluated using TDDFT (f_{XC}=ALDA) for aluminum under ambient conditions at $q = 0.54\,\mathrm{\AA}^{-1}$ for various values of Lorentzian broadening (η), b) Dynamic structure factor evaluated using TDDFT (f_{XC}=ALDA) for aluminum in atomic units under ambient conditions at $q = 0.54\,\mathrm{\AA}^{-1}$ for various values of Lorentzian broadening (η) in eV. 113

5.3.1 Phase diagram of aluminum. The melting curve is shown as dashed line. The data is taken from Ref. [Kudasov et al., 2013, Bouchet et al., 2009]. 113

5.3.2 Aluminum plasmon dispersion under extreme conditions (T=0.3 eV) for densities 2.7 g/cm^3 (uncompressed-top panel) and 3.5 g/cm^3 (compressed-bottom panel). The Fermi wavevector is indicated by the vertical line. Experimental and theoretical data for RPA, MA, RPA+LFC stems from Ref. [Witte et al., 2017a, Preston et al., 2019]. TDDFT-RPA/TDDFT-XC/TDDFT-LFC results of this work are indicated with blue and red symbols. Reprinted figure with permission from **K. Ramakrishna** *et al.*, Phys. Rev. B **103**, 125118 (2021). Copyright 2021 by the American Physical Society. 114

5.3.3 Aluminum plasmon peak FWHM under extreme conditions for 2.7 g/cm^3 at T=0.3 eV (top) and T=6 eV (bottom). The Fermi wavevector is indicated by the vertical line. Experimental and theoretical data for RPA, MA stems from Ref. [Witte et al., 2017a, Witte et al., 2018]. Reprinted figure with permission from **K. Ramakrishna** *et al.*, Phys. Rev. B **103**, 125118 (2021). Copyright 2021 by the American Physical Society. 117

5.3.4 Dynamic structure factor for aluminum (2.7 g/cm^3) in atomic units at T=2 eV and T=6 eV with respect to k-points and the number of electrons considered in the pseudopotential. AE refers to the use of an all electron pseudopotential (11 electrons ignoring the 1s^2 core) compared to the 3 valence electrons otherwise. Reprinted figure with permission from **K. Ramakrishna** *et al.*, Phys. Rev. B **103**, 125118 (2021). Copyright 2021 by the American Physical Society. 118

5.3.5 Dynamic structure factor evaluated using TDDFT (f_{xc}=ALDA) for aluminum in atomic units for 1.68 Å^{-1} at 6 eV using PZ and PBE XC functionals. Reprinted figure with permission from **K. Ramakrishna** *et al.*, Phys. Rev. B **103**, 125118 (2021). Copyright 2021 by the American Physical Society. 118

5.3.6 Dynamic structure factor for aluminum in atomic units at a) $q = 0.47$ Å^{-1}, b) $q = 0.94$ Å^{-1}, c) $q = 1.42$ Å^{-1} for various temperatures. The TDDFT-RPA results are shown only at 12 eV. The TDDFT-XC results are shown from 1 to 12 eV in the blue area (black curves for 1 and 12 eV) and are broadening with temperature. The purple and green dashed lines are the RPA and RPA+T-LFC results at 1 eV respectively. The RPA results are normalized with respect to the TDDFT-XC results at 12 eV to allow plotting them at the same scale. Reprinted figure with permission from **K. Ramakrishna** *et al.*, Phys. Rev. B **103**, 125118 (2021). Copyright 2021 by the American Physical Society. 119

5.3.7 Static structure factor for aluminum ($r_s = 2.07$) computed using PIMC and RPA including LFCs at $\theta = 0.75$ (T=8.77 eV). The ESA results are shown for $\theta = 0$, $\theta = 0.68$ (T=8 eV) and $\theta = 1.03$ (T=12 eV). The TDDFT-XC results are shown from ambient to T=12 eV for q/q_F up to $\sim$1.0. Reprinted figure with permission from **K. Ramakrishna** *et al.*, Phys. Rev. B **103**, 125118 (2021). Copyright 2021 by the American Physical Society. 120

6.0.1 a) Sigmoidal pulse in the $\vec{z}$ direction vs time, b) Induced current density vs time, c) Dynamical electrical conductivity of iron computed using LR-TDDFT (RPA- yellow, ALDA - red) and RT-TDDFT (blue) at ambient conditions. Experimental data stems from Ref. [Paquin, 1995]. 125

.1 List of Acronyms

- ALDA : adiabatic local density approximation
- B3LYP : *Becke*-*3*-parameter-*L*ee–*Y*ang–*P*arr xc functional
- BLYP : *Becke*-*L*ee–*Y*ang–*P*arr xc functional
- BC8 : body centered cubic diamond
- BCC : body centered cubic
- BOMD : Born-Oppenheimer molecular dynamics
- BSE : Bethe-Salpeter equation
- CDOP : *C*orradini-*D*el Sole-*O*nida-*P*alummo parametrization
- CEIMC : coupled electron ion Monte Carlo
- DFT : density functional theory
- DOS : density of states
- DZVP : double-zeta valence polarization basis set
- DZVP-SR : double-zeta valence polarization short-range basis set
- DSF : dynamic structure factor
- EOS : equation of state
- EELS : electron energy loss spectroscopy
- ESA : effective static approximation
- EXX : exact exchange
- FCC : face centered cubic
- FP-LAPW : full-potential linearized augmented plane wave
- GDSMFB : *G*roth-*D*ornheim-*S*jostrom-*M*alone-*F*aulkes-*B*onitz finite temperature XC functional
- GGA : generalized gradient approximation (includes the density and the first derivative in the XC potential)
- GPW Gaussian plane waves
- GW : Green's (*G*) screened interaction (*W*)

- **HCP** : hexagonal close packed
- **HSE** : *H*eyd-*S*cuseria-*E*rnzerhof xc functional
- **IXS** : inelastic x-ray scattering
- **KG** : Kubo-Greenwood formula
- **KS** : Kohn-Sham
- **KSDT** : *K*arasiev-*S*jostrom-*D*ufty-*T*rickey finite temperature XC functional
- **LDA** : local density approximation
- **LFC** : local field correction
- **LRC** : long range correlation
- **LR-TDDFT** : linear-response time-dependent density functional theory
- **MA** : extended Mermin ansatz
- **meta-GGA** : XC functional dependent on higher derivatives of the density (second derivative) than a GGA
- **MD** : molecular dynamics
- **NRIXS** : non-resonant inelastic x-ray scattering
- **PAW** : projector augmented wave
- **PBE** : *P*erdew-*B*urke-*E*rnzerhof xc functional
- **PBE0** : XC functional with 25% Hartree-Fock exchange, 75% PBE exchange and full PBE correlation
- **PIMC** : path integral Monte Carlo
- **PW** : *P*erdew-*W*ang xc functional
- **PZ** : *P*erdew-*Z*unger xc functional
- **QMC** : quantum Monte Carlo
- **RPA** : random phase approximation
- **RT-TDDFT** : real-time time dependent density functional theory
- **SCAN** : *s*trongly *c*onstrained and *a*ppropriately *n*ormed XC functional
- **SZV** : single-zeta valence basis set
- **TDDFT** : time-dependent density functional theory
- **T-LFC** : temperature-dependent local field correction

- **TPSS** : *T*ao-*P*erdew-*S*taroverov-*S*cuseria XC functional
- **TZVP** : triple-zeta valence polarization basis set
- **UEG** : uniform electron gas
- **VASP** : Vienna *ab-initio* simulation program
- **WDM** : warm dense matter
- **XC** : exchange–correlation
- **XRD** : x-ray diffraction
- **XRS** : x-ray Raman scattering
- **XRTS** : x-ray Thomson scattering

.2 Codes Utilized in this Work

- CP2K

  CP2K is a general public license (GPL) code for performing electronic structure calculations using a mix of Gaussian and plane waves method.

- ELK

  ELK is an all-electron full-potential linearised augmented-plane wave (FP-LAPW) code.

- Exciting

  Exciting is an FP-LAPW code. The main emphasis is on the excited states within many-body perturbation theory.

- FDMNES

  Finite difference method near edge structure (FDMNES) is an open source code developed by Institut NEEL for the simulation of x-ray absorption and scattering spectroscopies.

- Quantum ESPRESSO

  Quantum ESPRESSO is a GPL code using pseudopotentials and plane wave basis sets for calculations involving electronic structure.

- VASP

  Vienna Ab initio Simulation Package (VASP) is a proprietary code available under license for performing electronic structure calculations using pseudopotentials, plane wave basis sets and projector augmented wave method (PAW).

- YAMBO

  Yet Another Many Body code (YAMBO) available under GPL for performing calculations involving excited state properties using the Kohn-Sham wavefunctions generated using Quantum ESPRESSO.

Acknowledgments

The work and underlying educational insight portrayed by this study are most prominently a result of the continuous encouragement and inspiration of my supervisor, Jan Vorberger. Jan gave me excellent guidance and established a high level of excellence in cultivating my scientific career.

During my scientific progress there are also other people who have taught me or played a part. I would like to thank Andrew Baczewski, Attila Cangi, Dominik Kraus, Hideaki Takabe, Lingen Huang, Mani Lokamani, Michael Bonitz, Michael Bussmann, Simon Groth, Thomas Cowan, Tobias Dornheim for the general guidance and support.

I owe my family many thanks for the immense support throughout this journey: Amma, Akka, Appa, Anil, Shrudha, Appachu, Sumitra, Ganesh. Thank you for the patience and kindness.

I would also like to thank friends and others from the institute, division, lunch break, football, quizzing for making the journey memorable in no particular order: Alexander Debus, Anja Schuster, Anna Ferrari, Anne Varga, Axel Hübl, Christoph Eisenmann, Florian Brack, Florian Kroll, Francisco Correa, Henrik Schulz, João Branco, Karolina Horodecka, Katja Voigt, Malte Zacharias, Marco Garten, Maximilian Böhme, Melanie Rödel, Nicholas Hartley, Philipp von Haymerle, René Gebhardt, René Widera, Richard Pausch, Uwe Hernandez-Acosta, Weronika Mazur, Wildan Abdussalam, Zhandos Moldabekov.

Statement of authorship

I hereby certify that I have authored this entitled *Ab Initio Simulation of Warm Dense Matter: Combining Density Functional Theory and Linear Response Methods* independently and without undue assistance from third parties. No other than the resources and references indicated in this thesis have been used. I have marked both literal and accordingly adopted quotations as such. There were no additional persons involved in the intellectual preparation of the present thesis. I am aware that violations of this declaration may lead to subsequent withdrawal of the degree.

Dresden, July 11, 2022

Kushal Ramakrishna M.Sc.